

Alma Mater Studiorum – Università di Bologna

RESEARCH DOCTORATE IN

***Mechanics and Engineering Advanced Sciences - Project n° 2:
“Fluid Machines and Energy Systems Engineering”***

Cycle XXV

Affiliation sector: 09/C1

Scientific-disciplinary sector: ING-IND/08

PhD Thesis title

***Theoretical and Experimental Analysis
of
micro-CHP Energy Systems***

Presented by: Dr. Eng. Roberta Vecci

PhD School Coordinator:

***Chiar.mo Prof. Ing.
Vincenzo Parenti Castelli***

Supervisor:

***Chiar.mo Prof. Ing.
Michele Bianchi***

Final exam year 2013

Alma Mater Studiorum – Università di Bologna

DOTTORATO DI RICERCA IN

***Meccanica e Scienze Avanzate dell'Ingegneria –
Progetto n° 2: “Ingegneria delle Macchine e dei Sistemi
Energetici”***

Ciclo XXV

Settore Concorsuale di afferenza: 09/C1

Settore Scientifico disciplinare: ING-IND/08

TITOLO TESI

**Analisi teorico-sperimentale
di
Sistemi Energetici micro-Cogenerativi**

Presentata da: *Dott.ssa Ing. Roberta Vecci*

Coordinatore Dottorato:

Chiar.mo Prof. Ing.
Vincenzo Parenti Castelli

Relatore:

Chiar.mo Prof. Ing.
Michele Bianchi

Esame finale anno 2013

*To my daughter, Alissa
who has endured with patience my choice and
who encourages me to pursue my dreams, every day.*

ACKNOWLEDGMENTS

My thanks to my superiors for welcoming me into their group giving me the opportunity to realize my dream.

My thanks to Professor Giorgio Negri di Montenegro, my professor during the degree years, for whom I have profound respect.

My thanks are to my supervisor, Professor Michele Bianchi, my guide, for his precious teachings and advice.

A sincere thanks to Professor Antonio Peretto, for the total trust he has given me during all these years.

Finally, a thanks are due to laboratory technicians, Mr. Tarì and, especially, Mr. Stefano Benaglia, for their help and total disponibility.

And above all

My heartfelt thanks go to my parents, and to two special persons who always walked to my side "for better or for worse" during all these years.

INTRODUCTION

The micro-CHP (Combined Heat and Power) energy systems, using renewable energy sources are an excellent response to the current issues of environmental impact. Producing, in combined and efficient mode, electricity and heat at low temperature directly on-site, using plants of size less than 50 kWel, they, especially for stationary applications in residential and small industries, represent the realization the energy Distributed Generation (GD) concept, an important strategy in the production scenario in the medium term.

Following this idea, the Ph.D. activity has pursued the aim of conceptual development and subsequent implementation of an Integrated Energy System (IES), capable of meeting the energy requirements and thermal properties of specific users, using different types of fuel, with the integration of electric generators in Renewable Energy Sources (RES), and electric and thermal accumulation systems, totally controlled by an automatic management control system.

To this end, in the first doctoral years the study of micro-CHP energy systems components, such as the combustion chambers of Micro Gas Turbines (MGT), reactors, and pyrolyzer for the production of syngas from scrap tires has been addressed.

Specifically, the thermo-fluid dynamics (CFD) numerical analysis activity of MGT combustion chambers was carried out, evaluating turbulence and combustion models, and also by defining chemical kinetics mechanisms valid for the combustion of syngas, biogas and natural gas. Finally, the validation of the results obtained through the comparison with the experimental data has been made (*De Pascale, M.Fussi, A.Peretto, R.Vecci, "Numerical investigation of a swirled flame model combustor fed with pyrolysis gas," ECOS 2011 - The 24th International*

Conference on Efficiency, Cost, Optimization, Simulation and Environmental Impact of Energy Systems, Novi Sad - Serbia, July 4-7, 2011., - M. Fussi, R.Vecci, 'potential' of renewable fuels "low-Btu" gas turbine "- The search there and you see - Palazzo D'Accursio-Bologna, 28-29 May 2010, Poster).

The need to environmentally recover scrap tires has led to the study (using three-dimensional CFD codes), the design and the definition of the control methods of a pyrolysis pilot plant. The plant is pending patents definition.

Having the availability of a Polymeric Exchange Membrane Fuel Cells (PEMFC), the coupling of which with an electrochemical storage system was developed and tested in a previous Ph.D. activity, at the DIN's (previously DIEM) laboratory, the research has continued with the implementation of the conceptually conceived Integrated Energy System (IES).

After having built the system, the attention has been focused on the energy source of the above system, a 5 kW_{el} PEMFC, on which numerous experimental campaigns for determining the PEMFC system electrical performance (polarization curve, powers, efficiencies of the fuel cell system) and CHP performance (thermal power, optimum cooling system temperatures, heat exchange with users, efficiencies), under different operating conditions.

Furthermore, the degradation mechanisms of the PEMFC system, in particular due to the flooding of the anodic side, have been assessed.

The analysis of the effect of the water management of the anodic exhaust at variable FC loads has been carried out, and the purge process programming logic was optimized, leading also to the determination of the optimal flooding times by varying the AC FC power delivered by the cell.

Then, for the analysis of the fuel (hydrogen, H₂) utilization factor, an algorithm for its calculation from the experimental data, able to determine the amount of not-reacted H₂ and, therefore, the causes which produce the loss has been developed. The algorithm considers the FC like a black box, so it doesn't need access to its internal component and can be applied during the normal FC lifecycle. Through this algorithm the presence of the H₂ crossover phenomenon was experimentally demonstrated.

Therefore, the ageing suffered by the FC system has been analyzed. An experimental tests campaign, comparing recent data with historical ones, was carried out to verify the aging suffered by the cell, the components involved and their main causes.

This thesis is completely dedicated to the detailed description of the latter investigation, conducted on experimental IES realized. This study, joining together theoretical and conceptual realization of an idea and its exploration by innovative mean is, I think, by mechanical engineer "old-fashioned" as I am, the culmination of personal fulfillment from an engineering standpoint.

ABSTRACT

In the framework of the micro-CHP (Combined Heat and Power) energy systems and the Distributed Generation (DG) concept, an Integrated Energy System (IES) able to meet the energy and thermal requirements of specific users, using different types of fuel to feed several micro-CHP energy sources, with the integration of electric generators of renewable energy sources (RES), electrical and thermal storage systems and the control system was conceived and built. A 5 kW_{el} Polymer Electrolyte Membrane Fuel Cell (PEMFC) has been studied. Using experimental data obtained from various measurement campaigns, the electrical and CHP PEMFC system performance have been determined.

The analysis of the effect of the water management of the anodic exhaust at variable FC loads has been carried out, and the purge process programming logic was optimized, leading also to the determination of the optimal flooding times by varying the AC FC power delivered by the cell.

Furthermore, the degradation mechanisms of the PEMFC system, in particular due to the flooding of the anodic side, have been assessed using an algorithm that considers the FC like a black box, and it is able to determine the amount of not-reacted H₂ and, therefore, the causes which produce that.

Using experimental data that cover a two-year time span, the ageing suffered by the FC system has been tested and analyzed.

Keywords

Micro-CHP, Distributed Generation DG, PEMFC, Integrated Energy System

TABLE OF CONTENTS

Nomenclature.....	i
Introduction.....	vii
1. The fuel cell technology.....	1-1
1.1 The history of the fc technology [1-12].....	1-2
1.2 Description of the FC technology.....	1-11
1.3 FCs tipology.....	1-14
1.3.1 The AFC (Alkaline FC)	1-15
1.3.2 The DMFC (Direct Methanol FC).....	1-17
1.3.3 The PAFC (Phosphoric acid fuel cells)	1-19
1.3.4 The MCFC (Molten Carbonate FC)	1-20
1.3.5 SOFC (Solid Oxide FC)	1-23
1.3.6 The PEM (Proton Exchange Membrane FC).....	1-25
1.4 The Proton Exchange Membrane Fuel Cell: PEMFC	1-26
1.4.1 PEMFC: principle of operation and components.....	1-27
1.5 The stack	1-34
1.6 Balance of Plant.....	1-36
1.7 Thermodynamics.....	1-37
1.7.1 Enthalpy of reaction.....	1-37
1.7.2 Reversible cell potential.....	1-38
1.7.3 Voltage losses.....	1-41
1.7.4 Efficiency of the fuel cell.....	1-44

1.7.5	Operating Condition:.....	1-46
1.8	PEMC application and current status.....	1-49
	References to chapter 1.....	1-53
2.	The Integrated Energy System.....	2-1
2.1	The IES test system.....	2-3
2.2	The components of the Integrated Energy System.....	2-11
2.2.1	The fuel cell (FC) system.....	2-11
2.2.2	The batteries and the bidirectional inverter.....	2-24
2.2.3	The photovoltaic (PV) emulator.....	2-32
2.2.4	The electrical load.....	2-34
2.2.5	The control system.....	2-36
2.2.6	Sensors.....	2-40
2.3	The IES operation states.....	2-45
2.4	The FC operation programming logic.....	2-50
	References of the chapter 2.....	2-52
3.	Experimental analysis of thr IES performance.....	3-1
3.1	The acquired and calculated variables.....	3-2
3.2	PEMFC performance analysis.....	3-6
3.2.1	PEMFC electric performance analysis.....	3-6
3.2.2	The FC thermal performance analysis.....	3-28
	References to the chapter 3.....	3-33
4.	The degradation mechanisms of the PEMFC.....	4-1
4.1	The main degradation mechanisms of the PEMFC stack components.....	4-7
4.1.1	Chemical and/or physical effects.....	4-8
4.1.2	Extreme external factors.....	4-15
4.1.3	Poor water management.....	4-18
4.2	Contamination of the PEMFC components.....	4-25
4.3	Hydrogen crossover.....	4-26
	References to the chapter 4.....	4-32
5.	Anodic exhaust management: analysis and optimization.....	5-1

5.1	The hydrogen purging: motivation, limit and optimization strategies	5-3
5.2	Experimental investigation on the effects of purging.....	5-8
5.2.1	Piecewise model of the voltage drop due to flooding...	5-12
5.3	Optimized purging strategy	5-14
5.3.1	Application of the optimized strategy.....	5-16
5.4	Efficiency evaluation of the FC purge programming logic.....	5-21
5.5	Analysis of the utilization coefficient.....	5-27
5.5.1	Effect of the flooding duration.....	5-27
5.5.2	Definition of the not-reacted hydrogen fraction.....	5-28
5.5.3	Algorithm for the evaluation of the not-reacted hydrogen fraction	5-30
5.5.4	Analysis of the efficiency using the fractions X_{DE} and X_A	5-35
5.6	Experimental result.....	5-38
5.6.1	Results of the 2010 tests (Old purge programming logic)	5-39
5.6.2	Results of the 2012 tests (New purge programming logic).....	5-43
	References to the chapter 5	5-56
6.	Ageing of the PEMFC	6-1
6.1	The FC ageing analysis	6-3
	References for Chapter 6.....	6-15
	Conclusions.....	c-1

Nomenclature

Symbols

A	active area
c_w	water specific heat
C	capacity of the battery
E^0	standard state reversible cell potential
E_r	reversible cell potential
$E_{r,T}$	actual cell voltage
F	Faraday constant, $F=96485$ [C/mol]
h_f	heat of formation of a reactant
i	current
$I_{H_2}^{CROSS}$	current induced by H ₂ crossed over
$J_{H_2}^{CROSS}$	H ₂ crossover rate
K	membrane gas permeability
l_{PEM}	membrane thickness
m	mass
\dot{m}	mass flow rate
M_{flow}	volume flow rate
m_{mol}	molecular weight
n	number of electrons
N_{cel}	number of fuel cells in the stack
p	correction factor for grid losses
P	electric power
$P_{H_2}^a$	anodic side H ₂ partial pressure
Q	thermal power
Q_{th}	recovered thermal power
Q_{av}	available thermal power
R	universal gas constant
R_{Ohm}	overall cell resistance
RH	Relative Humidity
T	temperature
T_{fl}	flooding time
T_o	operating time

T_{pu} purge time
 U_o air utilization factor
 U_f fuel utilization factor
 v, V voltage

Greeks

α slope of the straight line of the FC voltage
 α_p activity of the products
 α_R activity of the reactants
 ΔE fuel chemical energy introduced into the FC
 ΔG Gibbs free-energy change
 ΔH enthalpy change
 ΔS entropy change
 ΔT_w CHP water temperature difference
 ΔV_a activation polarization
 ΔV_c mass transport or concentration losses
 ΔV_O Ohmic losses
 ΔV_{fl} FC voltage drop during the flooding time
 ΔV_{max} maximum allowable FC voltage loss
 ΔV_p FC voltage drop during the purge time
 ΔV_{rec} FC voltage recovery after the OCV opening
 δ_{PITM} PITM location
 η efficiency
 θ electrolyte temperature
 $\psi_{H_2}^{PEM}$ H₂ membrane permeability coefficient
 ρ density
 τ time with FC at constant power

Acronyms and subscripts

<i>a</i>	anode
A	refers to H ₂ not-reacted for other causes
AC	Alternate Current
AFC	Alkaline FC
air	of the air
aux	of the auxiliaries
B	blower
Batt	of the battery
BOL	Beginnig Of Life
BOP	Balance Og Plant
BP	Bipolar Plates
<i>c</i>	cathode
CCP	Combined Cooling and Power
<i>cell</i>	refers to fuel cell
CHP	Combined Heat and Power
CO / CO ₂	carbone monoxide /carbone dioxide
D _{PEM}	membrane diffusion coefficient
DC	Direct Current
DE	dead end
DM	Diffusion Media
DMFC	Direct Methanol Fuel Cell
DSP	Digital Signal Processing
DV	Directional Valve
<i>el, ref</i>	reference value for electric production
EOL	End Of Life
FC	Fuel Cell
<i>f</i>	faradaic
<i>fl</i>	flooding
FPGA	Field-Programmable Gate Array
GD	Distributed Generation
GDL	Gas Diffusion Layer
GFC	Gas Flow Channel
GGH	Gas-Gas Humidifier
H ₂ (H ₂)	hydrogen
H ₂ O	water
HHV	Higher Heating Value

HX	Heat eXchanger
HT	High Temperature
IES	Integrated Energy System
in	inlet
id	ideal
<i>L</i>	Liter
LHV	Lower Heating Value
LT	Low Temperature
$M_{\text{through the FC membrane}}$	
MEA	Membrane-Electrode Assembly
mot	motor
N	Normal temperature and pressure conditions
NR	No-Reacted
MCFC	Molten Carbonate FC
O ₂	oxygen
OCV	Outlet Control Valve
OLTC	On-Load Tap-Changer transformer
out	outlet
P	pump
PAFC	Phosphoric Acid FC
PEM	Proton Exchange Membrane
PES	Primary Energy Saving
PID	Proportional-Integral- Derivative controller
PMS	Power Management System
PRV	Pressure Reducing Valve
Pt	platinum
PTFE	PolytetraFluoroEthylene
PITM	Platinum-Into-The-Membrane
pu	purge
rec	recovery
RES	renewable energy source
s, (stack)	of the stack
S	measuring Sensors
SCV	Safety Control Valve
SOC	State Of Charge of the battery
SOFC	Solid Oxide FC

tank of the tank
tot total
th, ref reference value for thermal production
vent loss due to the utilization factor
u output of PID controller
w water

INTRODUCTION

The electricity and heat energy consumption of residential and small businesses units is currently satisfied through the separate supply of electricity and heat. In fact, to date, this requirement is satisfied by a traditional model in which the electricity is generated in large power stations, far from the urban catchment area, and from there, transferred later to individual users through the complex transmission and distribution network.

The thermal energy, instead, is generated directly at the single user via combustion systems for space heating. The above model, although it is well established and tested, is still suffering from multiple disadvantages, in particular a low overall thermodynamic efficiency, not negligible pollutant emissions and the necessary presence of an electricity distribution network, onerous in terms of operating cost and investment. All of this leads to the end user a quite high cost of energy purchased

An alternative to the traditional model are networks of district heating (also named teleheating) which, fed by cogeneration plants, involving the combination of electrical energy production and heat and/or cold generation in a centralized manner. These networks, although solve most of the disadvantages listed above, are still ineffective in terms of pollutant emissions reduction but, most importantly, require a double network of electricity and thermal distribution and, therefore, high costs anyway. Recently is gradually emerging a new concept of energy generation (considered in its three forms: electricity, heat and cold), called "*Distributed Generation*" (GD), that involves the insertion, in metropolitan areas, of multiple high-efficient micro-cogenerative plants, able to satisfy a significant portion of the household, commercial and office buildings energy requirements (electrical, heating and air conditioning).

The outstanding feature of the GD is the ability to combine the well-known thermodynamic benefits of the cogeneration with high perspective performance of the most promising systems for micro-Combined Heat and Power (CHP). This fact involves both a more rational use of the energy resources and a significant simplification of the infrastructure required for the energy conveyance.

In the context of the micro-CHP energy systems, one of those currently most promising for residential uses are the fuel cells (FCs) - based energy.

The fuel cell is an energy conversion device that converts the chemical energy of the fuel (typically hydrogen) directly into electrical energy without the need to go through a combustion process. In fact, because it uses a fuel without carbon atoms and sulfur emission pollutants such as CO, CO₂, NO_x and SO_x and particulates and metals are not present. The only product of the FC is the 'water, originating from the oxidation of hydrogen.

The hydrogen, however, is not present in nature as a single molecule, but it is necessary to produce it. To date, despite the promotion of the development of clean technologies for hydrogen production (e.g. by algae or bacteria exploiting solar energy), unfortunately the most economically advantageous industrial systems are those that use fossil fuels as a fuel, in particular methane. Currently, the only alternative used is the electrolysis process, which through the electrolytic cell powered by direct current, allows the water molecule splitting into hydrogen and oxygen. Clearly, this alternative is only viable if the process used for the production of the electrical energy required for the process comes from renewable sources, such as biomass, hydropower, wind power and photovoltaic. Consequently, the massive diffusion of hydrogen will occur only when these sources will be economically competitive with conventional sources.

Nevertheless, nowadays, all industrialized countries are promoting "H₂ economy", that is, a society based on the use of hydrogen and electricity seen as clean energy carriers, both derived from fossil fuels in the first development and from renewable (and possibly also by nuclear power) in a later and permanent phase.

The fuel cell is therefore a direct application of two highly topical issues in industrialized countries, i.e. the hydrogen as a potential fuel of the future to cope with the problems of air pollution, in particular the increase in greenhouse gases, and the scarcity of primary energy sources used up to now. In fact, although the extraction technologies and geology techniques for the discovery of new fields are in continuous development, the developing countries energy demands and the world's population are still strongly increasing. It is estimated that the population will amount to 8.5 billion in 2020 and 10 billion in 2050 (<http://www.bp.com>).

Therefore is in this context that the fuel cell (FC) energy systems are inserted. In fact, they have energy efficiency significantly higher than that of conventional systems. This property coupled with their different operating principle lead to a significant reduction of the amount of carbon dioxide (CO₂) emitted, on equal power and heat products. The reduced local air pollutants emissions are also coupled to an extremely low noise level (less than 60 dBA at 10 meters), due the absence of great alternative moving mechanical components like the ones in compressors and internal combustion engines. Another characteristic that distinguishes the FC systems is the modularity, which offers the possibility of increasing the installed power in proportion to the growth of the electricity request, with considerable economic savings and considerably reduced construction times.

To maximize the benefits from distributed generation in terms of service continuity and participation to the energy free market, energy systems that can operate even in stand-alone mode or when the network to which they belong is disconnected from the main national ones are sought. For both traditional and innovative type distributed generation systems such as fuel cells or solar photovoltaic (PV) panels, the island mode operation is made possible by the presence of energy storage systems and the development of systems that implement energy management logics.

It is in this context that the research carried out in this Ph.D. thesis is inserted. The aim of this work was the study and implementation of a micro-Combined Heat and Power (micro-CHP) Integrated Energy System (IES) capable of responding to the electric and thermal energy demands of specific users, using

different types of fuel, with the integration of renewable energy sources (RES) electric generators and electric and thermal storage systems.

The system has been realized in the laboratory of the Departement of Industrial (DIN) and, to date consists of a 5 kWel Polymeral Exchange Membrane (PEM) FC from 5 kWel, as micro-CHP energy source, powered by hydrogen taken directly from cylinders, from a 100 Ah lead-acid battery storage system and a 500 W photovlotaic (PV) module emulator, all connected to a 230 V AC bus through the inverters with specific characteristic. Also electric active and reactive loads are present, feed by the common AC bus.

The developed integrate energy system (IES) is able to operate both in stand-alone operating conditions, in which the energy system feeds the load and in grid connected operating conditions, in which the energy system is connected with the national distribution network. The passage from one to the other above operating conditions is allowed by the battery bidirectional inverter.

The key features of the IES are essentially the flexibility and the dynamicity. In fact the system must be able to operate to vary the number and type of the micro-CHP sources, the available type of fuel and any renewable energy source. Furthermore, regardless of the number and type of components, the IES must be able to meet the variable heat demand of the electricity and heat from the users.

One of the major problems affecting the development of this technology is the lifetime that to date is still excessively short.

The research conducted and exposed in this PhD thesis has addressed this problem by making an innovative contribution that consists in the development of external indices by which is possible monitor not only the electric and CHP performance but also the degradation of the PEMFC during the useful life

In fact, particular attention has been focused on the PEMFC, present into the IES, performance with a black box, component of the IES, without analyzing the individual sub-component (single elementary cells, bipolar plates, electrodes, gas diffusion layers, membrane, etc.) and not with post-mortem inspection of its individual components, as generally done until now.

Specifically, in this Ph.D. thesis:

- *Chapter 1* provides a description of the FC technology, with a brief summary of the technology history and of the different typological FC. In this chapter are also described the principle of operation, the characteristics and the thermodynamics that govern the FC system, focusing in particular on PEM fuel cell type.

- *Chapter 2* describes in detail the developed Integrated Energy System (IES), all its individual components and the principles of operation.

- *Chapter 3* shows the experimental test campaigns carried out on the IES in order to analyze the electric and thermal performance at variable load of the PEMFC in study.

- *Chapter 4* present a brief description of the main degradation mechanisms that affected the PEMFC technology, as reported in the literature.

- *Chapter 5* describes the experimental analysis performed on the PEMFC degradation mechanisms. In particular, the investigations of the flooding at the anode side of the stack and the anodic exhaust management optimization developed have been here illustrated. Furthermore, the fuel utilization factor analysis and the developed algorithm for calculating the amount of the hydrogen (H_2) reacted, not-reacted and expelled through the dead-end valve and of the H_2 not-reacted due to crossover phenomenon are shown.

- *Chapter 6* describes the analysis carried out on the aging of the PEMFC, whereas 50 h of not-continuous operation, which led to show that the main cause of the PEMFC performance degradation at low loads is due to the H_2 crossover mechanism.

Chapter 1

THE FUEL CELL TECNOLOGY

Fuel cells (FCs) are defined as electrochemical device that directly convert chemical energy stored in fuels such as hydrogen to electrical energy.

Unlike internal combustion engines, the fuel is not combusted, but the energy is released electrocatalytically. This allows to FCs to be a low emission energy sources and also to own highly energy efficient, especially if the heat produced by the reaction is also harnessed for space heating, hot water or to drive refrigeration cycles. In fact the FCs efficiency can reach as high as 60% in electrical energy conversion and overall 80% in co-generation of electrical and thermal energies with reduction in main pollutants greater than 90% [1].

1.1 THE HISTORY OF THE FC TECHNOLOGY [1-12]

Although the FC is considered a modern technology, its invention dates back more than two centuries ago. But it was only after the Second World War that the technology began to be seen as promising technological solution and its development was promoted.

In the 1830s, a Welsh judge and physical scientist, *Sir William Grove* (1811-1896) conducted a series of experiments on water electrolysis. His device (Figure 1.1) consisted of two platinum electrodes dipped into water acidified with sulfuric acid. After disconnecting the current, the electrodes, at which hydrogen and oxygen had been evolved earlier as gases, were polarized, that is, a certain potential difference was preserved between them. When in this state they were linked by an external circuit, a current was found to flow in this circuit. Grove called his invention a “voltaic battery”. His results were published in 1839 in the *Philosophical Magazine*. This date is historically regarded as the beginning of fuel cells, although Grove himself did not regard his battery as a practical means for producing electrical energy.

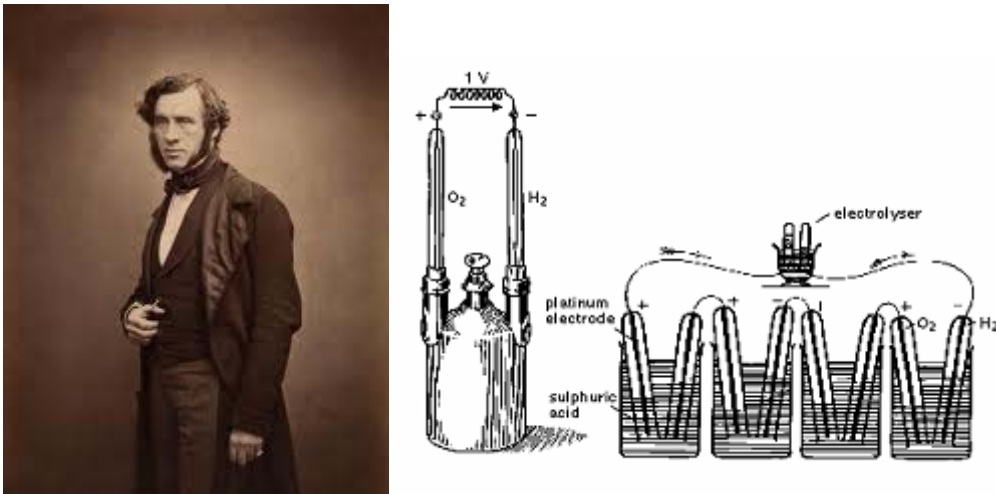


Figure 1.1: *W. Grove* (1811-1896) and the “*Grove's cell*” present in the letter “*On the Gas Voltaic Battery*”.

In 1889, *Ludwig Mond* and *Carl Langer* conducted relatively successful experiments concerning the generation of electric currents using hydrogen-oxygen cells. They researched fuel cells using coal gas as a fuel. For the first time, the “fuel cell” term was used. Further attempts to convert coal directly into electricity were made in the early twentieth century but the technology generally remained obscure.

In 1894 the German physical chemist *Friedrich Wilhelm Ostwald* (1853-1932, Nobel Prize 1909) overcame the limitation of heat engines by eliminating the interim stage of fuel combustion (the formation of thermal energy), using single-step conversion of the fuel’s chemical energy into electrical energy. He proposed to build devices for the direct oxidation of natural fuels with the oxygen of the air, using the electrochemical mechanism occurring in ordinary batteries (“cold combustion” of natural fuels). A device to perform this direct conversion was named “fuel cell”.



Figure 1.2: *Friedrich Wilhelm Ostwald* (1853-1932), Nobel Prize 1909.

In the 1920 the cell research is promoted in Germany leading the way in the development cycle and carbonate cells "solid oxide fuel cells (SOFC)" today. Meanwhile is discovered and understood the process of the combustion chamber and the oil begins to spread.

In 1932, Cambridge engineering professor *Francis Thomas Bacon* (1904 – 1992) developed the first AFC but it was not until 1959 that Bacon demonstrated a practical 5 kW fuel cell system. At around the same time, Harry Karl Ihrig fitted a modified 15 kW Bacon cell to an Allis-Chalmers agricultural tractor. Allis-Chalmers, in partnership with the US Air Force, subsequently developed a number of fuel cell powered vehicles including a forklift truck, a golf cart and a submersible vessel.



Figure 1.3: *Francis Thomas Bacon* (1904 – 1992) and his AFC.

Then, only in the late 1950s and early 1960s NASA, in collaboration with industrial partners, began developing fuel cell generators for manned space missions. The first PEMFC unit was one of the results of those partnerships this, with *Willard Thomas Grubb* at General Electric (GE) credited with the invention. Another GE researcher, *Leonard Niedrach*, refined Grubb's PEMFC by using platinum as a catalyst on the membranes. The Grubb-Niedrach fuel cell was further developed in cooperation with NASA, and was used in the Gemini space program of the mid-1960s.

Contextually, International Fuel Cells (IFC, later UTC Power) developed a 1.5 kW AFC for use in the Apollo space missions. The fuel cell provided electrical power as well as drinking water for the astronauts for the duration of their mission. IFC subsequently developed a 12 kW AFC, used to provide onboard power on all space shuttle flights. While research was continuing on fuel cells in the West, in the Soviet Union fuel cells were being developed for military applications, although much of this early work is still secret. On the other hand, General Motors (GE) had experimented with its hydrogen fuel cell powered Electrovan fitted with a Union Carbide fuel cell. Although the project was limited to demonstrations, it marked one of the earliest road-going fuel cell electric vehicles (FCEV). From the mid-1960s, Shell was involved with developing DMFC, where the use of liquid fuel was considered to be a great advantage for vehicle applications.

In the 1970s the emergence of air pollution promoted clean air legislation in the United States and Europe. This mandated the reduction of harmful vehicle exhaust gases. At the same time, the OPEC oil embargo there was. This led governments, businesses and consumers to embrace the concept of energy efficiency. Clean air and energy efficiency were to become two of the principal drivers for fuel cell adoption in subsequent decades, in addition to the more recent concerns about climate change and energy security. Moreover, concerns over oil availability led to the development of a number of one-off demonstration fuel cell vehicles, including models powered by hydrogen or ammonia, as well as of hydrogen-fuelled internal combustion engines. Many German, Japanese and US vehicle manufacturers began to experiment with FCEV, increasing the power density of PEMFC stacks and developing hydrogen fuel storage systems. The, the focus shifted back to pure hydrogen fuel, which generates zero harmful emissions. Concerns over energy shortages and higher oil prices, also prompted the PAFC technology. There were significant field demonstrations of large stationary PAFC units for prime, off-grid power, including a 1 MW unit developed by IFC.

Furthermore, funding from the US military and electrical utilities enabled developments in MCFC technology, such as the internal reforming of natural gas to hydrogen. The use of an established natural gas infrastructure was a key advantage in developing fuel cells for large stationary prime power applications.

Also in the 1980s, technical and commercial development continued in particular for the PAFCs. Several experimental large stationary PAFC plants were built, but saw little commercial traction. With subsequent advancements in membrane durability and system performance, PAFC were rolled out in greater numbers almost two decades later for large-scale combined heat and power applications.

US Navy commissioned studies for the use of fuel cells in submarines where highly efficient, zero-emission, near-silent running offered considerable operational advantages.

In 1983 the Canadian company *Ballard* began research into fuel cells, and was to become a major player in the manufacture of stacks and systems for stationary and transport applications in later years.

In the 1990s the attention turned to PEMFC and SOFC technology particularly, for small stationary applications. These were seen as offering a more imminent commercial possibility, due to the lower cost per unit and greater number of potential markets - for example backup power for telecoms sites and residential micro-CHP. In Germany, Japan and the UK began to be significant government funding devoted to developing PEMFC and SOFC technology for residential micro-CHP applications.

Government policies to promote clean transport also helped drive the development of PEMFC for automotive applications. The California Air Resources Board (CARB) introduced the Zero Emission Vehicle (ZEV) Mandate. This was the first vehicle emissions standard in the world predicated not on improvements to the internal combustion engine (ICE) but on the use of alternative power trains. Carmakers such as the-DaimlerChrysler, General Motors, and Toyota, all of which had substantial sales in the US, responded to this by investing in PEMFC research. Companies other than automakers, such as Ballard, continued PEMFC research for automotive and stationary clean power. Ballard went on to supply PEMFC units to Daimler and Ford. The programmes initiated in the 1990s still continue, albeit with some changes to the strategic focus of some key players.

Significant advances in DMFC technology occurred around the same time, as PEMFC technology was adapted for direct methanol portable devices. Early applications included portable soldier-borne power and power for devices such as laptops and mobile phones.

MCFC technology, first developed in the 1950s, made substantial commercial advances, in particular for large stationary applications in which it was sold by companies such as Fuel Cell Energy and MTU.

SOFC technology also underwent substantial developments in terms of power density and durability for stationary applications. Boosted by general optimism in high-technology industries, many fuel cell companies listed on stock exchanges in the late 1990s, only for prices to fall victim to the crash in technology stocks shortly after.

The 2000s were characterized by increasing concerns on the part of governments, business and consumers over energy security, energy efficiency, and carbon dioxide (CO₂) emissions. Attention has turned once again to fuel cells as one of several potential technologies capable of delivering energy efficiency and CO₂ savings while reducing dependence on fossil fuels.

Government and private funding for fuel cell research has increased markedly in the last decade. There has been a renewed focus on fundamental research to achieve breakthroughs in cost reduction and operational performance to make fuel cells competitive with conventional technology. A good deal of government funding worldwide has also been targeted at fuel cell demonstration and deployment projects. The European Union, Canada, Japan, South Korea, and the United States are all engaged in high-profile demonstration projects, primarily of stationary and transport fuel cells and their associated fuelling infrastructure. The genuine benefits that fuel cell technology offers over conventional technologies has played a part in promoting adoption. Several fuel cell buses were deployed in the mid-2000s as part of the HyFleet/CUTE project in Europe, China and Australia. Buses were, and still are, seen as a promising early market application of fuel cells due to their combination of high efficiency, zero-emissions and ease of refueling, and due to the vehicles running on set routes and being regularly refueled with hydrogen at their bases.

In the 2007, fuel cells began to become commercial in a variety of applications, when they started to be sold to end-users with written warranties and service capability, and met the codes and standards of the markets in which they were sold. As such, a number of market segments became demand driven, rather than being characterized by oversupply and overcapacity. In particular, thousands of PEMFC and DMFC auxiliary power units (APU) were commercialized in leisure applications, such as boats and campervans, with similarly large numbers of micro fuel cell units being sold in the portable sector in toys and educational kits. Demand from the military also saw hundreds of DMFC and PEMFC portable power units put into service for infantry soldiers, where they provided power to communications and surveillance equipment and reduced the burden on the dismounted soldier of carrying heavy battery packs.

A large-scale residential CHP program in Japan helped stimulate commercial stationary PEMFC shipments. These units began to be installed in homes from 2009 Demonstration programs for backup power systems in the USA gave further impetus to the stationary sector. This was also driven by practical concerns over the need for reliable backup power for telecoms networks during emergencies and rescue operations. The inadequacy of diesel generators was illustrated during the Gulf of Mexico Hurricane Katrina disaster, when many ran out of fuel, disrupting the telecoms network and hampering relief efforts. The need for reliable on-grid or off-grid stationary power in developing countries also gave a boost to fuel cells.

Hydrogen and natural gas fuelled PEMFC units began to be sold in parts of India and east Africa to provide primary or backup power to mobile phone masts. The rapidity of mobile phone adoption in these regions means that the conventional grid infrastructure cannot keep pace with new power demands, or is too unreliable for an effective mobile network. Fuel cells provide a solution to this previously unmet need.

In transport applications, the greatest commercial activity occurred in the materials handling segment, where there is a strong business case for their use in place of the incumbent technology, lead acid batteries. Funding for demonstration fleets of fuel cell materials handling vehicles saw increasing numbers deployed in warehouses across the USA, although the overall numbers remained small

compared with those for stationary and portable fuel cells. Fuel cell buses have been commercially available for several years and their usefulness has been well demonstrated. However their cost, at around five times that of a diesel bus, plus the cost of hydrogen infrastructure means that they are only used where a city deems the environmental benefit to be worth the extra investment. Fuel cell cars are currently only available for lease; these vehicles are being made available by manufacturers to gain experience ahead of a commercial launch planned from 2015.

In the past decade, PEMFC and DMFC have dominated the total market share in the portable, stationary and transport sectors. Their uptake by consumers has been facilitated by the development of codes, standards and government policies to lower the barriers to adoption; such as allowing methanol fuel cartridges on board of aircraft and feed-in tariffs for fuel cell CHP installations.

Over the last five years growth in shipments of fuel cells has accelerated rapidly as various applications have become commercial. Portable fuel cells saw the most rapid rate of growth over the period since 2009 as increasing numbers of fuel cell educational kits were sold to consumers. This genuine commercial market generated much-needed revenue for several key players and has allowed those companies to invest in research into larger stationary and transport applications. The portable sector has also been boosted by shipments of APU products for the leisure market, in particular camping and boating. Shipments in the portable sector were also augmented by the launch of Toshiba's Dynario fuel cell battery charger in 2009. On a limited production run of 3,000, demand for the Dynario far outstripped supply. Stationary fuel cell adoption has increased rapidly as the roll-out of the Japanese Ene-Farm project took place and fuel cells for uninterruptible power supplies (UPS) were adopted in North America.

The supply chain has also been steadily growing alongside the increase in the number of fuel cell system manufacturers. There has been an expansion of the component supply chain and related services, from the manufacturers of MEA to fuel and infrastructure providers. Manufacturing capacity has tended to increase more rapidly than output. This is particularly true in North America, one of the leading regions for fuel cell manufacturing.

The global economic recession of the late 2000s undoubtedly had negative effects for certain fuel cell companies. Limited credit availability and restrictions in government funding, as well as lack of profitability for organizations that were still mainly R&D focused, caused a number of firms to go out of business.

The fuel cell industry has faced and continues to face challenges as it comes through a period of recession and completes the transition from R&D to commercialization. On the whole, it has survived extremely difficult circumstances. Although many fuel cell companies are still far from being profitable, the opportunities for growth in the future are very promising. The success of certain application segments in recent years means that there has been a move to consolidate particular technologies into a standard reference design for a particular type of fuel cell. This has led to fuel cells increasingly being developed as scalable energy solutions capable of serving several different market segments, be they APU or to power devices such as unmanned aerial vehicles (UAV).

1.2 DESCRIPTION OF THE FC TECHNOLOGY

As it defined by its inventor Grove, a fuel cell (FC) is a “galvanic cell”, e.g. a device that generates electrical energy by converting the energy of chemical reactions. Other varieties of electrochemical power sources are the throw-away batteries for domestic use and storage batteries, used for example in automobiles, personal computers, cell phones.

On the contrary of these batteries, in which the chemical reactions are used to create electricity, and the reacting materials, as well as the reaction products, are typically metals or other solid compounds (oxides, salts, etc.) In fuel cells both the reactants and the products are typically liquids or gases. This permits the continuous supply of reactants to the cells and a continuous removal of the reaction products. Thus, fuel cells can be used for power generation without interruption, as long as the reactants are continuously supplied and the reaction products are removed, without the need to be recharged and/or discharged.

The FC consists of two porous electrodes separated by an electrolyte which carry out the electrochemical conversion of the energy contained in the fuel introduced to one of the two electrodes.

Although FCs are classified according to the type of electrolyte, because it changes in a decisive way the kinetics and the type of chemical reactions, they present anyway similar thermodynamic principles and gas diffusion mechanisms to the electrodes. In particular, a FC unit consists of a stack, which is composed of a number of individual cells.

Each cell (Figure 1.4) within the stack has two electrodes, one positive called the cathode, and one negative, called the anode. The reactions that produce electricity take place at the electrodes. Every fuel cell also has either a solid or a liquid electrolyte, which carries ions from one electrode to the other, and a catalyst, which accelerates the reactions at the electrodes. The electrolyte plays a key role - it must permit only the appropriate ions to pass between the electrodes. If free electrons or other substances travel through the electrolyte, they disrupt the chemical reaction and lower the efficiency of the cell.

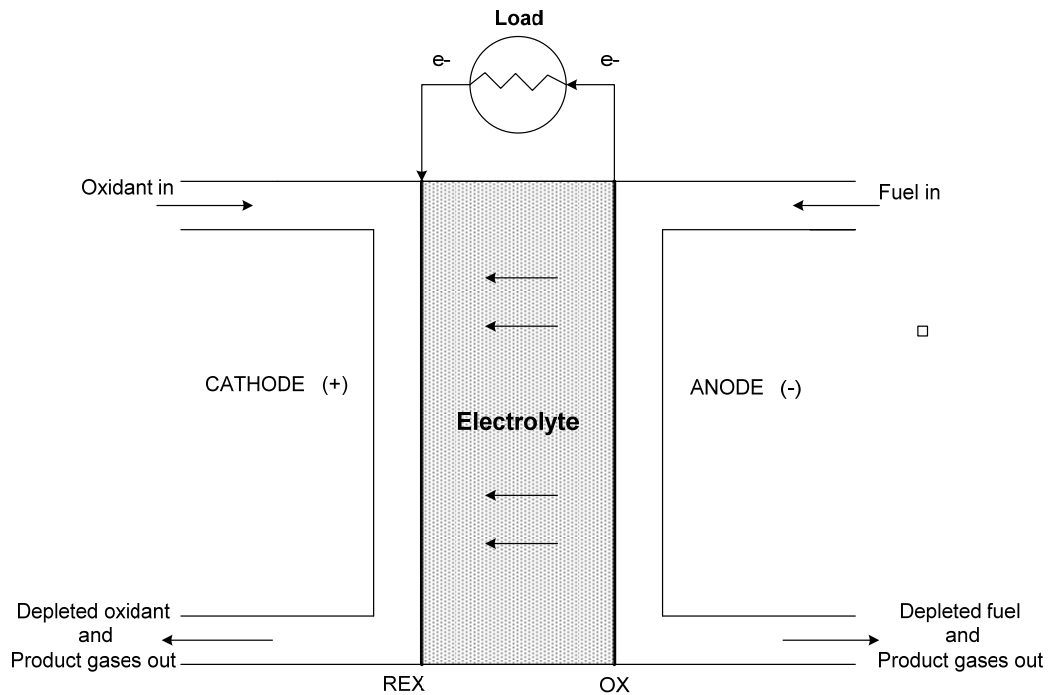


Figure 1.4: Single cell scheme.

Precisely, the reacting gases, hydrogen and oxygen (typically is air), are supplied to the individual electrodes. The overall reaction is split into two partial reactions. On anode, hydrogen molecules are oxidized, that is, they transfer their electrons to the metallic electrode with the formation of positive hydrogen ions (protons). At the other electrode, the cathode, oxygen molecules are reduced, that is, electrons are transferred to them from the metallic electrode. These two partial reactions taken together yield the same product as the overall reaction. Thus, in the electrochemical reaction scheme, the overall reaction occurs as two partial reactions spatially separated at two different electrodes immersed into the electrolyte solution. During this reaction, the anode acquires electrons and becomes negatively charged, while the cathode loses electrons and becomes positively charged. To avoid accidental contacts between anode and cathode (producing an internal short of the cell) and to avoid the intermixing of the fuel and oxygen, an insulating porous separator is often placed in the gap between the two electrodes.

When the two electrodes are connected outside the cell through some electrical device, the electrons flow from the anode (the negative pole of the cell) to the cathode (positive pole). Within the cell, the hydrogen ions formed at the anode are

transferred to the cathode where they participate in the electrode reaction. The moving ions in the solution and electrons in the metal together yield a closed electrical circuit. When the circuit is closed through the external device, the partial reactions proceed and the external electric current is maintained continuously, as long as the reacting gases are supplied to the electrodes. Thus, some of the chemical energy of the overall reaction is converted to electrical energy used in the external device. The remaining part of the chemical energy is lost for practical purposes and it is dissipated as heat, because extra energy is needed to force the reaction to proceed at a finite rate (overvoltage). However, this loss can be considerable less than the loss occurring in the conventional thermal-mechanical-electrical energy conversion systems.

1.3 FCs TIPOLOGY

Fuel cell types are generally classified according to the nature of the electrolyte they use. Although each type requires particular materials, fuels, operation temperature and is suitable for different applications.

The main FC typologies are seven:

- PEM (Proton Exchange Membrane FC)
- AFC (Alkaline FC)
- DMFC (Direct Methanol FC)
- PAFC (Phosphoric Acid FC)
- MCFC (Molten Carbonate FC)
- SOFC (Solid Oxide FC)

The first four types (AFC, PEMFC, and DMFC) are called low temperature FCs, while the last two (PAFC, MCFC and SOFC) are known as middle and high-temperature FCs. The characteristics for each type are summarized in Table 1.1.

	PEMFC	PAFC	MCFC	SOFC
Temperature [°C]	60÷110	190÷200	600÷700	650÷900
Pressure [atm]	1÷3	1÷8	1÷8	1÷14
Size (Pel) [kW]	1÷250	100÷1000	250÷10000	1÷10000
Efficiency [%]	30÷40%	38÷45%	45÷55%	45÷60%
Power density [mW/cm²]	~700	~200	~160	200(circular) 500(planar)
Fuel	H ₂	H ₂	H ₂ /CH ₄ /CO	H ₂ /CH ₄ /CO
Oxidant	O ₂ /Air	O ₂ /Air	O ₂ /Air/CO ₂	O ₂ /Air
Impurity Tolerance	CO<10 ppm	CO< 1% H ₂ S,COS<50ppm	H ₂ S,COS<1 ppm	H ₂ S < 1 ppm
Reforming	Ext. or int.	External	Ext. or int.	Ext. or int.
Cogenerazione	Water @ 70-80°C	Water/steam	Steam	Steam

Table 1.1: The FC properties for each typology

1.3.1 THE AFC (ALKALINE FC)

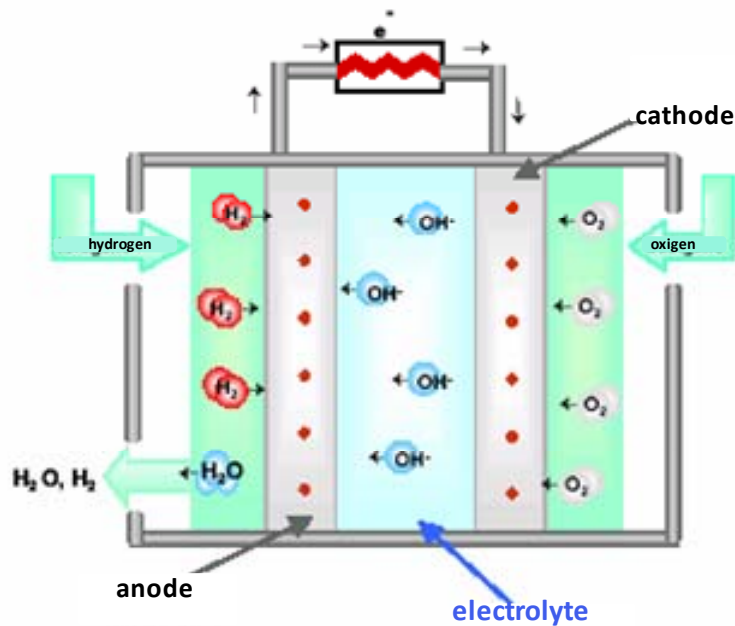
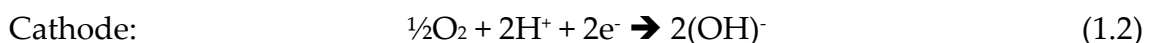
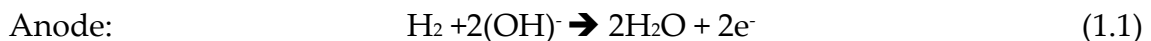


Figure: 1.5: The AFC scheme.

AFCs use an alkaline electrolyte such as potassium hydroxide in water and are generally fuelled with pure hydrogen. The first AFCs operated at between 100 °C and 250 °C but typical operating temperatures are now around 70 °C. As a result of the low operating temperature, it is not necessary to employ a platinum catalyst in the system and instead, a variety of non-precious metals can be used as catalysts to speed up the reactions occurring at the anode and cathode. Nickel is the most commonly used catalyst in AFC units.

The reactions that occur to the electrodes are:



The oxygen reduction reaction and hydrogen oxidation taking place within the alkaline medium involving hydroxyl ions. The hydroxyl ion formed by the cathodic reduction of the water migrates through the electrolyte, to the anode, where, recombining with hydrogen, just oxidized to produce water.

Due to the rate at which the chemical reactions take place these cells offer relatively high fuel to electricity conversion efficiencies, as high as 60% in some applications [13].

One of the major problems of an AFC is the formation of carbonates, through the oxidation of the carbon support present on the electrode "gas diffusion" (in open circuit condition), it clogs the pores rapidly decreasing the performance of the cell, By the recirculation of the solution of KOH, however, avoids the formation of carbonates. Furthermore, the carbon dioxide can be removed from the hydrogen and the air stream through a system "iron-sponge", which is similar to the shift reaction which takes place in a reformer, or via the CO₂ absorption swing.

This type of fuel cell was the first to be developed, but due to their sensitivity to the presence of carbon dioxide have been progressively abandoned in favor of other types of cell. Remain very promising if you have pure hydrogen.

1.3.2 THE DMFC (DIRECT METHANOL FC)

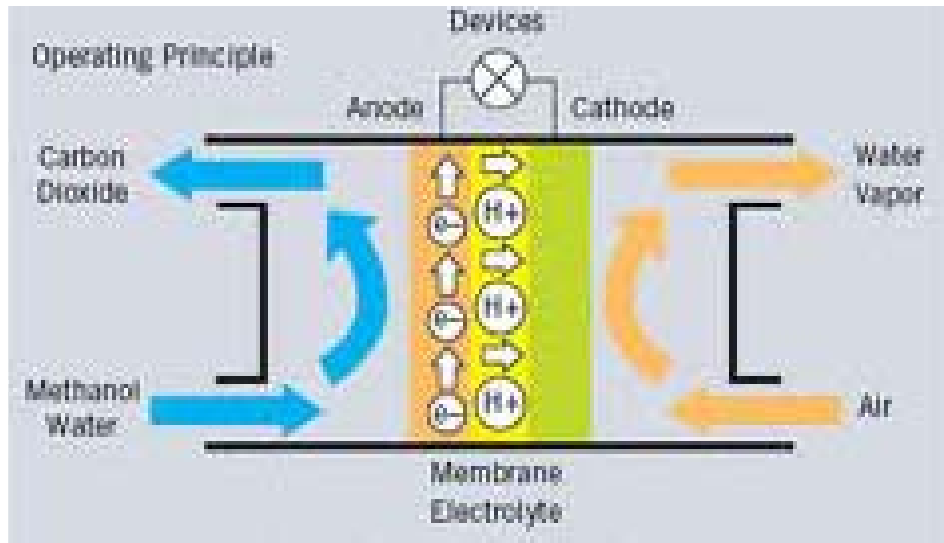


Figure 1.6: The DMFC scheme.

DMFC uses a polymer membrane as an electrolyte. However, the platinum-ruthenium catalyst on the DMFC anode is able to draw the hydrogen from liquid methanol, eliminating the need for a fuel reformer. Therefore pure methanol can be used as fuel, hence the name.

The reactions at the electrodes are:



Methanol offers several advantages as a fuel. It is inexpensive but has a relatively high energy density and can be easily transported and stored. It can be supplied to the fuel cell unit from a liquid reservoir which can be kept topped up, or in cartridges which can be quickly changed out when spent.

DMFCs operate in the temperature range from 60 °C to 130 °C and tend to be used in applications with modest power requirements, such as mobile electronic devices or chargers and portable power packs. One particular application for DMFC power units for commercial materials handling vehicles. A number of these units have been sold to commercial warehouses, where the forklift trucks had been conventionally powered with battery packs. By switching to fuel cells, the warehouses can refuel their trucks in a matter of minutes, compared to the hours it would take to charge a battery. The fuel cells also eliminate the need for a battery charging infrastructure within the warehouse, thereby making more floor space available for other uses.

1.3.3 THE PAFC (PHOSPHORIC ACID FUEL CELLS)

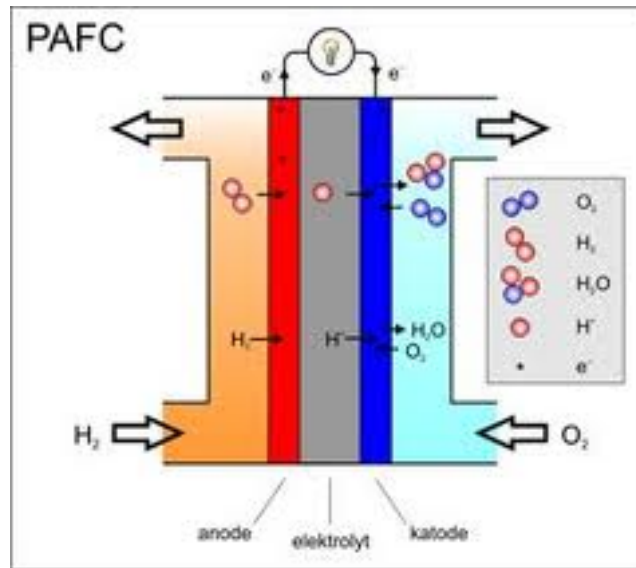
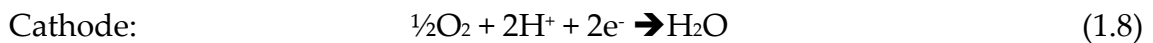
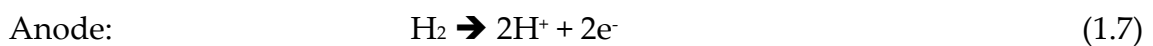


Figure 1.7: The PAFC scheme.

PAFCs consist of an anode and a cathode made of a finely dispersed platinum catalyst on carbon and a silicon carbide structure that holds the phosphoric acid electrolyte.

The reactions at the electrodes are:



They are quite resistant to poisoning by carbon monoxide but tend to have lower efficiency than other fuel cell types in producing electricity. However, these cells operate at moderately high temperatures of around 180°C and overall efficiency can be over 80% if its process heat is harnessed for cogeneration.

This type of fuel cell is used in stationary power generators, with output in the 100 kW to 400 kW range, to power many commercial premises around the world, and they are also finding application in large vehicles such as buses. Most fuel cell units sold before 2001 used PAFC technology.

1.3.4 THE MCFC (MOLTEN CARBONATE FC)

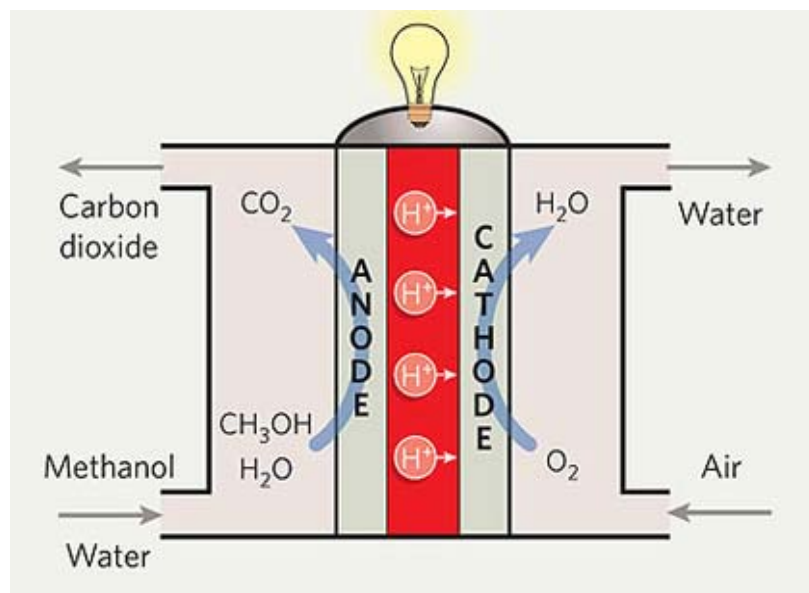
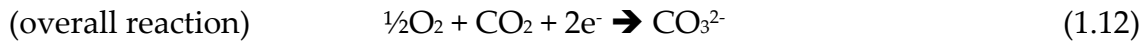


Figure 1.8: The MCFC scheme.

Molten carbonate fuel cells (MCFCs) use a molten carbonate salt suspended in a porous ceramic matrix as the electrolyte. Salts commonly used include lithium carbonate, potassium carbonate and sodium carbonate.

The reactions at the electrodes are:

- Using hydrogen as fuel:



- Using carbone monoxide as fuel:



They operate at high temperature, around 650 °C and there are several advantages associated with this. Firstly, the high operating temperature dramatically improves reaction kinetics and thus it is not necessary to boost these with a noble metal catalyst. The higher temperature also makes the cell less prone to carbon monoxide poisoning than lower temperature systems. As a result, MCFC systems can operate on a variety of different fuels, including coal-derived fuel gas, methane or natural gas, eliminating the need for external reformers.

Disadvantages associated with MCFC units arise from using a liquid electrolyte rather than a solid one and the requirement to inject carbon dioxide at the cathode as carbonate ions are consumed in reactions occurring at the anode. There have also been some issues with high temperature corrosion and the corrosive nature of the electrolyte but these can now be controlled to achieve a practical lifetime.

MCFCs are used in large stationary power generation. Most fuel cell power plants of megawatt capacity use MCFCs, as do large combined heat and power (CHP) and combined cooling and power (CCP) plants. These fuel cells can work at up to 60% efficiency for fuel to electricity conversion, and overall efficiencies can be over 80% in CHP or CCP applications where the process heat is also utilized.

1.3.5 THE SOFC (SOLID OXIDE FC)

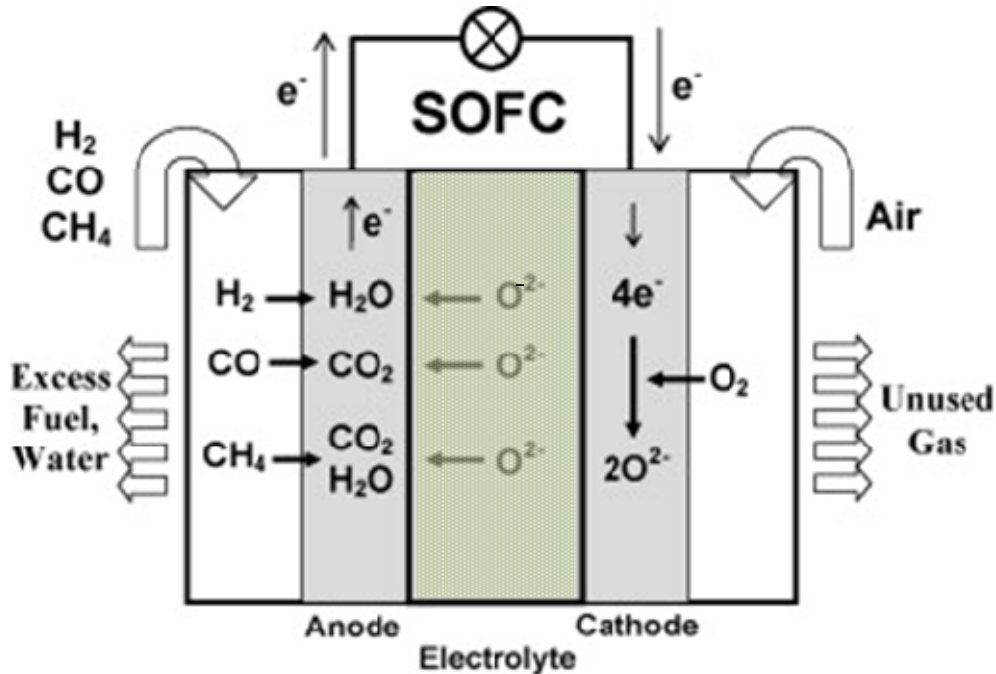
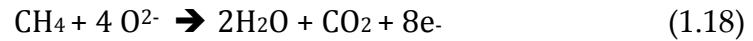
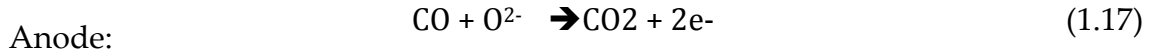


Figure 1.9: The SOFC scheme.

SOFCs use a solid ceramic electrolyte, such as zirconium oxide stabilized with yttrium oxide, instead of a liquid or membrane. Their high operating temperature means that fuels can be reformed within the fuel cell itself, eliminating the need for external reforming and allowing the units to be used with a variety of hydrocarbon fuels. They are also relatively resistant to small quantities of sulphur in the fuel, compared to other types of fuel cell, and can hence be used with coal gas.

This FC typology work at very high temperatures, the highest of all the fuel cell types at around 800 °C to 1,000 °C. They can have efficiencies of over 60% when converting fuel to electricity; if the heat they produced is also harnessed; their overall efficiency in converting fuel to energy can be over 80%.

The reactions at the electrodes are:



A further advantage of the high operating temperature is that the reaction kinetics are improved, removing the need for a metal catalyst. There are however some disadvantages to the high temperature: these cells take longer to start up and reach operating temperature, they must be constructed of robust, heat-resistant materials, and they must be shielded to prevent heat loss.

There are three different SOFC geometries: planar, coplanar and micro-tubular. In the planar design, components are assembled in flat stacks where the air and hydrogen traditionally flow through the unit via channels built in to the anode and cathode. In the tubular design, air is supplied to the inside of an extended solid oxide tube (which is sealed at one end) while fuel flows round the outside of the tube. The tube itself forms the cathode and the cell components are constructed in layers around the tube.

SOFCs are used extensively in large and small stationary power generation: planar types find application in, for example, Bloom Energy's 100 kW off-grid power generators and SOFCs with output of a few kilowatts are being tested for smaller cogeneration applications, such as domestic combined heat and power (CHP). Micro-tubular SOFCs with output in the watt range are also being developed for small portable chargers.

1.3.6 THE PEM (PROTON EXCHANGE MEMBRANE FC)

This typology of the fuel cell will be described in detail in the next paragraph, being the FC type that has been studied and implemented in the experimental plants realized in the PhD years and described in this thesis.

1.4 THE PROTON EXCHANGE MEMBRANE FUEL CELL: PEMFC

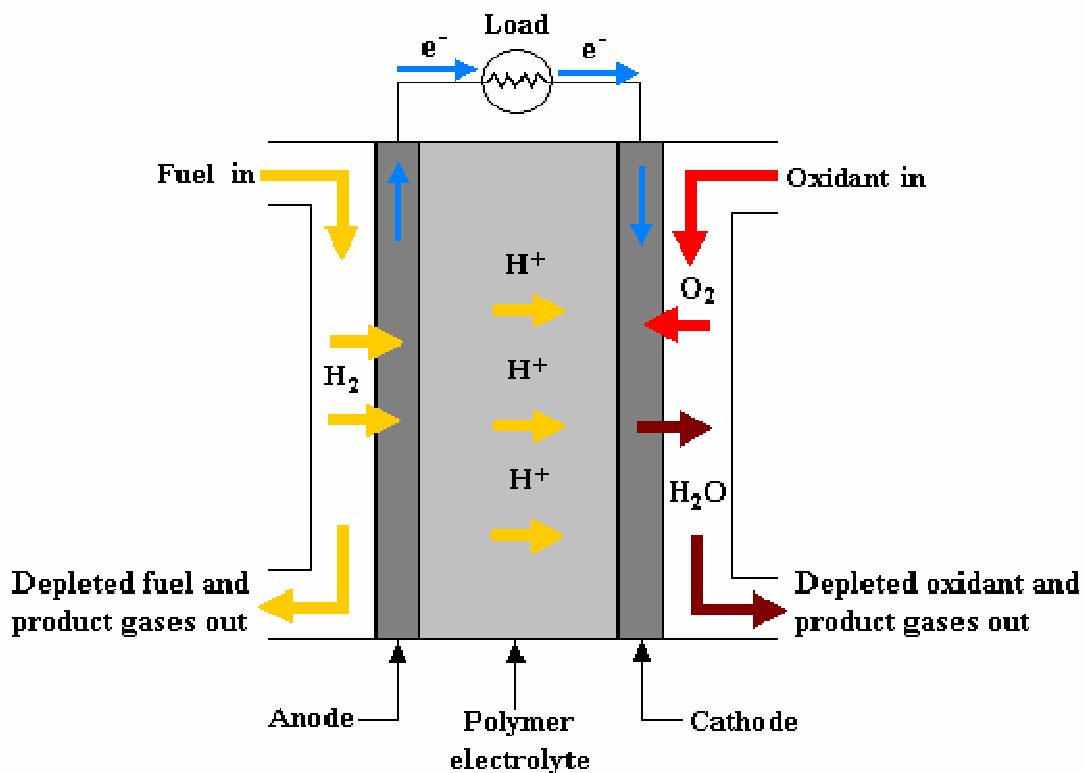


Figure 1.10: The PEMFC scheme.

The Proton Exchange Membrane fuel cell (also called Polymer Electrolyte Membrane Fuel Cell), PEMFC are constructed using polymer electrolyte membranes (notably Nafion) as proton conductor and Platinum (Pt)-based materials as catalyst.

PEMFCs operate at relatively low temperatures (below 100 °C) and can tailor electrical output to meet dynamic power requirements. Due to the relatively low temperatures and the use of precious metal-based electrodes, these cells must operate on pure hydrogen. Electrons travel in an external circuit, generating the electrical output of the cell. On the cathode side, another precious metal electrode combines the protons and electrons with oxygen to produce water, which is expelled as the only waste product; oxygen can be provided in a purified form, or extracted at the electrode directly from the air.

A variant of the PEMFC which operates at elevated temperatures is known as the high temperature PEMFC (HT PEMFC). By changing the electrolyte from being water-based to a mineral acid-based system, HT PEMFCs can operate up to 200 °C. This overcomes some of the current limitations with regard to fuel purity with HT PEMFCs able to process reformat containing small quantities of Carbon Monoxide (CO). The balance of plant can also be simplified through elimination of the humidifier.

1.4.1 PEMFC: PRINCIPLE OF OPERATION AND COMPONENTS

In a single PEMFC cell (Figure 1.10, Figure 1.11) hydrogen fuel is processed at the anode where electrons are separated from protons on the surface of a Pt-based catalyst. The protons pass through the membrane to the cathode side of the cell while the electrons travel in an external circuit, generating the electrical output of the cell. On the cathode side, another precious metal electrode combines the protons and electrons with oxygen to produce water, which is expelled as the only waste product; oxygen can be provided in a purified form, or extracted at the electrode directly from the air.

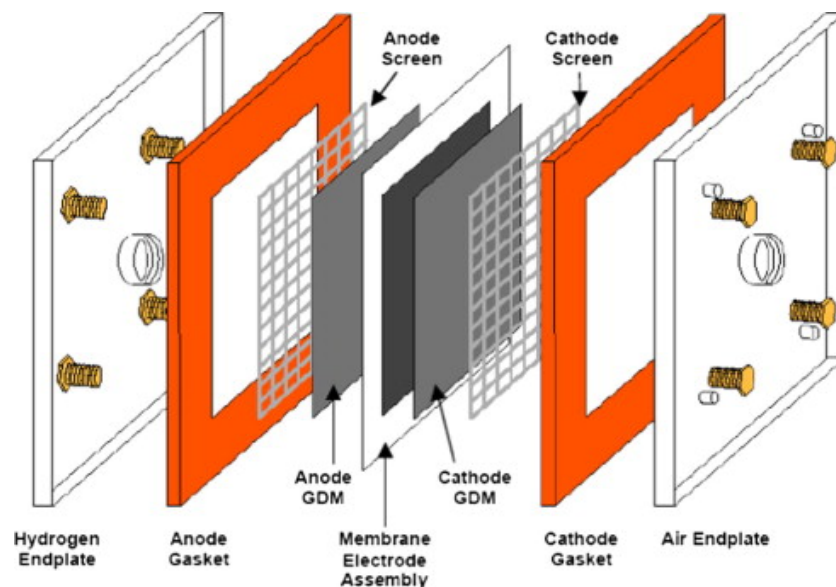
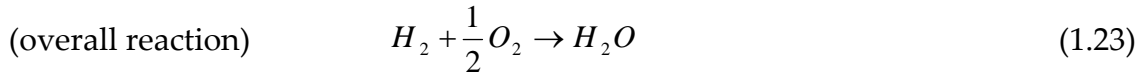
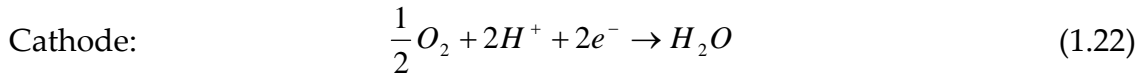
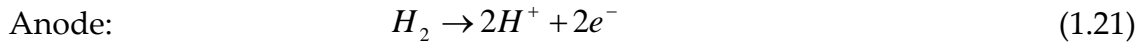


Figure 1.11: A single PEM fuel cell.

The reactions at the electrodes are (Fig. 1.12):



Phenomena involved in PEM fuel cell operation are complex; they involve heat transfer, species and charge transport, multi-phase flows, and electrochemical reactions [14]. In particular these multi-physics, highly coupled and non-linear transport and electrochemical reaction. The phenomena that take place during fuel cell operation are:

- 1) hydrogen gas and air are forced (by pumping) to flow down the anode and cathode gas flow channels (GFCs), respectively;
- 2) H_2 and O_2 flow through the respective gas diffusion layers /Micro porous layers (GDLs/MPLs) and diffuse into the respective catalyst layers (CLs);
- 3) H_2 is oxidized at the anode catalyst layer (CL), forming protons and electrons;
- 4) protons migrate and water is transported through the membrane;
- 5) electrons are conducted via carbon support to the anode current collector, and then to the cathode current collector via an external circuit;
- 6) O_2 is reduced with protons and electrons at the cathode CL to form water;
- 7) product water is transported out of the cathode CL, through cathode GDL/MPL, and eventually out of the cathode GFC;
- 8) heat is generated due to inefficiencies, mainly in the cathode CL due to the sluggish oxygen reduction reaction and is conducted out of the cell via carbon support and bipolar plates (BPs).

A single PEMFC (Figure 1.11) is composed by Membrane Electrode Assembly (MEA) consisting of the Catalyst Layers (CL) and membrane, Gas Diffusion Layer (GDL) and Micro-Porous Layer (MPL) also called Diffusion Media (DM), gas flow channels (GFCs), and bipolar plates (BP).

MEMBRANE

Membrane refers to a thin layer of electrolyte which conducts protons from the anode to the cathode. Desirable membrane materials are those that exhibit high ionic conductivity, while preventing electron transport and the cross-over of hydrogen fuel from the anode and oxygen reactant from the cathode. In addition, they must be chemically stable in an environment with HO⁻ and HOO radicals, thermally stable throughout the operating temperatures, and mechanically robust.

Current membranes are mostly based on the perfluorosulfonic acid, the most prominent of which, Nafion, was first developed by the DuPont Company in 1960s. Nafion_® has a backbone structure of polytetrafluoroethylene (PTFE, known by the trade name Teflon), which provides membrane with physical strength. The sulfonic acid functional groups in Nafion provide charge sites for proton transport. [14].

Additionally, other perfluorinated polymer materials such as Neosepta-F™ (Tokuyama), Gore-Select™ (W.L. Gore and Associates, Inc.), and Flemion™ (Asahi Glass Company), Asiplex™ (Asahi Chemical Industry) are also adopted for PEM fuel cell applications [8, 12].

The membrane layer contains the solid polymer membrane, liquid water, water vapor and trace amounts of hydrogen, H₂, oxygen, O₂, or dioxide carbonate, CO₂ depending upon the purity of the H₂ coming into the system.

CATALYST LAYER

The catalyst layer (CL) is where the hydrogen oxidation reaction or oxygen reduction reaction takes place. CL is usually very thin (about 10 μm). Several phases contained in a CL are key to the electrochemical reaction (Figure 1.12):

- (1) carbon support with Pt catalyst particles dispersed on the carbon surface,
- (2) ionomer, and
- (3) void space.

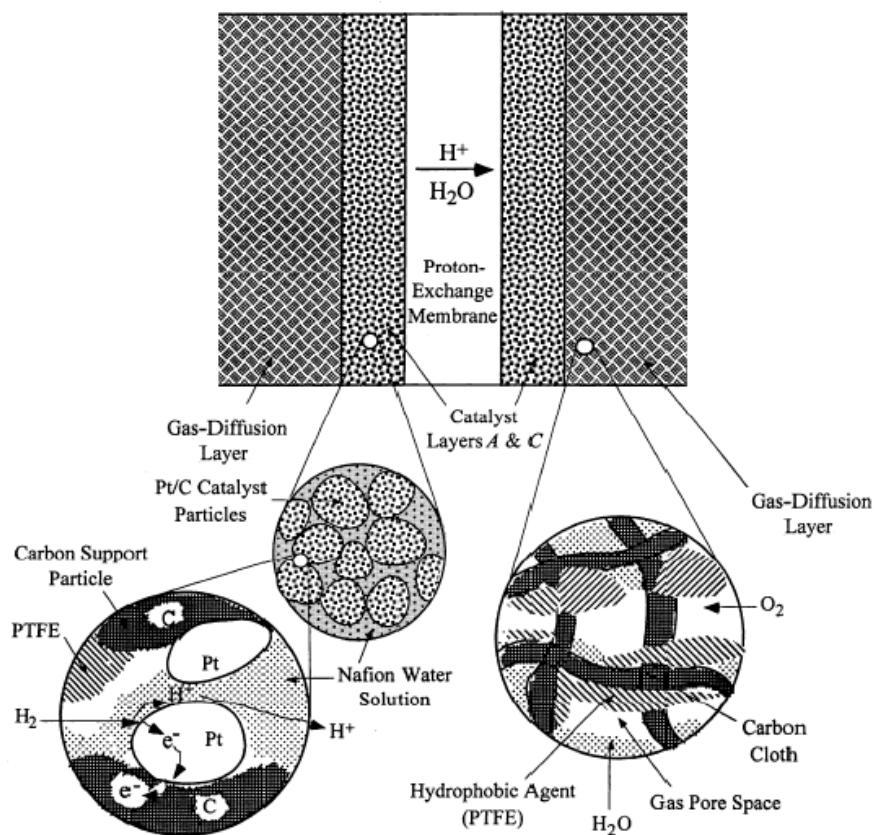


Figure 1.12: PEMFC components: Catalyst Layers.

The catalyst plays the critical role of reducing the reaction activation barrier. The reactions in the catalyst layers are exothermic; therefore, heat must be transported out of the cell. The heat can be removed through the convection in the flow channels, and conduction in the solid portion of the catalyst layers, gas diffusion media and bipolar plates.

Since liquid water is produced by the PEM fuel cell, the condensation and evaporation of water affects the heat transfer in a PEM fuel cell. Therefore, the water and heat management in the fuel cell are closely linked.

The catalyst layers are usually made of platinum (Pt) or Pt and its alloys (Pt-Co, Pt-Ni, Pt-Fe, Pt-V, Pt-Mn and Pt-Cr). In fact Pt presents good catalyst kinetics... Consequently the CL contributes a significant portion of cost for a fuel cell, thus the Pt loading is an important factor in the CL development. The DOE target is 0.3 and 0.2 mg/cm² for 2010 and 2015, respectively. Another important issue related to CLs is their durability. The catalyst layer is susceptible to material degradation during operation.

GAS DIFFUSION LAYER

Gas Diffusion Layers (GDLs) and Micro-Porous Layer (MPLs), together called Diffusion Media (DM), (Figure 1.13), play multiple roles [7, 8, 14, 23]:

- 1) electronic connection between the bipolar plate with channel-land structure and the electrode;
- 2) passage for reactant transport and heat/water removal;
- 3) mechanical support to the membrane electrode assembly (MEA);
- 4) protection of the catalyst layer from corrosion or erosion caused by flows or other factors.

Transport inside GDLs, closely related to the GDL structural feature, plays an important role in fuel cell energy conversion. GDLs are usually 100–300 μm thick. A popular GDL material is the carbon fiber based porous media: the fibers are either woven together to form a cloth, or bonded together by resins to form a paper.

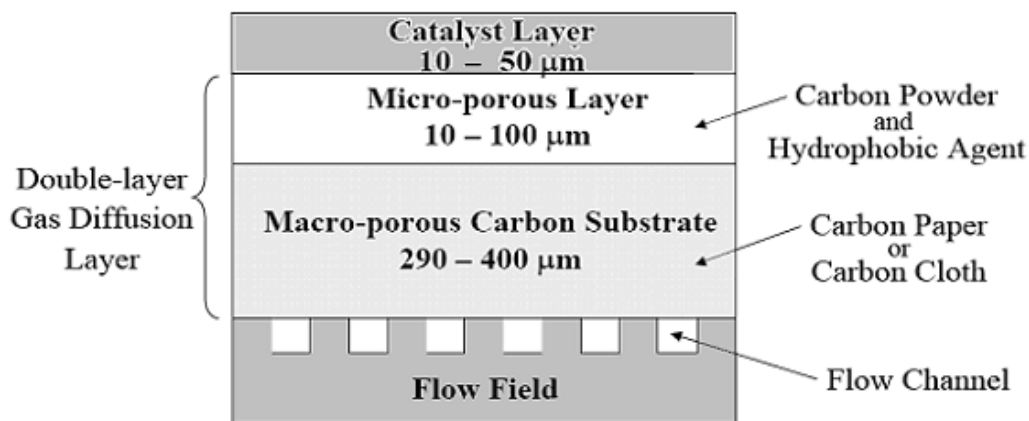


Figure 1.13: PEMFC components: Gas Diffusion Layers.

Multi-phase flow, originated from the water production by the oxygen reduction reaction, is critical to fuel cell water management and it may refer the flooding phenomenon. To help remove water from the pores of the carbon paper, the diffusion layer can be treated with PolyTetraFluoroEthylene (PTFE, a.k.a. DuPont's Teflon™).

GAS FLOW CHANNEL AND BIPOLAR PLATES

Gas Flow Channels (GFCs) are important components of PEM fuel cell and they supply and distribute hydrogen fuel and oxygen reactant for reactions and remove byproduct water. They are located within the bipolar plates with a typical cross-section dimension of around 1 mm. Insufficient supply of reactants will lead to hydrogen/oxygen starvation, reducing cell performance and durability.

Bipolar Plates (BP) provide mechanical support over DMs and conductive passages for both heat and electron transport. Furthermore, they distribute fuel and oxidant within the cell, separate the individual cells in the stack, collect the current, carry water away from each cell, humidify gases, and keep the cells cool. Bipolar plates also have reactant flow channels on both sides, forming the anode and cathode compartments of the unit cells on the opposing sides of the bipolar plate.

In order to simultaneously perform these functions, specific plate materials and designs are used. Commonly used designs can include straight, serpentine, parallel, interdigitated or pin-type flow fields.

A popular BP material is the non-porous graphite, which is chemically stable and highly conductive to electrons and heat. There are several disadvantages such as its brittleness and costly manufacturing associated with using graphite. Other materials under development are: metals such as aluminum, iron, stainless steel, titanium, nickel, polymer composites, carbon-based materials... Metallic alloys can be ideal materials for BPs because they are amenable to low-cost/high-volume manufacturing, offer high thermal and electrical conductivities, and can be made readily in thin sheet or foil form (<1 mm thick) for high fuel cell power densities.

Fabrication of BPs, together with GFCs, may contribute an important portion of a fuel cell cost [1], so the DOE target on the BP weight is <0.4 kg/kW by 2015.

1.5 THE STACK

Typical fuel cells operate at a voltage ranging from 0.6 – 0.8 V and produce a current per active area (current density) of 0.2 to 1 A/cm². Hence, a single cell cannot be satisfied the voltage or the power request by most applications, many cells are connected in series to make a fuel cell stack (Figure 1.14).

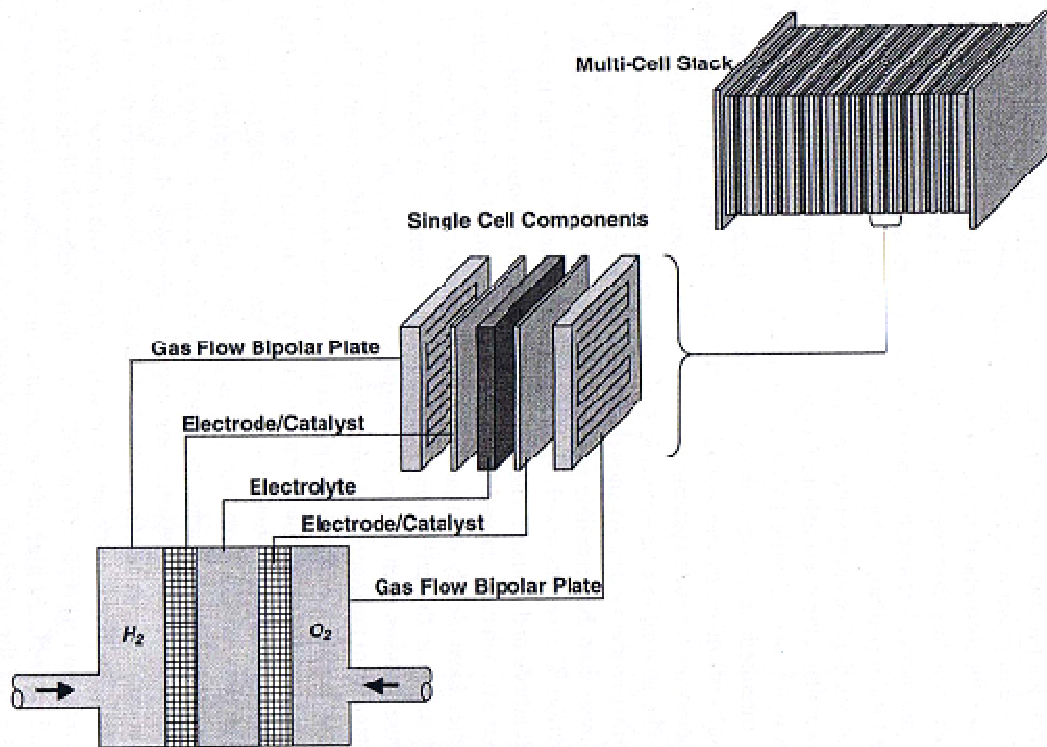


Figure 1.14: A single cell, its exploded view and the stack of a PEMFC.

A PEM fuel cell stack is made up of bipolar plates, membrane electrode assemblies (MEA) and end plates (Figure 1.14, Figure 1.15). Two consecutive cells in the stack are separated by flow field plates. Notice that increasing the number of cells in the stack increases the voltage, while increasing the surface area of the cells increases the current.

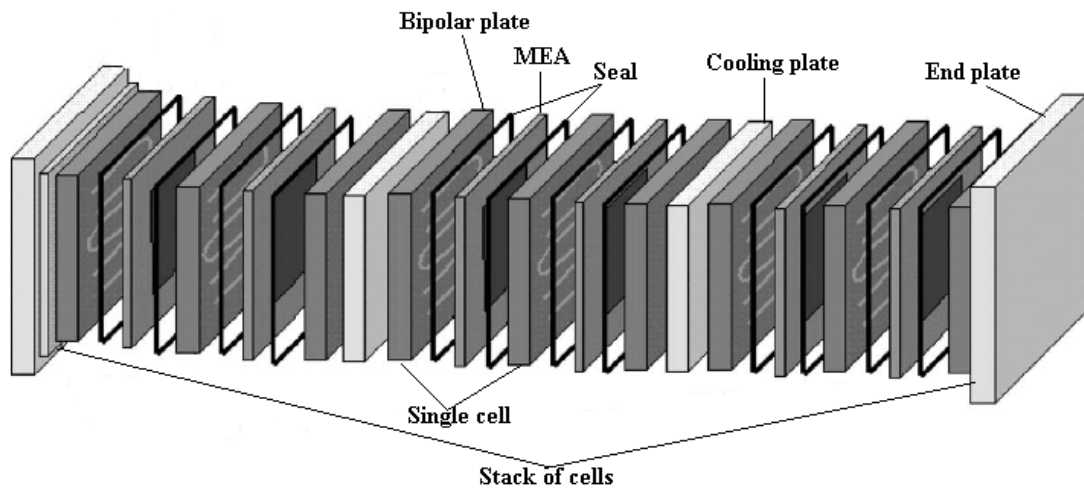


Figure 1.15: The stack.

1.6 BALANCE OF PLANT

Operation, control, and monitoring of the fuel cell stack require several essential subsystems that as a whole form the Balance Of Plant (BOP). Thus, in addition to the stack itself, a FC system, are composed of the following subsystems (Fig. 1.16):

- Fuel storage subsystem (e.g. natural fuels such as hydrocarbons, coal);
- Hydrogen supply system: (purification, reforming, or gasification);
- Air supply oxidant system (must be supplied to the cathode at a specific pressure and flow rate. Air compressors, blowers, and filters are generally used).
- Water management subsystem (removal of reaction heat excesses or heating of the stack to the temperature needed for the reaction);
- Thermal management subsystem (stack temperature must be monitored and controlled through an active or passive stack cooling systems as well as a separate heat exchanger in the case of an active system).
- Devices for the removal of reaction products;
- Valves, pumps, and all components necessary for the reactant supply;
- Different regulating and controlling devices;
- Power conditioning devices (meters, converters).

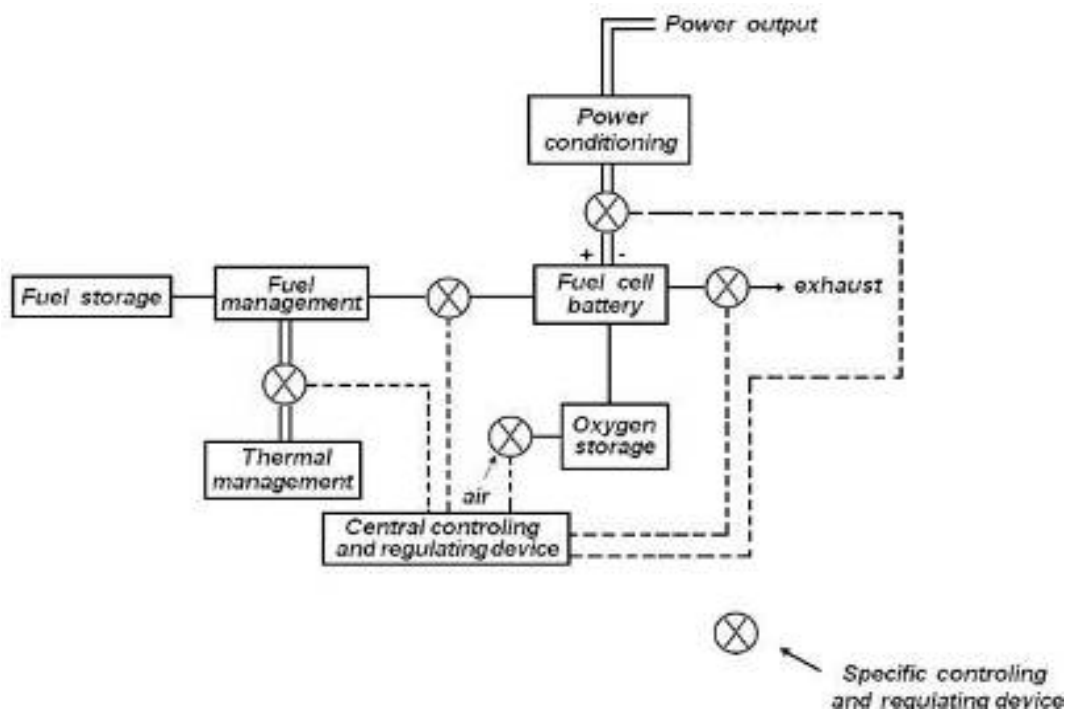


Figure 1.16: Power plant scheme.

1.7 THERMODYNAMICS

1.7.1 ENTHALPY OF REACTION

The heat of reaction is the difference between the heat of formation of the reactants and products. The equation for the reaction of hydrogen and oxygen is exothermic (heat producing), and is the same whether it proceeds by electrochemical or thermochemical routes:



The heat of reaction is calculated by subtracting the sum of all the heats of formation of the reactants from those of the products:

$$\Delta H = (h_f)_{H_2O} - (h_f)_{H_2} - \frac{1}{2}(h_f)_{O_2} \quad (1.25)$$

where h_f represents the heat of formation, for each reactant.

Assuming the reactants and products are both under standard condition ($p=1$ atm; $T = 25$ °C) where the product water will be in liquid form, by definition, the heat of formation of any element is zero, while that of liquid water is -285.8 kJ/mol, thus:

$$\Delta H = -285.8 \text{ kJ/mol} - 0 - 0 = -285.8 \text{ kJ/mol.} \quad (1.26)$$

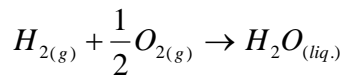
The sign convention states that the heat of reaction for all exothermic reactions is negative. The heat of reaction is known as hydrogen's heating value; the enthalpy of hydrogen combustion is known as the higher heating value (HHV) if liquid product water is produced through exact stoichiometric amounts of hydrogen and oxygen. If however, the oxygen is supplied in excess, the heat of combustion of hydrogen is known as the lower heating value (LHV) with a value of -242 kJ/mol.

1.7.2 REVERSIBLE CELL POTENTIAL

The Gibbs free-energy change, ΔG , of a chemical reaction is a measure of the maximum net work obtainable from the reaction. Only if the entropy change, ΔS , is zero, the free-energy change is equal to the enthalpy change, ΔH , of the reaction, as may be seen from the following equation:

$$\Delta G = \Delta H - T\Delta S \quad (1.27)$$

If the entropy change is negative, which is the case for the reaction between H_2 and O_2 to water that occur in FC, the free-energy change is less negative than the enthalpy change: $\Delta G \leq \Delta H$. In case of the liquid-phase reaction between hydrogen and oxygen the respective values are [3], under stationary condition ($p=1\text{atm}$; $T=25\text{ }^\circ\text{C}$):



$$\Delta G = -237.3 \text{ kJ/mol}; \quad (1.28)$$

$\Delta H = -285.8 \text{ kJ/mol}$, as shown above in the eq. 1.26.

Notice that the Gibbs free-energy change strongly depends on the temperature and state (liquid or gas) [15].

In the ideal conditions, i.e. when the process is reversible, in the fuel cell no losses are present, so all this Gibbs free-energy change is converted into electrical energy.

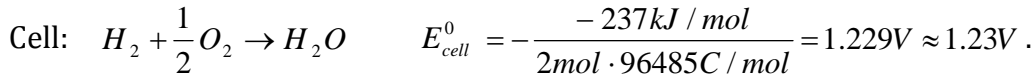
The *reversible (or ideal) cell potential*, E_r , is calculated from the following equation:

$$E_r = -\frac{\Delta H - T\Delta S}{nF} = -\frac{\Delta G}{nF} \quad (1.29)$$

where: n is the number of electrons exchanged in the reaction (equal to 2 if the reaction of water production occurs is from H_2 and O_2) and F is the Faraday constant, equal to 96485 C/mol .

For the half-cell reactions and the overall reaction between hydrogen and oxygen the following *standard - state reversible potential*, E^0 , (i.e., the ideal potential when all reactants and products are in their standard state ($p = 1 \text{ atm}$; $T = 25^\circ\text{C}$)) are obtained [16].

In the case of a hydrogen–oxygen fuel cell under standard-state conditions:



At standard conditions, this is the highest voltage obtainable from a hydrogen–oxygen fuel cell. Thus, to obtain higher voltages, several cells have to be connected together in series.

The dependence of the standard potential on the temperature is found by differentiating Eq. 1.29 with regard to the temperature, T , at constant pressure, p :

$$\left(\frac{\partial E_r^0}{\partial T} \right)_p = -\frac{1}{nF} \left(\frac{\partial \Delta G}{\partial T} \right)_p = \frac{\Delta S}{nF} \quad (1.31)$$

Integrating Eq. 1.5, it has:

$$E_r^0(T) = E_r^0(T^0) + \frac{\Delta S}{nF} (T - T^0) \quad (1.32)$$

since the change in entropy is negative; the open circuit voltage output decreases with increasing temperature. This means that the fuel cell is theoretically more efficient at low temperatures.

However, mass transport and ionic conduction is faster at higher temperatures and this more than offsets the drop in open circuit voltage [19].

For non-standard conditions, the reversible voltage of the fuel cell may be calculated from the energy balance between the reactants and the products [44]. The theoretical potential for an electrochemical reaction can be expressed by the *Nernst equation* [19]:

$$E_{r,T} = E_r^0 - \frac{RT}{nF} \ln \left(\frac{\prod \alpha_P^{v_i}}{\prod \alpha_R^{v_i}} \right) \quad (1.33)$$

where $E_{r,T}$ is the actual cell voltage, E_r^0 is the standard-state reversible voltage, R is the universal gas constant, T is the absolute temperature, n is the number of electrons consumed in the reaction, and F is Faraday's constant (96485 C/mol). The terms α_P, α_R are the activity of the products and of the reactants, respectively.

The Nernst equation gives the ideal open circuit potential, and provides a relation between the ideal standard potential, E^0 , for the cell reaction, and the ideal equilibrium potential, E_r , at the partial pressures of the reactants and products.

For the reaction that occurs in the fuel cell, at standard conditions:

$$E_{r,T} = 1.229(V) - \frac{8.314(J/(mol \cdot K)) \cdot 298.15(K)}{2 \cdot 96485(C/mol)} \ln \left[\frac{1}{1 \cdot 0.21^{1/2}} \right] = 1.219V \quad (1.34)$$

is the potential between the two electrodes of the fuel cell, at standard conditions and without current flow.

Considering that the gases are ideal: the activities of the gases are equal to their partial pressures, and the activity of the water phase is equal to unity, thus, the Nernst equation 1.33 can be written as:

$$E_{r,T} = E_r^0 - \frac{RT}{nF} \ln \left[\prod_i \left(\frac{p_{P,i}}{p_R} \right)^{v_i} \right] \quad (1.35)$$

That is, for the case of H₂/O₂ reaction:

$$E_{r,T} = E_r^0 - \frac{RT}{2F} \cdot \ln \left(\frac{p_{H_2O}}{p_{H_2} \cdot p_{O_2}^{1/2}} \right) \quad (1.36)$$

where: p_{H_2O} is the partial pressure of the water, p_{H_2} is the partial pressure of hydrogen and p_{O_2} is the partial pressure of oxygen.

1.7.3 VOLTAGE LOSSES

Useful electrical work is obtained from a fuel cell only when a reasonably large current is drawn. However, an increase in current leads to a decrease of the actual cell voltage from the reversible cell potential due to irreversible losses in a practical fuel cell. Several sources contribute to these irreversible losses (also called *overpotential* or *polarization*), although they originate primarily from three sources:

- 1)- activation losses, ΔV_a ,
- 2)- Ohmic losses, ΔV_o ,
- 2)- mass transport or concentration losses, ΔV_c .

Activation losses results from the control of the electrochemical rate on the electrode surface by sluggish electrode kinetics. Similar to a chemical reaction the electrochemical reaction has to overcome an activation barrier which depends on the electrode surface (electrocatalyst). It is influenced by processes involving the adsorption/desorption of reactant species and/or product species, the transfer of electrons through the double layer, and the nature of the electrode surface (rough or smooth surface). Generally, the activation polarization is described by the Tafel

equation:

$$\Delta V_a = \frac{RT}{\alpha_c nF} \ln\left(\frac{i_{FC}}{i_0}\right) \quad (1.37)$$

where i_{FC} is the cell current density, i_0 is the reaction exchange current density, n is the number of exchange protons per mole of reactant, F is Faraday's constant, and α_c is the charge transfer coefficient used to describe the amount of electrical energy applied to change the rate of the electrochemical reaction [23].

Ohmic losses are caused by resistance to the flow of ions within the ion conducting electrolyte and resistance to the flow of electrons through the electrode materials. These losses are expressed by Ohm's law:

$$\Delta V_O = I_{FC} \cdot R_{Ohm} \quad (1.38)$$

where I_{FC} is the cell current and R_{Ohm} the overall cell resistance (including electronic, ionic, and contact resistances).

Concentration losses are typically observed at high reaction rates when the reactants are rapidly consumed and a concentration gradient is formed between the electrode surface and the bulk. Slow diffusion of the reactants gases in the electrodes is a major contributor to concentration losses, although slow transport through the electrolyte to or from the reaction site also plays a role. If the limiting current density, i_L , is known, the concentration losses are calculated as:

$$\Delta V_c = \frac{RT}{nF} \ln\left(1 - \frac{i_{FC}}{i_L}\right) \quad (1.39).$$

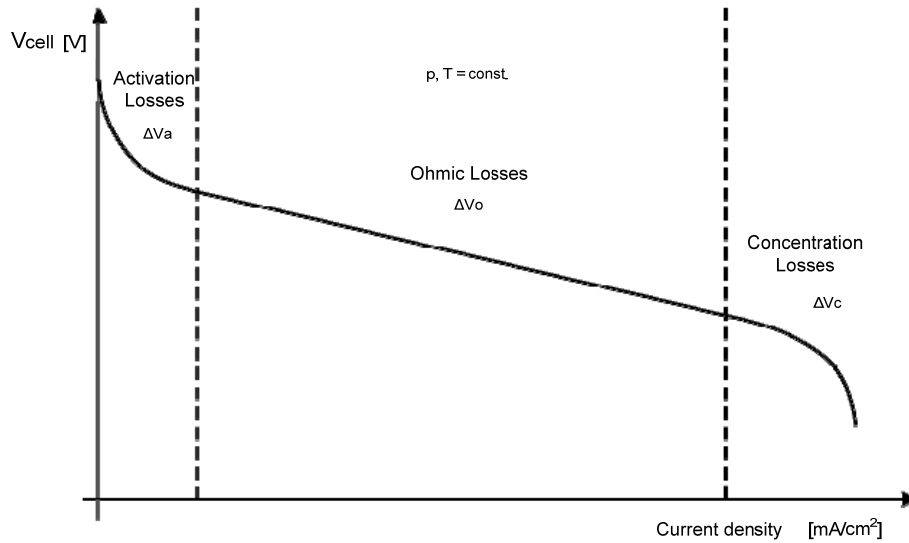


Figure 1.17: Typical polarization curve of a PEMFC with the loss voltages.

PEMFC exhibits qualitatively similar voltage/current relationships, as illustrated in Figure 1.17.

The semi-exponential behavior at low current densities is due to the activation polarization of the oxygen reduction reaction. In the intermediate current density region the pseudo-linear behavior is caused predominantly by Ohmic losses. At high current densities, the cell potential decays rapidly due to mass-transport limitations. The highest voltage is obtained at zero current. Its value should be given by the standard potential of the chemical reaction (i.e. 1.23 V at standard conditions for reaction in equation 1.30).

However, under practical conditions, the open-circuit potential (voltage at zero current) settles at values slightly below 1 V. This deviation can be explained if the open-circuit potential is considered to be a mixed potential due to the simultaneous occurrence of the four-electron (direct reduction) and two-electron (indirect reduction via hydrogen peroxide as an intermediate) oxygen reduction reactions. Impurity oxidation can also contribute to this deviation.

Activation polarization and concentration losses can occur at both electrodes. The effect of polarization is a shift of the electrode potentials to new values. Thus, the anode (cathode) voltage is described by the reversible electrode potential increased (decreased) by electrode polarization [7]:

$$V_{A(C)} = E_{A(C)} \pm |\Delta V_{a,A(C)} + \Delta V_{c,A(C)}| \quad (1.40)$$

The overall cell voltage, V_{FC} , is given by the difference between cathode and anode voltage diminished by the Ohmic losses in the cell [15]:

$$V_{cell} = V_C - V_A - \Delta V_O \quad (1.41)$$

and thus equal to:

$$V_{cell} = (E_C - |\Delta V_{a,C}| - |\Delta V_{c,C}|) - (E_A - |\Delta V_{a,A}| - |\Delta V_{c,A}|) - \Delta V_O \quad (1.42).$$

1.7.4 EFFICIENCY OF THE FUEL CELL

The *thermodynamic efficiency*, η_{id} , is the ideal efficiency, i. e. the efficiency in reversible condition. Thus, for an FC can be defined as the ideal electric work divided by the total energy theoretically released by reaction:

$$\eta_{id} = \frac{\Delta G}{\Delta H} \quad (1.43)$$

In this case fuel cell working ideally, so the free-energy change may be totally converted into electrical energy.

Using the Higher Heating Value of hydrogen a maximum efficiency value of 83% is obtained [7].

The *voltage efficiency*, η_{cel} is used to describe the quality of a fuel cell, when comparing different cell designs. It is defined as [9]:

$$\eta_{cel} = \frac{-nF \cdot V_{cell}}{\Delta H} = \frac{V_{cell}}{E_{th}} \quad (1.44)$$

where E_{th} is the theoretical standard electrode potential obtained from the enthalpy change. E_{th} may refer to the heating value of the fuel, and in the case in which Low Heating Value (LHV) is used it is named V_{LHV} , while it is called V_{HHV} .

If the Higher Heating Value (HHV) is considered:

$$\eta_{cel} = \frac{V_{cell}}{V_{LHV}}, \quad \text{using LHV;} \quad (1.44')$$

$$\eta_{cel} = \frac{V_{cell}}{V_{HHV}}, \quad \text{using HHV;} \quad (1.44'')$$

Referring to H_2/O_2 reaction, V_{LHV} is 1.23 V and V_{HHV} is 1.48 V [3, 10].

The *faradaic efficiency*, η_f , describes the relationship between the observed current, I_{FC} , and the theoretically expected current, I_{id} , on the basis of the hydrogen inlet flow, assuming that all hydrogen is consumed [5]:

$$\eta_f = \frac{I}{I_{id}} \quad (1.45)$$

The faradaic efficiency may be less than unity due to low hydrogen utilization, parallel electrochemical reactions, and hydrogen crossover [5].

The η_f is expressed also as fuel utilization factor, i.e. as the ratio between fuel (H_2) actually reacted, \dot{m}_i , i.e. the hydrogen that makes up to the electrochemical reactions and the amount of fuel really introduced into the cell, \dot{m}_{H_2} :

$$U_f = \frac{\dot{m}_i}{\dot{m}_{H_2}} \quad (1.46).$$

The efficiency of the cell may be expressed as a product between them, as:

$$\eta_{cell} = \eta_{id} \cdot \eta_V \cdot U_f \quad (1.47).$$

1.7.5 OPERATING CONDITION

The main PEMFCs operating parameters are the temperature, pressure and the relative humidity. The range of operating conditions and the optimal conditions parameter present in literature, are summarized in the Table 1.2

Operating parameter	Range	optimal
Fuel	Hydrogen, H ₂	H ₂ - 99.99995 %
Oxidant	Oxygen, O ₂ or air	O ₂
Temperature	20°C - 90 °C	60 °C - 80 °C
Pressure	1 - 3 atm	2 - 3 atm
Relative Humidity (RH)	50 - 100 %	100 %

Table 1.2: Operating parameter.

As the table shows, the range of temperatures in the literature are 20 ÷ 90 °C, and it is well known that higher temperatures result in better fuel cell performance. The polymer membrane that is used for the majority of PEMFCs limits the upper temperature to below the glass transition temperature of the polymer. In addition, proton conductivity of the membrane is affected by the water content in the membrane; therefore, the temperature is also limited by the amount of liquid water content in the membrane. However, it may not be advantageous for the fuel cell system design to require high operating temperatures.

The pressure range for most PEMFCs in literature is from 1 ÷ 3 atm. Fuel cells that operate at 3 atm require additional equipment to regulate and monitor the pressure. Consequently, it may not be advantageous to run the fuel cell system above ambient pressure.

The relative humidity should be monitored since it changes daily under ambient conditions.

Also, the humidity, pressure, temperature, and hydrogen and oxidant flow rates should all be monitored and controlled depending upon ambient conditions and system requirements.

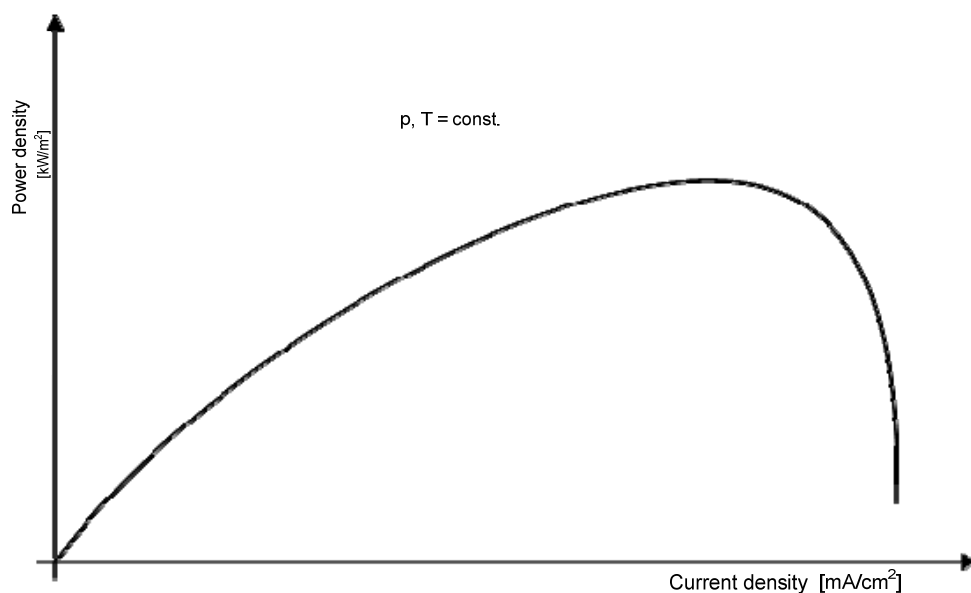


Table 1.3: The typical trend of the power density versus current density of a PEMFC.

Furthermore, typically a cell is operated at voltage values comprised between 0.6 ÷ 0.8 V, that is fed in such a way that at full load the current corresponds to voltages of this magnitude. At partial loads is observed an increase in both the cell voltage is the voltage output, while if the current values become too high, which is obtained by introducing a larger amount of fuel to the anode, the power grows more and

more slowly up to when it reaches a maximum, beyond which prevail losses for concentration. This effect is visible in the figure 1.46 which shows the trend of the power density as a function of current density.

The operation of the cell at voltage values around 0.7 V is due, therefore, to achieve a compromise between the two conflicting requirements: to maintain the efficiency at high values, avoiding the tensions are too high, and to retain the value of the power density to acceptable levels, avoiding tension are too low. In the choice of the optimal value of the operation voltage, also, it must be consider that too low power density values cause excessive overall dimensions of the cell and too high costs, caused by increasing amounts of valuable materials necessary for the electrolytes, for the electrodes and especially for the catalysts.

A single cell normally produces a current density of $300 \div 800 \text{ mA/cm}^2$. Therefore, to obtain the power and the voltage desired, various cells should be connected in series, by means of bipolar plates, and thereby form a stack, and then assemble them into modules, in order to obtain the required power generators.

1.8 PEMC APPLICATION AND CURRENT STATUS

PEM fuel cells are being applied in the three areas(Figure 1.18): transportation, portable power generation and stationary.

The major application of PEM fuel cells focuses on transportation above all because of their potential impact on the environment, e.g. the control of emission of the green house gases. Other applications include distributed/stationary and portable power generation. Most major motor companies work solely on PEM fuel cells due to their high power density and excellent dynamic characteristics as compared with other types of fuel cells. Fuel-cell vehicles (FCV) have been developed and demonstrated, e.g. GM Hydrogen 1, Ford Demo IIa (Focus), DaimlerChrysler NeCar4a, Honda FCX-V3, Toyota FCHV, Nissan XTERRA FCV, VW Bora HyMotion, and Hyundai Santa Fe FCV . Auto makers such as Toyota, Honda, Hyudai, Daimler, have announced that they will commercialize their vehicles by 2015 [5].

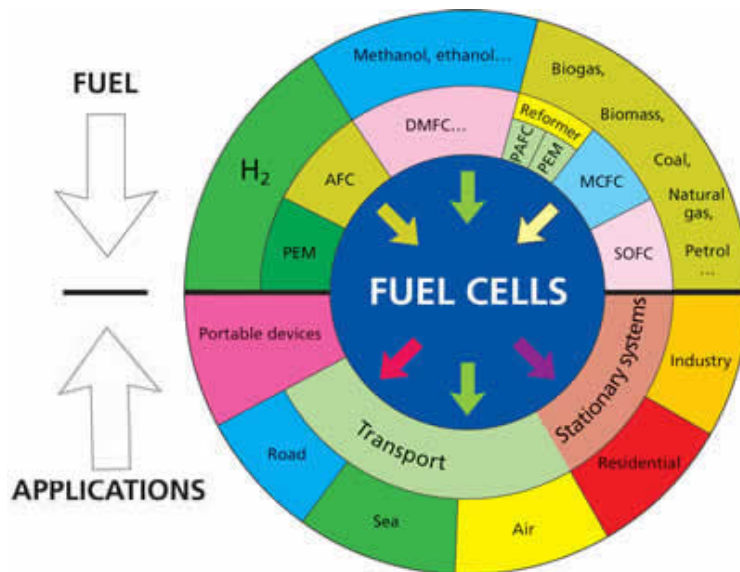


Figure 1.18: The applications and the fuel for the various FC typologies.

Back-up power for banks and telecommunication companies receives growing interests recently because of the extremely high cost associated with power breakdowns. Several units like Plug Power GenSys_ and Ballard FCgen™ 1020 ACS fuel cell systems have been developed.

A promising area is portable power supply, considering that limited energy capacity of batteries unlikely meets the fast-growing energy demand of the modern portable electric devices such as laptops, cell phones and military radio/communication devices. Major electronics companies, such as Toshiba, Sony, Motorola, LG, and Samsung, have in-house R&D units for portable fuel cell.

Distributed PEM fuel cell power system is primarily focused on small scale (50–250 kW for decentralized use or <10 kW for households) [6]. The main stationary PEMFC producers are Ballard, Plugpower, Nuvera, ReliOn, Aktergy, and ClearEdge. Early design considered fuel cells for residential power supply, in which the waste heat of fuel cells can be utilized for household usage – this significantly increases the overall efficiency [7]. In fact PEMFC micro-CHP, for example have an electrical efficiency of 37% and an overall efficiency of 82% in CHP mode. However, the high cost of PEM fuel cells remains a major barrier that prohibits their widespread applications in this area.

In particular, current stationary electric power is primarily generated by large central power stations. Large-scale central power stations have many benefits such as high efficiency, but exhibit several inherent disadvantages, e.g. the waste heat that usually cannot be efficiently utilized (due to the costly long-distance transport) and power loss during transmission. Distributed power decentralized generation is a way to resolve these disadvantages, which cogenerates heat and power for local usage.

Furthermore, fuel cells can be applied for decentralized small-scale stationary power generation. Except cost, fuel cells exhibit several important advantages such as high electric power conversion efficiency, low noise, zero emission, and easy scale-up. In this sector, distributed PEM fuel cell systems can be employed to several areas such as heat-power co-generation for household/residential use and uninterrupted power supply. Several units are now available in the market: the GenSys™ Blue CHP (combined heat and power) system by Plug Power was developed to be compatible with existing home heating systems such as forced air or hot water.

COMMERCIAL BARRIERS

The two greatest barriers to PEMFC commercialization are durability and cost [5].

In fact, the components of the PEMFC, in particular the MEA (membrane electrode assembly) [24], suffer degradation during long-term operations. Several research are promoted to

The lifetime required by a commercial fuel cell is over 5000 operating hours for light-weight vehicles and over 40,000 h for stationary power generation with less than 10% performance decay.

At current, most fuel cells exhibit major performance decay after around a thousand hours of operation [25,27,28]. The DOE targets are to achieve a life time of 40,000 h by 2011 with 40% efficiency for distributed power and 5000-h durability by 2015 with 60% efficiency for transportation.

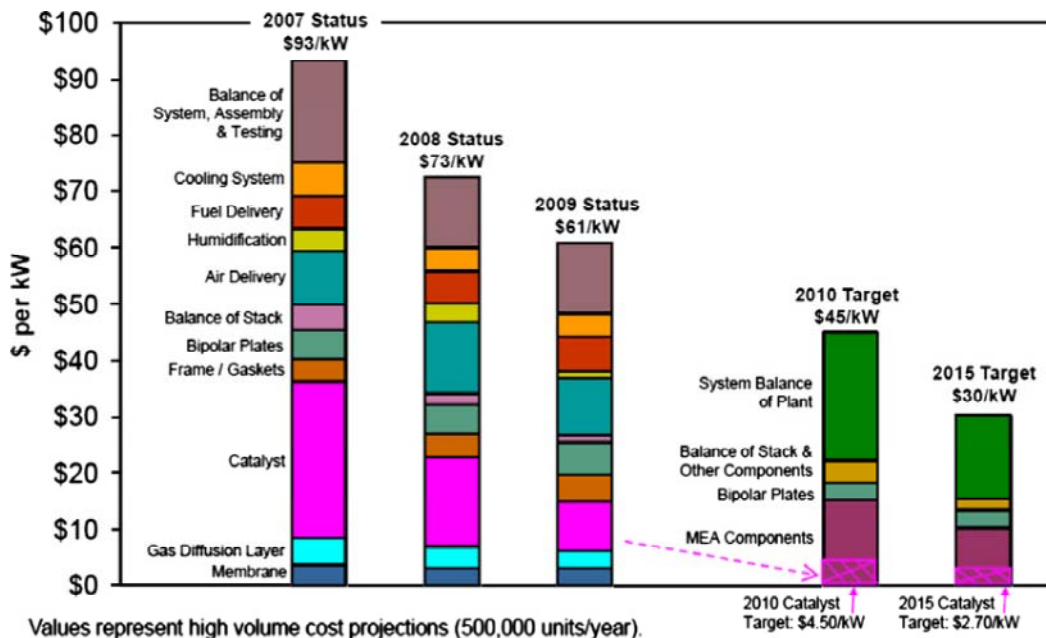


Figure 1.19: The breakdown of fuel cell cost [1].

Figure 1.19 shows the breakdown of fuel cell cost. It may see that in 2009, the cost was further bought down to \$61/kW (\$34/kW for balance of plant including assembly and testing, and \$27/kW for stack) and more than 35% reduction in the last two years. One primary portion of a fuel cell cost is due to the MEA that consists of a Nafion_ membrane and catalyst (usually Pt-based) layers [29]. The Pt loading has been reduced by two orders of magnitude in the past decade and there is still room for further loading reduction. The 2010 and 2015 DOE targets for the fuel cell cost are \$45/kW and \$30/kW, respectively, for transportation applications.

To date, research has promoted its aim to break down these limits as witness this study.

	2012			2015			2020		
	LT PEM	HT PEM	SOFC	LT PEM	HT PEM	SOFC	LT PEM	HT PEM	SOFC
Electrical efficiency at rated power, ^b %	38	42	40	40	42	45	40	45	60
CHP energy efficiency,%	85	85	85	87	87	90	87	87	90
Factory cost, ^c \$/kW	1,000–1,500	1,000–2,000	1,300–4,500	750–1,200	550–1,500	1,000–3,000	450–750	450–750	1,000–2,000
Transient response (10%–90% rated power), min	< 1	<1	5	< 1	< 1	3	< 1	< 1	2
Start-up time from 20°C ambient temperature, min	30	30	60	20	20	45	15	15	30
Degradation with cycling, %/1,000 h	<0.3	<0.3	<0.7	<0.3	<0.2	<0.5	<0.2	<0.2	<0.3
Operating lifetime, ^d h	30,000	30,000	30,000	40,000	40,000	35,000	40,000	40,000	40,000
System availability, %	97	97	97	98	98	98	99	99	99

^a Standard utility natural gas delivered at typical residential distribution line pressures.

^b Regulated AC net/lower heating value of fuel.

^c Cost defined at 50,000 unit/year production (250 MW in 5-kW modules). The basic unit includes all processing necessary for conversion of natural gas to unregulated DC power; i.e., the basic unit does not include power conditioning.

^d Time until > 20% net power degradation.

Table 1.4: Panel Perspective on Cost and Technical Potential for 1–10 kW CHP Stationary Fuel Cell Systems Operating on Natural Gas (<http://www.osti.gov/bridge>).

References to chapter 1

- [1] Papageorgopoulos D. DOE fuel cell technology program overview and introduction to the 2010 fuel cell pre-solicitation workshop in DOE fuel cell pre-solicitation workshop. Department of Energy, Lakewood, Colorado; 2010.
- [2] Perry and T. F. Fuller A Historical Perspective of Fuel Cell Technology in the 20th Century, M.L., "Journal of the Electrochemical Society" Vol. 149, pp S59-S67, 2002.
- [3] P. Costamagna and S. Srinivasan Quantum Jumps in the PEMFC Science and Technology from the 1960s to the Year 2000, "Journal of Power Sources" Vol.102, pp 242-269, 2001.
- [4] S. Srinivasan ,Fuel Cells: From Fundamentals to Applications, Springer, New York, 2006.
- [5] S. K. Kamarudin, W. R. W. Daud, A. Md.Som, M. S. Takriff, and A. W. Mohammad, Technical Design and Economic Evaluation of PEM Fuel Cell Systems, "Journal of Power Sources" Vol. 157, pp 641-649, 2006.
- [6] G. Wand, Fuel Cell History Part 1, "Fuel Cell Today", June 16, 2006.
- [7] W. Vielstich, A. Lamm, and H. Gasteiger , Wiley, Chichester, Handbook of Fuel Cells: Fundamentals, Technology, Applications , UK, volume 4, 2003.
- [8] Polymer Electrolyte Fuel Cells, S. Gottesfeld and T. A. Zawodzinski, in "Advances in Electrochemical Science and Engineering" Vol. 5, pp 195-301, R. C. Alkire, H. Gerischer, D. M. Kolb, and C. W. Tobias (editors), Wiley-VCH, Weinheim, Germany, 1997.
- [9] Fuel Cells and Their Application, K. Kordesch and G. Simader, VCH, Weinheim, Germany, 1996.
- [10] K. Kordesch ,25 Years of Fuel Cell Development (1951-1976), "Journal of the Electrochemical Society" Vol. 125, pp 78C-91C, 1978.
- [11] Vladimir S. Bagotsky A.N. Frumkin Institute of Electrochemistry and Physical Chemistry Russian Academy of Sciences, Moscow, Russia - E-mail: vbag@mail.ru (August, 2009)

- [12] Ryan Baker and Jiujun Zhang Institute for Fuel Cell Innovation National Research Council of Canada 4250 Wesbrook Mall - Vancouver, British Columbia V6T 1W5, Canada (April, 2011)
- [13] Carette, L.; Friedirch, A.; Stimming, U.; *Chemphyschem.* 2000,1,161-193.
- [14] Y. Wanga, K. S. Chen, J. Mishler, S. C. Cho a, X. C. Adroher, A review of polymer electrolyte membrane fuel cells: Technology, applications, and needs on fundamental research, *J. of Applied Energy*, 88 .(2011), 981–1007.
- [15] J. Larminie, A. Dicks: *Fuel Cell Systems Explained*, John Wiley & Sons, Chichester, 2000
- [16] Gittleman C, DM, Jorgensen S, Waldecker J, Hirano S, Mehall M. Automotive fuel cell R&D needs. In: DOE fuel cell pre-solicitation workshop. Department of Energy, Lakewood, Colorado; 2010.
- [16] L. Guzella, A. Sciarretta, *Vehicle propulsion system - Introduction to Modeling and Optimization*, Second Ed., 2007.
- [17] Garche J, Jorissen L. PEMFC fuel cell. In: Vielstich W, Gasteiger H, Lamm A, editors. *Handbook of fuel cells: fundamentals, technology and applications*. John Wiley & Sons, Ltd.; 2003.
- [18] Geiger S, Copper MAJ. Fuel cell small stationary market survey. *Fuel Cell Today* 2003.
- [19] Bard, A.J. and Faulkner, L.R. (2001) *Electrochemical Methods: Fundamentals and Applications*, 2nd ed., New York: John Wiley & Sons.
- [20] Ay, M., Midilli, A., and Dincer, I. (2006) Thermodynamic modeling of a proton exchange membrane fuel cell. *Int. J. Energy*, 3: 16-44.
- [21] Perry, R.H. and Green, D.W. (1997) *Perry's Chemical Engineers' Handbook*, 7th ed., New York: McGraw Hill.
- [22] Barbir, F. (2005). *PEM Fuel Cells: Theory and Practice*. 1st ed., New York: Elsevier Science
- [23] Mench, M., Wang, Y., and Tynell, S.T. (2007). *An Introduction to Fuel Cells and Related Transport Phenomena*. Department of Mechanical and Nuclear Engineering, Pennsylvania State University. Draft. Retrieved March 4, 2007, from <http://mtr11.mne.psu.edu/Document/jtpoverview.pdf>.

- [24] Zhang S et al. A review of accelerated stress tests of MEA durability in PEM fuel cells. *Int J Hydrogen Energy* 2009;34(1):388–404.
- [25] Borup R, et al. PEM fuel cell durability. 2008 DOE hydrogen program review June 9–13, 2008, 5.
<http://www.hydrogen.energy.gov/pdfs/review08/fc_26_borup.pdf>.
- [26] Schmittinger W, Vahidi A. A review of the main parameters influencing longterm performance and durability of PEM fuel cells. *J Power Sources* 2008;180(1):1–14.
- [27] Borup R et al. Scientific aspects of polymer electrolyte fuel cell durability and degradation. *Chem Rev* 2007;107(10):3904–51.
- [28] Wood DL, Borup RL. In: Buchi MIFN, Schmidt TJ, editors. *Polymer electrolyte fuel cell durability*. New York: Springer; 2009. p. 159.
- [29] Directed technologies I. Mass production cost estimation for direct H2 PEM fuel cell systems for automotive applications: 2008 update 2009. p. 10.

Chapter 2

THE INTEGRATED ENERGY SYSTEM

In order to meet the energy and thermal requirements of users with different necessity, a system composed by several micro-CHP (Combined Heat and Power) energy sources, feed with different types of fuel, integrated with renewable energy sources (RES) electric generators, electrical and thermal storage systems and also a control system, an Integrated Energy System (IES) (Figure 2.1), was conceived and built.

An IES test rig can be split into two parts: the "micro-cogenerative energy system" (Figure 2.1, red area), hereinafter called "*System*", and the "*test bench*" proper (Figure 2.1, blue area).

The "*System*" is composed by multiple distributed sources, by an electric storage system and a thermal storage system. All the measuring sensors, inverters and On-Load Tap-Changer (OLTC) transformers are included into the System part.

"*Test bench*", instead, refers to the fuel supply system, the renewable energy source (RES), the electrical load, the thermal load and the automatic control system.

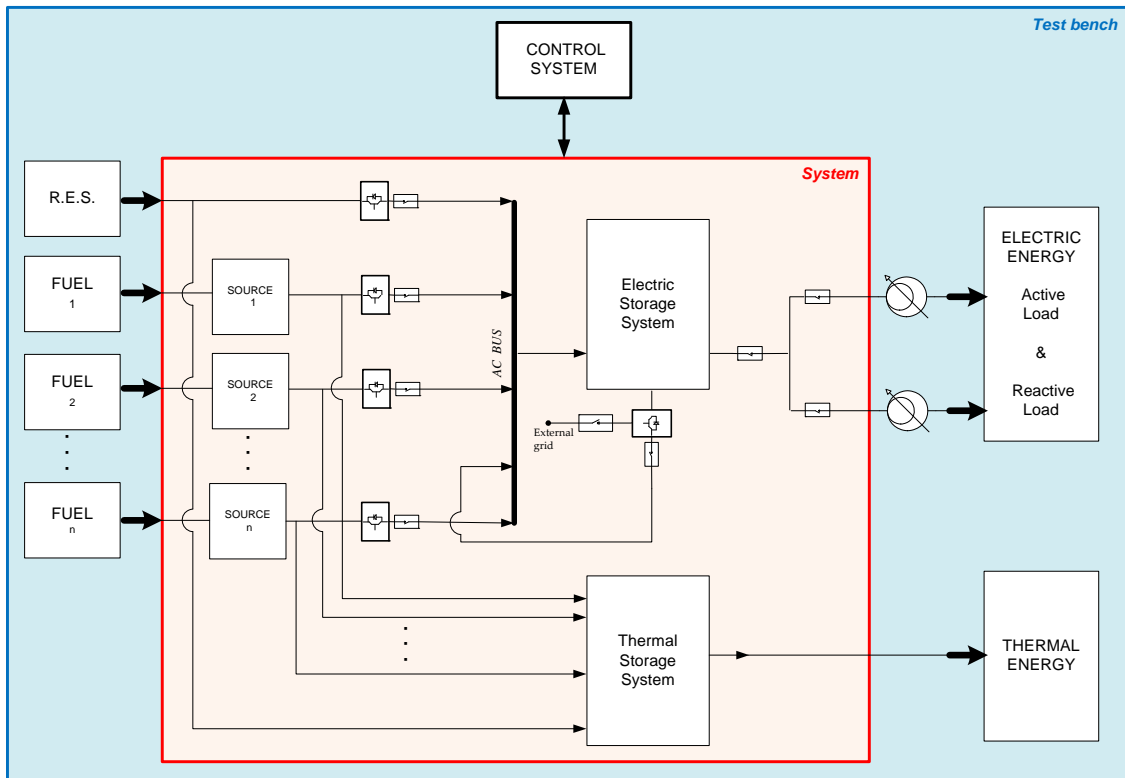


Figure 2.1: Conceptual layout of the Integrated Energy System (IES).

Conceptually the IES test rig must be designed to be able to provide the energy for the power loads in absence of grid-connection (island mode or stand-alone operating condition), but also be capable of grid-connected operating mode. The passage from grid-connected to stand-alone conditions is assured by the battery inverter.

2.1 THE IES TEST SYSTEM

The test IES (Figure 2.2) has been realized at the Department of Industrial Engineering (DIN) laboratory of the University of Bologna in collaboration with the Department of Electric Engineering (DEI), that realized the embedded and real-time automatic control system.

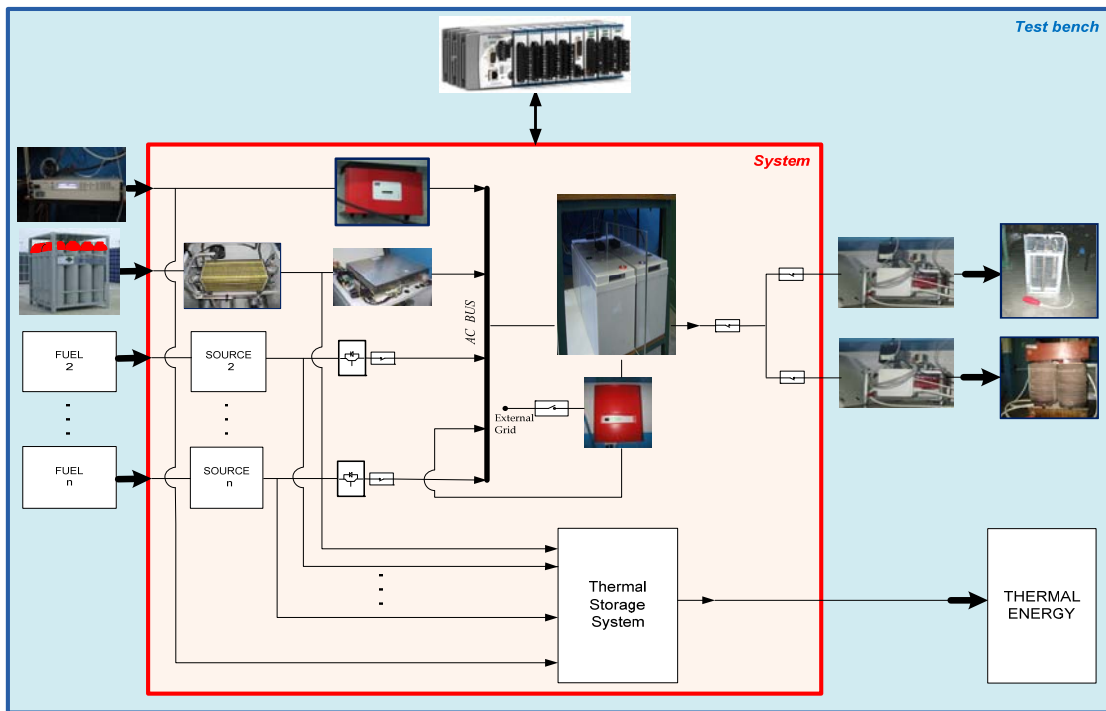


Figure 2.2: Realized layout of the test Integrated Energy System developed to date.

Actually, the IES test rig consists of the following power-related components (Figure 2.2, Figure 2.3):

- a PEMFC capable to provide a 5 kW electric AC power with a 80-cells stack fed with pure hydrogen, connected to a dedicated inverter;
- an electrochemical storage system (100 Ah lead-acid batteries) with a bidirectional inverter;
- a 500 W photovoltaic module emulator (PV) as renewable energy source (RES), with its inverter;
- an electric load emulator (active and reactive load);
- an embedded and real-time automatic control system.



Figure 2.3: A photo of the test Integrated Energy System (IES), to date.

All the sources that make up the distributed energy system produce energy in the form of Direct Current (DC); also the Integrated Energy System is designed to operate in island mode. In these conditions the system must provide the AC power for the utilities even in the absence of connection to the network.

The different energy sources can mutually be connected to the AC grid, following two different approaches: a) adoption of a DC node; b) adoption of an AC node. The plant schemes that can be realized for the hybrid configuration FC - batteries, are:

- characterized by the parallel of the various sources on a DC node connected in turn to the network via AC inverter (Figure 2.4);

- characterized by independent connection of the various sources to the AC network via a suitable power electronic converter (Figure 2.5).

In any case the electrochemical storage system is always connected to the network via a bidirectional electronic converter, able to ensure the possibility of both the charging and the discharging of the electric accumulation system in any operating condition, depending on various no-balance conditions between electricity production and consumption.

Depending on the configuration for supplying the loads in AC, it is necessary in case a) a single inverter, or in case b) two inverters.

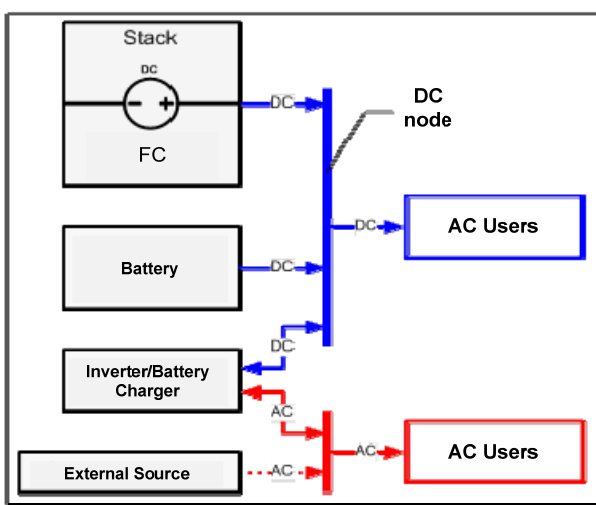


Figure 2.4: Connection of the generating system to the AC grid. Common AC/DC inverter layout.

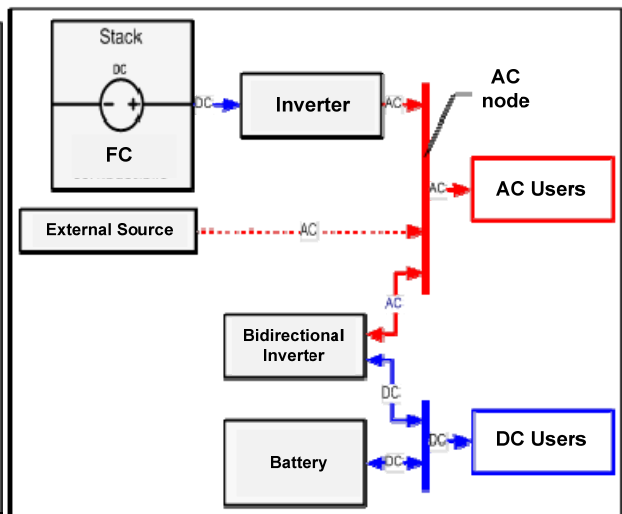


Figure 2.5: Connection of the generating system to the AC grid. Dedicated AC/DC inverter layout.

For the IES, a system diagram characterized by the connection of the various independent sources on a single AC node via dedicated electronic power converters (booster, inverter and charger), has chosen. This choice has allowed to realize the direct coupling of electrochemical sources that have different V-I characteristics and also a standard connection of the components with the external network.

Moreover, although the chosen layout has an simple design, it is very flexible from the point of view of the interconnection with other sources. However, in order to control the system, it is necessary to develop a fully automatic loads management system able to always guarantee optimum operation and to safeguard the life of the FC that is the weak element of the system.

Finally, although more expensive, this configuration has several advantages;

- i). a standard interface between the components and the network;
- ii). simplified system design and operation;
- iii). compatibility with existing networks;
- iv). the reduction of system costs;
- v). a better reliability;
- vi). the possibility to expand the system.

All of the sources of the developed system are connected to a 230 V AC bus through inverters with specific characteristics.

The electrochemical storage system (batteries) is connected to the AC bus through a voltage set-bidirectional electronic converter. This inverter is able to control the voltage and the frequency of the AC bus when the IES operate in island-mode and ensures both the charge and the discharge of the batteries in each operating condition depending on the balance between production and consumption of electricity.

The FC inverter controls the power production taking into account FC limitations and requirements. It needs a set voltage on the AC side, since such energy source comes to work in grid-connected mode exclusively.

The inverter of the PV emulator tracks its maximum power operating point and reproduces the randomness of the generated energy due the not-regularity and not-controllability of the light beam intensity that hit the surface of the photovoltaic panel.

Finally, the AC bus feeds electric active and reactive loads which reproduce programmable profiles through separate On-Load Tap-Changer (OLTC) transformers. This operation mode of the system allows the energy flows balancing through the charging and discharging of the battery in different operation conditions. For example, in case of excess of energy (e.g. fuel cell operation, strong solar radiation and low users consumption) power to charge the battery is drawing from the AC node. Instead, in the

case of lack of energy (e.g. fuel cell turned off, weak solar radiation and high utilities consumption) the loads are supplied with the aid of batteries. To achieve these aims, a micro-controller with monitoring AC node has been implemented in the system.

The electric scheme of the developed IES is show in Figure 2.6. It consists of three power branches (in addition to the external network branch of which there is only considered the presence and the possible interfacing):

- 1). the fuel cell (FC) branch;
- 2). the battery branch;
- 3). the photovoltaic (PV) branch.

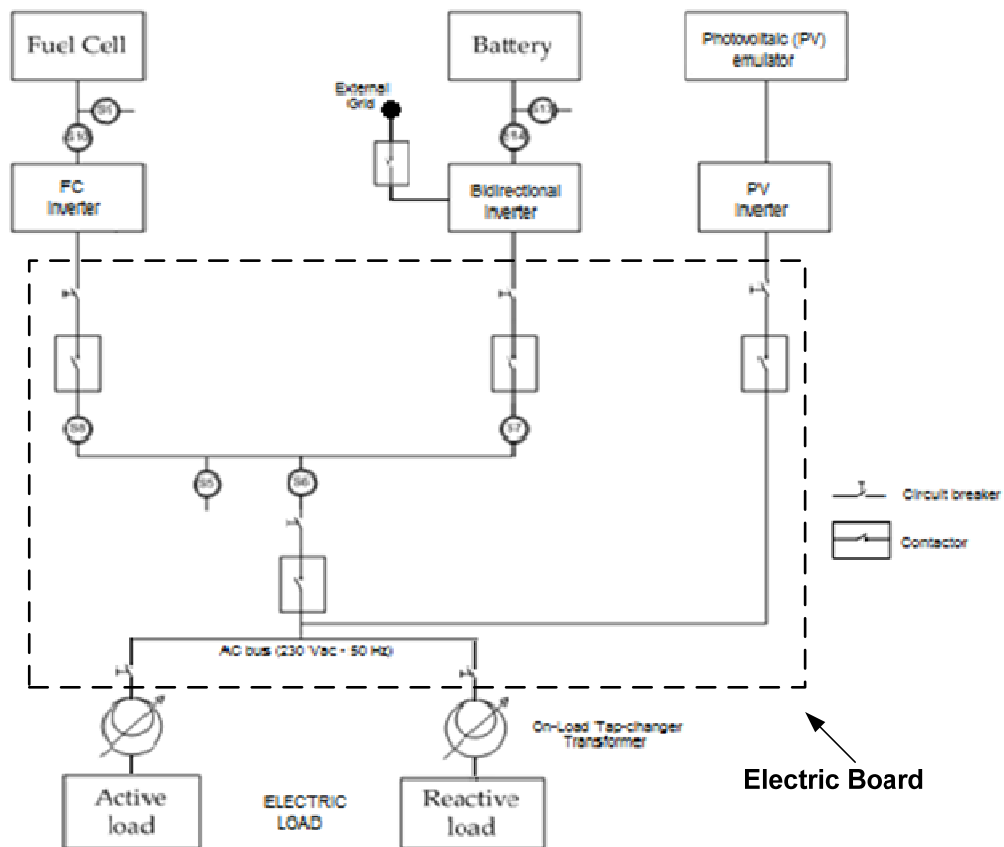


Figure 2.6: Electrical architecture of the Integrated Energy System.

Moreover on each branch are installed the thermal magnetic circuit brakers and the contactors (Figure 2.6), that allows the opening or closing of the lines. The control

logic of the three contactors positioned on the battery branch, on the FC branch and on the loads branch, respectively, has been designed to be driven by the control system. This command is absent only for the network, for which only a circuit breaker is intended. Therefore, when the system that operates in island mode is connected to the network, it begins to absorb power from the network.

All the branches are installed on a common electric board, are realized with a bipolar cable (section: 6 mm², plus ground) and are protected by a circuit breaker "hager" (Table 2.1). Moreover the phase of each branch is passed through a Hall effect transducer for the current flow measurement.

BRANCH	CIRCUIT BREAKER	CONTACTOR
Network	"hager" MY240 4552403 4500 C40 400V	Not present
Battery	"hager" MY240 4552403 4500 C40 400V	"hager" ES240 2392407 Ith: 40A Ui: 400 V 230V 50Hz 8,5kW AC1 400V
FC	"hager" MY232 45523283 4500 C32 400V	"hager" ES240 2392407 Ith: 40A Ui: 400 V 230V 50Hz 8,5kW AC1 400V
Load	"hager" MB250 4327285 6000 B50 400V	"hager" ES240 2392407 Ith: 40A Ui: 400 V 230V 50Hz 8,5kW AC1 400V
Active Load	"hager" MB250 4327285 6000 B50 400V	Not present
Reactive Load	"hager" MB250 4327285 6000 B50 400V	Not present

Table 2.1: Circuit breakers and contactors.

The built up architecture is also equipped with measuring sensors (indicated with S) that are in the "electric board" (Figure 2.7). In particular, a voltage sensor (S1) and current sensors (S4, S5, S6) which allow characterizing the electric power flows supplied or absorbed by each component are installed.

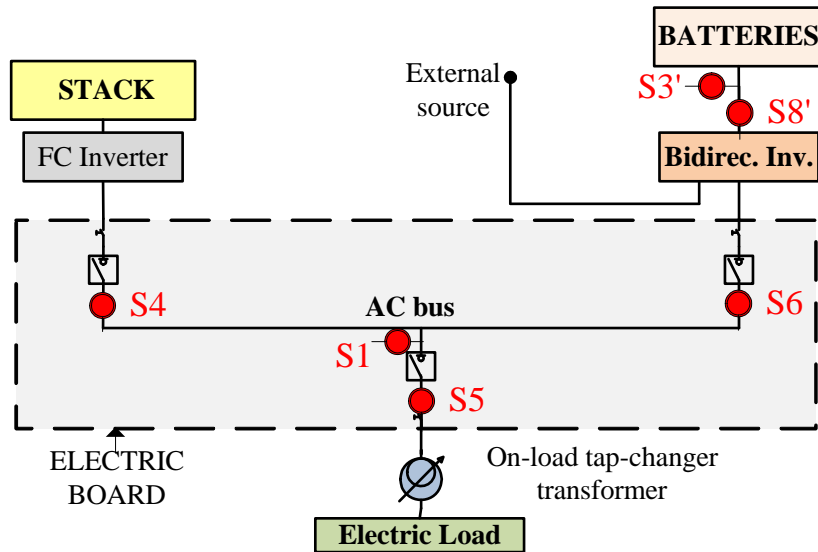


Figure 2.7: Measuring sensors in the electric board.

The characteristic of the measuring sensors presents in the electric board are shown in Table 2.2.

Sensor	Type	Accuracy	Measured quantity
S1	LEMLV25-P voltage transducers	±1.6% of reading (rdg)	v_{AC}
S2			v_{Aux}
S3 S3'			V_{DC}, V_{DC_Batt}
S4	LEMLA100-P current transducers	±0.45% of rdg	i_{AC}
S5			i_{Load}
S6			i_{Batt}
S8'	LEMLA200-P current transducer	±0.40% of full scale	i_{DC_Batt}

Table 2.2: Measuring sensors of the electric board.

The developed IES can operate in three different modes (Figure 2.8):

- stand-alone mode with simultaneous operation of FC and battery, when power load request is greater than the FC power, the battery will discharge to deliver the missing energy;
- stand-alone mode with simultaneous operation of FC and battery, when the FC power is greater than that required by the load, the battery will charge;
- grid-connected mode. In this case, the FC is turned off and the national network feeds the entire load and it charges the battery.

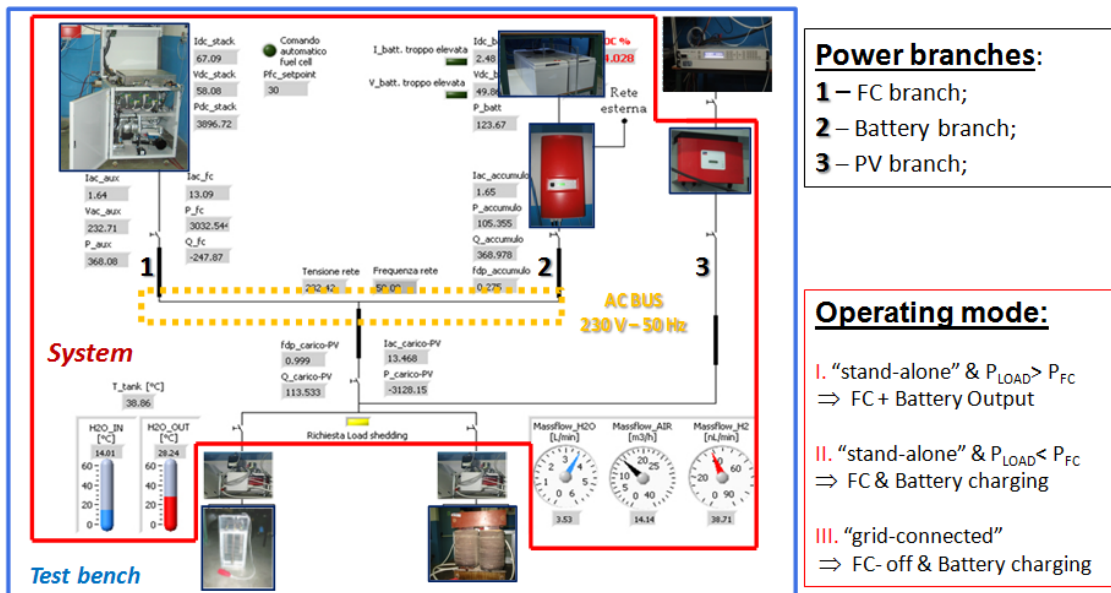


Figure 2.8: The power branches and the operating modes of the Integrated Energy System.

The “only FC operating mode” is not provided because the fuel cell works at unity power factor. Therefore, the FC is not able to provide the reactive power required by the loads. The FC cannot work alone even with purely resistive loads for two important reasons: the first concerns the inverter that equipped the cell, which needs the reference data from an external source; the second concerns the FC, not well suited to follows load variations, rather sudden for the required applications.

2.2 THE COMPONENTS OF THE INTEGRATED ENERGY SYSTEM

2.2.1 THE FUEL CELL (FC) SYSTEM

In the developed IES there is only one energy source, a commercial Polymer Electrolyte Membrane Fuel Cell (PEMFC) system (Figure 2.9), called “Penta H2” developed by ARCOTRONICS FUEL CELL S.r.l. This FC system is a micro-CHP (micro-Combined Heat and Power) system, suitable for stationary application and it is the main study object of this Ph.D. thesis.

The FC system, in parallel to the network, is able to provide 5 kW of electric AC power (via an electronic converter with output a single phase 230 V_{AC} - 50 Hz) and about 4.8 kW thermal output and it has been designed to operate at low temperatures nearly 65°C at full load.



Figure 2.9: The polymer electrolyte membrane fuel cell (PEMFC) system.

The FC system consists of two compartments(Figure 2.10): in the lower there are the stack and the thermo-fluid dynamics components; in the upper, the electrical auxiliaries.

The FC system (Figure 2.11) is divided into four subsystems:

- the supply circuits of fuel (e.g. hydrogen, H₂) (red line);
- the air line (light blue line);
- the FC cooling system (dark blue line);
- the stack and electric auxiliaries (black line).

The anode side is supplied with pure hydrogen draw from a 200 bar pressurized external gas reservoir, the pressure is first reduced with an external pressure reducing to 3 bar, before entering the convey line.

Before entering the stack the hydrogen stream has the pressure again reduced, by means of a second Pressure Reducing Valve (PRV) located into the FC system, to about 1.3 bar and passes through a Safety Control Valve (SCV).

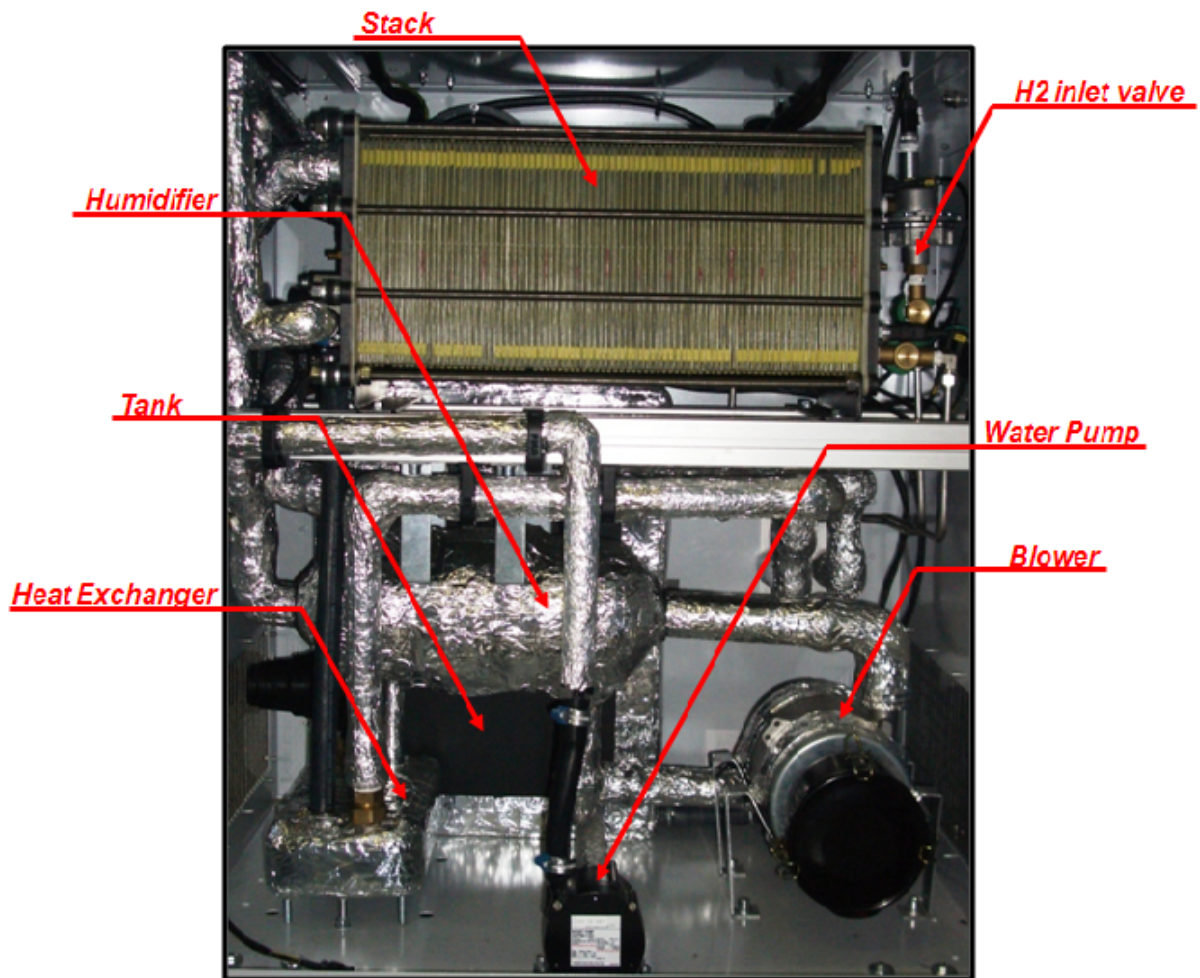


Figure 2.10: Photo of the FC system.

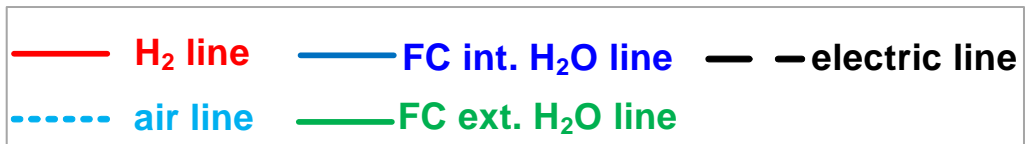
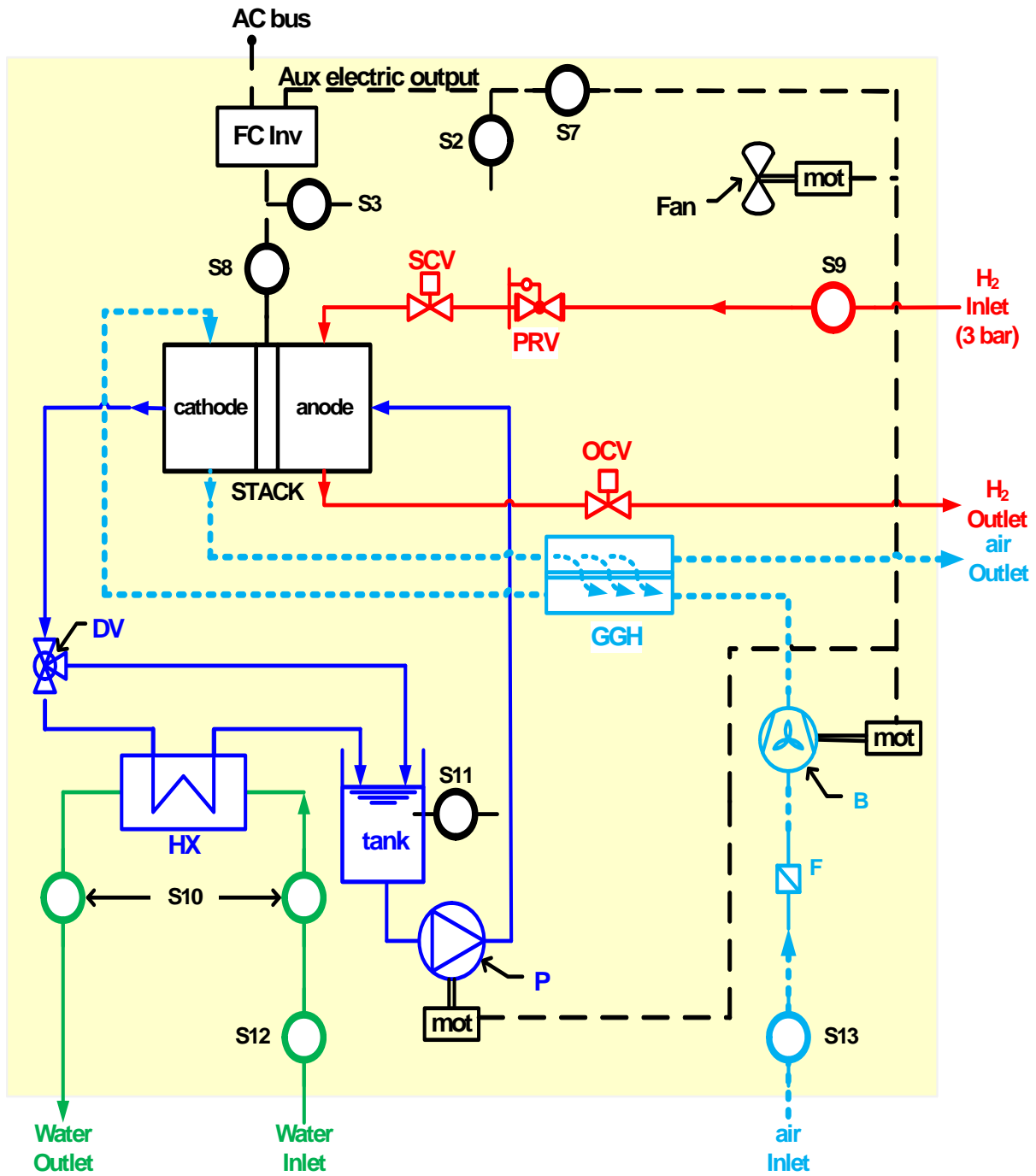


Figure 2.11: The FC system layout.

At the outlet side of the anodic line an Outlet Control Valve (OCV) is installed, this valve operate in dead-end mode, i.e. accomplishing a periodic purging of the water (FC reaction product migrating in the anode compartment) and of the accumulating impurities, but also a fraction of not reacted pure hydrogen.

On the other hand, the required air is admitted at the cathode side of the FC by means of an air Blower (B), which provides air at a pressure value equal to about 1.2 bar (Table 2.1, Table 2.3). The characteristic curves and the efficiency curves of the blower are shown in Figure 2.12 with continuous and dotted lines, respectively.

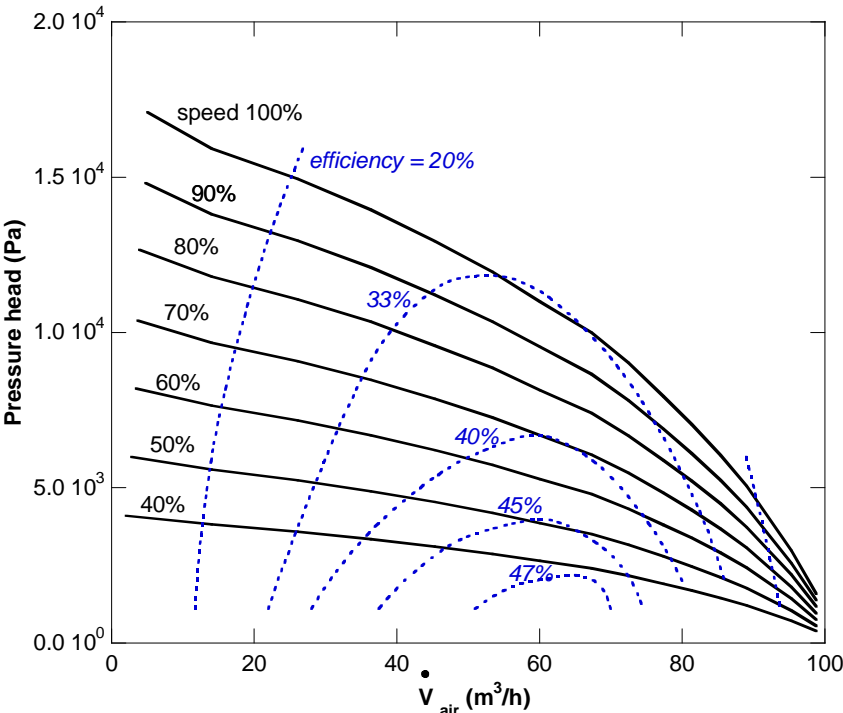


Figure 2.12: Blower characteristic and efficiency curves.

Variable	Rated voltage range	Frequency	Air volume	Speed	Power input	Current	Noise level	Max. ambient Temperature	Approx. weight
Unit	VAC	Hz	m ³ /h	min ⁻¹	W	A	dB(A)	°C	kg
Value	208-250	50/60	70	13000	600	2.6	71	50	3.7

Table 2.3: The main variables of the blower at each pressure of 10³Pa.

The air inlet stream is humidified before entering the stack by exploiting the humid air stream at the cathode outlet, through a counter flow Gas-Gas Humidifier (GGH).

The DC electric power output of the stack is collected and converted into AC electric power by the Fuel Cell Inverter (FC Inv).

The FC cooling system (Figure 2.13) is divided into two subsystem: the *primary cooling circuit* (blue line), and the *secondary cooling circuit* (green line).

The primary cooling circuit is a closed circuit that cools the stack using demineralized water (15 l ; quality DI <5 $\mu\text{S}/\text{cm}$.); it include the circulation pump (P), a water tank and a water-water Heat Exchanger (HX), which conveys heat to the secondary cooling circuit.

The secondary cooling circuit is an external water stream that can be used for the cogenerative applications.

The cooling system is provided with a Directional Valve (DV) to deviate, in particular operating conditions, the cooling water coming from the stack either towards the water tank or towards the HX in order to guarantee:

- (i) a fast FC heating up during the system start-up;
- (ii) a steady value of the stack internal temperature during the FC generating operation.

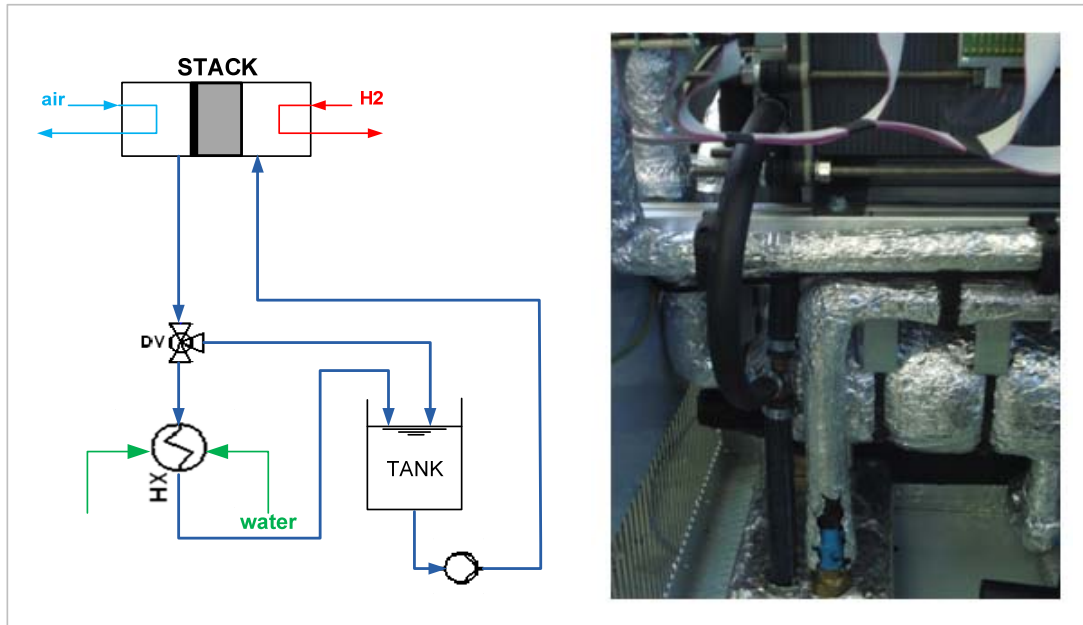


Figure 2.13: The FC cooling system: the primary cooling circuit (blue line) and the secondary cooling circuit (green line).

The heart of the FC system is the *stack* (Figure 2.14) consisting of 80 cells with an active area of 275 cm² each. The cells are electrically connected in series, while the reactant gases and the cooling liquid are fed to the cells in parallel.

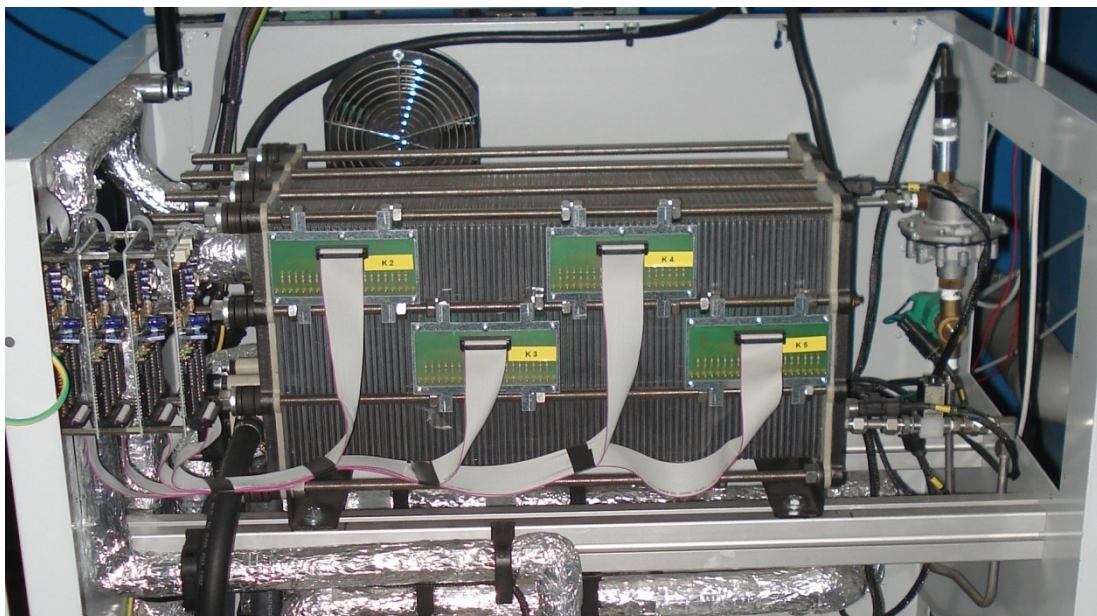


Figure 2.14: The 80-cells stack of the PEMFC.

Table 2.4 show the nominal data of the PEMFC stack. The DC electrical output capability of the stack is 1-5 kW at voltage in the range 50-70 V and current intensity variable in the range 1 –118 A.

<i>DATA</i>	<i>Units</i>	<i>Values</i>
DC stack power	kWe	1-5
DC voltage	V	50-70
DC Current	A	10 -118
H ₂ consumption max	Nm ³ /h	4.2
H ₂ purity (vol.)	%	99.9995
Anode side pressure	bar	1.3
Cathode side pressure	bar	1.2
Internal temperature	°C	65
N. of cells	-	80
AC Power	kWe	4.5
AC Voltage	V	220
mass	kg	200
Noise	dBA@1m	55
Start up	s	12 @500 W 1min @ full load

Table 2.4: The nominal data of the test stack.

The single cell (Figure 2.15) is composed by two main parts: the Membrane-Electrodes-Assemblies (MEA) and the Bipolar Plates (BPs).

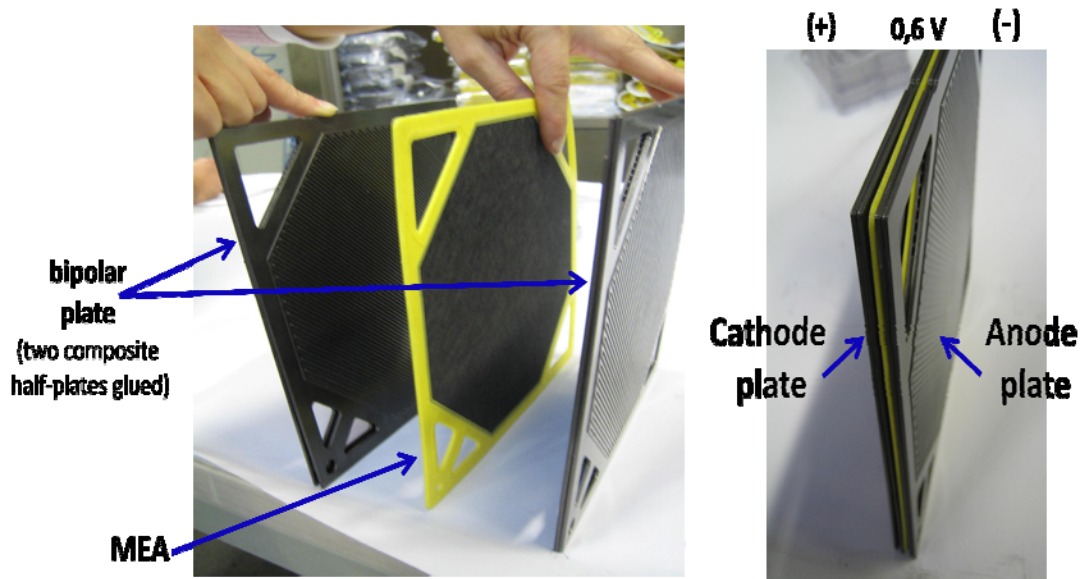


Figure 2.15: A single cell of the test PEMFC stack.

The bipolar plates consist of two composite graphite half-plates which are glued together (Figure 2.15). Each plate of a single cell has a weight of 130 g and a thickness of 0.7 mm (Figure 2.16).

The bipolar plates, together with the sealing must prevent any mixing of the various fluids, and ensure that none of them leak to the exterior. Moreover, they conduct the current between the cells.

To distribute air and hydrogen to the MEA each plate show a single channel, with a depth of 5 mm, along all its surface, the channel geometry (Figure 2.16) on the air and on the hydrogen side are identical. The channels for the cooling media are integrated into the back of the hydrogen half-plate. Hence, the cooling channels are situated in the partition between anode and cathode after the two half-plates are glued together.

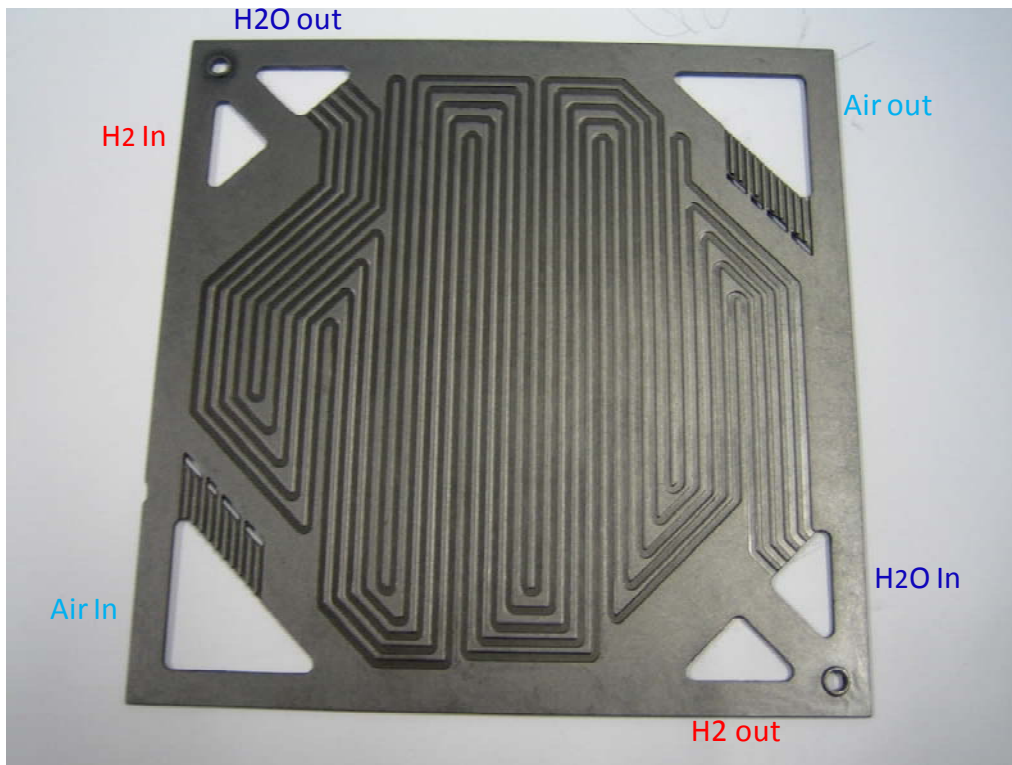


Figure 2.16: Composite graphite plates for stationary applications, hydrogen side, back view.

The Membrane–Electrode Assembly (MEA), built with a mould-to-size process using a graphite-polymer compound, is composed of two electrodes of porous material, separated by an electrolyte (Figure 2.17), the area between electrode and electrolyte is covered with a catalytic material, which allows chemical reactions to occur at the desired speed.

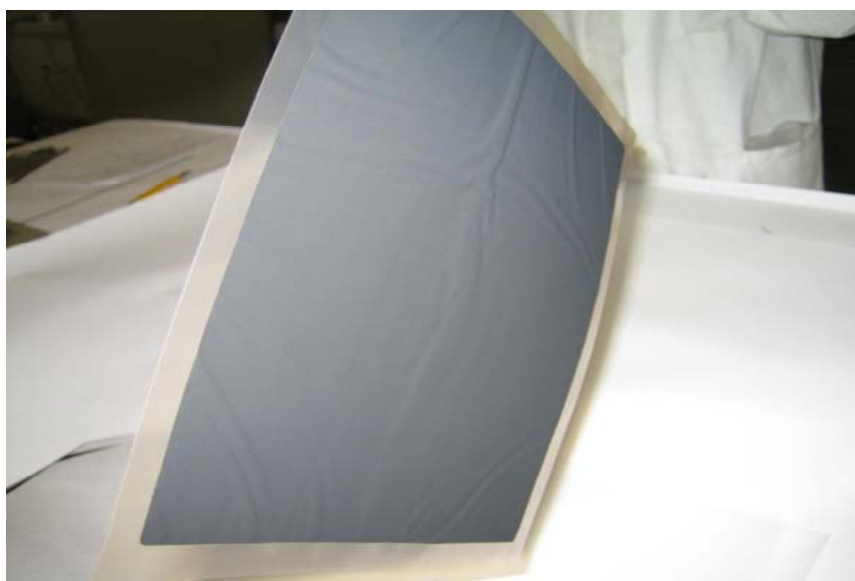


Figure 2.17: A photo of the Nafion membrane with the catalysts layers glued.

The electrolyte is a commercially available Polymer Exchange Membrane (PEM), *Nafion DuPont* [1]. The Nafion membrane (Figure 2.18) consists of a polymer structure with pendant sulfonic acid groups (SO_3H -groups). By swelling the membranes with water, the SO_3H -groups separate into mobile hydrated hydrogen ions (H^+) and immobile sulfite ions (SO_3^-). Moreover, the sulfonic groups are highly hygroscopic, absorbing about 13 molecules of water per sulfonic group within the polymer, giving high ionic conductivity. The mobility of the H^+ ion and thus the conductivity of the membrane depend strongly on the water content [2].

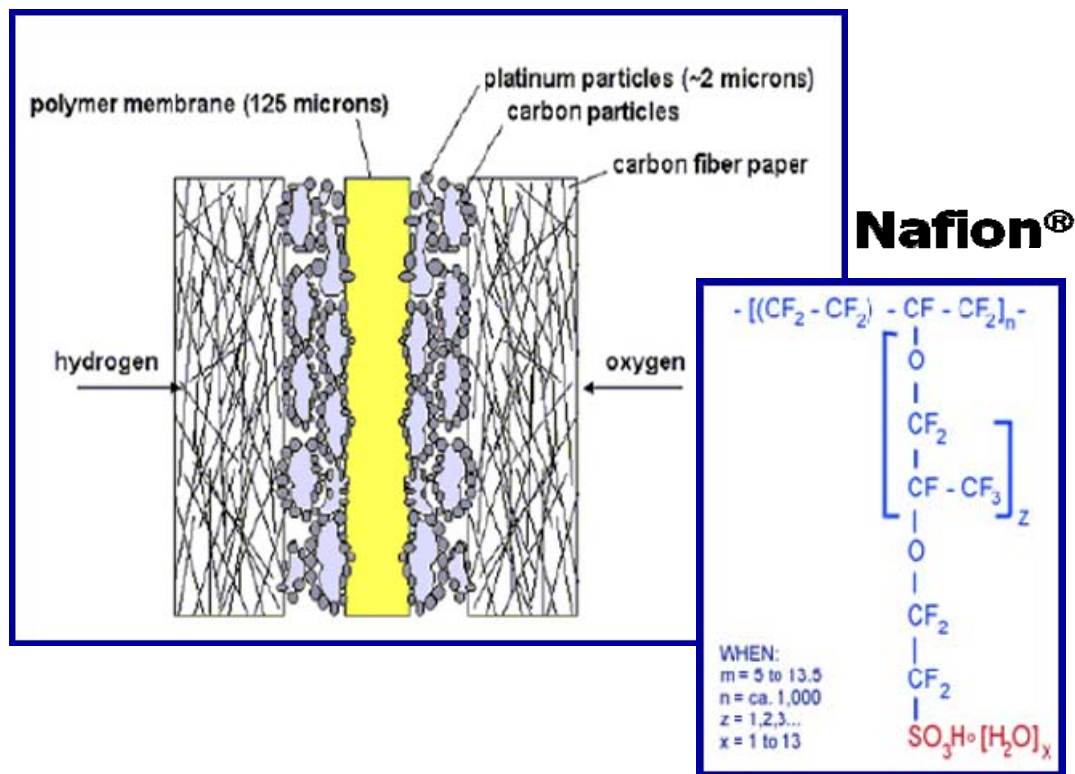


Figure 2.18: The polymer electrolyte membrane (Nafion @Du Point) of the FC system.

Therefore, proper water management of the membrane is essential for an efficient and reliable operation of the fuel cell [3]. The humidification of the membrane is, to date, obtained by mixing water steam with the reagents in input to the fuel cell.

To accelerate the electrochemical reactions on both sides of the membrane is deposited a thin layer of platinum (tenths of a milligram per cm^2 of surface).

Nafion membranes are generally characterized by their equivalent weight and their thickness. The equivalent weight describes the dry weight of the polymer per mol sulfonic acid group and presents a measure for the mass based concentration of the SO_3H groups. For example, the first two digits into the Nafion 112 name indicate an equivalent weight of 1100 g/mol. The thickness of the membrane is characterized by the third digit and amounts to 2/1000 inches in the dry state.

Compared to other commonly used membranes, such as Nafion 115 or Nafion 117, Nafion 112 is a thin membrane. Typically, thinner membranes show a better performance due to the smaller overall electrolyte resistance. A further advantage is the more effective water diffusion, leading to a better hydration of the anode, thus lower Ohmic losses even at high current densities [1].

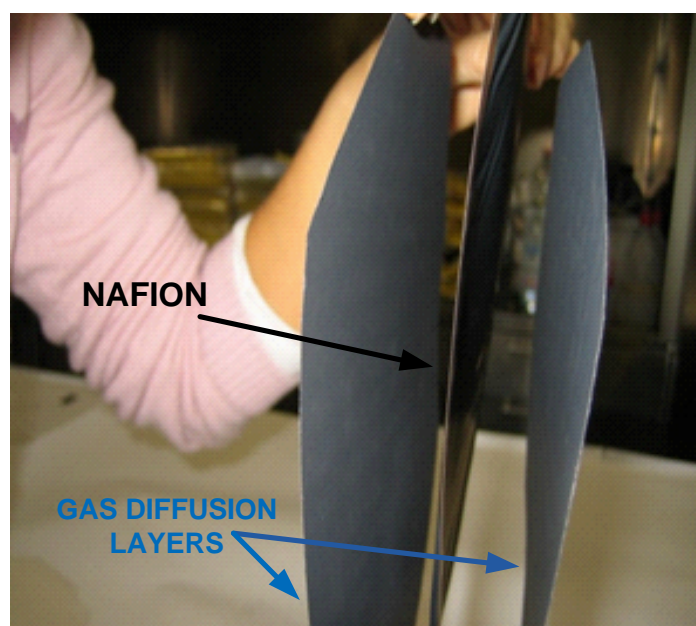


Figure 2.19: Card-stock gas diffusion layers.

The electrodes (Figure 2.19) must be porous to ensure the supply of the reactant gases to the reaction zone via gas diffusion. Gas diffusion occurs through the backing layer and the carbon support to the catalyst particles. A three-phase boundary between the gas phase, the electronic conductor (carbon supported catalyst particles) and the ionic conductor (solid polymer electrolyte) is prerequisite for the reaction to take place.

Usually the catalyst is impregnated with some ionomeric solution (such as Nafion solution) before pressing the electrode onto the membrane. This ensures a good contact between catalyst particle and ionomer material, extends the reaction zone and increases the catalyst utilization [4].

At the top of the FC system an electronic inverter (Figure 2.20) provides 230 V_{AC} single-phase voltage output at 50 Hz (within 1.25 Hz respect to the network frequency). This inverter manages the connection of the cell with the AC bus automatically, adapting both the frequency and the output voltage of the cell to the one generated by the battery inverter.



Figure 2.20: The inverter of the fuel cell system

The inverter output is connected to two terminals: one dedicated to feeding the load on the AC bus together with the battery, the other for the auxiliary power supply. The auxiliary components operate at different voltage and power values. Therefore, during the tests, it is necessary to identify the distinct powers absorbed by these components to characterize the performance of each part.

2.2.2 THE BATTERIES AND THE BIDIRECTIONAL INVERTER

The main tasks of the electrical storage system are:

- rapidly reproduce variable load profiles to overcome the FC inertia;
- provide the reactive power required by the load (the FC is able to deliver only active power);
- impose a fixed voltage at AC bus (the main parameter for the correct functionality of all other devices interfaced with that branch);
- offset the difference between the FC power and the one absorbed by the loads.

The electrochemical storage system installed in the test IES (Figure 2.21) is composed by four lead-acid batteries. Each battery has voltage of 12 V and a capacity of 100 Ah [5]. Assembling the four batteries in series a 48 V and 100 Ah storage system has been obtained.

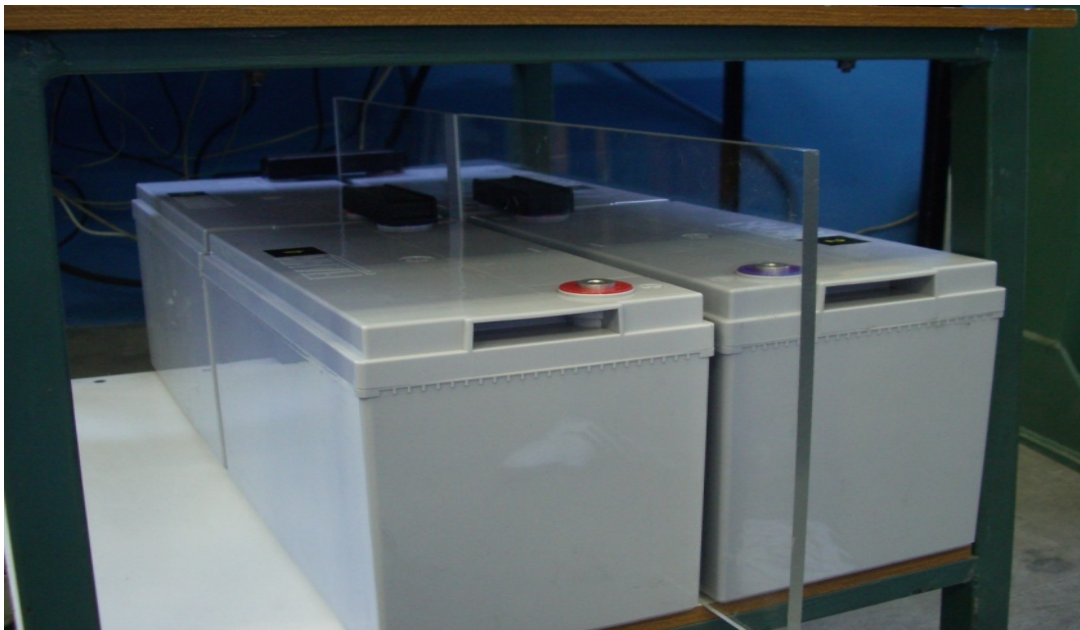


Figure 2.21: The electrochemical storage system of the test IES

An insulating material panel (Figure 2.22) has been interposed between the batteries to prevent accidental direct contact between the two poles, which would bring the storage system in short-circuit conditions and, then, to an incorrect discharge. Moreover, in the middle of the battery pack there is a slot that allow the insertion of a thermocouple to acquire the pack temperature.

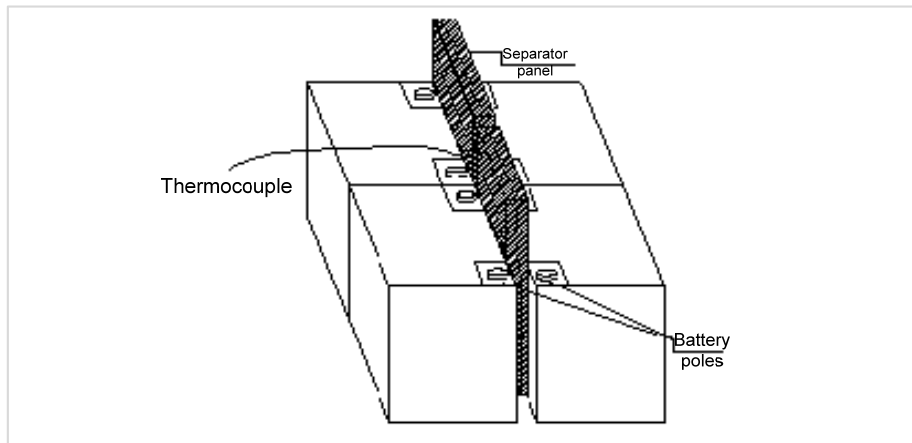


Figure 2.22: The batteries pack scheme with the panel and thermocouple.

The temperature monitoring is important for two reasons: the first is the presence of this temperature in the algorithm used to calculate the state of charge (SOC) of the batteries, under the assumption that this temperature is similar to the internal temperature of the electrolyte, since the speed of the redox reactions which occur in the batteries are directly proportional to the operating temperature of the reactants, according to the Arrhenius¹ law. The second is that the charge capacity of the lead batteries, although nominally equal to 100 Ah, strongly depends on the battery temperature. At temperatures below 20°C, the charging voltage should be slightly increased; with temperatures above 20°C, it must be reduced. These attentions are important to prevent overloads and underloads at all batteries temperatures.

On the battery branch a *Sunny Island 4248* inverter is installed (Figure 2.23). This is a bidirectional power converter designed for use in stand-alone condition. Using the energy stored in the batteries, it imposes a reference voltage of 230 V and an output frequency of 50 Hz, making possible the stable operation of the components that interface on the AC bus, such as the FC inverter, the photovoltaic emulator inverter and the on-load tap-changer transformer (OLTC) on the branch loads.

¹ *Arrhenius Law*: $K = Ae^{-Ea/RT}$, where: T is the reactants temperature; Ea is the activation energy of the reactions; A is the frequency factor and R is the Boltzman constant..



Figure 2.23: Island 4248, the inverter of the batteries.

For regulating, the inverter is provided with suitable voltage and network frequency control. Figure 2.24 shows the diagram of the regulation with statism (proportional control) implemented in the inverter, which has no need for communication between inverters. The regulation with statism involves a slight modification of the inverter circuit with the insertion of an inductor in AC side.

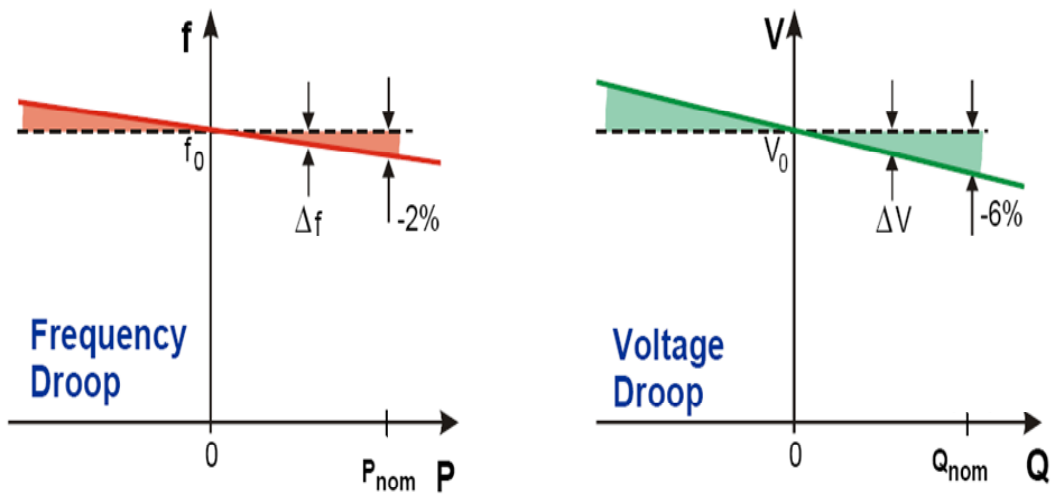


Figure 2.24: The control with statism.

The device can provide a nominal power of 4200 W and has two distinct AC ports (Figure 2.25).

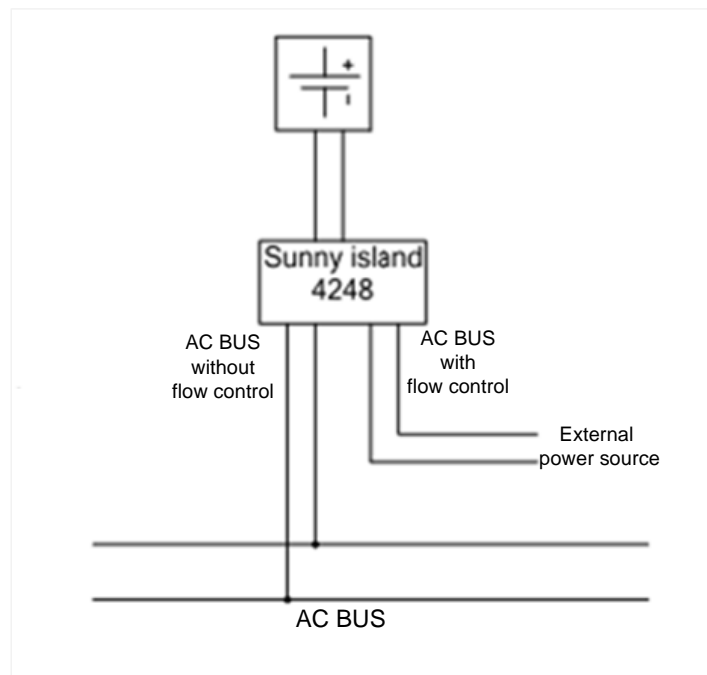


Figure 2.25: Ports of the bidirectional invert of the batteries.

The port connected to the external network is always bidirectional but with a control of the power flow, implemented for the possible link with the external network (or any other external power source) and it is actually used to charge the batteries.

Instead, the port connected to the AC bus of the system is bidirectional without control logic of the power flow [5]. This means that in stand-alone operating conditions, the batteries absorb the excess AC bus power supplied by the fuel cell and not used by the loads, or, in the opposite case, compensate for the missing power required by the loads. Hence, the electrochemical energy storages are not properly loaded through the charging port, but the effect of the charge is achieved through the mismatch of power on the AC bus.

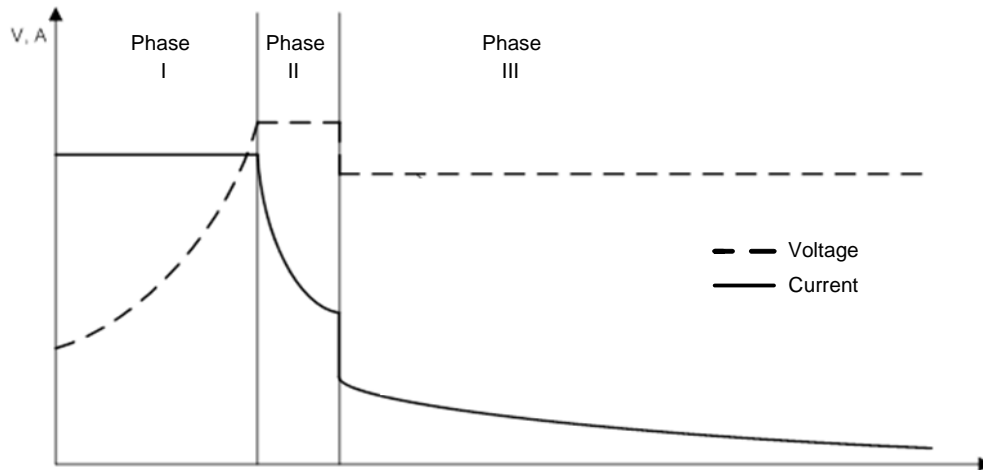


Figure 2.26: Batteries charge control.

Before each test run the batteries are put through a multiphase load cycle (Figure 2.26), that uses the grid connection. In the first charging phase the current is kept constant equal to 10 A, while the voltage increases. When the battery voltage is 60 V the second phase begins, which keeps the voltage constant and begins a gradual current reduction. After a prescribed time is passed, the charging mode switches to the final third phase in which the current is always reducing but at a slightly lower voltage of 54 V.

The exact time set for the duration of the second phase is autonomously chosen by the inverter between three different processes: Boost Charge, Full Charge and Equalizing Charge:

- the Boost charge is the process used principally, is designed to recharge the batteries in the fastest time possible;

- the Full Charge is carried out every 14 days or after eight recharges, in order to fully charge the battery or to compensate the effects of insufficient charging;

- the Equalizing Charge is conducted every 60 days. Each battery, in fact, is made by 2 V cells, connected in series. The state of charge of the single cells tends to diverge during the normal functioning, which can lead to premature failure, first of individual cells and then of the entire system. Thus, this mode allows the charging of the weaker cell, by means of targeted overloading, restoring the uniform state of charge of the battery system.

The choice of the FC-batteries coupling and of their active configuration was motivated by the following considerations: first, the FC-batteries coupling allows to take full advantage of the good characteristics in terms of the FC energy density and the batteries power density. Second a FC-batteries hybrid system can distinguish two configurations indicated in the literature as "active" or "passive", depending on the presence or absence of an electronic component in the connection between the fuel cell and the battery, for the flow energy adjustment.

The voltage-current characteristics curves, V-I, of both the fuel cell and the battery are shown in Figure 2.27.

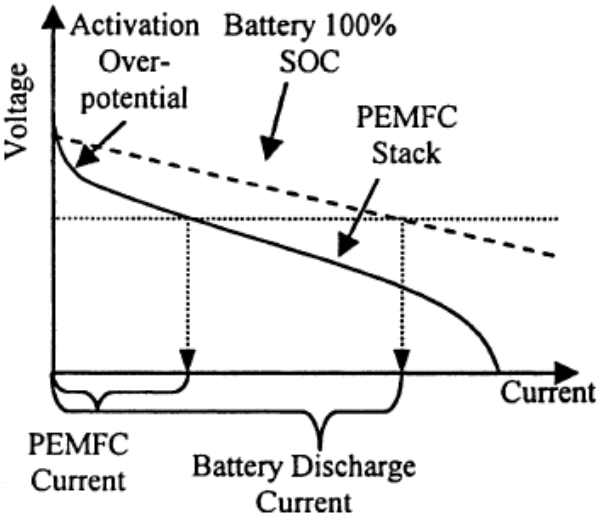


Figure 2.27: The V-I characteristics curves of the fuel cell (continuous line) and the battery (dotted line).

In the case of passive configuration the voltage at the terminals of the battery and the fuel cell must be similar and compatible, in every operating condition.

If the FC and the battery are approximately the same size, their V-I characteristics will usually also be characterized by a similar slope. However, the FC polarization curves show a clear voltage reduction at low loads, which leads to discharge the battery, without using the full power of the fuel cell.

On the contrary case, if the size of the battery cell is higher than that of cell this negative aspect is even more evident, since the V-I characteristic of the battery has a lower slope than that of the cell.

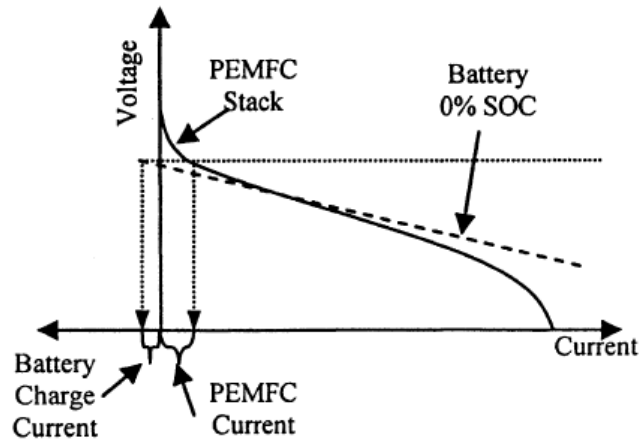


Figure 2.28: Coupling between FC and a battery with 0% SOC.

Figure 2.28 shows the characteristics for a partially discharged battery. The battery can be charged only at very low current values, where the cell voltage exceeds the amount of the battery. So it is possible to recharge the battery only in the case where the load is very low.

The problem is solved with the active configuration, which provides the interposition of an electronic component between the battery and the cell. The electronic component can be:

- 1) a simple voltage limiter that reduces the FC voltage at low load, which allows, both a better distribution of the load between cell and battery and a faster battery charging (Figure 2.29);

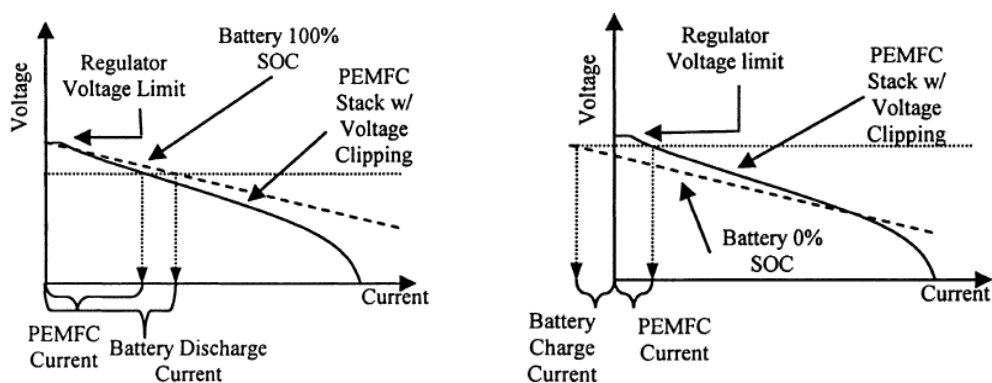


Figure 2.29: A simple voltage limiter.

- 2) a limiter with the voltage set equal to the voltage of maximum power of the cell.
The voltage is controlled charging of the battery (Figure 2.30);

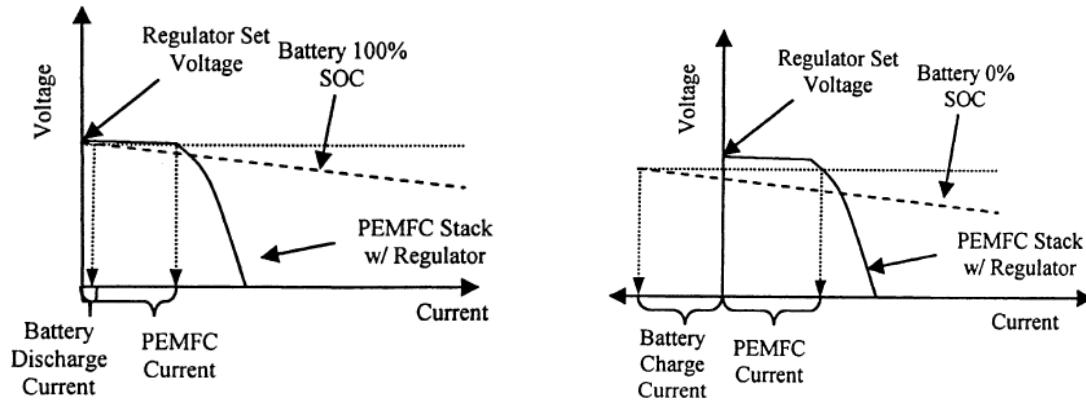


Figure 2.30: Limiter with voltage set equal to the maximum power voltage of the FC.

- 3) a DC/DC converter, which controls the voltage to the battery, limits the FC current, for example to a value not exceeding the maximum power value, and that limits the battery charging current. For the connection to the network is proposed the use of a PWM (pulse-width modulation) cycloconverter according to the scheme shown in Figure 2.31:

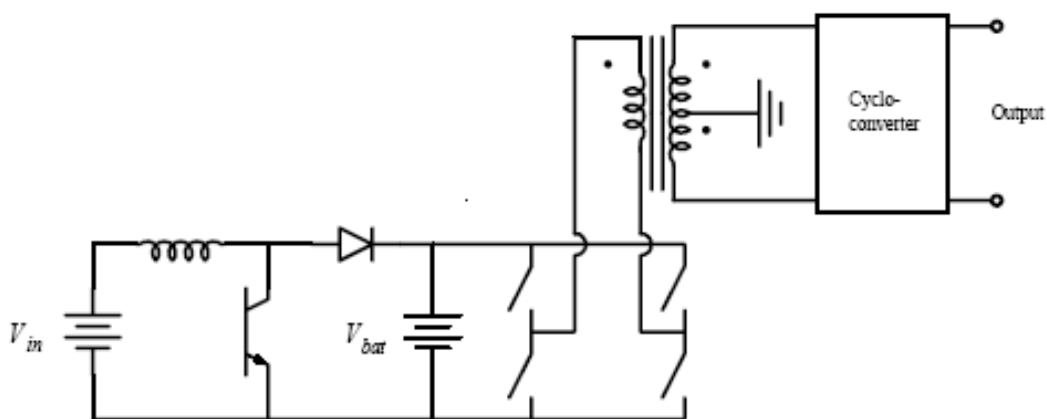


Figure 2.31: Scheme of circuit with a PWM Cycloconverter.

2.2.3 THE PHOTOVOLTAIC (PV) EMULATOR

The photovoltaic (PV) branch, in which a PV-array emulator and its inverter are installed in series, has the task of adding a random power source. This branch can be active or passive as it is not possible to modulate the amount of power produced by the solar radiation on the PV panel surface. Therefore, the amount of energy produced is random, only depending on the irradiation to which the panel is subjected. The photovoltaic (PV) emulator installed in the plant is the *E4360A Solar Array* (Figure 2.32).



Figure 2.32: The photovoltaic (PV) emulator.

The emulator reproduces the V-I characteristic of a PV module using four parameters:

- the solar array cells open circuit voltage, V_{oc} ;
- the solar array cells short circuit current, I_{sc} ;
- the current, I_{mp} and the voltage, V_{mp} , of the solar array cells corresponding to the maximum power.

The V-I characteristic is the exponential model developed by Britton et al. [6] (Figure 2.33).

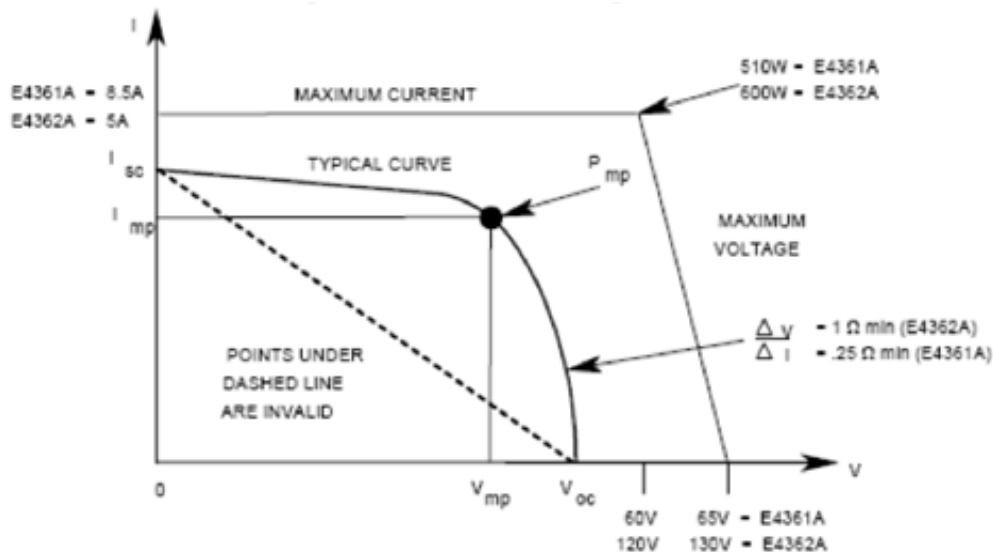


Figure 2.33: The V-I curve of the PV emulator VS the one of the solar array.

The four parameters can be set manually, directly on the user interface provided on the emulator or remotely on the control panel of the control system. Furthermore, it is also possible to give as input a solar energy production profile that simulates a variable radiation versus time.



Figure 2.34: *Windyboy*, the PV inverter.

The inverter "*Windyboy*" (Figure 2.34) realizes the interface between the AC bus and the PV emulator. This device operates in the grid-connected mode; therefore it requires a reference voltage on AC bus. Thanks to the software implemented, this inverter is able to implement maximum power point tracking.

2.2.4 THE ELECTRICAL LOAD

The load emulator consists of an active load and a reactive load.



Figure 2.35: The electric load emulators: left) the active load (a resistor); right) the reactive load (an inductive reactance).

The *active load* (Figure 2.35-left) was constructed using three resistors connected in parallel achieving a total impedance value of 9Ω approximately. At nominal voltage of 220 V it absorbs 23 A, then a dissipating active power of about 5 kW. The three resistors were mounted on a metal support equipped with a fan in order to reduce the temperature effect on the resistance close to the electric cables sheaths.

To simulate the *reactive load* (Figure 2.35-right), an inductive reactance of 12 mH in the linear region has been used. The maximum voltage power source of the load is 120 V, nearly corresponding to a reactive power loss of 3650 VAR. Over such limit, the absorbed current would be greater than the OLTC nominal one.

Each load is powered by an On-Load Tap-Changer (OLTC) transformer (Figure 2.36) which controls the voltage in the range between 0 and 230V.



Figure 2.36: The On-Load Tap-Changer (OLTC) transformers.

The main characteristics of the OLTC transformers installed in the test bench are shown in Table 2.5.

<i>Nominal data</i>	<i>Units</i>	<i>Values</i>
Nominal power	VA	7000
Nominal current	A	32
Input voltage	V	220
Output voltage	V	0 - 230

Table 2.5: The OLTC nominal data.

In particular, the load control is realized by an hysteresis regulator that adjust the transformer tap changer positions in order to track active and reactive power set points within an hysteresis window of ± 100 W or VAR.

2.2.5 THE CONTROL SYSTEM

The main tasks of the control system are:

Monitor the value of the quantities characterizing the system status. In particular, information on instantaneous power flows on each branch of the system are obtained from measures of the AC bus voltage and the AC current of each of the three branches. This allows to evaluate the rates of power delivered by the fuel cell and the battery.

Acquire all the quantities directly measured or processed that characterize the system behavior. This data is saved in a text file in the DSP internal memory and can be accessed by a personal computer via a cable connection. This file contains a table with the measured values which may be subsequently processed and plotted to study the behavior of the system in different operating conditions.

Check the contactors and the circuit breakers located on the branches (FC, battery, PV and loads branches), the FC power set-point. Moreover, through a dedicated card (card of load control) DSP controls OLTC transformers to vary the load (ohmic-inductive), allowing you to play different load scenarios.

Interface with the operator, a personal computer (PC) allows the display of the monitored variables and provides a virtual panel for the commands management.

The control system, realized [5] with the help of Department of Electric Energy and Information Engineering (DEI) of the University of Bologna, consist in a microcontroller with a Digital Signal Processing (DSP) data acquisition system and a Field-Programmable Gate Array (FPGA).

The FPGA is a digital interface programmable via software, able to realize logic functions.

The DSP is an embedded and real-time microcontroller with a high-performance chipsets, which is efficient in performing user-defined control algorithms [7]. Checking the flow of all data, the microcontroller is therefore the brain of the test bench.

In particular, the microcontroller inputs are:

- the data required to estimate the battery State Of Charge (SOC), i.e.: the batteries DC current, the battery DC voltage and the battery temperature;
- the information necessary to monitor the FC stack: the DC voltage and DC current of the stack ;
- the data related to FC: the hydrogen mass flow rate, the AC current and AC voltage of the FC auxiliaries;
- the AC bus data relative to the electric board: the AC bus voltage, the FC AC current, the load AC current, the battery AC current (usually referred to as current accumulation, to distinguish it from batteries DC current, upstream of the bidirectional inverter).

The microcontroller outputs are:

- the signal for the FC connection status;
- the FC power set point;
- the load shedding signal across the contactors state of the electric board.

Moreover, to the DSP is entrusted with the control of all data and component, with the exception of the load setting, which is performed by a separate board to make the users simulation unit and the energy management unit physically separated. In fact, the load control board has the following outputs: i). the active load set-point ii). the reactive load set-point, iii). measuring instruments signals.

In addition, the DSP must preserve the system through the implementation of virtual protections, such as a minimum/maximum voltage relay that intervenes when malfunction caused by voltage variations respect to its nominal value, occurs, and a directional relay that intervenes, if there is a not provided power flow to the network.



Figure 2.37: Left: The National Instrument CompactRIO™, on the right a single module.

The DSP is a National Instrument CompactRIO™ system, (Figure 2.37), equipped with the following modules:

- **NI cRIO 9004:** the embedded real-time controller equipped with a 200 MHz Pentium-class processor and an Ethernet port for network communication.
- **NI cRIO 9215:** has four synchronous analogic inputs (in the developed system these are: the network voltage, the AC FC current, DC battery current and AC loads current) and it is able to sample the channels simultaneously.
- **NI cRIO 9201:** consisting of height multiplexed analogue inputs (currently they are used only two: one for the air mass flow and the other for the water mass flow).
- **NI cRIO 9263:** analog output module, consisting of 4 channels (empty now).
- **NI cRIO 9481:** digital output module with four channels (called also "relay module"), used to control the circuit breakers of the load, battery, FC and photovoltaic branch.
- **NI cRIO 9472:** digital output module, consisting of height channels (empty now).
- **NI cRIO 9215:** analogic input module (it has the following inputs: DC FC voltage and DC FC current, AC voltage and AC current of the auxiliary systems).
- **NI cRIO 9215:** analog input module with four channels (now, one of which is empty, while the other three are used for the hydrogen mass flow rate, DC battery voltage and DC battery current, respectively).
- **NI cRIO 9211:** has four analogic inputs for thermocouples (e. g. input and output cooling water temperature from the FC, the tank temperature and the batteries temperature).

The control software was written using the LabView programming language then uploaded into the DSP.

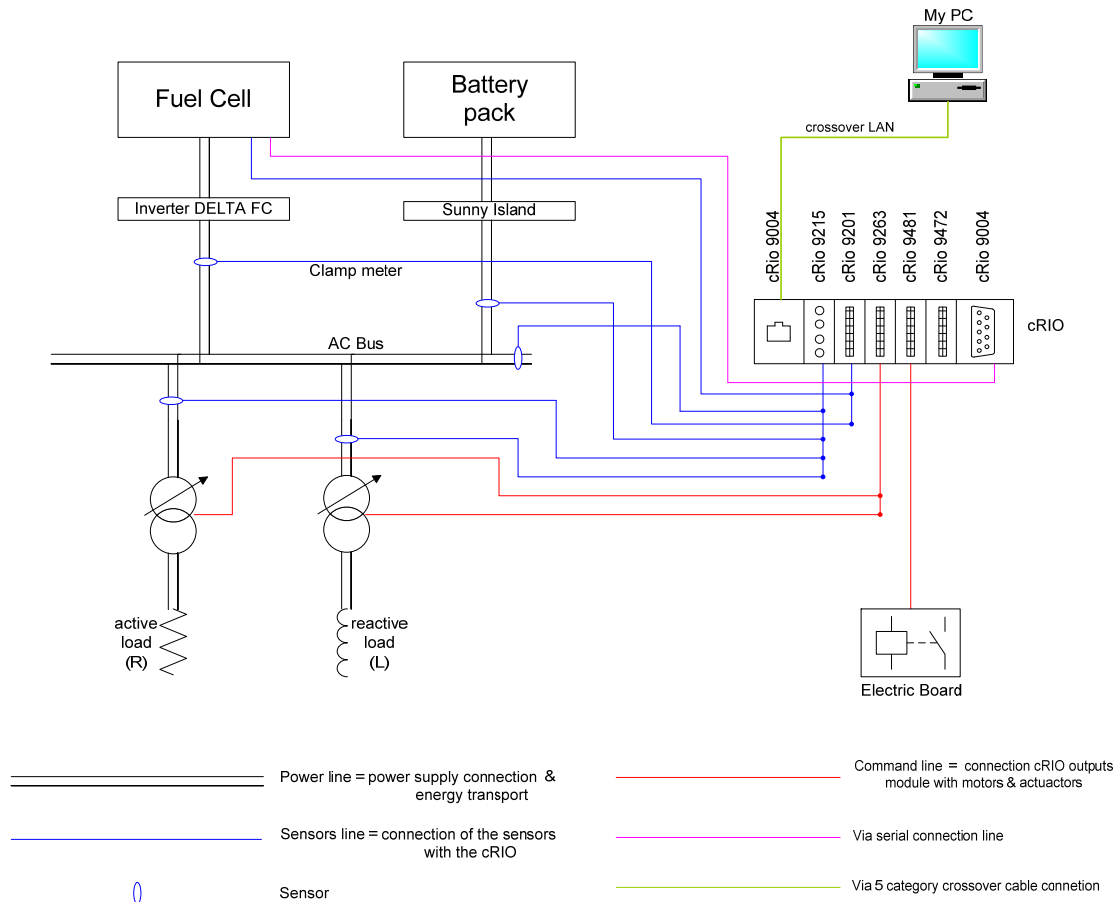


Figure 2.38: Layout of the acquisition and control system.

The DSP is connected to the various components of the IES “micro-grid via different lines (Figure 2.38):

- **Power line (black line):** it is composed of the set of lines that connect different branches to the AC bus, the AC bus itself and the load supply lines which depart from OLTC transformers.
- **Sensors Line (blue line):** consisting of the connections between the input modules of the DSP (both analog and digital) and all sensors installed in the system.

- Command line (red line): composed by the set of lines connecting the output modules of the DSP with actuators installed in the system. These actuators are stepper motors that change the transformation ratio of the OLTC transformers and contactors wired into the electrical board.
- Serial communication line (purple line): it connects the FC with DSP through a serial port RS232C.
- Connection line (green line): a 5 category 5 crossover cable that connects the DSP to the remote real-time monitoring station.

2.2.6 SENSORS

The IES is fully equipped with thermo-fluid dynamic and electrical sensors (Figure 2.39)

The thermo-fluid dynamic sensors are three flow meters and two thermocouples (Table 2.6):

- S9: hydrogen flow meter located on the fuel supply circuit inlet, at the anode side of the fuel cell;
- S10: two K-series thermocouples, positioned at the inlet and outlet of the secondary cooling circuit.
- S11: a J-series thermocouple, positioned in the tank of the FC system primary cooling circuit;
- S12: water flow meter placed on the secondary cooling circuit inlet;
- S13: air flow meter positioned upstream of the blower, on the air circuit inlet.

SENSOR	TYPE	ACCURACY	MEASURED QUANTITY
S1	LEM LV25-P voltage transducers	$\pm 1.6\%$ of reading (rdg)	V_{AC}
S2			V_{aux}
S3 ; S3'			$V_{DC} ; V_{DC-Batt}$
S4	LEM LA100-P current transducers	$\pm 0.45\%$ of rdg	i_{AC}
S5			i_{Load}
S6			i_{Batt}
S7			i_{Aux}
S8 ; S8'	LEM LA200-P current transducer	$\pm 0.40\%$ of full scale	$i_{DC} ; i_{DC-Batt}$
S9	BRONKHORST H2 El- Flow thermal flow meter	$\pm 0.8\%$ of rdg plus $\pm 0.2\%$ of full scale	$M_{flow_H_2}$
S10	K-series thermocouple	$\pm 1\text{ }^{\circ}\text{C}$	ΔT_W
S11	J-series thermocouple	$\pm 1\text{ }^{\circ}\text{C}$	T_{tank}
S12	McMILLAN FLO- SENSORS Turbine flow-meter	$\pm 0.50\%$ of rdg	$M_{flow_H_2O}$
S13	GL gx Turbine flow- meter	$\pm 0.5\%$ (linearity)	M_{flow_air}

Table 2.6: Measuring sensors and acquired variables.

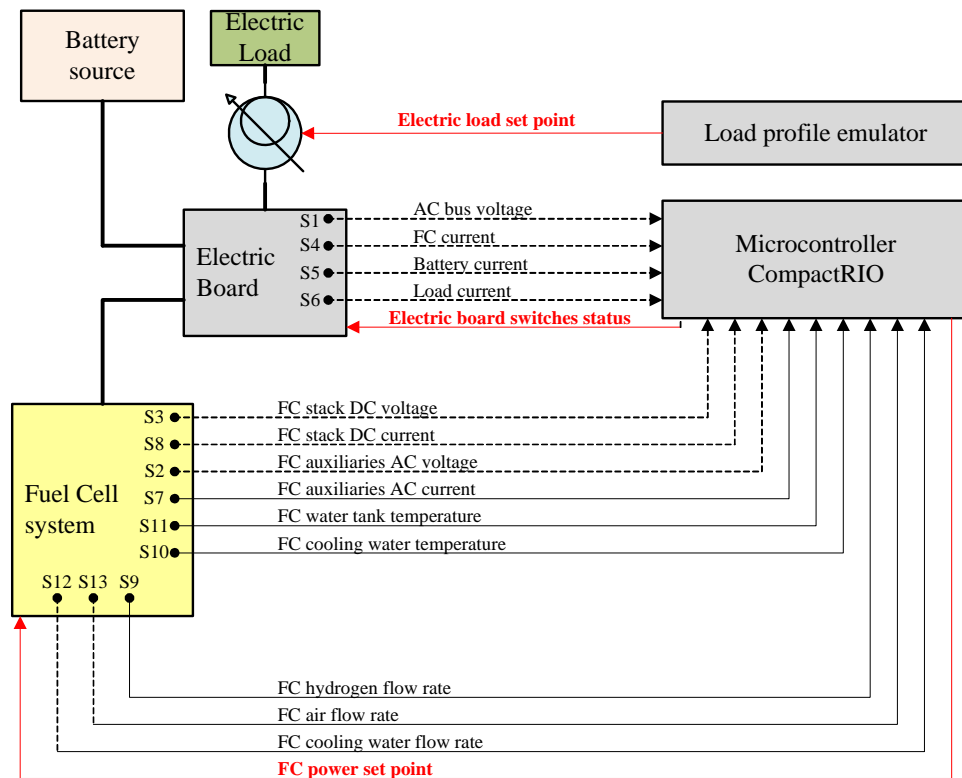


Figure 2.39: The data acquisition system layout.

The electric sensors are (Table 2.6):

- S1: voltage transducer placed on the AC bus, in the node where load is connected to the parallel of the FC and the battery branches, inside the electric board;
- S2: voltage transducer placed on the auxiliary branch, downstream the FC inverter;
- S3: voltage transducer placed on the FC branch upstream the inverter;
- S4: current transducer placed on the FC branch, inside the electric board;
- S5: current transducer placed on the load branch, inside the electric board;
- S6: current transducer placed on the battery branch, inside the electric board;
- S7: current transducer placed on the auxiliary branch, downstream the FC inverter;
- S8: current transducer placed on the FC branch, upstream the inverter.

Also a voltage transducer and a current transducer placed directly on the battery terminals (not shown in figures) have been installed to verify the battery state of charge.

The measured values allow the control system to verify the battery state of charge, SOC (function of the DC voltage, Current and temperature of the batteries), to monitor the FC stack and to evaluate the load power required.

Figure 2.40 shows the electric board realized in the test bench: in top part all measuring sensors, contactors, circuit breakers and the AC bus are installed, while in the bottom part the NY-CompactRio are positioned.

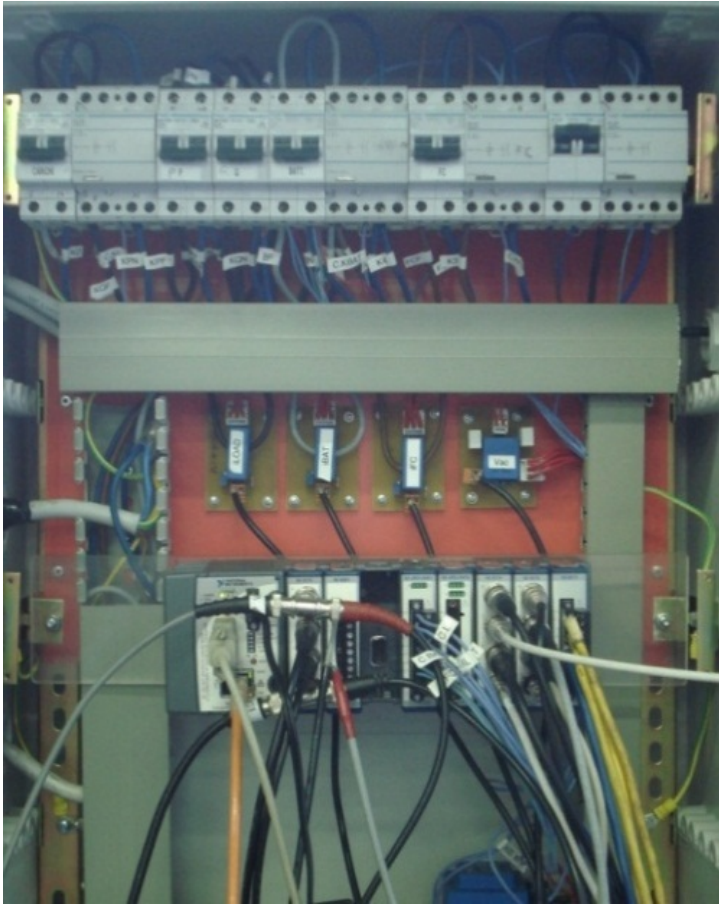


Figure 2.40: The electric board.

The energy fluxes and the produced/lost electric and thermal power contributions are shown in the flow chart reported in Figure 2.41.

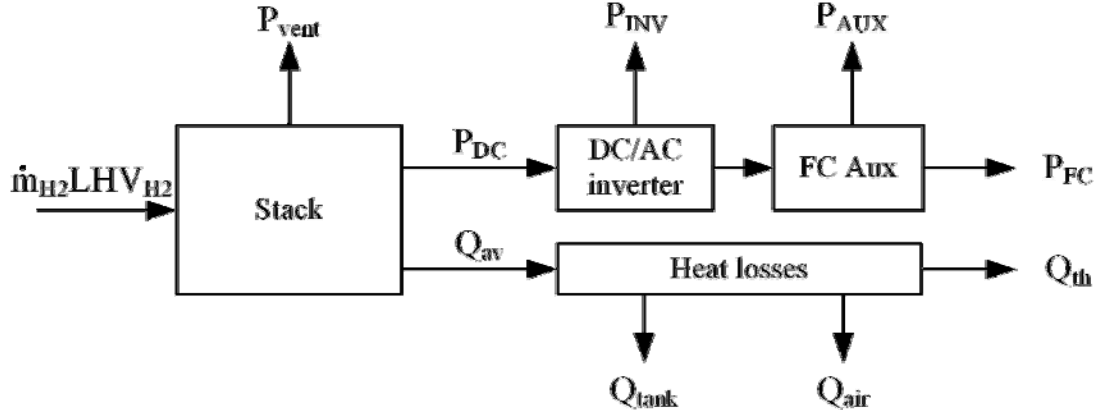


Figure 2.41: The chart of the FC system energy fluxes.

Table 2.7 reports the calculated values of the different power contributions measured.

FC DC POWER OUTPUT	$P_{DC} = i_{DC} \cdot V_{DC}$	STACK EFFICIENCY	$\eta_S = \frac{P_{DC}}{\dot{m}_i LHV_{H_2}}$
FC AC NET POWER OUTPUT	$P_{FC} = i_{AC} \cdot V_{AC}$	FC SYSTEM ELECTRIC EFFICIENCY	$\eta_{FC} = \frac{P_{FC}}{\dot{m}_{H_2} LHV_{H_2}}$
POWER CONSUMED BY THE AUXILIARIES	$P_{aux} = i_{aux} V_{aux}$	EFFICIENCY OF AUXILIARIES	$\eta_{aux} = \frac{P_{FC}}{P_{FC} + P_{aux}}$
POWER CONSUMED BY THE INVERTER	$P_{inv} = P_{DC} - P_{FC} - P_{aux}$	INVERTER EFFICIENCY	$\eta_{inv} = \frac{P_{DC} - P_{inv}}{P_{DC}}$
BATTERY EXCHANGE POWER	$P_{Batt} = i_{Batt} \cdot V_{AC}$	AVAILABLE THERMAL POWER	$Q_{av} = \frac{1 - \eta_S}{\eta_S} i_{DC} \cdot V_{DC}$
HYDROGEN MASS FLOW THROUGH THE MEMBRANE	$\dot{m}_i = i_{DC} \frac{m_{mol_{H_2}} \cdot N_{cel}}{2F}$	RECOVERED THERMAL POWER	$Q_{th} = \dot{m}_w c_w \Delta T_w$
FUEL UTILIZATION FACTOR	$U_f = \frac{\dot{m}_i}{\dot{m}_{H_2}}$	THERMAL EFFICIENCY	$\eta_{th} = \frac{Q_{th}}{\dot{m}_{H_2} \cdot LHV_{H_2}}$
POWER LOSS DUE TO THE UTILIZATION FACTOR	$P_{vent} = (\dot{m}_{H_2} - \dot{m}_i) LHV_{H_2}$	PRIMARY ENERGY SAVING INDEX	$PES = 1 - \frac{1}{\frac{\eta_{FC}}{\eta_{el,ref}} + \frac{\eta_{th}}{\eta_{th,ref}}}$

Table 2.7: Calculated parameters.

2.3 THE IES OPERATION STATES

The IES operation is governed by an automatic Power Management System (PMS), based on software implemented in Labview, which define different operating modes depending on the accurate estimation of the State Of Charge value (SOC).

The SOC control is important in order to minimize the stress due to the of FC start and shutdowns alternation. In fact, the regulation of the power that the FC has to deliver (the only "controllable" energy source) depends strongly on the battery state of charge. Is also necessary that the batteries voltage don't exceed the limits imposed by the inverter, this violation would lead to the inverter disconnection and, consequently, the system blackout.

The State of Charge (SOC) of a battery is the discharge capacity of the battery for a fixed current. In other words, the SOC can be defined as the amount of energy available (in percentage) compared to the nominal energy. In the literature, [10-13] several models have been proposed in order to estimate the SOC, such as: the electrolyte specific gravity measurement method, the battery impedance evaluation method, the impedance of the battery open circuit voltage evaluation, the method of current integration.

The algorithm for estimating the SOC value, implemented in the DSP of the IES, developed [10, 11] and validated [12, 13] by a joint effort between the DIN and the DEI, is based on the latter two methods and takes also into account the battery temperature and the battery discharge velocity, two factors that, if neglected, might affect the proper SOC value.

The microcontroller acquires as input (Figure 2.42) the data needed to estimate the SOC, i.e.: i) .battery DC voltage; ii). battery DC current; iii). battery temperature, then the software has the task of coordinating the FC and batteries activity, in order to satisfy the instantaneous load.

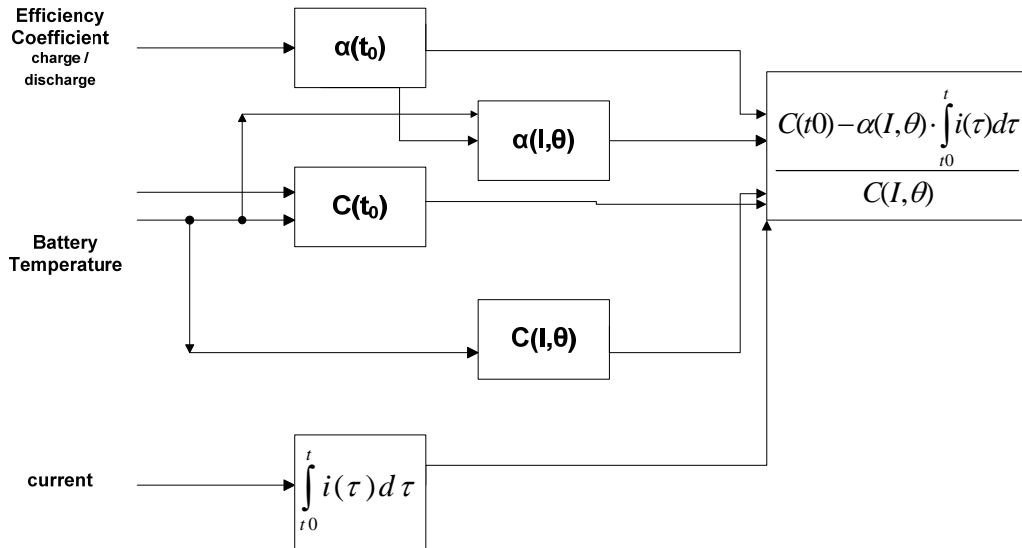


Figure 2.42: SOC estimation algorithm scheme.

The battery SOC is described by the following equation:

$$SOC(t) = \frac{C(t_0) - \alpha(I, \theta) \int_{t_0}^t i(t) dt}{C(I, \theta)} \quad (2.1)$$

where:

$C(t_0)$ is the battery capacity at time t_0 ;

$i(t)$ is the battery current instantaneous value;

α is the efficiency coefficient associated with the efficiency of the battery charge or discharge.

$C(I, \theta)$ is the battery capacity at a constant discharge velocity, I and at electrolyte temperature, θ defined as shows in the following equation:

$$C(I, \theta) = \frac{K_c \cdot C_0^* \cdot \left(1 + \frac{\theta}{\theta_f}\right)^\varepsilon}{1 + (k_c - 1) \cdot (I/I^*)^\delta} \quad (2.2)$$

where:

C is the battery capacity;

ϑ is the electrolyte temperature;

I is the battery current during a constant discharging profile;

ϑ_f is the electrolyte solidification;

$K_c, C_0^*, \varepsilon, \sigma, I^*$ experimental constants.

To maximize the autonomy and independence of the experimental system, when operates in island mode, the battery SOC and limitations of the battery voltage [13, 14] are of paramount relevance. The aim of the SOC control is to maintain this value close to the optimal batteries voltage value, SOC* a value that has been determined as a compromise of the SOC values that are able to:

- maintain the batteries to a such level that they are able to transfer energy, when the power absorbed by the load is greater than that generated by the photovoltaic system and the fuel cell, or vice versa to store it;
- minimize the number of FC start and shutdowns. The PMS switches on the fuel cell only when the SOC value is less or equal to the SOC start value, while switching off the FC when the battery is fully charged.

Under the hypothesis of fuel cell switched on, the PMS is able to distinguish between different states of operation [8, 9] (Figure 2.43), defined as interval associated with the battery SOC:

- State 1: $SOC \leq SOC^*_{min}$;
- State 2: $SOC^*_{min} < SOC < SOC^*_{max}$;
- State3: $SOC^* \leq SOC < SOC^*_{max}$;
- State 4: $SOC^*_{max} \leq SOC$.

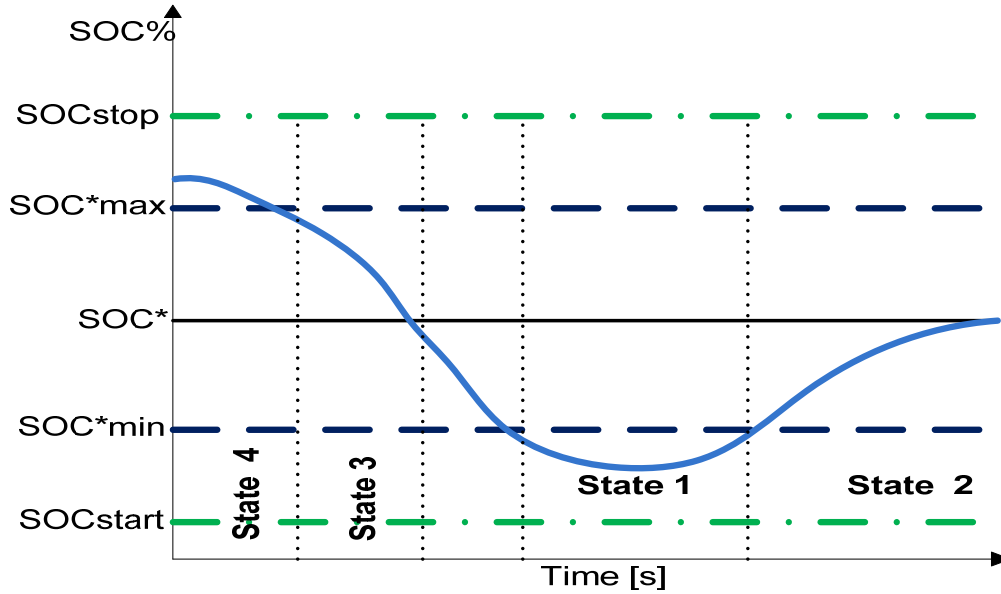


Figure 2.43: The SOC allowable values.

For each of the four operating states, the power management system determines the value of $P_{FC\text{-setpoint}}$, which is the power value that the fuel cell should dispense in order to control and maintain the battery state of charge around the optimal value SOC^* .

The equations implemented in the control software to calculate the $P_{fc\text{-setpoint}}$ value are the following:

$$\text{State 1: } P_{FC\text{-setpoint}} = -P_{PV\text{-load}} + (P_{FC\text{max}} + P_{PV\text{-load}}) \cdot (1 - u_{\text{max}}) \quad (2.3)$$

$$\text{State 2: } P_{FC\text{-setpoint}} = -P_{PV\text{-load}} + (P_{FC\text{max}} + P_{PV\text{-load}}) \cdot \frac{SOC^* - SOC}{SOC^* - SOC^{\text{min}}} \cdot (1 - u_{\text{max}}) \quad (2.4)$$

$$\text{State 3: } P_{FC\text{-setpoint}} = -P_{PV\text{-load}} + (P_{FC\text{min}} + P_{PV\text{-load}}) \cdot \frac{SOC - SOC^*}{SOC^{\text{max}} - SOC^*} \cdot (1 - u_{\text{min}}) \quad (2.5)$$

$$\text{State 4: } P_{FC\text{-setpoint}} = -P_{PV\text{-load}} + (P_{FC\text{min}} + P_{PV\text{-load}}) \cdot (1 - u_{\text{min}}) \quad (2.6)$$

where:

$$P_{FC\text{max}} = 4.5 \text{ kW}$$

$$P_{FC\text{min}} = 0.5 \text{ kW};$$

$P_{PV\text{-load}}$ is the difference between the power produced by the photovoltaic system and the power required by the active load.

u_{min} and u_{max} are the Proportional-Integral- Derivative (PID) controller outputs.

Analyzing the equations that defined the operating states, it observes that in states 1 (eq. 2.3) and 4 (eq. 2.6), the PMS calculates the $P_{FC\text{-setpoint}}$ modifying the SOC value bringing it in the range defined by the limits SOC^*_{min} and SOC^*_{max} : this charge or discharging the battery rapidly, the battery discharging and charging velocity also depends on the power required by the active and reactive loads. For states 2 (eq. 2.4) and 3 (eq. 2.5), the $P_{FC\text{-setpoint}}$ is defined by adding or subtracting to the $P_{PV\text{-load}}$, a quantity proportional to the difference between the SOC and the SOC^* normalized on the expression $(SOC^* - SOC^*_{min})$ for the state 2 and on $(SOC^*_{max} - SOC^*)$ for the state 3.

Moreover, the $P_{FC\text{-setpoint}}$ value is limited by the amount u_{min} and u_{max} , variables, that varies between 0 and 1, in order to limit the value of the power that should be delivered by the fuel cell. Each of them is determined through the realization of a Proportional Integral and Derivative (PID) controller:

$$u(t) = K_p e(t) + \frac{K_p}{T_i} \int_0^t e(\tau) d\tau + K_p T_d \frac{de(t)}{dt} \quad (2.7)$$

where $e(t)$ is the input (the error to be controlled), while K_p , T_i and T_d parameters are appointed proportional gain, integral time constant and derivative time constant, respectively [15].

The main performance required to the PID controller implemented in the IES system are: i) respect the voltage limits, $V_{batt\text{-min}}$ and $V_{batt\text{-max}}$, inside the battery inverter in order to avoid the disconnection of this component and, consequently, the blackout of the system; ii) dampen the battery voltage hysteresis; iii) maintain the battery voltage, V_{batt} , values within a range defined by two threshold values: $V_{batt\text{-nom-min}}$ and $V_{batt\text{-nom-max}}$, greater than the under voltage threshold of the inverter, $V_{batt\text{-min}}$, and less than the overvoltage $V_{batt\text{-max}}$, respectively.

This type of regulator has a fixed structure in which it is possible to change the parameters value, in order to obtain the desired performance. In the present case, for the determination of u_{min} and u_{max} variables were chosen the same values parameters: $K_p = 1$; $T_i = 30$ s; $T_d = 0.06$ s.

2.4 THE FC OPERATION PROGRAMMING LOGIC

The logic adopted for the PEMFC operation considers the energy delivered by the cell varies continuously as a function of the battery state of charge, SOC, as shown in Figure 2.44.

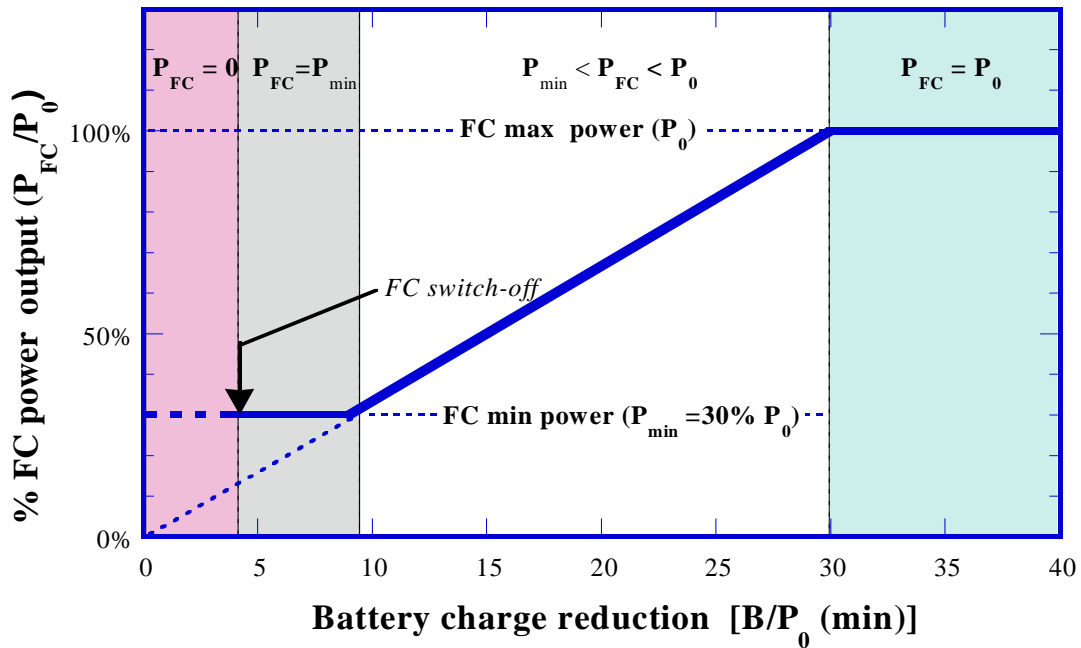


Figure 2.44: FC programming logic: FC power VS battery charge reduction [5].

Specifically for this programming logic, the power delivered by the cell (P_{FC}) is defined so as to be proportional to the energy reduction in the battery, E_i . Only if the cell operates between the load nominal value, P_0 (upper limit) and a minimum value (P_{min} , set equal to 30% of maximum load). For too low values of E_i the cell is turned off, while for high values work at maximum load. This condition on the interval allowed for the working power of the cell is adopted since its efficiency would decrease drastically for load values outside this range.

Analytically, the power which runs to the fuel cell is chosen as the minimum value between the following ones:

$$P_{FCi+1} = \min \left(\begin{array}{ll} 0 & \text{se } E_i < 0.3 \cdot P_0 \cdot \Delta t \\ P_0 \cdot \Delta t; & 0.3 \cdot P_0 \cdot \Delta t \quad \text{se } 0.3 \cdot P_0 \cdot \Delta t < E_i < 0.6 \cdot P_0 \cdot \Delta t \\ & 0.5 \cdot E_i \quad \text{se } E_i > 0.6 \cdot P_0 \cdot \Delta t \end{array} \right) \quad (2.8)$$

while the stop condition of the fuel cell, can be indicated with the expression:

$$E_{i-1} + R_i \cdot \Delta t < P_{\min} \cdot \Delta t \quad (2.9)$$

where:

P_{FCi} FC power delivered in the time interval, i ;

Δt duration of the single interval time;

E_i battery energy reduction up to the time interval i

R_i energy request by the users in the i^{th} period.

Precisely, in the time interval i , the cell is disconnected if the energy supplied at minimum load exceeds the battery energy reduction considering the loads demand.

By adopting this programming logic, the on-off system of the FC is more regular, the number of starts decrease and the contribution of the cell to meet the utilities load increases [5].

References of the chapter 2:

- [1] DuPont: "Dupont Nafion PFSA Membranes N-112, NE-1135, N-115,N-117, NE-1110 Product Information",2003, <http://www.dupont.com>
- [2] T. A. Zawodzinski, J. Davey, J. Valerio, S. Gottesfeld: "The WaterContent of Electro-Osmotic Drag in Proton-Conducting PolymerElectrolytes", *Electrochimica Acta*, Vol.40, No.3, pp. 297-302, 1995.
- [3] H. van Bussel, F. Koene, R. Mallant: "Dynamic Model of solidpolymer fuel cell water management", *Journal ofPower Sources*, Vol.71, pp. 218-222, 1998.
- [4] Carrette, K. A. Friedrich, U. Stimming: "Fuel Cells - Fundamentals and Applications", *Fuel Cells*, Vol. 1, No. 1, pp. 5 - 39, 2001
- [5] B. Belvedere, M. Bianchi, A. Borghetti, A. De Pascale, M. Di Silvestro, M. Paolone, DSP-Controlled Test Set-up for the Performance Assessment of an Autonomous Power Unit Equipped with a PEM Fuel Cell, Proc. of the International Conference on Clean Electrical Power, Capri – Italy, May 21st-23rd, 2007.
- [6] Britton, Lunscher, Tanju, A 9 kW high-Performance Solar Array Simulator, Proc. Of the European Space Power Conference, (1993).
- [7] CompactRIO™ Reference and Procedures Help (FPGA Interface), 2004–2010 National Instruments Corporation. <http://www.ni.com/dataacquisition/compactrio/>.
- [8] Belvedere B., Bianchi M., Borghetti A., Paolone M., Design, Implementation and Testing of an Automatic Power Management System for Residential Stand-alone Microgrids with Hybrid Power Supply,The 18th IFAC World Congress , Milano (Italy) , August 28-September 2, 2011.
- [9] Belvedere B., Bianchi M., Borghetti A., Paolone M., A microcontroller-based automatic scheduling system for residential microgrids., Proc. of 2009 IEEE Power Tech Conference, (2009), Bucharest.
- [10] Piller, S., Perrin, M., Jossen, A. (2001). Methods for state-of-charge determination and their applications, *Journal of Power Sources*, 96, 113–120.
- [11] Pop, V., Bergveld, H.J., Notten, P.H.L., Regtien, P.P.L. (2005). State-of-the-art of battery state-of-charge determination, *Measurement Science and Technology*, Vol. 16, R93-R110.

- [12] M. Bagnoli, B. Belvedere, M. Bianchi, A. Borghetti, A. De Pascale, M. Paolone, A feasibility study of an auxiliary power unit based on a PEM fuel cell for on-board applications, *Journal of fuel cell science and Tech.*, vol.3, no.4, pp 445-451, 2006.
- [13] US department of energy, 2004, *Fuel Cell Handbook*, 7th ed., Eg&G Services Parsons, Inc., Morgantown, WV.
- [14] G. Hinds, NPL Report DEPC-MPE 002, 2004, pp. 25–42.
- [15] Z. Luo, D. Li, H. Tang, M. Pan, R. Ruan, Degradation behavior of membrane-electrode assembly materials in 10-cell PEMFC stack, *Int. J. Hydrogen Energy* 31 (2006) 1831-1837.

Chapter 3

EXPERIMENTAL ANALYSIS OF THE *IES* PERFORMANCE

In this chapter the experimental performance analysis of the developed Integrated Energy System (IES) is described. Both electrical and CHP performance of the PEMFC in study, "*Penta H2*", has been investigated. Different test campaigns were conducted to analyze the behavior of the system at variable loads. The aim of this analysis is to determine the main factors characterizing the FC system efficiency and, thus, to optimize its performance.

After a definition of the main variables necessary to processing the experimental data, the tests carried out to investigate the PEMFC electrical and thermal performance at different load conditions are shown.

In particular, different tests campaigns are conducted in order to investigate the FC electrical properties and thermal ones.

3.1 THE ACQUIRED AND CALCULATED VARIABLES

The variables used to processing the experimental data acquired by the sensors [1-3] and which stored by the microcontroller CompactRIO [1-4], as described in the previous chapter (Ch. 2 - Tables 2.2 and 2.6), are here defined in detail.

Denoting with the symbols: V the voltage, [V], i the current, [A], P the power [W] and with the acronyms DC the Direct Current, and AC the Alternate Current, the variables acquired by the sensor are:

- the voltages [V]:

- v_{AC} : the voltage measured with voltage transducers at the AC bus;
- v_{aux} : the voltage measured with voltage transducers at the FC auxiliaries;
- V_{DC} : the voltage measured with voltage transducers at the FC DC outlet;

- the currents [A]:

- i_{AC} : the current measured with current transducers at the FC AC outlet;
- i_{Load} : the current measured with current transducers at the load outlet;
- i_{aux} : the current measured with current transducers at the auxiliaries;
- i_{Batt} : the current measured with current transducers at the battery outlet;
- i_{DC} : the current measured with current transducers at the FC DC outlet;

- the flow rates:

$M_{\text{flow_H2}}$ [NL/min]: the H₂ consumption measured with a thermal flow meter;

$M_{\text{flow_air}}$ [m³/h] : the air flow rate supplied to the stack;

$M_{\text{flow_H2O}}$ [L/min] : the cogenerative water flow rate measured with a turbine flow meter;

- the temperatures [°C]:

T_{w_in} : the inlet cogenerative water temperature measured with a K-series thermocouple;

T_{w_out} : the outlet cogenerative water temperature measured with a K-series thermocouple;

T_{tank} : the temperature of the FC water cooling tank measured with a J-series thermocouple.

Obviously, considering that the hydrogen density at normal conditions (p=1 bar; T= °C) is $\rho_{H_2} = 0.0893 \text{ kg/m}^3$, note the hydrogen flow rate, $M_{\text{flow_H2}}$, expressed in NL/min, immediately hydrogen mass flow rate, \dot{m}_{H_2} , can be calculate in g/s, and vice versa. The same for the air flow rate, $M_{\text{flow_air}}$, considering its density at ambient conditions ($\rho_{\text{air}} = 1,204 \text{ kg/m}^3$), and for the water flow rate, $M_{\text{flow_w}}$, ($\rho_w = 1000 \text{ kg/m}^3$) at atmospheric conditions.

The CompactRIO microcontroller [1-4] elaborates and stores the measured quantities used to calculate the performance variables:

- P_{DC} [W] : FC DC power output, i.e. the power delivered by the stack;
- P_{FC} [W] : FC AC power output, i.e. the power fed into the network from the FC;
- P_{aux} [W] : power absorbed by the auxiliaries;
- P_{Batt} [W] : battery exchange power.

Notes these quantities, by means of appropriate equations, it is possible to calculate the following indirect variables:

- P_{inv} [W] : power losses by the FC inverter;
- \dot{m}_r [g/s] : mass flow rate of the actually reacted H_2 through the membrane;
- η_{inv} [-] : efficiency of the FC system inverter;
- η_{aux} [-] : efficiency of the FC system auxiliaries (water pump, blower);
- η_{stack} [-] : efficiency of the FC stack;
- η_{FC} [-] : efficiency of the FC system;
- η_{tot} [-] : total efficiency of the FC system;
- U_f [-] : fuel (H_2) utilization factor;
- U_o [-] : oxidant (air) utilization factor;
- P_{vent} [W] : power loss due to the fuel utilization factor;
- Q_{av} [W] : available thermal power;
- Q_{th} [W] : recovered thermal power;
- η_{th} [-] : thermal efficiency.

The analytic expressions of the above variables used to analyze the performance of the IES are summarized in Table 3.1.

Calculated variable	Analytical expression
FC DC power output	$P_{DC} = i_{DC} \cdot V_{DC}$
Power consumed by the auxiliaries	$P_{aux} = i_{aux} \cdot v_{aux}$
FC AC net power output	$P_{FC} = i_{AC} \cdot V_{AC}$
Power consumed by the inverter	$P_{inv} = P_{DC} - P_{FC} - P_{aux}$
Battery exchange power	$P_{Batt} = i_{Batt} \cdot V_{AC}$
Stack efficiency	$\eta_S = \frac{V_{DC} \cdot i_{DC}}{\dot{m}_i LHV_{H_2}}$
Hydrogen mass flow through the membrane	$\dot{m}_i = i_{DC} \frac{m_{mol_{H_2}} \cdot N_{cel}}{2F}$
Fuel utilization factor	$U_f = \frac{\dot{m}_i}{\dot{m}_{H_2}}$
Power loss due to the utilization factor	$P_{vent} = (\dot{m}_{H_2} - \dot{m}_i) LHV_{H_2}$
Inverter efficiency	$\eta_{inv} = \frac{P_{DC} - P_{inv}}{P_{DC}}$
Efficiency of auxiliaries	$\eta_{aux} = \frac{P_{FC}}{P_{FC} + P_{Aux}}$
FC system efficiency	$\eta_{FC} = \frac{P_{FC}}{\dot{m}_{H_2} LHV_{H_2}}$
Available thermal power	$Q_{av} = \frac{1 - \eta_S}{\eta_S} i_{DC} \cdot V_{DC}$
Recovered thermal power	$Q_{th} = \dot{m}_w c_w \Delta T_w$
Thermal efficiency	$\eta_{th} = \frac{Q_{th}}{\dot{m}_{H_2} \cdot LHV_{H_2}}$
Primary Energy Saving index	$PES = 1 - \frac{1}{\frac{\eta_{FC}}{\eta_{el,ref}} + \frac{\eta_{th}}{\eta_{th,ref}}}$

Table 3.1 : Definition and analytic expressions of the calculated variables.

3.2 PEMFC PERFORMANCE ANALYSIS

As described in Chapter 2, the developed IES is conceived so that both the FC output power and the load request may vary independently. For those operating conditions when the load request is higher than the FC output power, the batteries cover the required extra power otherwise the batteries work in self-charging mode condition [5, 6].

Although the system can operate both in grid-connected and island mode, in the performed tests the surplus power has been stored into the battery, avoiding power exchange with the external grid.

Furthermore, it must be noticed that, performing long run tests, special attention is required in managing the power fluxes, to avoid that the batteries reach the over or under voltage conditions, which would lead the entire system to break down.

To analyze the electrical and thermal performance of the 5 kW PEMFC in study, at different load conditions, different test campaigns have been carried out, as described more in detail in the following.

3.2.1 PEMFC ELECTRIC PERFORMANCE ANALYSIS

In order to investigate the electric performance of the test PEMFC, two different test campaigns have been performed: case *A* and case *B*.

The first campaign (case *A*) has been executed with increasing FC power output as reported in Figure 3.1 which shows the FC power, with continuous red line, versus time.

The second test campaign (case *B*) has been performed by decreasing the FC power output, as reported in Figure 3.2.

In both cases the FC power set point has been varied proceeding stepwise, with a discrete delta between two successive values equal to 500 W. Considering that the minimum FC power output is equal to 500 W and the maximum FC power output is 4500 W, nine different operating points have been investigated: 500 W, 1000 W, 1500 W, 2000 W, 2500 W, 3000 W, 3500 W, 4000 W, 4500 W, with a minimum waiting time between set point change of 40 s. Test were repeated more times in different days and with FC “hot” or “cold”.

For each power output set-point, the mean value of all the measured variables (showed previously, in Table 3.16) has been calculated from the performed test campaigns referring to the case A and case B.

Figure 3.1 and Figure 3.2 show the measured DC power delivered by the stack, P_{dc_stack} (purple line,), the AC FC power, P_{FC} (red line) and the flow rate of the hydrogen introduced, M_{flow_H2} (dotted gray line), as a function of the time. It is possible to note that the stack power is always greater than the FC AC power, for each time instant and in the both tests case carried out. The reason of this behavior is due to the fact that the energy produced by the electrochemical reactions on the stack must be able to provide the power required to feed the auxiliaries and the inverter of the FC system.

By the analysis of the measured hydrogen flow rate consumption, M_{flow_H2} , plotted with dotted gray line in the Figure 3.1 and Figure 3.2, it can be observed that, during each time period in which the power is kept constant, the hydrogen mass flow rate is not steady and periodic spikes occur. This peculiar hydrogen flow rate behavior is due to the OCV purging operating mode: each time the valve opening occurs, the mass flow rises due to the consequent leakage of hydrogen and stack pressure drop. During the performed tests the valve operating frequency and the valve opening time has been kept constant (equals to 20 s and 2.5 s, respectively), in order to guarantee the stack safety in spite of the best FC performance.

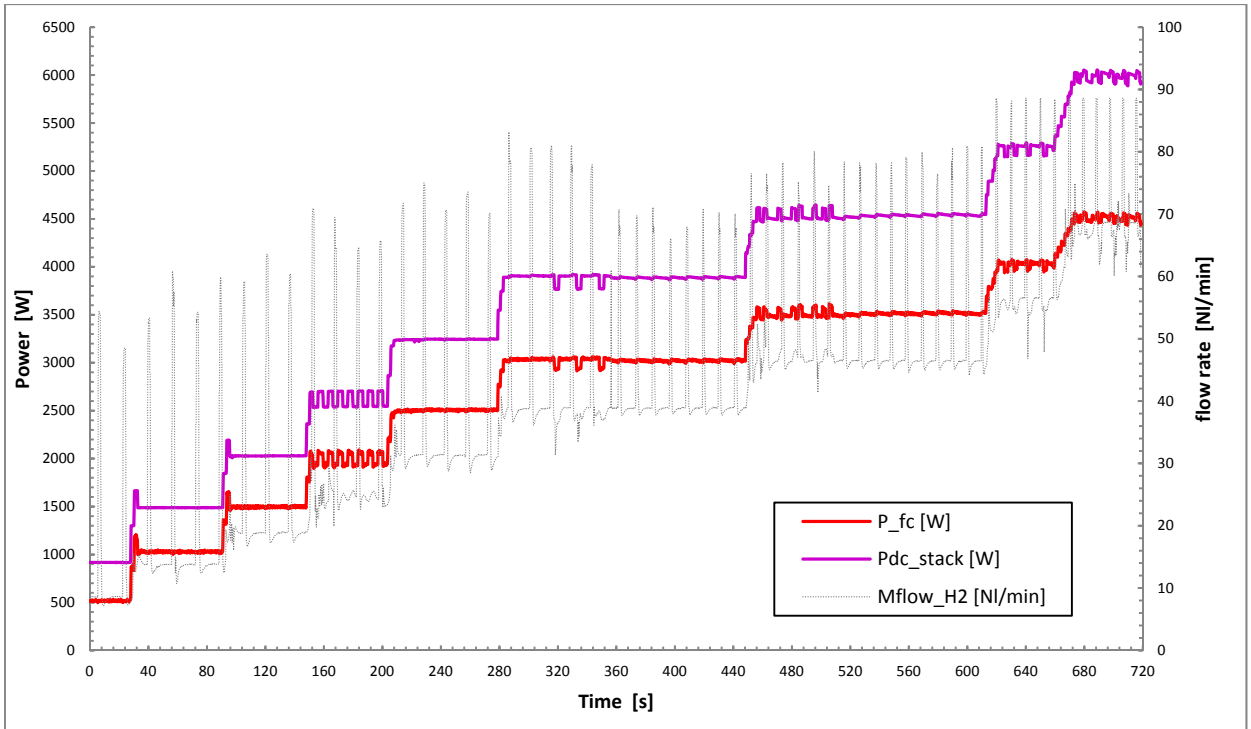


Figure 3.1: Test with increasing FC power output: case A.

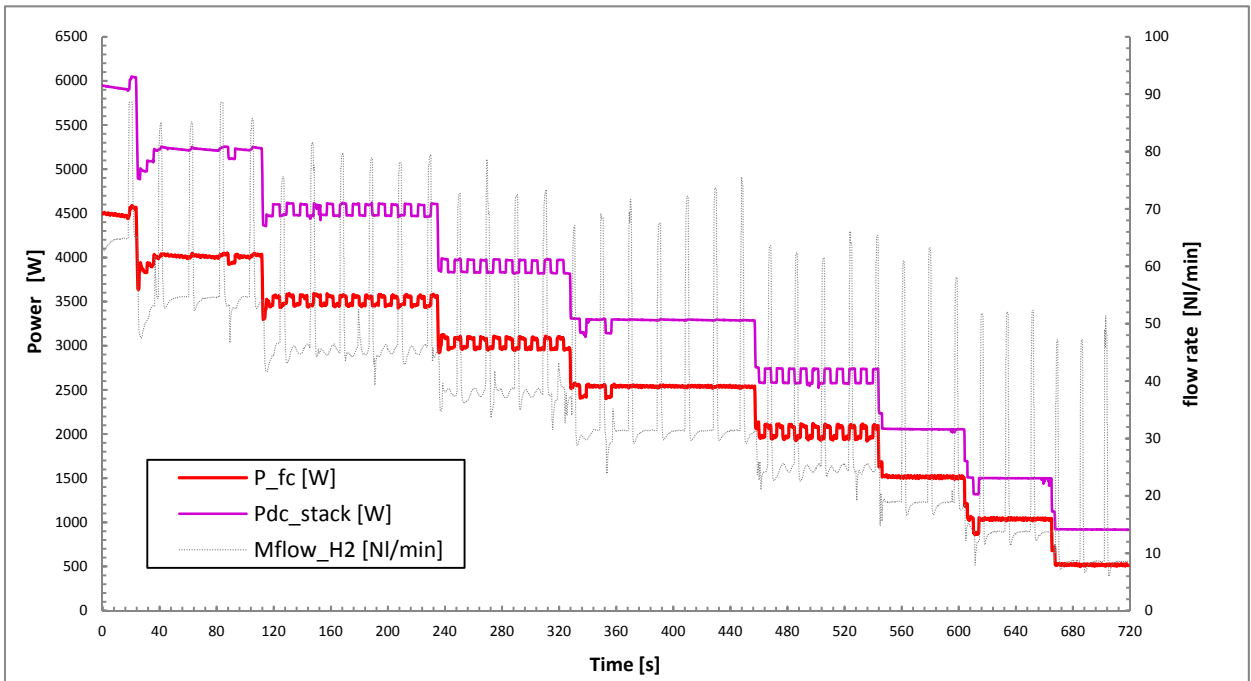
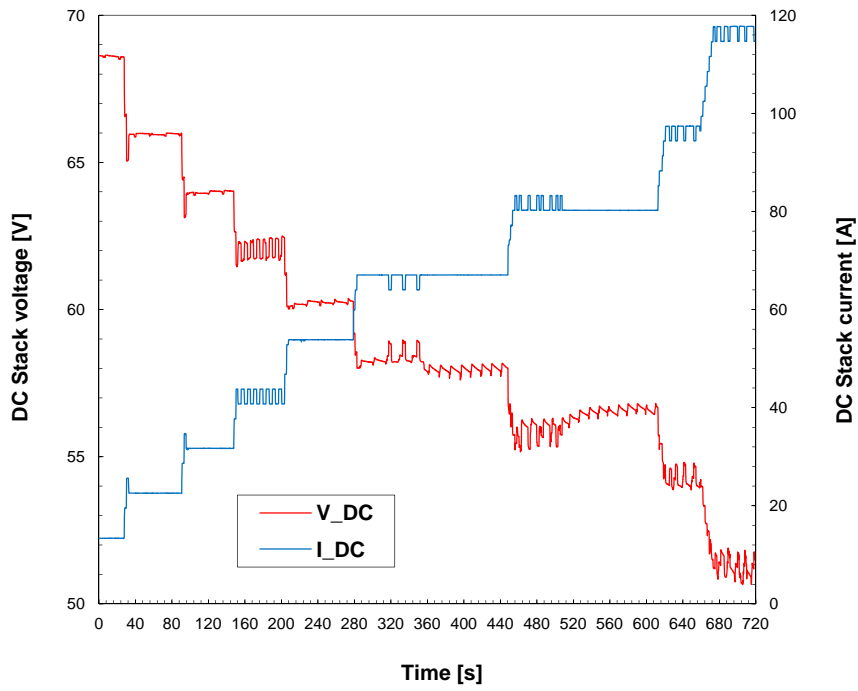
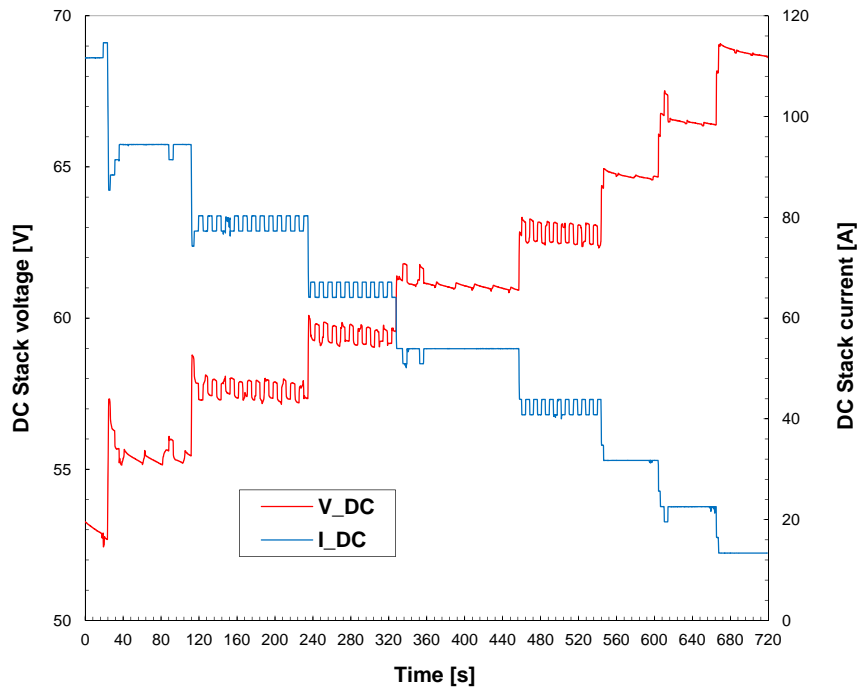


Figure 3.2: Test with decreasing FC power output: case B.

Figure 3.3 a) and b) show the stack instantaneous electric performance: FC DC voltage, V_{DC} , (red line) and FC DC current i_{DC} , (blue line) measured during the test carried out with FC power increasing (case A) and with FC power decrease (case B), respectively.



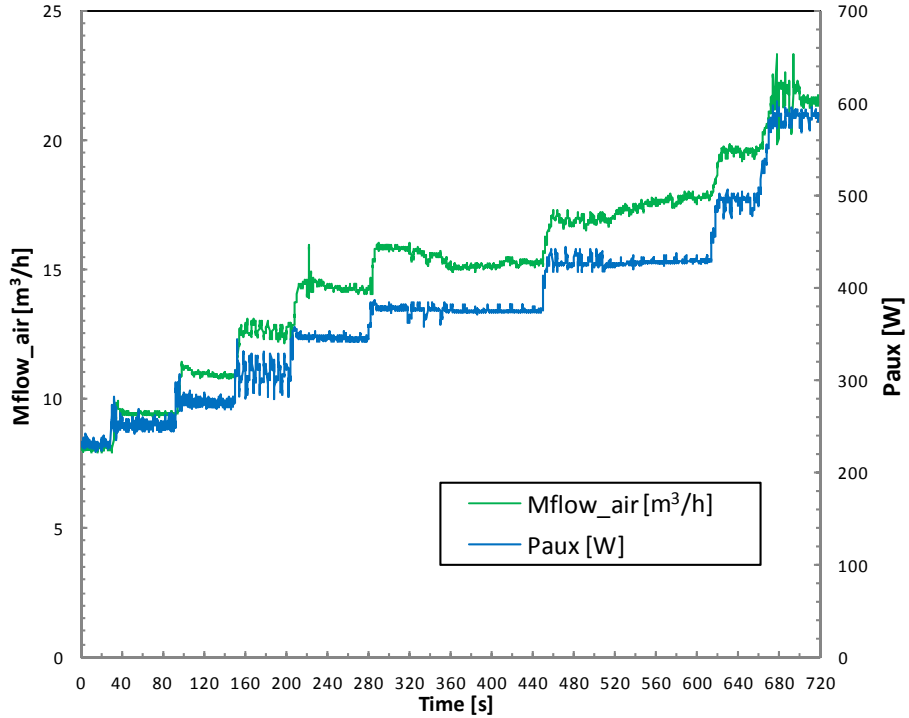
a)



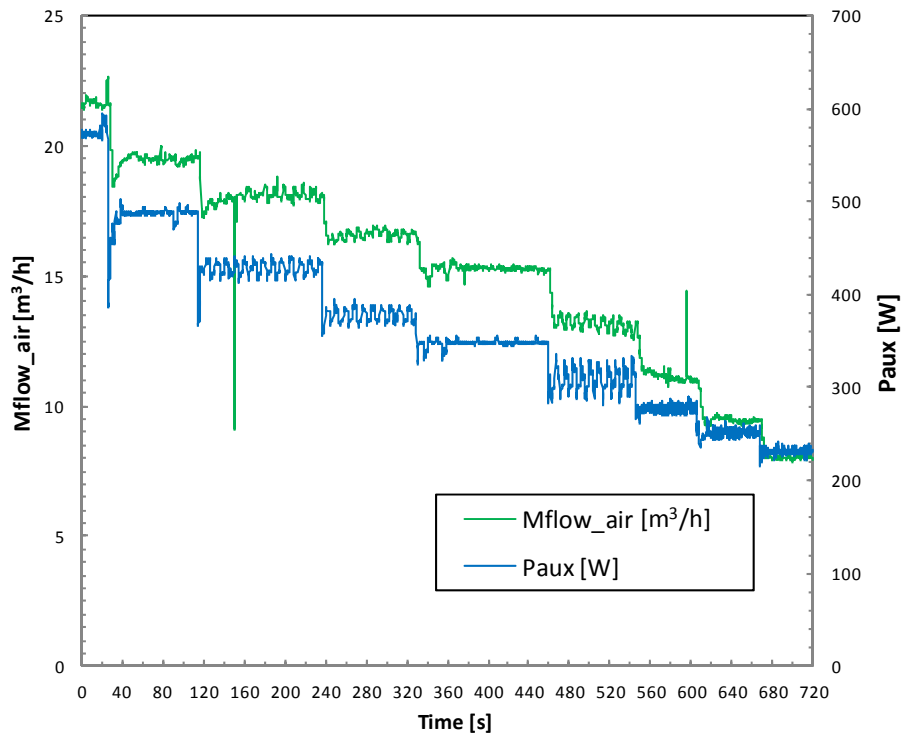
b)

Figure 3.3: The measured DC stack voltage (red line) and the DC stack current (blue line), VS time: a) in the case A test; b) in the case B test.

The air flow rate, $M_{\text{flow_air}}$ (green line) introduced to the cathode side of the stack through the humidifier, and the power absorbed by the auxiliaries, P_{aux} (blue line), has been plotted on Figure 3.4 a) and b).



a)



b)

Figure 3.4: The measured air mass flow rate (green line) and the auxiliaries power (blue line), VS time: a) in the case A test; b) in the case B test.

Figure 3.5 shows the behavior of the stack electric efficiency, η_s (red line), and of the mass flow rate of the hydrogen reacted through the membrane, \dot{m}_i (gray line), as a function of the time in the case A (Figure 3.5-a) and case B (Figure 3.5-b).

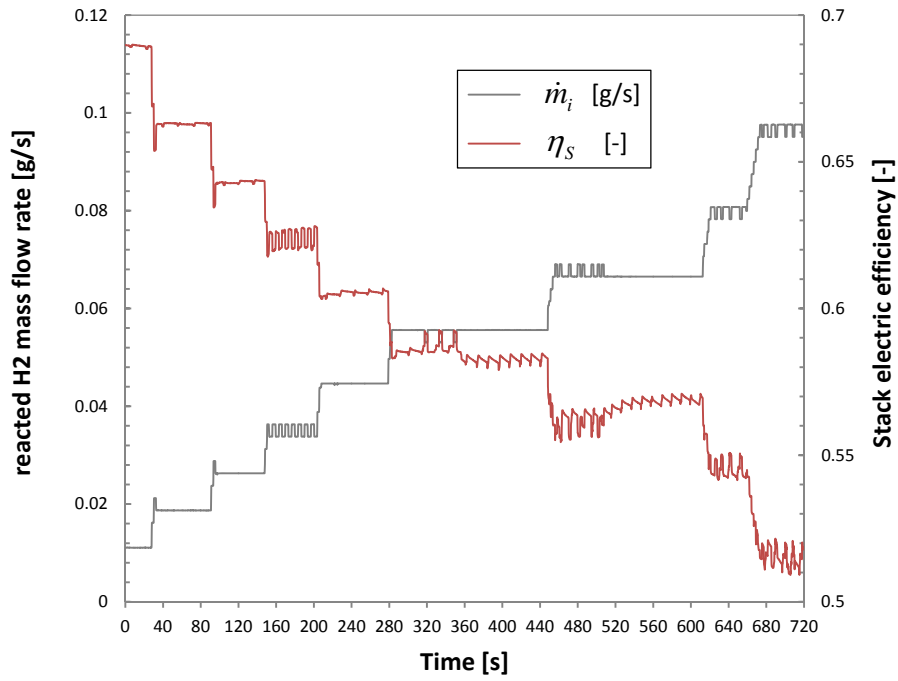
Specifically, the H₂ actually reacted is the hydrogen that has been used by the electrochemical reactions which take place at the electrodes of the stack, through the membrane. The mass flow rate of this H₂ amount was calculated, through the acquired stack current, i_{DC} , using the Nernst equation:

$$\dot{m}_i = i_{DC} \frac{m_{mol_{H_2}} \cdot N_{cells}}{2F} \quad (3.1)$$

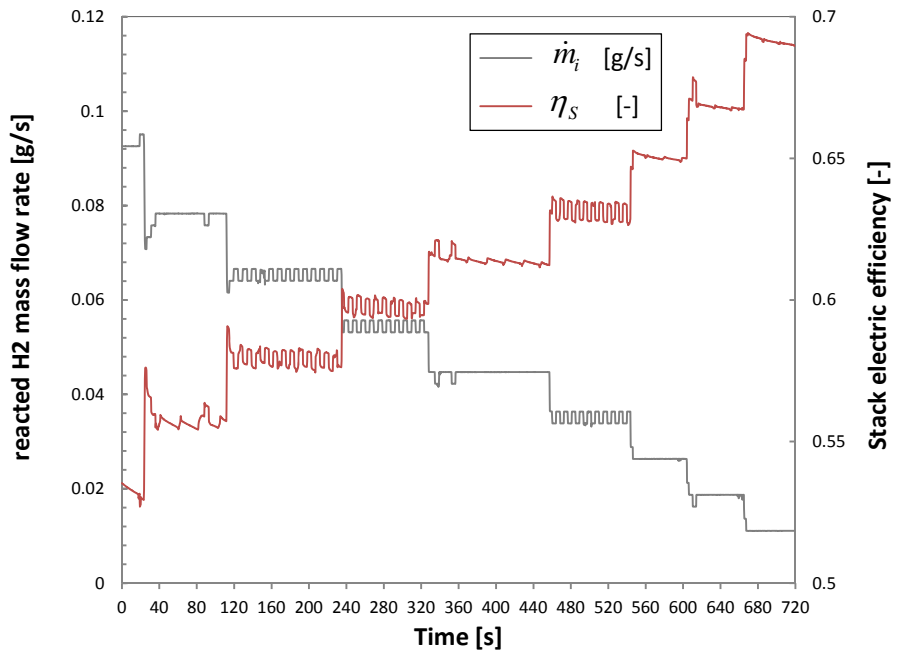
where:

- i_{DC} is the DC current generated by the FC stack;
- N_{cells} is the number of elementary cells that compose the FC stack (equal to 80 for the stack in study);
- $m_{mol_{H_2}}$ is the H₂ molar mass i.e. the mass (in grams) of one hydrogen mole, equals to 2.02 g/mole;
- $n_e = 2$ represents the number of electrons moles released on the external circuit each time unit. This value is related to the number of moles of the reagent H₂ through the oxidant reaction which occurs at the anode:

$$H_2 \rightarrow 2H^+ + 2e^- ;$$
- F is the Faraday constant, which represent the amount of charge per mole of electrons ($F = 96\,485$ C/mole of electrons).



a)



b)

Figure 3.5 The mass flow rate of the H₂ reacted, \dot{m}_i (gray line) and the stack electric efficiency, η_s (red line), VS time: a) in the case A tests; b) in the case B tests.

By means of the mass flow rate of the hydrogen that has reacted, \dot{m}_i , it is possible to calculate the electric efficiency of the stack (Eq. 3.2):

$$\eta_s = \frac{V_{DC}}{V_{LHV_{H_2}}} = \frac{V_{DC} \cdot i_{DC}}{\dot{m}_i LHV_{H_2}} = \frac{P_{DC}}{\dot{m}_i LHV_{H_2}} \quad (3.2)$$

where $V_{LHV_{H_2}}$ is the heating voltage and LHV_{H_2} is the Lower Heating Value of the hydrogen, equal to 120000 kJ/kg, being defined as:

$$V_{LHV_{H_2}} = \frac{LHV_{H_2} \cdot m_{mol_{H_2}} \cdot N_{cells}}{2F} \approx 99.5 \text{ [V]} \quad (3.3).$$

Figure 3.6 shows the stack polarization curve for the case A (continuous line) and for the case B (dotted line).

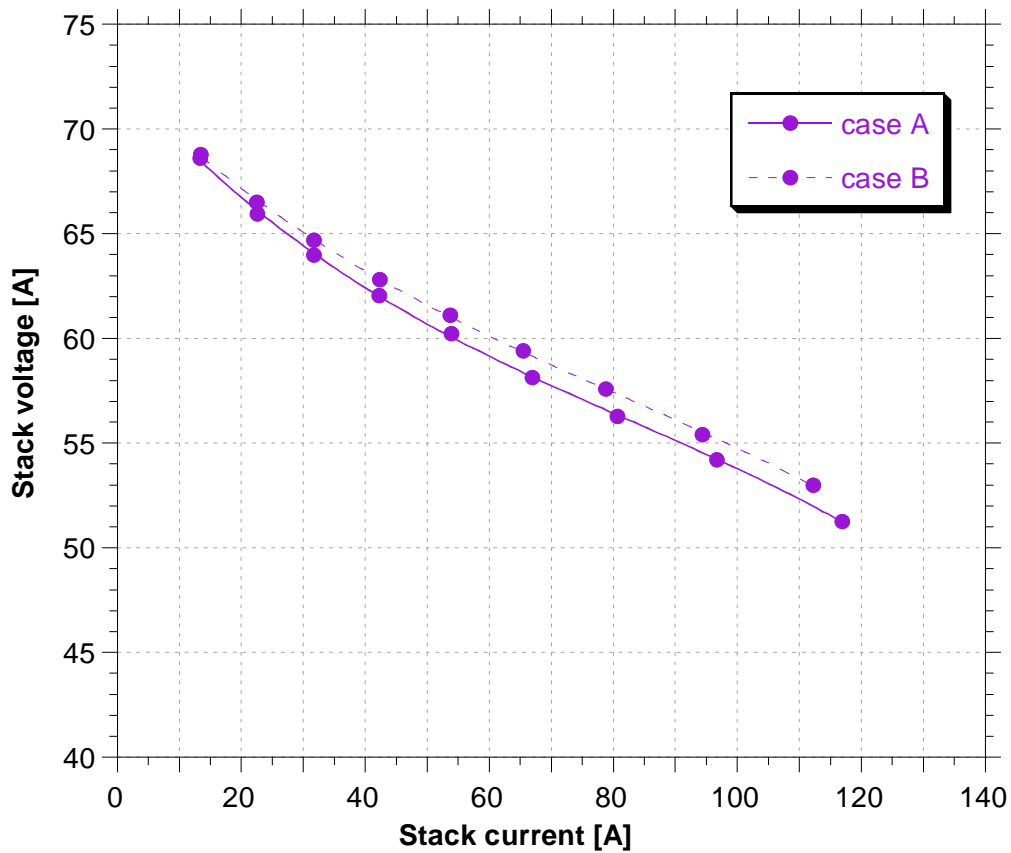


Figure 3.6: The polarization curves referring to case A (continuous line) and case B (dotted line) tests.

The polarization curves construction was conducted by setting the nine consecutive FC power values investigated. In particular, the power of the FC was manually set at the desired level, then maintained constant for the time necessary to acquire a sufficient number of data points, and then manually the fuel cell at the next power value has been set. Then, in order to determine the polarization curve, it is necessary to average the stack voltage (V_{DC} [V]) and the stack current (i_{DC} [A]) acquired data, for each FC power level.

It is noticed that on the X-axis of the polarization curve plot (Figure 3.6) the current values and not the current density values are present. In fact, since the purpose is not to compare the performance of different fuel cells but of the same cell, the active area does not change over the time.

Furthermore, it can be observed that the FC stack operates far from the regions where the activation and the concentration losses take place (showing Figure 3.7 in which the regions of the FC polarization losses are illustrated). This is due to the FC inverter that is able to keep the FC voltage values within the linear region of the Ohmic losses. In fact, the obtained polarization curves show the typical linear trend related to the Ohmic losses.

The stack polarization curves ($V_{DC} - i_{DC}$) obtained in similar tests carried out on seven different days are shown in Figure 3.8. It is possible to note how all the pairs of values ($i_{DC}; V_{DC}$) determined are comprised between two lines (dotted black lines in the graph) that represents the 95% confidence interval calculated on the basis of the experimental data.

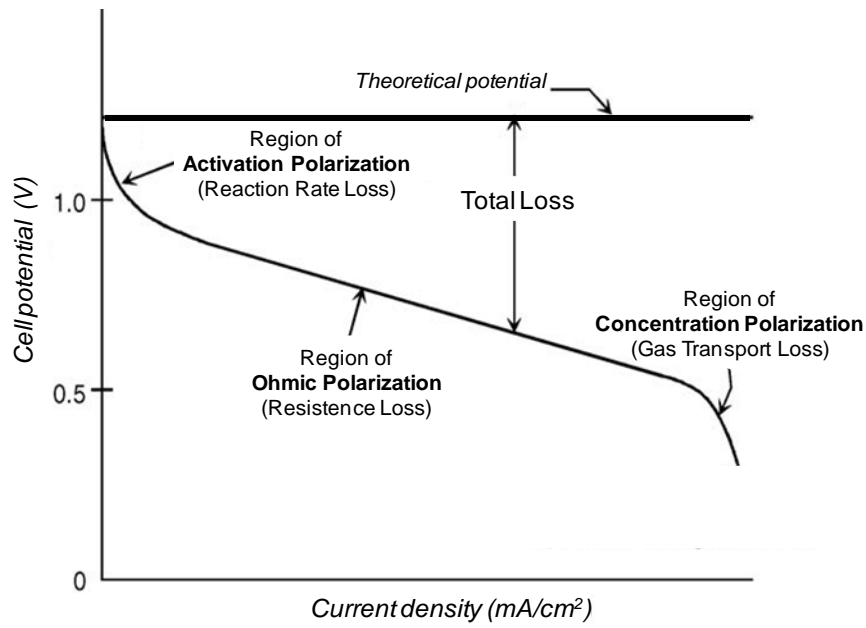


Figure 3.7: The theoretical polarization losses for a PEM fuel cell.

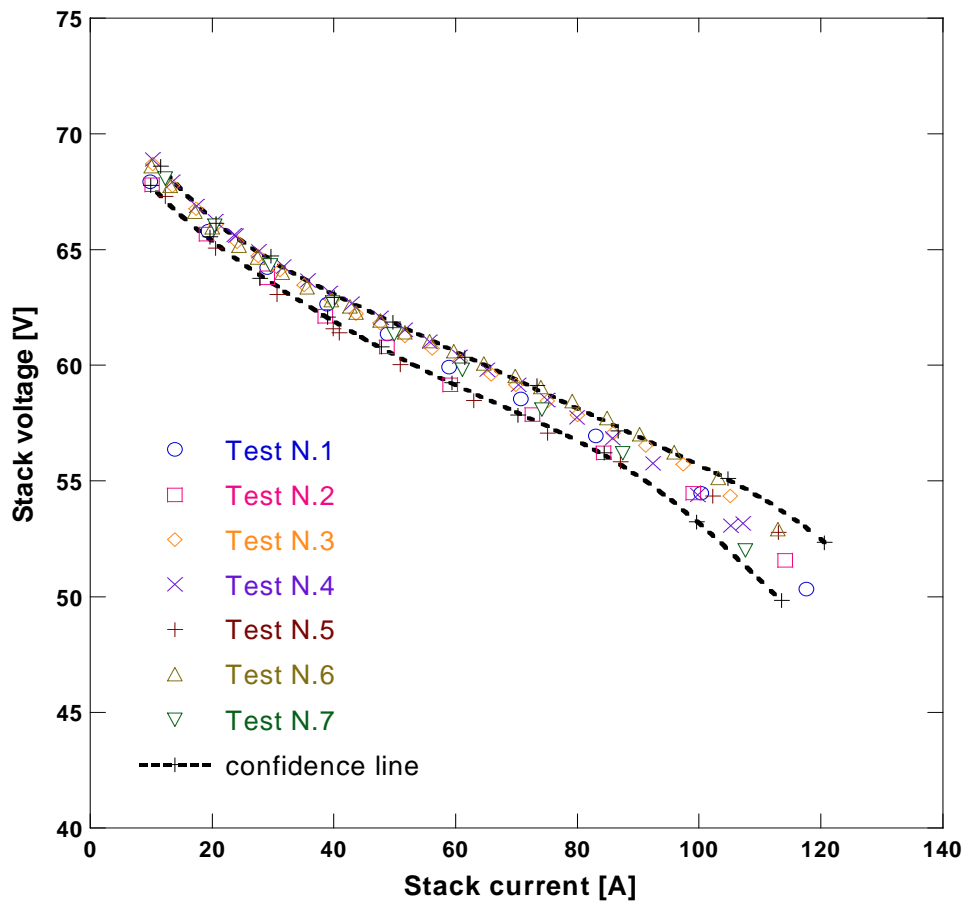


Figure 3.8: The polarization curves obtained during seven different tests and relevant 95% confidence limits (dotted black lines).

From the time resolved acquired data the power, efficiency, mass flow rate average are calculated for each step, from which have been deleted the values during the transitory between step.

Figure 3.9 shows the trends of the power delivered by the stack (P_{dc_stack} , purple lines), and the fuel power introduced at the anode side of the stack (P_{fuel} , black lines), the power absorbed by the auxiliaries (P_{aux} , blue lines) and lose by the inverter (P_{inv} , green lines), as a function of FC AC power, P_{FC} , in the case A tests (continuous lines) and in the case B tests (dotted lines).

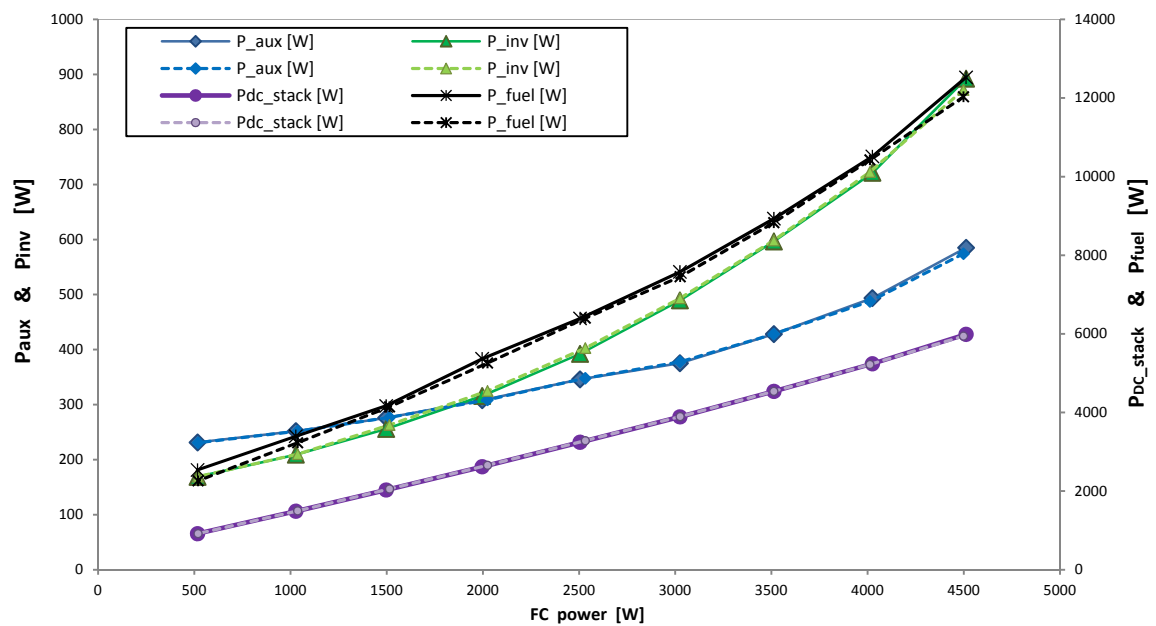


Figure 3.9: The calculate powers in the case A tests (continues lines) and in the case B tests (dotted lines).

Precisely, the above powers were calculate averaging the necessary acquired values as aforementioned, then using the following equations:

- the AC power delivered by the FC defined as the product between the current and the voltage measured after the inverter:

$$P_{FC} = i_{AC} \cdot V_{AC} \quad (3.4)$$

- the DC power delivered by the stack defined as the product between the current and the voltage of the stack:

$$P_{DC} = i_{DC} \cdot V_{DC} \quad (3.5)$$

- the power absorbed by the auxiliaries, defined as a product of their current and voltage direct measured by the sensors:

$$P_{aux} = i_{aux} \cdot V_{aux} \quad (3.6)$$

Notice that the FC system auxiliaries considered are the blower and the water pump.

- the power absorbed by the inverter is calculated by the difference between the DC stack power (here named with the acronym, P_{DC} or P_{dc_stack} in the plot), the AC power delivered by the fuel cell, P_{FC} , and the power absorbed by the auxiliaries, P_{aux} :

$$P_{inv} = P_{DC} - P_{FC} - P_{aux} \quad (3.7)$$

- the power introduced into the fuel cell through the fuel as a product of the H_2 mass flow rate introduced at the anode side of the stack and the Lower Heating Value of the hydrogen, LHV_{H_2} , equal to 120000 kJ/kg:

$$P_{fuel} = \dot{m}_{H_2} LHV_{H_2} \quad (3.8).$$

Through using the averaged mass flow rate of the hydrogen introduced into the FC, \dot{m}_{H_2} , and of the H_2 actually reacted, \dot{m}_i , it is possible to calculate the fuel utilization factor, U_f , defined as:

$$U_f = \frac{\dot{m}_i}{\dot{m}_{H_2}} \quad (3.9).$$

Through the above calculated power, the efficiency of the all components of the FC system has been determined (Figure 3.10).

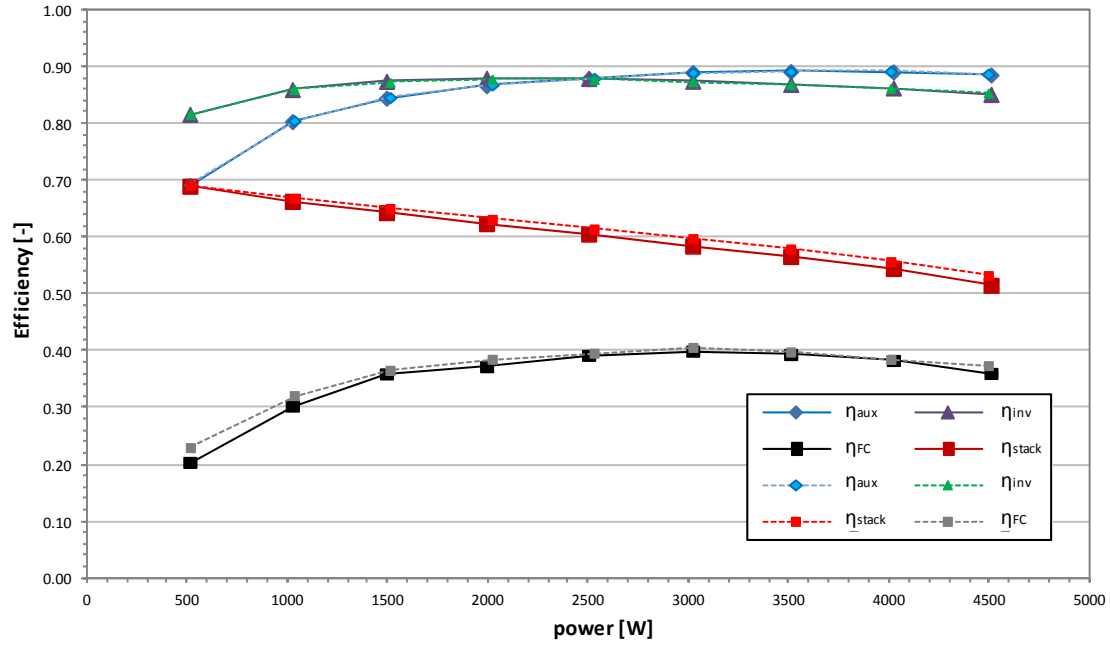


Figure 3.10: The calculate efficiencies in the case A tests (continuous lines) and in the case B tests (dotted lines).

- The stack efficiency (red lines, η_{dc_stack} in figure 3.10) that is defined as the ratio between the stack power, P_{DC} , and the power given by the H_2 actually reacted:

$$\eta_s = \frac{P_{DC}}{\dot{m}_i LHV_{H_2}} \quad (3.10);$$

- the auxiliaries' efficiency (blue lines):

$$\eta_{aux} = \frac{P_{FC}}{P_{FC} + P_{aux}} \quad (3.11)$$

defined as the ratio between the AC FC power, P_{FC} , and the available power output of the inverter, defined from the equation 3.7: $P_{FC} + P_{aux} = P_{DC} - P_{inv}$.

- the efficiency of the inverter (green lines) is the ratio of the difference between the stack power output and the inverter power, and the power delivered by the stack:

$$\eta_{inv} = \frac{P_{DC} - P_{inv}}{P_{DC}} \quad (3.12);$$

- the efficiency of the FC system (black lines) defined as the ratio between the AC FC power and the power introduced in the stack through the fuel:

$$\eta_{FC} = \frac{P_{FC}}{\dot{m}_{H_2} LHV_{H_2}} \quad (3.13)$$

that is also equal to:

$$\eta_{FC} = \frac{P_{FC}}{\dot{m}_{H_2} LHV_{H_2}} = U_f \cdot \eta_s \cdot \eta_{inv} \cdot \eta_{aux} \quad (3.14).$$

Comparing the results obtained from the increase loads campaign (A) with the decrease ones (B) it can be noted that the values almost match. This show that the fuel cell, if correctly managed is free from hysteresis phenomenon.

More in detail, Figure 3.11 provides the plot of the power, P_{DC} (purple lines) and the efficiency, η_s (red lines) of the stack by varying the FC power in the case A test (continuous lines) and in the case B test (dotted lines).

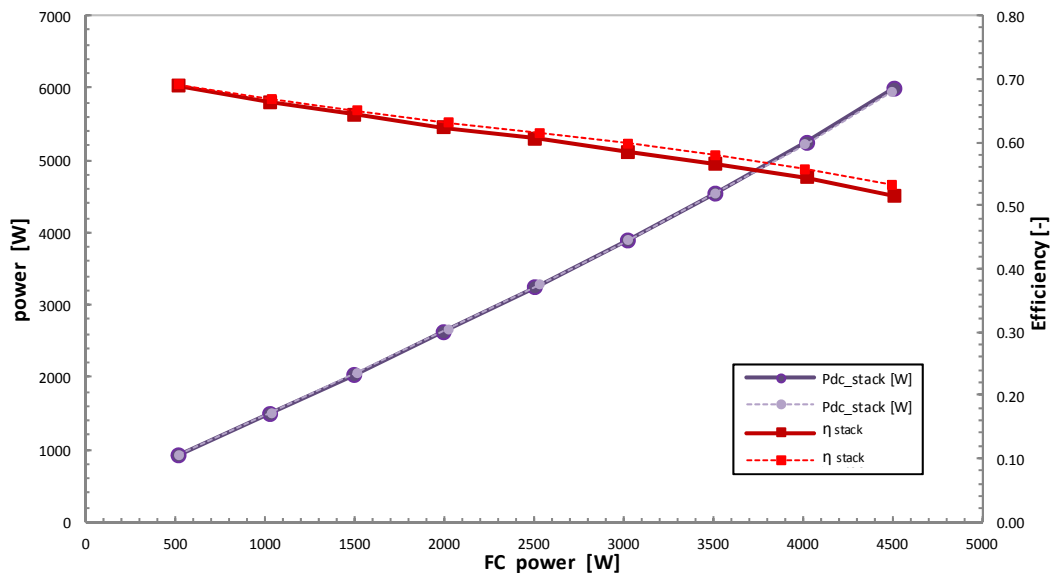


Figure 3.11: The power (purple lines) and efficiency (red lines) of the stack VS the FC power, in the case A tests (continuous lines) and in the case B tests (dotted lines).

The power supplied by the stack, P_{DC} (Figure 3.11) increase with the increase of the FC power for both the test campaigns conducted. Hence, the difference between the two powers is not constant with increasing of the AC power level, because at very high speeds the auxiliaries tend to consume more energy.

Instead, the efficiency of the stack, η_s (Figure 3.11), decreases linearly with FC power in each test case analyzed. It assumes maximum value at minimum loads conditions (0.69) and this is equal in the two case tests. Instead, the minimum value is reached at full loads and it is slightly different for the two cases, being equal to 51.5 % and 53.2 %, respectively.

The η_s difference from the two curves is achieved also at partial loads and is increasing proportional to the FC power increasing.

Figure 3.12 shows the comparison between the powers (blue lines) and the efficiencies (red lines) of the auxiliaries.

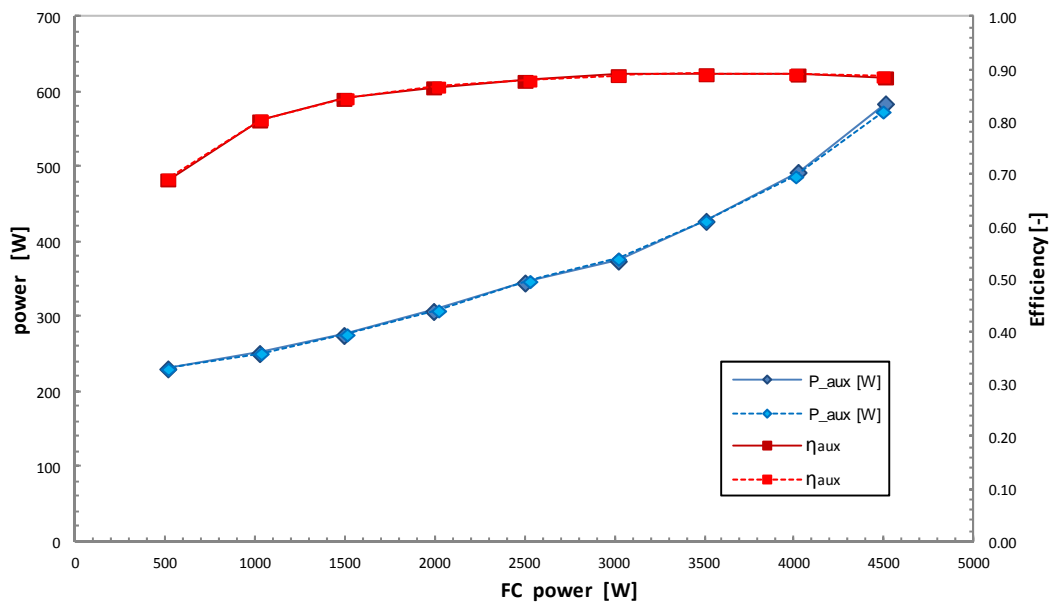


Figure 3.12: The auxiliary power (blue lines) and efficiency (red lines) VS FC power, in the case A tests (continuous lines) and in the case B tests (dotted lines).

The power absorbed by the auxiliaries, P_{aux} (blue line in Figure 3.12), increase with the increase of the FC power. Its value goes from about 230 W at low loads to 585 W at maximum power condition; this is due to the air blower power dependency to the square of the air flow velocity.

For maintaining the stoichiometry of the reaction the increase of the FC power require more hydrogen and more air, the latter impose the raise of the consumption noted.

The auxiliary efficiency, η_{aux} (red line in Figure 3.12), instead, remains almost constant in a wide range of the operating conditions (nearly 0.88). Only at low loads it decreases assuming the value 0.69.

Figure 3.13 shows the power (green lines) and efficiency (red lines) of the inverter versus the FC electric power. It is possible to notice that there is no differences between the curves obtained in the two different test campaigns, A and B case, analyzed.

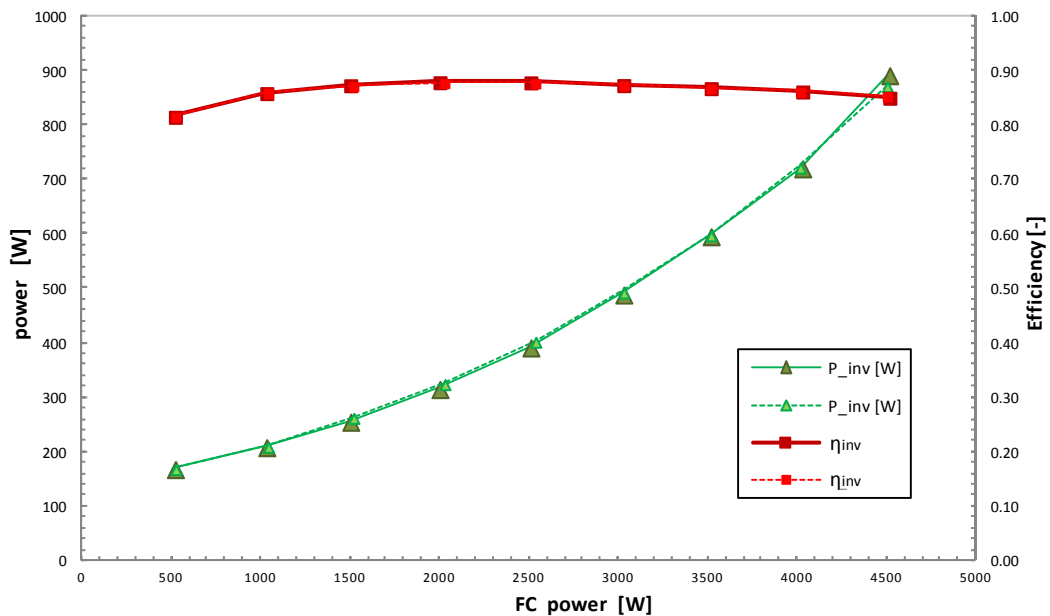


Figure 3.13: The inverter power (green lines) and efficiency (red lines) VS FC power, in the case A tests (continuous lines) and in the case B tests (dotted lines).

Also for the inverter can be deduced the same consideration exposed above for the auxiliaries. In fact, (Figure 3.13) the power of the inverter increases proportionally to the FC power, showing a parabolic trend, assuming the minimum value (170 W) at very low loads (P_{FC} 500 W) and the maximum value equal to 892 W at full load, due to its dependency to the square of the circulating current.

Again the efficiency of the inverter is constant (nearly 0.87) at medium and high loads and decrease at minimum load condition to a value equal to 0.82.

Figure 3.14 provides the plot of the fuel utilization factor, U_f , calculated on the basis of the measured mean fuel consumption (Eq. 3.8) and the FC electric efficiency, η_{FC} (Eq. 3.13), as a function of the FC power output.

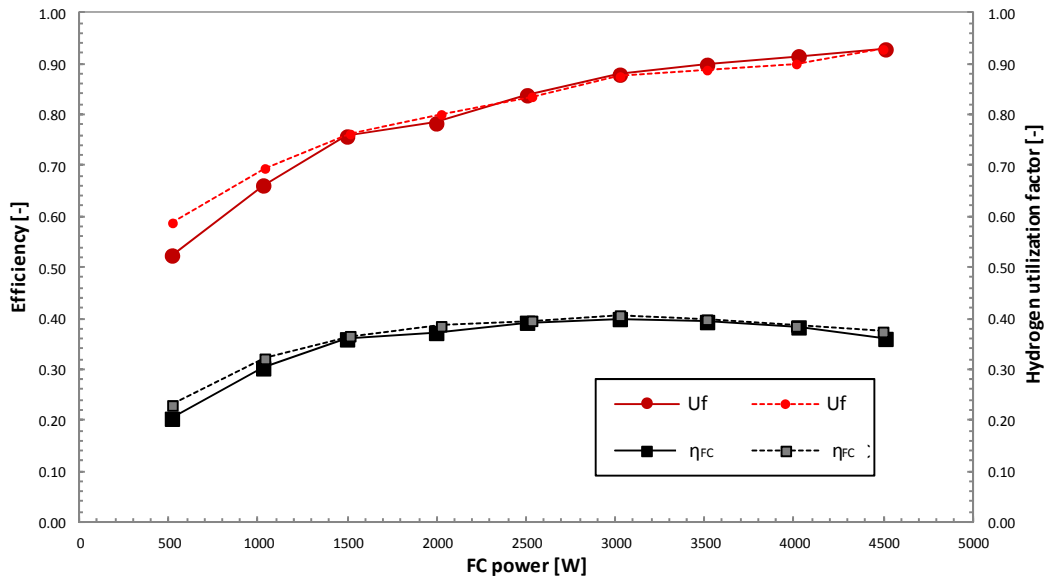


Figure 3.14 : The fuel utilization coefficient, U_f (red lines) and the FC electric efficiency, η_{FC} (black lines), VS FC electric power, in the case A tests (continuous lines) and in the case B tests (dotted lines).

The U_f (Figure 3.14) increases with the FC electric power. This because the OCV operation, with constant opening time and frequency, equal to 2.5 s and 20 s, respectively, it is conceived to reach the highest performance at the FC rated power. But, at part-load, the amount of purged hydrogen is more significant in comparison with the reacted hydrogen utilized by the stack and, thus, the U_f value drops below 60 %.

The η_{FC} , in spite of its directly dependence to the U_f , remains almost constant (nearly 0.38) in a wide operating range, showing a penalization at very low power output.

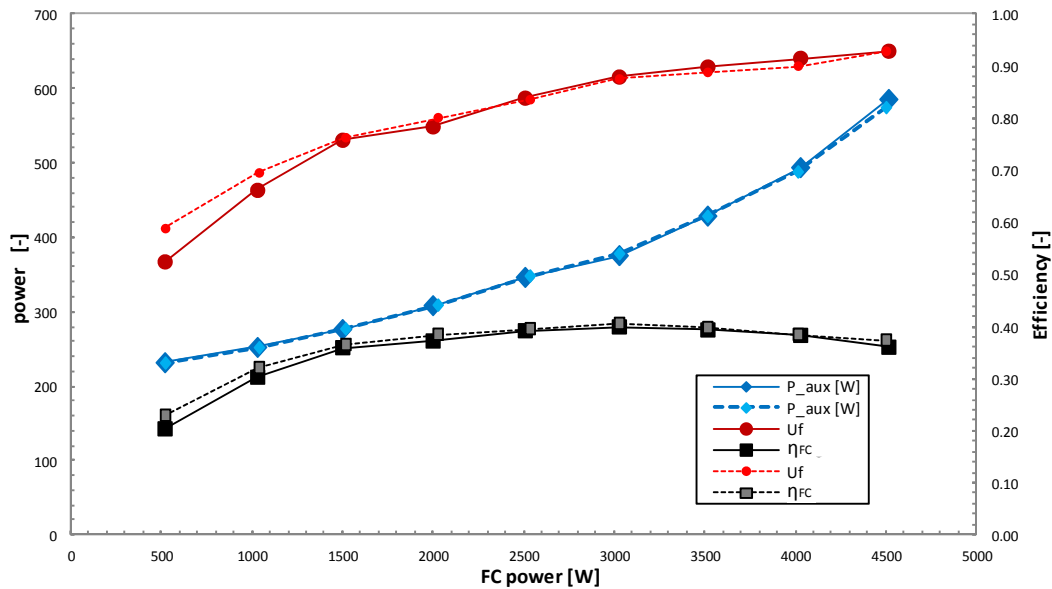


Figure 3.15 : Utilization factor, U_f (red lines), FC electric efficiency, η_{FC} (black lines), and auxiliary power consumption, P_{aux} (blue lines) referring to case A tests (continuous line) and case B tests (dotted line).

To better understand the causes of U_f behaviour, especially at low loads, it necessary to compare also the auxiliary power absorption, P_{aux} , versus the FC electric power (Figure 3.15).

It can be noticed (Figure 3.15) that the power consumed by the auxiliaries (mainly due to the air blower power consumption, as aforementioned) is not negligible. In fact it is equal to about 15% of the FC power output, at full load and to about 50% at minimum power condition.

In order to minimize the amount of the H_2 purged and to maximize the FC efficiency at different loads, the anodic exhaust management optimization as well as the degradation mechanism analysis has been carried out, as described in detail in the chapter 4.

Note the efficiency of the stack, η_s , was possible to calculate also the available thermal power, Q_{av} , usable through the cooling system (Figure 3.15), defined as:

$$Q_{av} = \frac{1 - \eta_s}{\eta_s} i_{DC} \cdot V_{DC} \quad (3.15)$$

Also the power loss due to the utilization factor, P_{vent} , (Figure 3.16) was calculated through the equation:

$$P_{vent} = (\dot{m}_{H_2} - \dot{m}_i) \cdot LHV_{H_2} \quad (3.16).$$

in the case A tests (continuous lines) and in the case B tests (dotted lines).

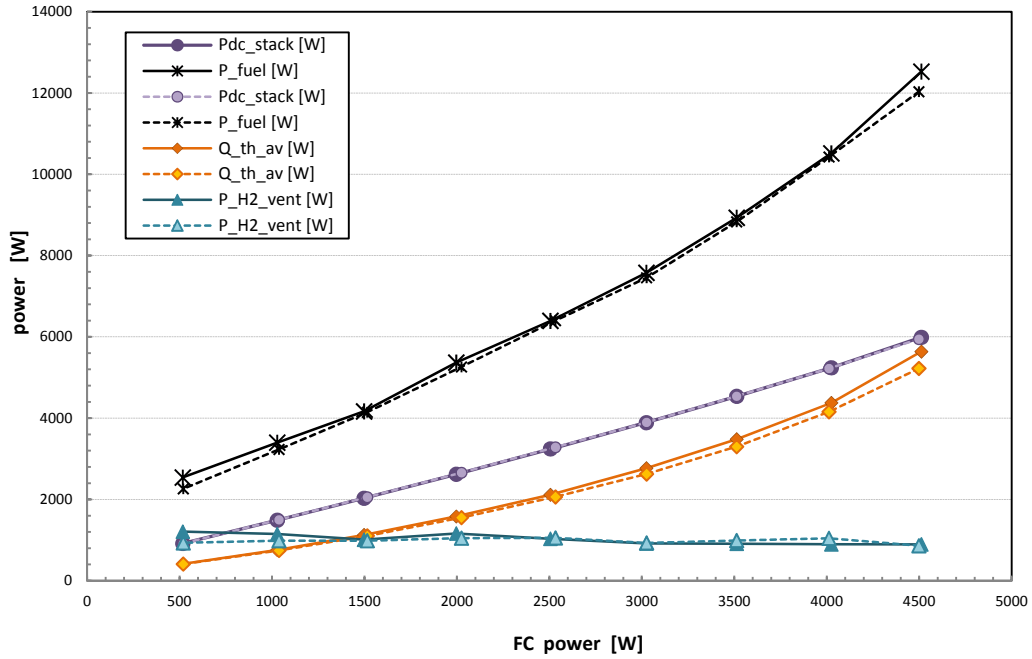


Figure 3.16: The available thermal power, Q_{av} (orange lines), the power loss due to the utilization factor, P_{vent} (blue lines), the stack power, P_{dc_stack} (purple lines) and the power introduced through the fuel, P_{fuel} (black lines), as a function of FC AC power.

Finally, the air utilization factor, U_o , was provided. The U_o is defined as:

$$U_o = \frac{(\dot{m}_{air} / \dot{m}_{H_2})}{(\dot{m}_{air} / \dot{m}_{H_2})_{st}} \quad (3.17)$$

where:

- $(\dot{m}_{air} / \dot{m}_{H_2})_{st}$ is the stoichiometric air-hydrogen mass flow ratio, equal to 34.78;
- \dot{m}_{air} is the mass flow rate of the air introduced calculated according to the following equation:

$$\dot{m}_{air} = \rho_{air} \cdot M_{flow_air} = M_{flow_air} \cdot \frac{m_{mol-air} \cdot P_{air}}{\mathfrak{R}_o \cdot T_{air}} \quad (3.18)$$

in which ρ_{air} is the air density (kg/m³), expressed through the Law of gas state, and $M_{flow-air}$ (m³/h) is the volumetric air flow rate (acquired by the sensor) produced by the variable speed blower (Figure 3.17).

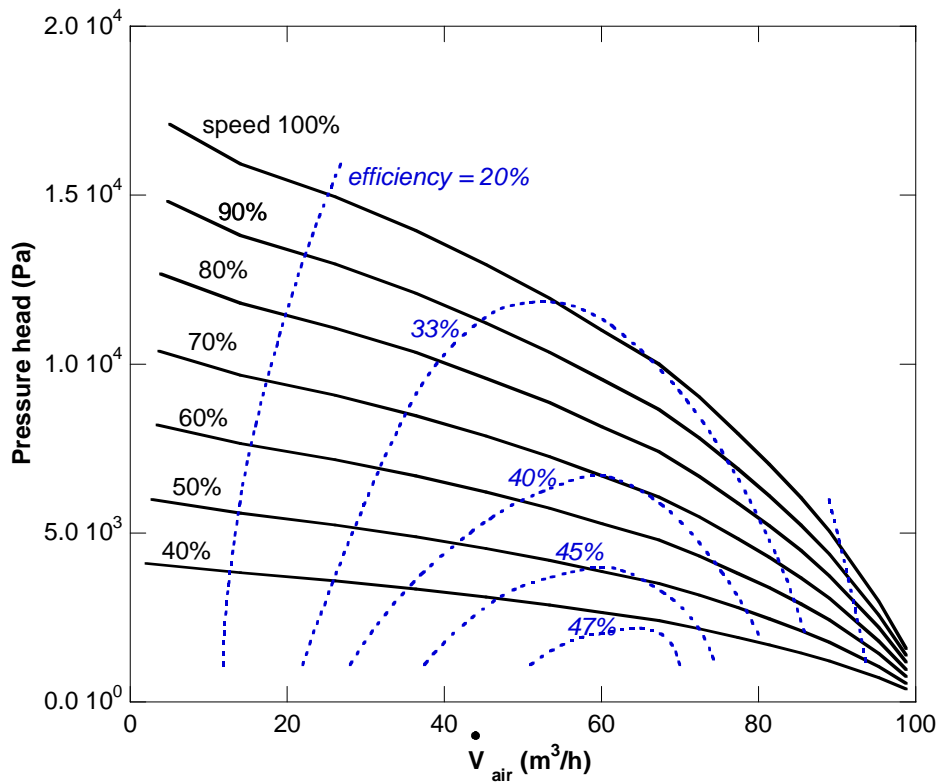


Figure 3.17: Characteristic curves of the air blower.

U_o is useful for a black box model that return the blower operating point using the blower characteristic curves (Figure 3.17, continuous lines) and the hydrogen flow rate data [6].

Figure 3.18 shows the calculated, U_o (blue lines) and the flow rate of the air, M_{flow_air} (green lines), versus FC electric power, for both the test campaigns investigated: case A (continuous lines) and case B (dotted lines).

It is possible notice (Figure that the U_o decreases with FC power, assuming values between 0.27, at minimum load and 0.15, at full load, while the air mass flow rate increases proportionally to the power delivered by the fuel cell. This probably due to an not-optimal choice of the blower.

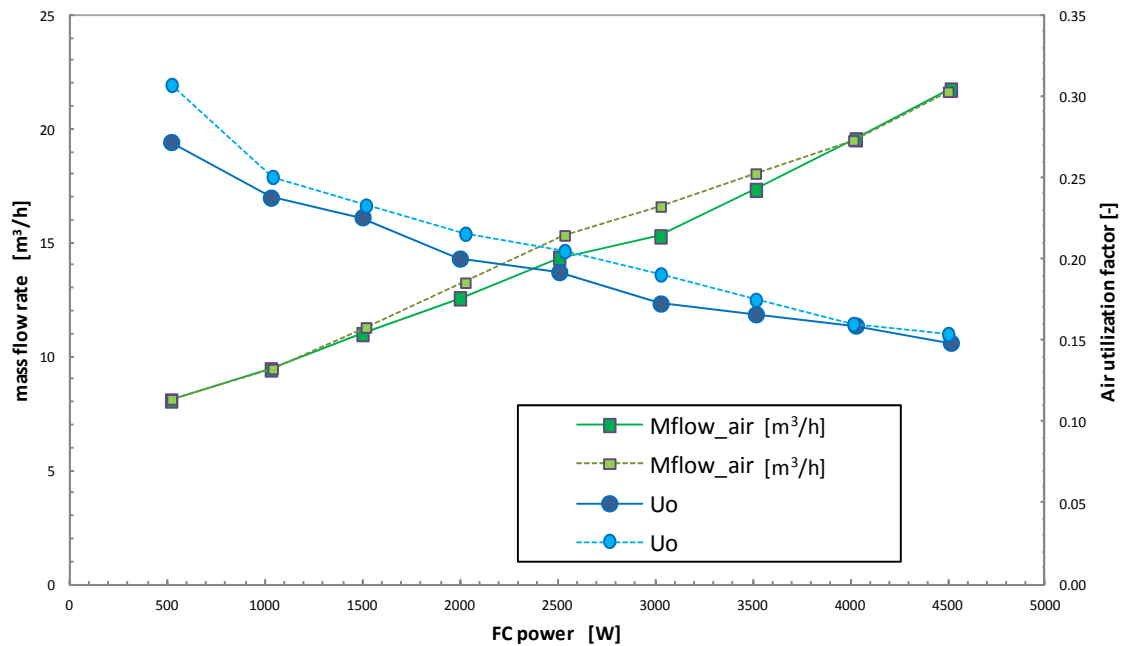


Figure 3.18 The air utilization factor, U_o (blue lines) and the air mass flow rate, M_{flow_air} (green lines), VS FC electric power, in the case A tests (continuous lines) and case B tests (dotted lines).

U_0 and the air flow rate show the great difference between A and B test, thus is probably due to a thermal effect on the air density inside the system that depends on the load history.

The values of the calculated electric variables at full load are summarized in the following tables: Table 3.1 and Table 3.2.

Power contribution [W] @ full load	Case A Value	Case B Value
P_{fuel}	12526	12032
P_{DC}	5989	5944
P_{inv}	892	872
P_{aux}	586	574
P_{FC}	4512	4498
Q_{av}	5637	5223
P_{vent}	896	861

Table 3.1: FC power values at design operating conditions.

Efficiency & utilization factor [%] @ full load	Case A value	Case B value
U_f	92.8	92.8
η_s	51.5	53.2
η_{inv}	85.1	85.3
η_{aux}	88.5	88.7
η_{FC}	36.0	37.4
U_0	14.8	15.4

Table 3.2: Efficiency and utilization factor values at design operating conditions.

3.2.2 THE FC THERMAL PERFORMANCE ANALYSIS

Under to evaluate the FC system thermal power production and to acquire its cogenerative performance, at different load conditions a different test campaign has been carried out.

The tests have been conducted increasing the FC power output from 500 W to the rated power, by varying stepwise the power setpoint with a step of 1000 W.

Moreover, each power set point is kept constant until the external water outlet temperature reaches steady state. This was done because when the mean values of the variables are evaluated considering only the measures which occur in steady state conditions, then it can be assumed that the measurements are not longer affected by the heat stored in the FC tank.

The condition to change the power output to a higher set point value consists in a temperature variation equal or lower to 0.2 °C per minute.

It is important to note that during the test the external water flow rate, M_{flow_H2O} , is maintained constant to about 2 liter per minute as well as the water inlet temperature, T_{w_in} , is continuously supplied from the laboratory well at about 22 °C.

Figure 3.19 shows the variables acquired during one of the tests. In particular these are: the tank temperature, T_{tank} (black line), the water inlet temperature, T_{w_in} (blue line), the external water outlet temperature, T_{w_out} (red line), and the external water flow rate, M_{flow_H2O} (green line).

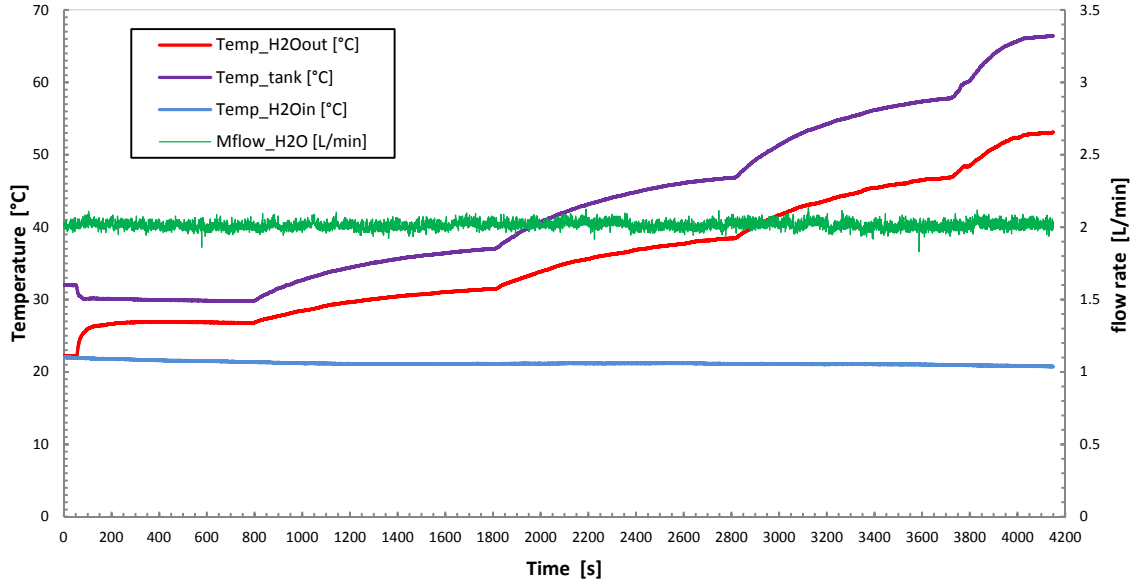


Figure 3.19: Temperatures behaviour performed during tests for thermal power estimation.

The results of the test campaign executed to evaluate the thermal performance are reported for five operating points. These results correspond to the mean values of the variables acquired during the periods in which the steady state conditions of the external water temperature occur.

Figure 3.20 shows the thermal power, Q_{th} , and the thermal efficiency, η_{th} , versus the FC power output. In particular, the thermal power was calculate through the equation:

$$Q_{th} = \dot{m}_w c_w \Delta T_w \quad (3.19)$$

where \dot{m}_w is the external water mass flow rate; c_w is the specific heat of water equal to 4.1868 kJ/(kg K) and ΔT_w is the difference between outlet and inlet water temperature.

The thermal efficiency was calculated through the equation:

$$\eta_{th} = \frac{Q_{th}}{\dot{m}_{H_2} \cdot LHV_{H_2}} \quad (3.20).$$

As shown in the Figure 3.20, the thermal power, Q_{th} , increases significantly with the FC power output. Moreover, in all the considered operating points, the thermal to electric power ratio of the system is close to 1.

Instead, the thermal efficiency, η_{th} , values remain almost constant equal to about 0.35 also at very low load conditions.

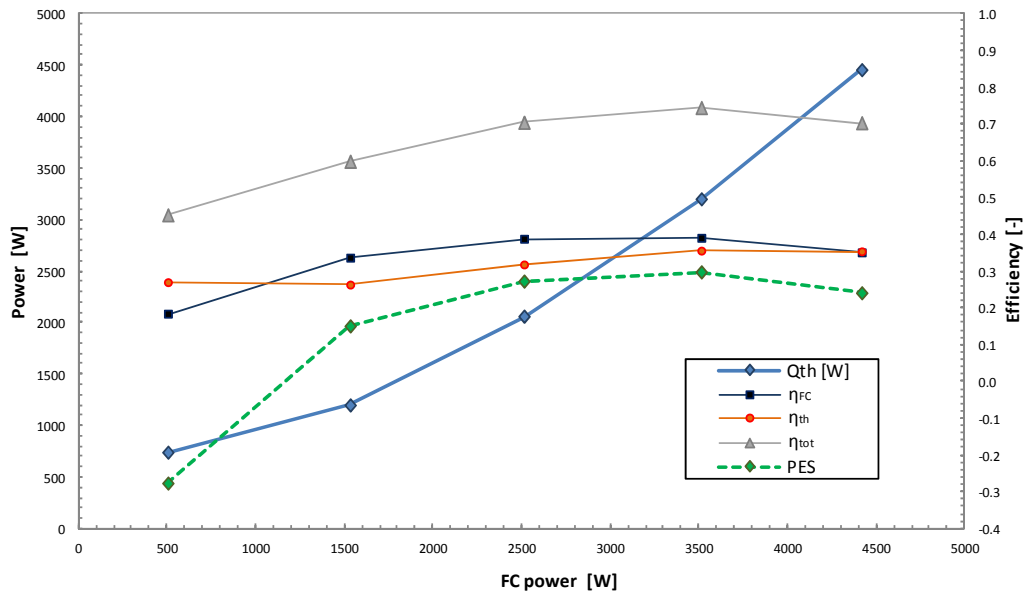


Figure 3.20: The thermal power, Q_{th} (blue line), the thermal efficiency, η_{th} (red line), the total efficiency, η_{tot} (gray line), the FC efficiency, η_{FC} (black line) and the Primary Energy Saving index, PES (green line), versus the FC electric power.

The total efficiency, η_{tot} (gray line – Figure 3.20), equal to the sum of the electric and thermal efficiency, has been also calculated and is provided in Figure 3.20. The obtained results show values ranging between 0.60 and 0.80.

The experimental results show that the thermal performance are strongly affected by the FC cooling system configuration. In fact, it has been observed that the thermal power can be recovered only for FC power set point higher than 3000 W. For this reason, the cooling circuit of the FC system in study could be modified, forcing the water to flow always into the heat exchanger, in order to better exploit the available heat by means of a controlled valve positioned at the external water inlet. When the FC operates at low electric power output a proper management of the valve is required.

Finally, the Primary Energy Saving (PES) index has been evaluated. The no-dimensional PES index represents the ratio between the amount of saved primary energy due to cogeneration and the primary energy consumption of the separated production of electric and thermal energy in reference conditions:

$$PES = 1 - \frac{1}{\frac{\eta_{FC}}{\eta_{el,ref} \cdot p} + \frac{\eta_{th}}{\eta_{th,ref}}} \quad (3.15)$$

where $\eta_{el,ref}$ is the reference electric efficiency and $\eta_{th,ref}$ is the reference thermal production efficiency (Table 3.3).

According to [7], the reference electric efficiency, $\eta_{el,ref}$, is here chosen equal to 44.2 %, the reference thermal production efficiency, $\eta_{th,ref}$, is fixed equal to 89 % and the correction factor for grid losses, p , is equal to 86 %.

Given the above assumptions, the PES of the FC system in study assumes positive values for FC power output higher than 1000 W, as shown in Figure 3.20 (green line). The obtained experimental results highlight also that positive PES values can be reached starting from above 900 W of FC power output, although the FC stack internal temperature limits the possibility to recover heat for very low FC power conditions.

The results of the thermal calculated variables at full load are included in Table 3.3.

Thermal calculated variables @ full load	Acronym	Value	Unit
Recovered Power	Q_{th}	4450	[W]
Efficiency value	η_{th}	35.2	[%]
Primary Energy Saving index	PES	24.0	[%]
- reference electric efficiency	$\eta_{el,ref}$	44.2	[%]
- reference thermal production efficiency	$\eta_{th,ref}$	89	[%]
- correction factor for grid losses	p	86	[%]

Table 3.3: The FC system thermal and cogenerative performance results at full load.

References to the chapter 3

- [1] M. Bianchi , A. Borghetti, A. De Pascale, U. Mencherini, D. Messori, F. Napolitano, C. A. Nucci, A. Peretto, R. Vecci, “*Analisi di sistemi energetici basati sull’impiego di Fuel Cell per applicazioni stazionarie cogenerative*”, Ecomondo 2011-Rimini.
- [2] M. Bianchi, A. De Pascale, U. Mencherini, A. Peretto, R. Vecci, “*Banco prova sperimentale per la caratterizzazione di FC per applicazioni microcogenerative*”, Giornata di Studio Roberto Bettocchi – Macchine Energia e Ambiente, 19 Settembre 2012, Cento (FE),
- [3] Italia CompactRIO™ Reference and Procedures Help (FPGA Interface), 2004–2010 National Instruments Corporation.
<http://www.ni.com/dataacquisition/compactrio/>
- [4] M. Bagnoli, B. Belvedere, M. Bianchi, A. Borghetti, A. De Pascale, M. Paolone, “ A feasibility study of an auxiliary power unit based on a PEM fuel cell for on-board applications”, *Journal of Fuel Cell Science and Tech.*, vol.3, no.4, pp 445-451, 20.
- [5] B. Belvedere, M. Bianchi, A. Borghetti, A. De Pascale, M. Di Silvestro, M. Paolone, *Experimental characterization of an autonomous power unit equipped with a PEM fuel cell*, Proceedings of the 62nd ATI National meeting, 2007, 899-904.
- [6] B. Belvedere, M. Bianchi, A. Borghetti, A. De Pascale, M. Paolone, R. Vecci, *Experimental analysis of a PEM fuel cell performance at variable load with anodic exhaust management optimization*, *Int. J. of Hydrogen Energy*, (2012) ,1-9.
- [7] Directive 2004/8/CE of the European Parliament and of the Council. Commission Decision, 21 December 2006.

Chapter 4

THE DEGRADATION MECHANISMS OF THE PEMFC

The short-lifetime of the Proton Exchange Membrane Fuel Cells (PEM-FCs) is a barrier to the deployment and commercialization of this power generation system [1]. FC lifetime requirements vary significantly, ranging from 3000 to 5000 h for car application, up to 20,000 h for buses and 40,000 h for stationary applications [1-4].

Degradation of PEMFC performance is unavoidable. The rate of degradation of the stack voltage is used as a principal indicator of the health status and, consequently, of the durability of a FC. Generally the range of voltage decay rate is of 1-10 [$\mu\text{V}/\text{h}$] [1-3], but it can also exceed these values due to harsh and extreme operating conditions. The limits to the degradation rate are usually based on Beginning-Of-Life (BOL) and End-Of-Life (EOL), currently only few PEMFC stack satisfy these targets [5]. Mercedes-Benz claims a lifetime of above 2000 h without degradation for their stacks installed in test-vehicles all over the world [6].

Table 4.1 gives an overview of degradation rates, determined in long-term durability tests by various authors, it must be noted that most of the tests evaluate

the stability of cell performance under steady load. When the fuel cell is subjected to more demanding conditions, such as fluctuating loads, freeze/thaw cycles and shut down/start up, the observed degradation rates are significantly higher. In fact, Fowler et al. [11] demonstrate that the voltage decay rate of a PEMFC that has been used with 600 h of non-continuous operation under a variety of conditions, including stop-start cycling, long term storage, dehydration and flooding, is 120 $\mu\text{V}/\text{h}$.

Authors	Test duration (h)	Degradation rate (μVh^{-1})
Sishtla et al. [7] (reformate fuel, 4 thermal cycles over 1200 h)	5100	6
Washington [8] (Ballard Mk5R)	4700	6
Washington [8] (Ballard Mk6000)	8000	2.2
Nakayama [9]	4000	4.3
Maeda et al. [10] (on reformate fuel)	5000	6
Fowler et al. [11] (non-continuous operation, start-stop cycling, long-term storage, dehydration, flooding)	600	120
Endoh et al. [12]	4000	2
Knights et al. [13]	13,000	0.5
Scholta et al. [14] (GDL Toray TGP 120, 600mAc _m -2, T _{stack} = 65–70°C, H ₂ , O ₂ humidified (short stack, methane reformate operation, 0.5Ac _m -2)	2500	20
Scholta et al. [14] (GDL SIGRACET® SGL-10BB, 300mAc _m -2, T _{stack} =55°C, H ₂ = 1.3 bar, dryO ₂ = ambient pressure, dry)	2500	60
Cheng et al. [15] (400mAc _m -2, T _{cell} =60°C, H ₂ O ₂ : RH= 100%, ambient pressure)	4000	3.1
Wang et al. [16] (~1.0Ac _m -2, 0.64 V)	1000	54
Lightner [17, 18] (first 1000 h steady state, degradation 2_Vh-1; then accelerated cyclic testing)	4000	20
Borup et al. [19, 20] (steady-state, T _{cell} =80°C, RHH ₂ /O ₂ = 75%, gas pressH ₂ /O ₂ = 15 psig, flow rate H ₂ /O ₂ = 1.2/2.0*1.5Ac _m -2 equiv.)	1000	12
Cleghorn et al. [21] (single cell, 800mAc _m -2, T _{cell} =70°C, RH H ₂ , O ₂ 100%	26,300	4 - 6

Table 4.1: Results of long-term durability tests under laboratory conditions.

The FC industry needs to improve the long term performance, to satisfy the market requirement in term of service stability of performance and reliability. Hence, the aim of the designer is to minimize the rate of degradation.

Component	Failure modes	Causes
Membrane	Chemical attack Conductivity loss Delamination from electrode	Contamination Non-uniform distribution of reactants/water/coolant Mechanical stress Drying of membrane Contamination Thermal/mechanical stress
Active layer	Loss of activation Decrease in mass transport rate of reactants Loss of reformate tolerance Decrease in control of water management	Sintering of electrocatalyst Corrosion of electrocatalyst Poisoning Mechanical stress Contamination Dealloying of electrocatalyst Change in hydrophobicity of materials
Gas Diffusion Layer (GDL)	Decrease in mass transport rate of reactants Conductivity loss Decrease in control of water management	Degradation of backing material Mechanical stress Corrosion Change in hydrophobicity of materials
Bipolar plate	Conductivity loss Fracture/deformation	Corrosion Mechanical stress
Gasket	Mechanical failure	Corrosion Mechanical stress

Table 4.2: The main failure modes in PEMFC [2].

If the performance of FC at BOL is relatively understood, instead, EOL analysis has been very few [2]. Indeed, all the deterioration mechanisms of PEM fuel cells' components, that affect the performance degradation, are not yet fully understood [1], and are open issues Qualitatively, the physical mechanisms of FC degradation are the result of irreversible changes in the kinetic and transport properties of the cell, to well understanding these phenomena a post mortem analysis of components and materials is, usually, required.

Table 4.2 summarized the main failure modes of the PEMFC stack components. Usually, the stack degradation is a combination of many of the reported causes, such as harsh operating conditions, the inherent reactivity of component materials, contamination and poor design/assembly.

The most common degradation causes [2, 3, 4] are fuel and oxidant starvation, fuel crossover, sintering and corrosion of the electrocatalyst, corrosion of the bipolar plate, unwanted chemical reactions, membrane failure, poisoning and flooding of the reaction sites. Thermal management is also very important when a FC is operated at sub-zero and elevated temperatures (e.g. freezing conditions and cold start-ups) [1, 3].

Degradation is most severe when the Membrane Electrode Assembly (MEA) is highly stressed, e.g. by rapid fluctuations in load, by running at high current densities for extended periods, or when non-uniform distribution of reactants and/or temperature occurs. Moreover, the membrane pinhole formation is catastrophic for fuel cell operation. Contamination of the MEA by impurities leached from the fuel cell components, usually due to their corrosion, or introduced through the reactant gases is a major cause of degradation [2, 3]. In fact, the anode gas may contain impurities from the reforming process, while systems operating in urban environments may be forced to operate on air containing pollutants such as NO_x, SO₂ and dust particles. While membrane failure is the major lifetime constraint, the other degradation modes cause a gradual decrease in the output voltage of the stack.

Another phenomenon that particularly affects the longevity of a PEMFC, contributing to cell degradation, is the quality of water management. Poor water management can cause dehydration or flooding. Operation under dehydrated condition could damage the membrane, whereas flooding facilitates the corrosion of the electrodes, of the catalyst layers, of the gas diffusion medium and of the membrane.

Furthermore, inadequate water content, either globally within the stack or locally at certain locations in the unit cell, results in reduced conductivity in the membrane [22] and in any ions present in the catalyst layer. This produces an increased ohmic losses and a drop of the cell's voltage [2, 13].

St-Pierre et al. [24] showed that the life and longevity of a FC is strongly affected by the quality of water management in the PEM-FC. In fact, proper management of water within the cell ensures high efficiency and the maintaining of the power density and stable operating conditions over long periods of operation [25]. A balance must be realized between reactants (hydrogen and oxygen) delivery and water supply and removal [23] to keep the membrane humidified and have a high proton conductivity which is proportional to water content, without an excessive accumulation of water (flooding) that may negatively impact on the performance and lifetime of fuel cell.

4.1 THE MAIN DEGRADATION MECHANISMS OF THE PEMFC STACK COMPONENTS

The PEMFC short life and performance degradation are principally due to:

- chemical and/or physical effects: degradation, corrosion, chemical reactions, contamination, sintering, poisoning and mechanical failure of the cell components; fuel (H_2) crossover.
- extreme external factors: reactant gas (fuel and oxidant) starvation; thermal management (elevate and freezing temperatures).
- poor water management: dehydration of the membrane, and flooding of the reaction sites.

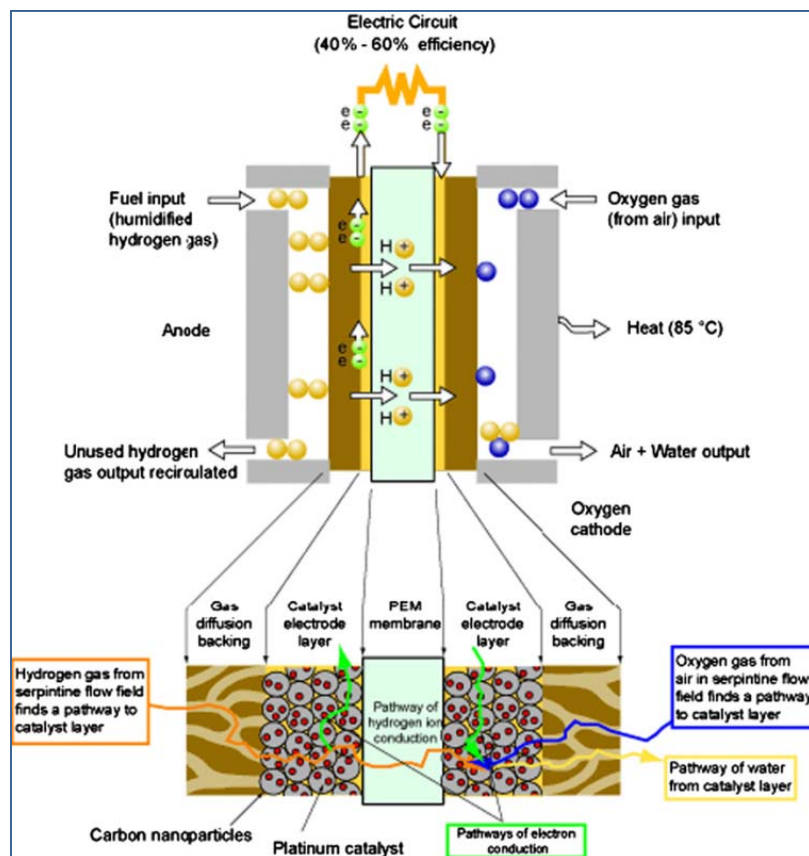


Figure 4.1: Components of a single PEMFC.

4.1.1 CHEMICAL AND/OR PHYSICAL EFFECTS

All components of the PEMFC stack (Figure 4.1), e.g. the electrodes/electrocatalyst, the membrane, the Gas Diffusion Layer (GDL) and bipolar plate (BP) may be affected by the corrosion [28].

This decay strongly depends on the operating conditions. In general, the longer the PEMFC stack is operated in transient or cyclic condition, the stronger is the corrosion and therefore the deterioration [29 - 33].

ELECTRODES/ELECTROCATALYST

Generally, the basic structure of the anodic and cathodic electrodes is similar, often exactly the same (see for example the electrodes of the “Penta H2” PEMFC analyzed in this PhD thesis [1, 27]). Frequently carbon paper or cloth constitutes the basic mechanical structure of the electrode. Since the carbon paper also facilitates the diffusion of the reactants onto the catalyst it is known as the GDL [4, 29, 34, 35]. Catalysts (for both anode and cathode) are usually made of pure platinum (Pt) or Pt alloy with nanometer size particles formed into very small particles applied on the carbon surface.

CATALYST

The catalyst corrosion strongly reduces the FC performance and the voltage output and it is one of main barriers to their commercialization. Corrosion promotes changes in the structure, chemistry and distribution of the electrocatalyst over time, which can lead to an increase in activation losses and therefore a decrease in cell performance. The factors that most contribute to the corrosion are potential cycling, number of cycles, cell temperature and humidification level (Table 4.3).

Cell potential cycling is one of the most important factors that contribute to the platinum agglomeration and/or oxidation and hence to a decrease in Electrochemical Active Surface Area (ECSA) [2, 3, 28, 29]. Borup et al. [29] show a loss of the ECSA of around 40% after 1500 potential cycles from 0.1 to 1.0 V. Wilson et al. [36] have shown that the number of Pt-particles smaller than 3 nm

was reduced from 40 to 5% at the cathode after operation of a PEMFC for 2200 h (operation at maximum power, over humidified gases, 80°C cell temperature). Borup et al. [29] also shows that the loss of Pt surface area proceeds through electrodisolution/re-deposition and surface migration of Pt atoms, with the driving force being the minimization of surface energy.

Authors	Experimental setup/testing conditions	Initial ECSA (%)	Loss of catalyst	Comments
Borup et al. [7]	RH 100%, 850 h, 2550 cycles RH 100%, 1500 cycles (0.1–0.75 V) RH 100%, 600 cycles (0.1–1.2 V) RH 100%, 1500 cycles (0.1–1.2 V)	~ 90 ~ 84 ~ 37 ~12	No	-
Borup et al. [46]	H2 RH 224%, O2 RH 100%, 1500 cycles (0.1–1.2 V)	~ 61	No	ECSA strongly correlates with number of cycles
Li et al. [54]	2500 cycles (0.1.2 V) 2500 cycles (0–1.0 V) Pt on Vulcan, 2500 cycles (0–1.2 V)	~ 0.3–0.56 ~ 0.68–0.74~30	-	ECSA decrease correlated with carbon weight loss, cycling to high voltages cause high ECSA loss
Wang et al. [18]	Cathode: ~1.0Acm ⁻² , 0.64 V 1000 h	(~0.68) from 25 to 17m ² g ⁻¹	Partly (diffusion in other electrochemically inactive parts)	Loss of Pt due to oxidation and dissolution
Wilson et al. [56]	Over humidified gases, Tcell =80 °C, 2200 h	Reduction of particles smaller than 3 nm from 40 to 5%	-	-

Table 4.3: Literature overview of the electrocatalyst degradation.

To maintain a large catalyst surface for a long time, operation of the fuel cell at both constant voltages and low voltage levels is preferred.

Different cell temperatures during operation also have an impact on the ECSA. Generally, kinetics goes up with increasing temperature and hence higher temperatures result in faster growth of Pt-particles [28, 29, 38].

St-Pierre et al [24] demonstrate that the hydration level will have an effect on particle growth in the electrocatalyst, moreover large particles of platinum oxide ($\sim 50 \mu\text{m}$) were also identified on the outside of the cathode GDL. These results demonstrate that the movement of platinum is favored by the presence of liquid water [2, 3, 24].

With water and especially at higher relative humidity, corrosion of the electrodes, mainly at the cathode, occurs [28, 29]. The anode catalyst is much less susceptible to corrosion than the cathode catalyst. In fact, the anode is almost unaffected by platinum agglomeration/sintering, dissolution and oxidation, irrespective of the conditions (constant voltage or cycling) at which the fuel cell was operated [3, 29, 39].

Only in extended fuel cell testing anode catalyst deterioration can be observed, after long operation periods platinum agglomeration does not occur, although the ECSA decreases. The reasons might be: i) the detachment from the carbon layer and loss of Pt-particles; ii) the loss of ionomer in the catalyst (Pt-particles which are not well-bound to the carbon support move in the ionomer and can be lost easier than well-bound particles [29, 39]).

GAS DIFFUSION LAYER (GDL)

Also the GDL is affected by the corrosion, since the carbon paper or cloth often serves as the support for the catalyst, carbon corrosion directly affects the lifetime of the cell [29]. Principally, the losses of carbon are due to the potential cycling, in particular on a high level and a high constant voltage and to a lower relative humidity of reactant gases, usually the water management is handled by the GDL.

To date the GDLs are treated to be hydrophobic to facilitate the water removal and to improve gas diffusion, so they are optimized for high relative humidity. Over time, they lose the hydrophobicity, which in turn reduces the mass transport rate of the gas. Higher hydrophilicity (thus lower hydrophobicity) means that more water tends to stay in the GDL blocking the pores and hinder transport of reactant gas molecules. This leads to a performance loss [28, 29, 37].

There is no experimental evidence of the influence of the operating temperatures on the GDL corrosion. In fact, many experiments show that GDL corrosion has not been affected by temperature [29]. Instead Li et al. [37], monitoring the carbon weight loss (gas-phase corrosion) of a fuel cell during a steady operation with humidified air at different temperatures, has showed that carbon weight loss increase with operating temperature.

MEMBRANE

Nowadays, DuPont's Nafion® and Gore's Primea® series are two of the mostly used ion exchange membranes and are considered the industrial standard [40]. In particular, Nafion® consists of a thermoplastic resin which, due to its perfluorinated composition, is relatively stable both chemically and thermally [41]. Nafion-type membranes have proved extremely stable for applications such as ion exchange and electrolysis, with lifetimes of tens of thousands of hours, but they are far more susceptible to degradation when placed in the harsh environment of a PEMFC [2, 4]. In fact, these type membranes are more vulnerable and degrade more rapidly, especially in automotive applications during potential cycling, during start-up and shut-down phases as well as in freezing periods when exposed to sub-zero temperatures [2].

The degradation of the membrane is a complicated multi-step mechanism, which can lead to catastrophic failure when the fuel cell is operated for an extended period of time. In fact, chemical attack of the membrane by contaminants is one of the main sources of reduction PEMFC lifetime.

These contaminants may originate from corrosion of the bipolar plates [42] or electrodes [43]. Ma et al. [44] postulated that such contaminants disable proton conductivity sites in the membrane, leading to a decrease in conductivity over time.

The accepted chemical degradation mechanism for Nafion membranes is peroxide radical attack [45]; the strongest evidence for this mechanism is the presence of hydrogen peroxide in the product water [2]. Hubner and Roduner [50] observed that the hydrogen peroxide radical attack is catalyzed by metal ions derived from corroded components of the MEA. The steps of these degradation

mechanism are: i) formation of hydroxyl (OH) and peroxy (OOH) radicals stemming from hydrogen peroxide (H_2O_2), which chemically attack the polymer end groups presented in the membrane [46, 47]; ii) the chemical attack, along with the transient operating conditions such as potential, temperature and humidification cycling, causes mechanical degradation and a change in membrane properties [46, 47–49].

Hydrogen peroxide can be formed both at the anode and the cathode. At the anode, H_2O_2 is formed when crossover of oxygen from the cathode occurs [47, 49]. Furthermore, air bleed in presence of carbon monoxide (from the fuel) at the anode can provide the oxygen to form hydrogen peroxide. At the cathode, H_2O_2 can be formed in the oxygen-reduction reaction prior to the formation of water [2].

The chemical attack causes both membrane degradation and thinning, which lead to reactant gas crossover due to the loss of membrane material [28]. Figure 4.2 has been reported as testimonial of the cracked membrane/MEA after long term operation [51].

Since the H_2O_2 formation occurs at both anode and cathode, mixed potentials can arise on both electrodes, when H_2 and O_2 travel through the membrane and react with the other reactant [53]. Since this reaction is highly exothermic, the released energy may cause hot spots on the membrane surface resulting in pinhole formation. Pinholes, again, make gas crossover easier. Hence, the increasing of gas crossover and pinholes formation gives origin at a membrane destructive cycle.

These hot spots are particular membrane regions characterized by high reaction density, high current density and also high temperature; consequently, they can also affect the Pt-catalyst. In fact, kinetics and therefore Pt-sintering are accelerated by high temperature [53].

An indicator for the membrane degradation state is also the concentration of lost fluoride [46, 47, 54]. In fact, when fluoride, which is part of the membrane polymer structure, can be found as fluoride ions in the exiting water, this indicates a chemical change in the membrane.

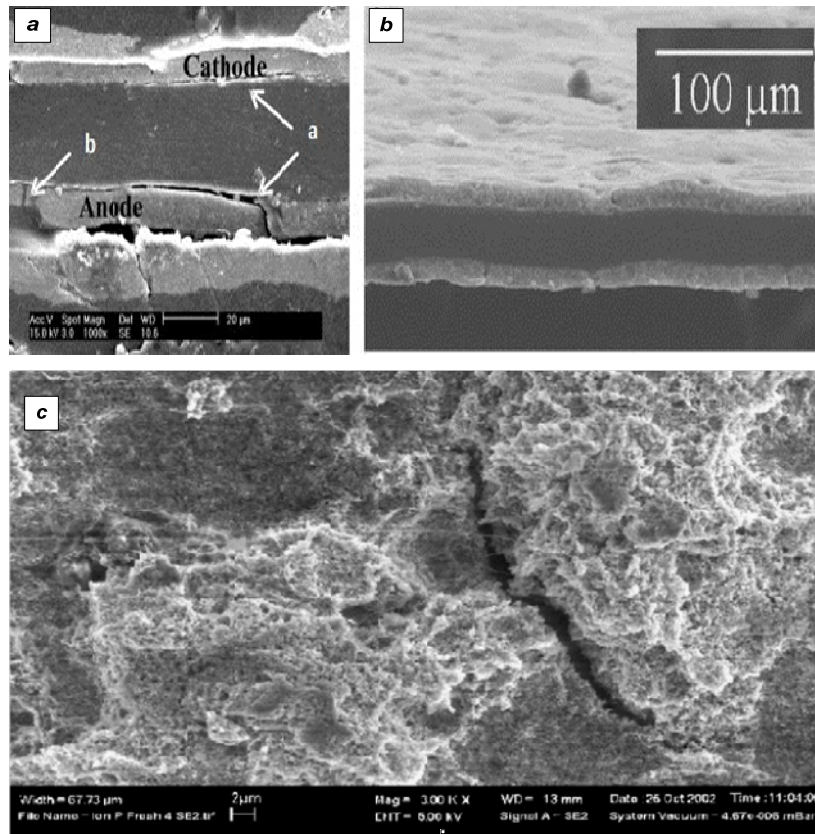


Figure 4.2: MEA cross section: a) Delamination phenomenon; b) Cracking phenomenon. c) A cracked membrane/MEA [66].

Another important factor in the durability of the membrane is its mechanical strength. In fact, membrane degradation is enhanced by mechanical stress [55], which is exacerbated by misalignment of components and/or unnecessarily high compressive forces. Wakizoe et al. [56] showed that a reinforced membrane performed better under start-stop cycling than an unreinforced membrane. Liu et al. [57] also observed that mechanically reinforced membranes may not suffer from the rapid and unpredictable failures which arise from hydrogen crossover; instead the degradation process for reinforced membranes is gradual, which is more desirable. Furthermore, they illustrate that some mechanical reinforced membranes exhibited a lifetime of an order of magnitude higher than non-reinforced membranes of the same thickness.

Hence, to increase the membrane durability it is necessary to achieve higher chemical and mechanical stability. In particular, to have a more stable chemical structure it is preferable to remove the reactive weak endgroups in the polymer. Curtin et al. [62] showed that a reduction of the reactive polymer endgroups of the

membrane is associated with a reduction of the fluoride ion release, a good life indicator as mentioned above.

A factor that can also accelerate the membrane degradation is poor water management. The performance degradations can usually due to the membrane dehydration. Generally this failure can recovered by humidification, but if the membrane is operating in dehydrated condition for an extended period, failure due to reactant crossover can occur [2]. A combination of low humidification and uneven distribution of reactant will lead to local hot-spots, which are very prone to membrane failure. Moreover a lower water content, due to the loss of the membrane hydrophilicity, gives a lower conductivity, subsequently the over time cell performance decrease.

BIPOLAR PLATES (BP)

Corrosion of bipolar plates also reduces the lifetime of PEMFC. This phenomenon has two adverse effects on PEM FC durability: contamination of the fuel cell with corrosion product and an increase in contact resistance [2 - 4].

The main degradation mechanism are: i) the dissolution of the bipolar plates material under permanent water contact, the dissolved material flush away or travels into the membrane; ii) the formation of a resistive surface film on the plates, which results in a higher ohmic resistance; iii) mechanical stress which can cause deformation and/or fracture of the plates under high compressive pressure [2].

Hence, in order to ensure a good balance between cost, performance and durability, bipolar plate materials must have good corrosion resistance, low resistivity (including contact resistance), high mechanical strength, low density, low reactivity, impermeability to reactant gases and low cost (both in terms of raw material and processing). The suitability of a variety of stainless steels was discussed by Davies et al [58], who showed that the thickness and resistivity of passive films varies with the type of alloy used.

GASKETS

Gasket materials are usually fluorine caoutchouc, ethylene-propylene diene monomer (EPDM) rubber and silicone. Poor sealing results in fuel losses and a reduced voltage due to the mixed potential at the electrodes. Schulze et al [59] analyzed the problem of degradation of sealing materials during fuel cell operation founding traces of silicone in the anode and electrocatalyst layers. They suggested that the accumulation of silicone in these areas could disturb the wetting characteristics of the electrodes, the water balance of the cell and react with the electrocatalyst at the cathode. A migration of silicone into the electrode but also into the membrane has been observed by Ahn et al. [60].

4.1.2 EXTREME EXTERNAL FACTORS

REACTANT GAS STARVATION

The reactant hydrogen (H_2) or oxygen (O_2) starvation causes the drop of the cell's voltage and the global performance decrease of the PEMFC. Generally, fuel or oxidant starvation refers to the FC operation at sub-stoichiometric conditions. The reactant starvation can be caused by several factors, for example a poor water management with flooding, or a poor heat management during sub-zero temperatures and cold start-ups with ice within the cell that can block the pores of the gas diffusion layers. Moreover, a poor gas feeding management can also lead to non-uniform distribution of the reactant gases resulting in partial or complete fuel and/or oxidant starvation or in sub-stoichiometric operation in individual cells. Also, an imperfect stack and cell design with an uneven distribution of mass in the flow fields, a poor stack assembly as well as quick load demands can contribute to the gas starvation [2, 67].

Liu et al. [67] has well analyzed the phenomenon, showing that lower cell potentials do not negatively influence durability, but what does influence a cell's durability is a subsequent cell reversal due to starvation. In fact, measuring the polarization curves of a segmented single fuel cell with several subcells under anode and cathode starvation, Liu et al. observed that during anode starvation, the

current density of the subcells nearest to the outlet (row 4 of 4) dropped immediately to zero, followed by a voltage decrease. Subsequently the current density of row 3 dropped to zero. Apparently, the subcells of rows 1 and 2 were not impacted.

Furthermore, reactant gas starvation can also result in generation of hydrogen in the cathode or oxygen in the anode. For example, if hydrogen starvation occurs, the cell current cannot be maintained causing a high anode potential [67]. Consequently, the water present at the anode may split into hydrogen and oxygen, producing oxygen in the anode and, similarly, during oxygen starvation hydrogen at the cathode [68]. The presence of oxygen at the anode and hydrogen at the cathode will lead to reversal of the cell potential, which is a negative potential difference between the anode and the cathode [69]. Cell reversal accelerates the corrosion of the carbon components, such as the backing layers with the ensuing electrocatalyst corrosion, and eventually leads to the components damage [67, 68, 70]. During hydrogen starvation, oxygen at the anode can react with the carbon present in the gas diffusion and backing layers to form carbon dioxide [2, 67, 68, 71].

THERMAL MANAGEMENT

Under extreme temperature conditions such as freezing or elevated temperatures, thermal management of the PEMFC is very important [2, 72, 73].

The repetitive cycles of ice formation on the membrane surface and its melting into water can delaminate the catalyst layer from both the membrane and the gas diffusion layer [3, 74, 75]. The result of the mechanical damage is a loss of thermal and electrical interfacial contact. He and Mench [76] correlated the ice formation on the membrane surface with its thickness and initial water content. Since the Nafion® membranes have a large compression under freezing condition; the contained liquid water can flow out of the membrane and will freeze immediately on the surface and in the catalyst layer. Thicker the membrane and the higher the initial water content are, thicker will be the developing ice layer. Chang et al. [77] shows that with decreasing temperature of the liquid water in the cell from 80 to 30°C the proton conductivity of a Nafion® membrane can decrease up to 30%, depending on the thickness and the measurement method.

Another result of freeze/thaw cycles is cracks in the membrane that lead to gas crossover and in turn uncontrolled reaction between hydrogen and oxygen with subsequent pinhole formation damaging the membrane and reducing the life of the cell [75].

Exposure of a non-operating PEM fuel cell to freezing temperatures is one of the issues affecting durability. In fact, when the fuel cell is subjected to sub-zero temperatures for an extended period of time the residual water contained within the cell can freeze. This leads to thermal and mechanical stress and hence to mechanical damage of the cell components or may even cause physical breakdown.

Furthermore the start-up of the PEMFC at sub-zero temperatures is also a critical issue. If the generated water in the cathode is not removed while the cell is running at sub-zero temperatures, ice will form causing voltage drop and even shuts down the electrochemical reaction. This is more likely to happen at higher current densities. Therefore it is important that before ice completely blocks the catalyst layer the cell temperature reaches above freezing [78, 79].

Operation of PEMFCs under higher temperatures ($>100\text{ }^{\circ}\text{C}$) seems to offer some advantages: the electrochemical kinetics and hence the efficiency improves, the tolerance for contaminants increases and water management and cooling are enhanced due to a higher temperature difference between the cell and the coolant. Moreover, waste heat can be recovered, CO-poisoning is reduced and therefore lower quality hydrogen from reformation can be used. However, the operation of cell at high temperatures accelerates the degradation of cell components and the decrease of longtime performance and durability [73, 80–82]. For example, Song et al. [81] studied the effect of Nafion[®] content on the electrode and the performance under different temperatures. They observed that at elevated temperature the water uptake of the membrane can be aggravated and proton conductivity may decrease, especially at low relative humidities. This leads to a significant resistive loss lowering the cell performance and efficiency.

4.1.3 POOR WATER MANAGEMENT

One of the most critical aspects of PEMFC durability is the water management [63, 69, 83]. In particular, in order to ensure stable operation, high efficiency and to maintain the power density of PEM fuel cells in the long run it is necessary to keep the membrane humidified and, at the same time, to avoid its flooding. The humidification of the membrane is important for high proton conductivity, because the membrane's conductivity is directly related to its water content [1, 3, 48]. On the other hand, accumulation of too much water also impacts performance and lifetime of the fuel cell. Excess water in fact can block the flow channels and the pores of the gas diffusion layer (GDL) and can instantly lead to reactant starvation. Reactant starvation denotes operation of a fuel cell under sub-stoichiometric reaction conditions. Too much water also aggravates other degradation mechanisms such as corrosion and contamination of components. Moreover, the degradation is proportional to the time in which the cell is exposed to excess water. Hence, a proper water balance between water formation and water removal is required [75, 76]. The water balance depends on the water carried in or formed inside the cell and the water removed from the cell. Reactant gases, which are pre-humidified or saturated and the oxygen-reduction reaction at the cathode generate water within the cell. Water is removed by evaporation into the gas streams, exiting humidified gases and exiting liquid water.

MEMBRANE DEHYDRATION

Generally occurs at the anode side. The main causes of this phenomenon seems to be a poor water management leading to a shortage of water [2, 63, 86]. In particular, the reasons for membrane dehydration can be three:

- sufficient humidification cannot be maintained when feeding the cell with low-humidified or dry reactant gas streams. Water formation reaction at the cathode alone is not able to compensate the lack of water;
- evaporation of water and subsequent vapor removal through the flow channels, mainly at higher cell operating temperatures can play a role [85];

- electro-osmosis. In fact, the electro-osmotic force is strong when a high electric field at high current densities exists. It has been observed that at high current densities the water replenishment by back-diffusion is not sufficient to keep the anode side of the membrane wet [99–101]. For example Wang and Wang [87] show that during a step increase of the current density the electro-osmotic force will immediately pull water molecules from the anode to the cathode.

The main consequence of dehydration is drying of the proton-conducting membrane. With decreasing water content the conductivity decreases which leads to higher ionic resistance and higher ohmic losses [2, 63, 84]. That results in a substantial drop in cell potential and thus a temporary power loss [63, 84, 87].

Although a temporary drop in voltage can usually be recovered by humidification, dry cell operation over a long time can cause serious and irreversible damage to the membrane. The recovery time depends on the membrane thickness and the water diffusion coefficient [63, 87]. Le Canut et al. [63] exposed a PEMFC to drying conditions for about 12 min, during this period the initial cell voltage of around 0.8 V (current density = 0.1 A cm^{-2}) dropped to about 0.75 V. After 15–20 min of rehumidification the initial value could be reached again (Figure 4.3).

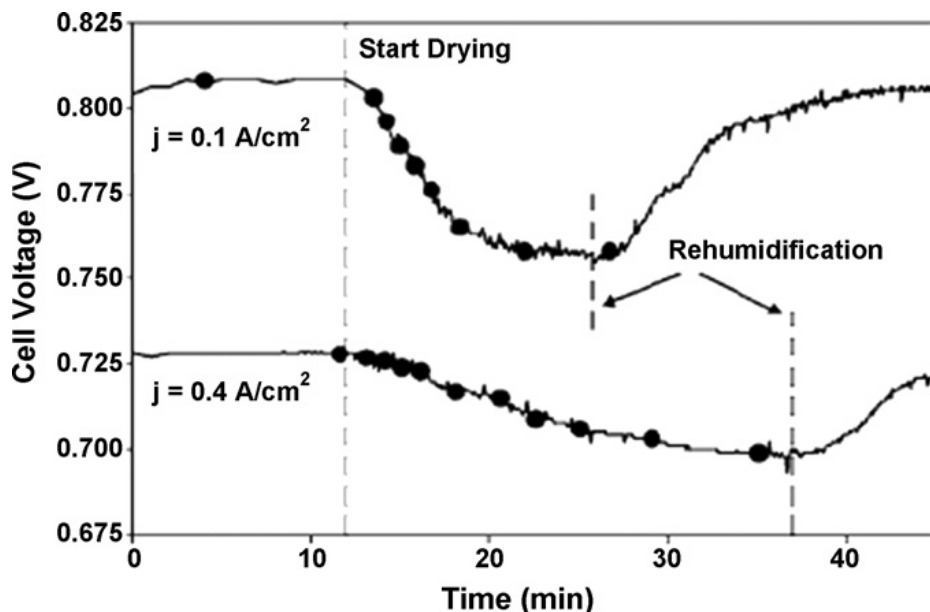


Figure 4.3: Cell voltage VS time for cell rehydration and re-humidification [63].

Anode dehydration is expected to be more serious at the inlet of the cell. That can be explained by the higher water back-diffusion to the anode at the bottom of the cell. Since the hydration state at the exit of the cathode is higher, caused by exiting water, the back-diffusion is higher as well [90]. Moreover, under dehydrated condition the membrane pores shrink which leads again to lower back-diffusion rates. During operation this effect can be aggravated by a poor thermal management [84]. Huang et al. [91] demonstrated that when membranes are exposed to dry conditions over a longer time, they can become brittle and develop crazes or cracks. This causes gas crossover and therefore uncontrolled reaction of H_2 and O_2 which results in formation of hot spots and, thus, of pinholes leading to more gas crossover. Once this process is initiated a “destructive cycle” of increasing gas crossover and pinhole production is established [53].

THE FLOODING PHENOMENON

Flooding is the accumulation of excess water which can occur at both the anode and cathode side of the membrane. The rated performance in terms of output DC current and voltage can be significantly diminished by the electrodes flooding phenomenon. The flooding phenomenon, whether it occurs in both electrodes or only in one, leads to a sudden increase of concentration losses (Figure 4.4) [1]. Indeed, water blocks the pores of the gas diffusion layers and it prevents the reagents to reach the catalysts, causing a sudden voltage drop [1, 23]. An excess of water promotes the corrosion of the electrodes, of the catalyst layers, of the bipolar plates and of the membrane [23]. Then, the impurities can be deposited on the catalysts. Hence, dissolved catalyst particles and the impurities can also be transported in the membrane replacing H^+ ions. Consequently, ohmic losses increase, the electrodes performances decrease and the conductivity is reduced over the time, leading to FC failure [1, 23].

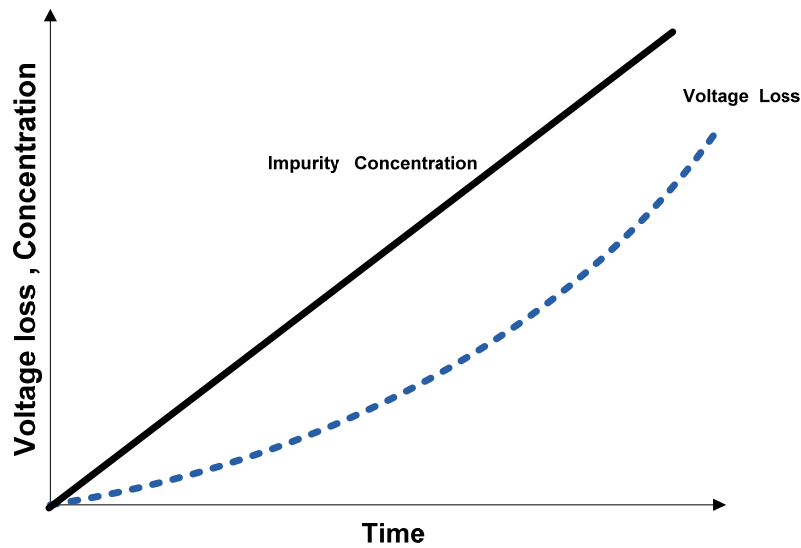


Figure 4.4: FC Impurities concentration (continuous line) and FC stack voltage (dotted line) in absence of purge [1].

Furthermore, the gas may be forced to flow through alternative channels which results in a partial pressure decrease across the backing layers [63, 84, 92]. He et al. [93] correlated partial pressure directly to the flooding level and considered it to be a good indicator for performance. They show that (Figure 4.5) if the cathode pressure-drop doubles from 1.5 kPa to around 3 kPa, the initial cell voltage of 0.9 V goes down to around one third of its initial value (cell temperature, 51 °C; H₂ flow rate, 2.0 A cm⁻² equiv.; air flow rate, 2.8 A cm⁻² equiv., ambient pressure; H₂ temperature, 50°C; air temperature, 27°C) [93]. Figure 4.5 shows clearly that cathode flooding has a negative effect on fuel cell performance. Especially at higher current densities (above 0.55 A/cm²) the partial-gas-pressure-drop at the cathode due to flooding increases significantly which results in a considerable cell voltage drop [93].

Also Dipierno and Fronk [94] have developed a method and a device to monitor the pressure drop across the flow fields to detect and correct flooding of common PEM fuel cells.

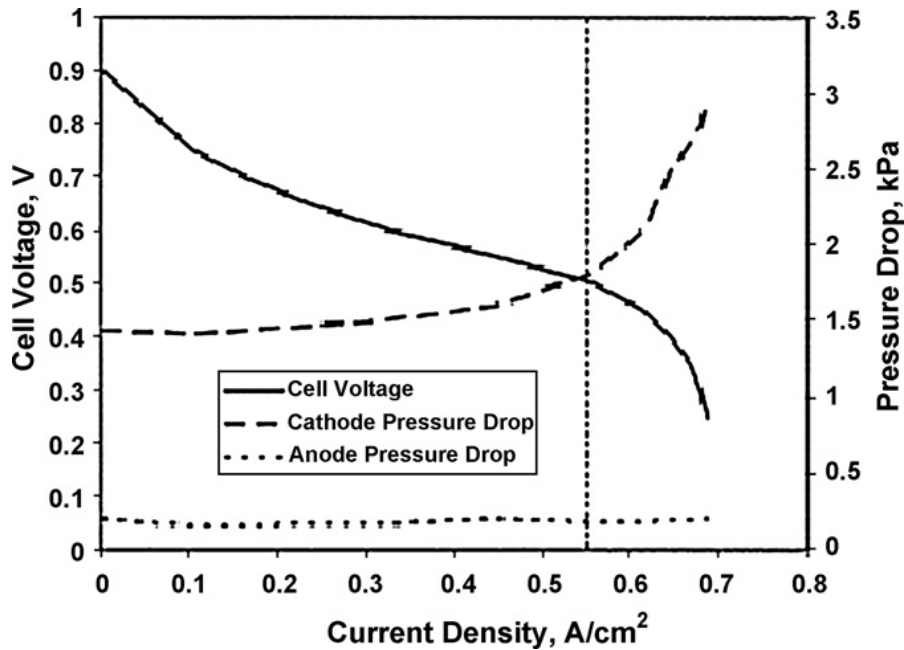


Figure 4.5: Effect of cathode flooding on fuel cell performance [93].

Weber et al. [95] developed a model for determining the water effects in GDLs and coupled it to a membrane model. They show that the fraction of hydrophobic pores, f_{H0} ($f_{H0} = 1 - f_{HI}$, where f_{HI} is the fraction of hydrophilic pores) of a GDL plays an important role in the maximum power and the limiting (maximum) current in a fuel cell. At low values of f_{H0} (that is high hydrophilicity, hence higher chance of excess water in the GDL) the maximum power is limited due to low values of limiting current, and due to mass transport limitations of oxygen in the cathode. The optimum value of f_{H0} was determined to be 0.45, where the maximum power ($W\ cm^{-2}$) of the cell could be reached. Turhan et al. [96] and Kowal et al. [97] demonstrated that in the case of over-humidified reactants, the water inside the cell increased with decreasing cell pressure; the contrary was observed for under-humidified inlet conditions.

At the cathode, the flooding is promoted by three mechanisms:

- water formation due to the oxygen reduction reaction generates water. More water is formed when the load or the current density of the fuel cell is increased;
- electro-osmosis under the influence of an applied electric field across the membrane takes place. The electro-osmotic drag causes protons moving through the membrane to pull water molecules from the anode

to the cathode. The rate of transported water depends on the humidification level of the membrane and increases with increasing current density [84]. Ngyuen and White [84] have shown that along 10 cm of a flowchannel, where the membrane hydration level at the inlet is higher than at the exit, the electro-osmotic drag coefficient at the inlet was around 5 times higher than at the exit;

- saturated or over-humidified reactant gases as well as liquid water injection.

Water removal mechanisms are water back-diffusion to the anode, evaporation, water-vapor diffusion and capillary transport of liquid water through the porous cathode backing layer [93].

Water back-diffusion takes place when the water content of the membrane cathode side exceeds that of the anode side [87]. In comparison to other mechanisms, back-diffusion does not contribute much to water removal. Only at low current densities (0.3 A cm^{-2}) the effect of back-diffusion can exceed electro-osmosis [84]. Water evaporation is facilitated by higher cell temperatures and a higher air flow rate is beneficial to carry water out of the cell. He et al. [93] show that by increasing the cell temperature from 40 to 50°C the cathode pressure can drop from 3 to 2 kPa and hence the flooding level drops within 15 min (air flow rate, 2.0 A cm^{-2} ; H₂ flow rate, 2.0 A cm^{-2} ; p = ambient pressure; H₂, 43 °C; air, 25 °C). At higher temperatures, water evaporation as well as the volumetric air flow rate (if the mass flow rate of air stays the same) will increase. Also, a decrease in surface tension and viscosity of water makes it easier to flush water out of the cell [93]. The capillary transport of water through the porous cathode backing layer to the flow channels also helps reducing the hydration level [28].

Although the flooding at the anode occurs less frequently than the cathode [1, 24, 98] (since the cathode is naturally the water generating electrode), it is the most hazardous for the correct functionality of the cell. In fact it is able to cause the failure of the fuel necessary for the realization of electrochemical reactions and causes corrosion of the catalyst layer [1]. Also, due to usually low hydrogen flow rates, liquid water is more likely to stay in the anode [93].

The flooding at the anode side is favored by [1]:

- low hydrogen flow rates and by low current densities (0.2 A/cm^2), while high current densities will generate most intense electro-osmotic forces able to reduce the amount of water at the anode [23];
- lower cell temperatures and then by higher water condensation in the anode channels. Ge et al. [16] confirm that at the anode inlet, the proton flux is high and a strong electro-osmotic force drags the water molecules from the anode to the cathode, resulting in low water content. At the anode outlet, the current density is lower, hence the water content is higher;
- liquid water injected for cooling and humidification with conditions of low temperatures [1, 25];
- water back-diffusion phenomenon, i.e. the diffusion of water from cathode to anode promoted by a low hydration state of the fuel gas stream [1, 25].

Even in the absence of impurities, the prolonged exposure of the membrane-electrode assembly (MEA) to a high amount of water can cause a permanent FC performance loss linked to the degradation of materials.

To remove excess water and impurities inside the FC, it is necessary to operate a periodic purging.

4.2 CONTAMINATION OF THE PEMFC COMPONENTS

Contamination is the process where impurities pollute and penetrate into the cell's components and/or initiate chemical attack and slow down the actual reactions taking place in the cell. The contamination products originate from components inside the cell or can be transported into the cell by the reactants. Consequently, metal, alkaline metal and ammonium ions, silicon and catalyst particles as well as carbon monoxide (CO), nitrogen oxides (NO_x) or sulfur dioxide (SO₂) can be present in the cell. Even trace amounts of impurities result in considerable degradation of performance [2, 61, 62].

The CO-poisoning is due to the adsorption of the CO-molecules [2] by the platinum that block the hydrogen from reaching the platinum particles. CO-poisoning can lead to a significant performance loss, but it does not seem to have an influence on lifetime. It was demonstrated that even 50 ppm of CO are sufficient to poison the anode reaction resulting in a lower cell potential output and lower energy conversion efficiency [66]. The CO poisoning, occurs only at the anode side, because the CO can be present in the hydrogen stream, when the fuel is obtained by reforming liquid hydrocarbons or alcohol fuels [2-4, 40, 63, 64, 65]. In order to stop the CO-poisoning it is necessary to remove carbon monoxide from the reactant. For example, Le Canut et al. [63], observed that the voltage could be fully recovered with injection of air into the fuel stream (air bleed 2%), considering a recovery time of 40 min for the low and around 10 min for the high CO concentration.

Also the membrane can be attacked by cationic contaminants. Alkaline metals and ammonium ions can in fact penetrate into the membrane resulting in considerable reduction of performance [61, 62]. Kienitz et al. [61] assume that the reduced performance of a contaminated cell is due to the limited proton flux at the cathode. Protons will be replaced, due to the higher affinity of the cations, with the sulfonic acid endgroups of the membrane, resulting in lower conductivity and water levels and in a higher electro-osmotic force. This will reduce the maximum current and the exchange current density in the cells.

4.3 HYDROGEN CROSSOVER

Hydrogen crossover is an undesirable diffusion of hydrogen from the anode to the cathode through the membrane (Figure 4.6).

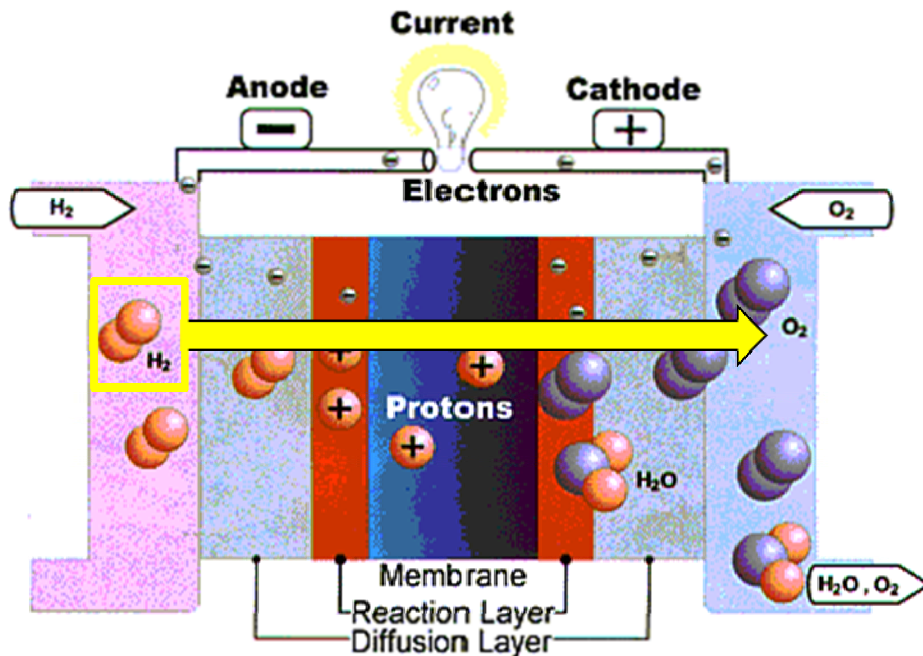


Figure 4.6: The H₂ crossover phenomenon in a PEMFC.

Hydrogen crossover can have at least three effects: the fuel efficiency reduction, the cathode potential depression and the aggressive peroxide radical formation [106].

Cheng et al. [107] have demonstrated that the hydrogen which crosses over can directly react with oxygen at the cathode surface, resulting in a reduction of the cathode potential.

More severely, the direct reaction between H₂ and O₂ at the cathode can produce peroxide radicals, which not only attack the catalyst layer, but also the membrane, causing significant catalyst-layer and membrane degradation [108]. In addition, Yu et al. [109] confirmed that the formation of hot-points by the highly exothermal chemical reaction between H₂ and O₂ can also lead to pin-holes into the membrane, destroying the MEA and causing safety problems. Therefore, Ianaba et al. [110] and Teranishi et al. [111] demonstrated that also hydrogen peroxide can

lead to pin-holes in the membrane causing the performance degradation of the PEMFC. Moreover, an accelerated sintering of catalysts could be caused by this hydrogen crossover [108].

The measurement of hydrogen crossover is of importance for the fundamental understanding and practical mitigation of fuel cell degradation and membrane failure [107].

Since H₂ crossover is a diffusion process, the PEM structure and fuel cell operating conditions [110, 112] can greatly influence the crossover process. In fact, Sakai et al [113] investigated the H₂ crossover at temperature up to 80 °C, showing that the uses of thinner membranes and the operation of fuel cells at high temperature and high pressure will facilitate H₂ crossover. Also the water content in the membrane [113] and gas pressure [110] had a great effect on the H₂ crossover.

Rama et al. [114] analyzed the effects of membrane thickness, operating pressure and temperature and current density on H₂ crossover using a concentrated solution membrane system containing four species: water, electrolyte membrane, proton and hydrogen. The simulated results indicate that the increase in the H₂ crossover found when temperatures increases were attributed to the dependence of the H₂ diffusion coefficient on temperature.

The structure and chemistry of PEM are critical in the control of proton and water transport and H₂ crossover. The use of Nafion-based composite membranes could reduce H₂ crossover with a less porous crystalline structure provided by well-dispersed small additive particles [115], or after heat-treating at 120 °C [116].

The three-region model [117] and cluster-network model [118] have been widely used to describe the microstructure of perfluorosulfonated membranes such as Nafion-type membranes. However, there is still no agreement as to whether the gas permeates through Nafion in the intermediate region, which consists mainly of the flexible amorphous part of the perfluorocarbon backbone [119, 120], or through the hydrated ionic clusters, which contain mainly water and sulfonic acid groups [113]. Brohka et al. [121] have suggested another solution according to which the gas permeates through both regions.

In order to improve our understanding of the H₂ crossover phenomena, it is necessary to clarify the nature of H₂ crossover from the anode to the cathode via the MEA.

Many studies have been conducted in order to investigate the causes and the effects of the H₂ crossover phenomenon. For example, Yasuda et al. [14] have studied the impacts of crossover hydrogen on the location of the platinum (Pt) band formed in the membrane after Pt dissolution. The Pt band or Platinum-Into-The-Membrane (PITM) was shown to be located closer to the anode under lower hydrogen partial pressure conditions [122].

Zhang et al. [15] examined the effects of hydrogen and oxygen partial pressures on Pt precipitation within the membrane, and developed a simple model to estimate the location of the PITM band defined as:

$$\delta_{PITM} = \frac{K_{H_2} p_{H_2} l_{PEM}}{K_{H_2} p_{H_2} + 2K_{O_2} p_{O_2}} \quad (4.1)$$

where: δ_{PITM} is the PITM location, l_{PEM} is the membrane thickness, K is the membrane gas permeability, and p is the gas partial pressure.

Holby et al. studied the influence of crossover hydrogen on the stability of Pt nanoparticles via a theoretical approach [124].

T. Cheng et al. [125] have evaluated the crossover hydrogen effects on Pt degradation and the subsequent impacts on the cathode catalyst layer.

Precisely, they have investigated the effects of crossover hydrogen on Pt dissolution and agglomeration in fuel cell stacks under dynamic cycling conditions that simulate fuel cell system start-ups and shutdowns.

The experimental results provided that H₂ crossover maychemically reducePt oxides and subsequently decreases the amount of Pt ions formed via the oxide pathway. Hence, with less H₂ crossover, the concentration of Pt ions in the cathode becomes higher and subsequently leads to more Pt growth and agglomeration, in agreement with the relative crystallite sizes and active surface area loss by CO stripping. Finally, based on Fick's Law of diffusion, the higher Pt ion concentration

may counterbalance the longer Pt ion diffusion path.

Kocha et al. [123] have confirmed the dependence of H₂ crossover on the membrane thickness. They compared the H₂ crossover currents measured in Nafion 112 and in Nafion 111 in the temperature range of 25–80 °C, suggesting that the dominant factor limiting the H₂ crossover rate is the membrane diffusion coefficient (D_{PEM}). For Nafion membranes, D_{PEM} has been defined empirically as a function of temperature (T) [126], but also of the backpressure (P) and of the relative humidity, RH [107].

X. Cheng et al. [107] have developed a multilayer diffusion model to describe H₂ crossover through the MEA (Figure 4.7). This investigation was carried out to examine the effects of temperature (T), pressure, and relative humidity (RH) on H₂ crossover. They have demonstrated that the H₂ crossover strongly depends on T , RH and backpressure (P).

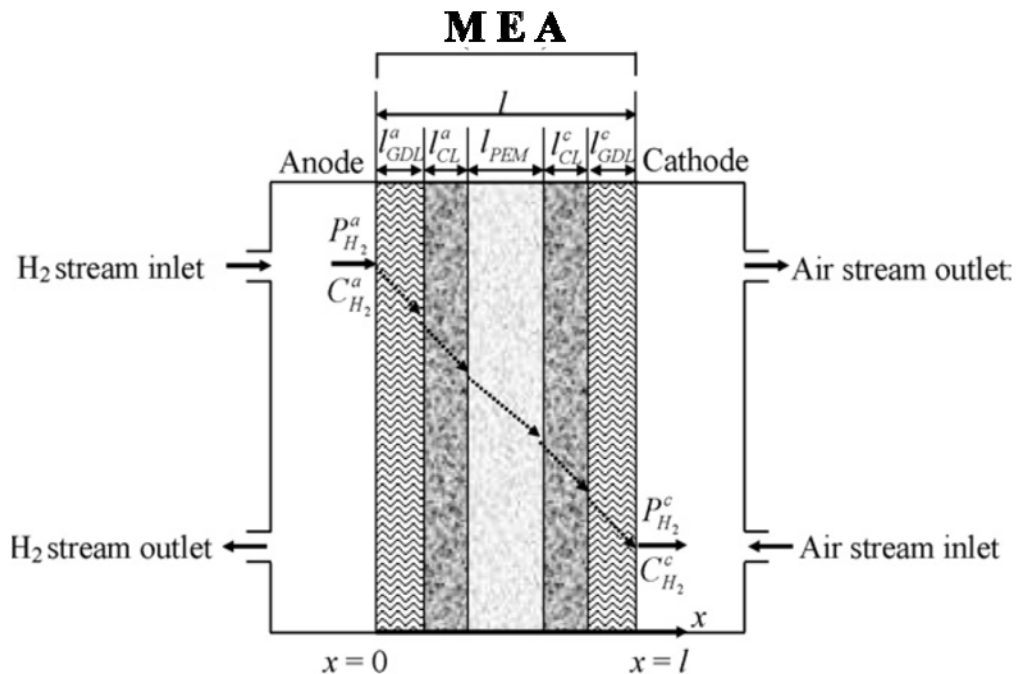


Figure 4.7: The H₂ crossover through the MEA in a PEMFC scheme [107].

In fact, the H₂ crossover rate, $J_{H_2}^{cross}$ (mol cm⁻² s⁻¹), can be expressed as:

$$J_{H_2}^{cross} = \left(\frac{\psi_{H_2}^{PEM}}{l_{PEM}} \right) (P_{H_2}^a) \quad (4.2)$$

where:

$\psi_{H_2}^{PEM}$ is the permeability coefficient of H₂ in the PEM (mol cm⁻¹ atm⁻¹ s⁻¹);

l_{PEM} is the PEM thickness;

$P_{H_2}^a$ is the H₂ partial pressure inside the anode chamber.

Each of these parameters is also function of the temperature, T , backpressure, P and relative humidity, HR .

In particular the permeability coefficient $\psi_{H_2}^{PEM}$ is a function of T , P , HR and also of the water content and the nature of the membrane [127]. It can be calculated at various conditions through the current induced by the crossed-over hydrogen, $I_{H_2}^{cross}$, that is directly related to the H₂ crossover rate through the Faraday's equation:

$$J_{H_2}^{cross} = \frac{I_{H_2}^{cross}}{nFA} \quad (4.3)$$

Where where n is the electron number of H₂ oxidation (=2), F the Faraday constant (A s mol⁻¹), and A is the MEA active area (cm²).

Instead, the thickness of the membrane, l_{PEM} does not vary substantially, for a given fuel cell system. For example it is equal to ~50 μm for Nafion 112 and 175 μm for Nafion 117.

Finally, the H₂ partial pressure, $P_{H_2}^a$ can be calculated based on the fuel cell anode inlet total pressure (P_{inlet}^a), the H₂ partial pressure in the inlet stream, ($P_{H_2-inlet}^a$) and the outlet total pressure, backpressure (P).

Assuming that the pressure drop along the superfine anode channel is linear, $P_{H_2}^a$ is defined by following equation:

$$P_{H_2}^a = \left(\frac{P_{H_2-inlet}^a}{P_{inlet}^a} \right) \left(\frac{P_{inlet}^a + P}{2} \right) \quad (4.4)$$

The magnitude of H₂ crossover (eq. 4.2) goes up monotonically with increases in temperature and backpressure. However, the RH effect is more complicated than those of temperature and backpressure [107].

More in detail, H₂ crossover rate increases with increasing temperature and, since the permeability coefficient, $\psi_{H_2}^{PEM}$ is directly related to the H₂ solubility and diffusion coefficients [123], any effect of temperature on these two coefficients could cause a change of $\psi_{H_2}^{PEM}$. The increase of this parameter with increasing temperature probably indicates that the effect of temperature on the diffusion coefficient is more significant than that on the solubility coefficient.

According to the Eq. 4.3, the H₂ crossover rate will be increased if the H₂ partial pressure, increases. In particular, X. Chang et al. [107].have observed a monotonic increase in the H₂ crossover rate with increasing backpressure Thus it is understandable that an increase in backpressure will result in a H₂ partial pressure increase, which then creates a larger pressure difference across the PEM.

The activation energies and maximum permeability coefficients of H₂ permeation through both Nafion 112 and Nafion 117-based showed similar values of these parameters for both MEAs, suggesting that the membrane thickness has no significant effect on the H₂ permeation mechanism.

The RH effect on the H₂ crossover rate seems to be more complicated than those of temperature and backpressure [107]. In fact, fixed the temperature the H₂ crossover rate increases as the RH increases, at higher backpressure, while the RH increase reduces the crossover rate, at lower backpressure.

However, the temperature effect is much larger than those caused by backpressure and RH.

References to the chapter 4

- [1] B. Belvedere, M. Bianchi, A. Borghetti, A. De Pascale, M. Paolone, **R. Vecci**, Experimental analysis of a PEM fuel cell performance at variable load with anodic exhaust management optimization, (Original Research Article) International Journal of Hydrogen Energy, Volume 38, Issue 1, 11 January 2013, 385-393.
- [2] Hinds G. Performance and Durability of PEM Fuel Cells: A Review. NPL Report DEPC-MPE 002, 2004, pp. 25-42.
- [3] Schmittinger W, Vahidi A. A review of the main parameters, influencing long-term performance and durability of PEM fuel cell, Journal of Power Sources, 2008;180: 1-14.
- [4] Fuel Cell Handbook, 7th Edition, US DOE, 2004.
- [5] <http://www.ballard.com/>
- [6] <http://www.mercedes-benz.de/content/germany/mpc/mpc-germany-website/de/home/mpc/buses/home/bus-world/>
- [7] C. Sishtla, G.Koncar, R. Platon, S. Gamburgzev, J. Power Sources 71 (1998) 249.
- [8] K. Washington, Proceedings Fuel Cell Seminar 2000, Portland, U.S.A., 2000, p. 468.
- [9] U. Pasaogullari, C.Y. Wang, J. Electrochem. Soc. 152 (2) (2005) A380–A390.
- [10] H. Maeda, A. Yoshimura, H. Fukumoto, Proceedings Fuel Cell Seminar, (2000), Portland, U.S.A., p. 379.
- [11] M. Fowler, J.C. Amphlett, R.F. Mann, B.A. Peppley, P.R. Roberge, J. New Mat. Electrochem. Syst. 5 (2002) 255.
- [12] E. Endoh, S. Terazono, H.Widjaja, Abstract 89, Electrochem. Soc. Meeting Abstracts, Salt Lake City, U.S.A., 2002.
- [13] S.D. Knights, K.M. Colbow, J. St-Pierre, D.P.Wilkinson, J. Power Sources 127 (2004) 127–134.
- [14] J. Scholta, N. Berg, P. Wilde, L. Jorissen, J. Garche, J. Power Sources 127, (2004) 206–212.

- [15] X. Cheng, L. Chen, C. Peng, Z. Chen, Y. Zhang, Q. Fan, J. Electrochem. Soc. 151 (2004) A48–A52.
- [16] X. Wang, D. Myers, R. Kumar, Proceedings of the Fuel Cells Durability, first ed., Washington, DC, 2006, pp. 151–162.
- [17] V. Lightner, DOE Hydrogen Program, Record 5036, 2006.
- [18] V. Lightner, DOE Hydrogen Program, Backup Ref. 5036a, 2006.
- [19] R. Borup, D.Wood, J. Davey, P.Welch, F. Garzon, DOE Hydrogen Review, Presentation, 2006.
- [20] R. Borup, D.Wood, J. Davey, P.Welch, F. Garzon, DOE Hydrogen Review, FY 2006 Annual Progress Report, 2006.
- [21] S.J.C. Cleghorn, D.K. Mayfield, D.A. Moore, J.C. Moore, G. Rusch, T.W. Sherman, N.T. Sisofo, U. Beuscher, J. Power Sources 158 (2006) 446–454.
- [22] Zawodzinski T, Derouin C, Radzinski S, Sherman R, Smith V, Springer T, Gottesfeld S. Water Uptake by and Transport Through Nafion 117 Membranes, J. Electrochem. Soc. Vol.140, No.4, (1993): pp. 1041-1047.
- [23] McKay DA, Siegel JB, Ott W, Stefanopoulou AG. Parameterization and prediction of temporal fuel cell voltage behavior during flooding and drying conditions, Journal of Power Sources, Volume 178, Issue 1, 15 March 2008, p. 207-222.
- [24] St-Pierre J, Wilkinson DP, Knights S, Bos M. Relationship between water management, contamination and lifetime degradation in PEFC, Journal of New Materials for Electrochemical Systems, 3, 99 -106 (2000).
- [25] Mokmeli A, Asghari S. An investigation into the effect of anode purging on the fuel cell performance, International Journal of Hydrogen Energy 35, (2010), 9276-9282.
- [26] B. Belvedere, M. Bianchi , A. De Pascale, Experimental analysis of a cogenerative performance of a PEM fuel cell based energy system, Proceedings of ICAE 2011, 16-18 May 2011 - Perugia, Italy.

- [27] B. Belvedere, M. Bianchi, A. Borghetti, A. De Pascale, M. Di Silvestro, M. Paolon, DSP-Controlled Test Set-up for the Performance Assessment of an Autonomous Power Unit Equipped with a PEM Fuel Cell, Proceedings of the 2007 International Conference On Clean Electrical Power (ICCEP'07), art. No. 4272427, pp. 468-473.
- [28] R.L. Borup, J.R. Davey, F.H. Garzon, D.L. Wood, M.A. Inbody, Proceedings of the Fuel Cells Durability, first ed., Washington, DC, (2006), 21-42..
- [29] R.L. Borup, J.R. Davey, F.H. Garzon, D.L. Wood, M.A. Inbody, J. Power Sources 163 (2006) 76-81.
- [30] P. Meyers, R.M.S. Darling, The Electrochem. Soc. Meeting Abstracts, Abstract 1212, Paris, France, 2003.
- [31] S. Motupally, T.D. Jarvi, The Electrochem. Soc. 208th Meeting, Abstract, Los Angeles, CA, 2005.
- [32] C. Paik, T. Skiba, V. Mittal, S. Motupally, T. D. Jarvi, The Electrochem. Soc. 207th Meeting, Abstract 771, Quebec City, Canada, 2005.
- [33] T. Patterson, Effect of potential cycling on loss of electrochemical surface area of platinum catalyst in polymer electrolyte membrane fuel cell, in: AICHE National Conference, New Orleans, LA, 2002.
- [34] M.S. Wilson, F.H. Garzon, K.E. Sickafus, S. Gottesfeld, J. Electrochem. Soc. 140 (1993) 2872-2877.
- [35] P. Ascarelli, V. Contini, R. Giorgi, J. Appl. Phys. 91 (2002).
- [36] M.S. Wilson, F.H. Garzon, K.E. Sickafus, S. Gottesfeld, J. Electrochem. Soc. 140 (1993) 2872.
- [37] W. Li, M. Ruthkosky, M. Balogh, R. Makharia, S. Oh, Proceedings of the Fuel Cells Durability, first ed., Washington, DC, 2006, pp. 101-114.
- [38] Horky, K. Beverage, O. Polevaya, Y. Shi, Proceedings of the Fuel Cells Durability, first ed., Washington DC, 2006, pp. 133-150.
- [39] K.L. More, K.S. Reeves, 2005 DOE Hydrogen Program Review, Arlington, VA, 2005.

- [40] K. Duff, Stainless Steel alloys for Polymer Electrolyte Membrane (PEM) Fuel Cells, presentation, 2005, <http://www.chemistry.oregonstate.edu/courses/ch407h/CH407Hprojectkeeganfuelcellsteels.ppt>.
- [41] Larminie, A. Dicks, Fuel Cell Systems Explained, John Wiley & Sons Ltd., Chichester, England, 2003.
- [42] M. Li, S. Luo, C. Zeng, J. Shen, H. Lin, C. Cao, Corros. Sci., 46, 1369 (2004).
- [43] E. Gulzow, M. Schulze, N. Wagner, T. Kaz, R. Reissner, G. Steinhilber, A. Schneider, J. Power Sources, 86, 352 (2000).
- [44] L. Ma, S. Warthesen, D.A. Shores, J. New Mat. Electrochem. Systems, 3, 221 (2000).
- [45] G. Hubner, E. Roduner, J. Mater. Chem., 9, 409 (1999).
- [46] G. Escobedo, K. Schwiebert, K. Raiford, G. Nagarajan, F. Principe, Proceedings of the Fuel Cells Durability, first ed., Washington, DC, 2006, 83–100.
- [47] D.E. Curtin, R.D. Lousenberg, T.J. Henry, P.C. Tangeman, M.E. Tisack, J. Power Sources 131 (2004) 41–48.
- [48] F. Finsterwalder, M. Quintus, M. Schaloske, T. Guth, G. Frank, The Electrochem. Soc. 210th Meeting, Abstract 0485, Cancun, Mexico, 2006.
- [49] V.O. Mittal, H.R. Kunz, J.M. Fenton, Abstract 0448, The Electrochem. Soc. 210th Meeting, Cancun, Mexico, 2006.
- [50] G. H'ubner, E. Roduner, J. Mater. Chem. 9 (1999) 409–418.
- [51] S. Kundu, M.W. Fowler, L.C. Simon, S. Grot, J. Power Sources 157, (2006), 650–656.
- [52] V. Ramani, H.R. Kunz, J.M. Fenton, The Electrochem. Soc. Interf. 17–19, (2004), 45.
- [53] J. Yu, T. Matsuura, Y. Yoshikawa, M.N. Islam, M. Hori, Electrochem. Solid-State Lett. 8 (2005) ,A156–A158.
- [54] R. Baldwin, M. Pham, A. Leonida, J. McElroy, T. Nalette, J. Power Sources 29 (1990) 399–412.
- [55] S. Stucki, G.G. Scherer, S. Schagowski, E. Fisher, J. Appl. Electrochem., 28, 1041 (1998).

- [56] M. Wakizoe, H. Murata, H. Takei, Proc. Fuel Cell Seminar 2000, Portland, U.S.A., p. 487.
- [57] W. Liu, K. Ruth, G. Rusch, J. New Mat. Electrochem. Syst. 4 (2001), 227–231.
- [58] D.P. Davies, P.L. Adcock, M. Turpin, S.J. Rowen, J. Power Sources, 86, 237 (2000).
- [59] M. Schulze, T. Knori, A. Schneider, E. Gulzow, J. Power Sources, 127, 222 (2004).
- [60] S.-Y. Ahn, S.-J. Shin, H.Y. Ha, S.-A. Hong, Y.-C. Lee, T.W. Lim, I.-H. Oh, J. Power Sources, 106, 295 (2002).
- [61] B. Kienitz, H. Baskaran, B. Pivovar, T. Zawodzinski Jr., ECS Trans. 11 (2007) 777–788.
- [62] X. Cheng, Z. Shi, N. Glass, L. Zhang, J. Zhang, D. Song, Z.-S. Liu, H. Wang, J. Shen, J. Power Sources 165 (2007) 739–756.
- [63] J. Le Canut, R.M. Abouatallah, D.A. Harrington, J. Electrochem. Soc. 153 (2006) A857–A864
- [64] A. Rodrigues, J.C. Amphlett, R.F. Mann, B.A. Peppley, P.R. Roberge, Proceedings of the 32nd Intersociety Energy Conversion Engineering Conference, IECEC-97 (1997) 768–773.
- [65] D.D. Penta, K. Bencherif, Q. Zhang, M. Sorine, Proceedings of the 2006 IEEE Int. Conference on Control Applications, Munich, Germany, 2006.
- [66] Z. Qi, Proceedings of the Fuel Cells Durability, first ed., Washington, DC, (2006), 163–190.
- [67] Z. Liu, L. Yang, Z. Maa, W. Zhuge, Y. Zhang, L. Wang, J. Power Sources 157, (2006), 166–176.
- [68] D.P. Wilkinson, J. St-Pierre, PEM fuel cell durability, in: W. Vielstich, H. Gasteiger, A. Lamm (Eds.), Handbook of Fuel Cells – Fundamentals, Technology and Applications, Fuel Cell Technology and Applications, vol. 3, John Wiley and Sons, 2003.
- [69] T. van Nguyen, M.W. Knobbe, J. Power Sources 114 (2003) 70–79.

- [70] T.W. Patterson, R.M. Darling, *Electrochem. Solid-State Lett.* 9, (2006), A183–A185.
- [71] M. Saito, K. Hayamizu, T. Okada, *J. Phys. Chem.* 109, (2005), 3112–3119.
- [72] M. Sundaresan, R.M. Moore, *J. Power Sources* 145 (2005) 534–545.
- [73] J. Zhang, Z. Xie, J. Zhang, Y. Tang, C. Song, T. Navessin, Z. Shi, D. Song, H. Wang, D.P. Wilkinson, Z.S. Liu, S. Holdcroft, *J. Power Sources* 160 (2006) 872–891.
- [74] E. Cho, J. Ko, H.Y. Ha, S. Hong, K. Lee, T. Lim, I. Oh, *J. Electrochem. Soc.* 150 (2003) A1667–A1670.
- [75] A. Pesaran, G.-H. Kim, J. Gonder, *Proceedings of the Fuel Cells Durability*, first ed., Washington, DC, (2006), 205–227.
- [76] S. He, M.M. Mench, *J. Electrochem. Soc.* 153 (9) (2006) A1724–A2173.
- [77] C.H. Lee, H.B. Park, Y.M. Lee, R.D. Lee, *Ind. Eng. Chem. Res.* 44 (2005) 7617–7626, *Sources* 165 (2007) 739–756.
- [78] R.K. Ahluwalia, X. Wang, *J. Power Sources* 162 (2006) 502–512.
- [79] L. Mao, C.-Y. Wang, *J. Electrochem. Soc.* 154 (2007) B139–B146.
- [80] A.S. Arico, A. Stassi, E. Modica, R. Ornelas, I. Gatto, E. Passalacqua, V. Antonucci, *ECS Trans.* 3 (2006) 765–774.
- [81] Y. Song, H. Xu, Y. Wei, H.R. Kunz, L.J. Bonville, J.M. Fenton, *J. Power Sources* 154 (2006) 138–144.
- [82] W. Bi, T.F. Fuller, Abstract 395, *The Electrochem. Soc.*, 212th ECS Meeting, Washington, DC, 2007
- [83] I. Manke, N. Kardjilov, A. Haibel, C. Hartnig, M. Strobl, A. Rack, A. Hilger, J. Scholta, W. Lehnert, W. Treimer, S. Zabler, J. Banhart, *DGZfPBerichtsband 94-CD*, 2005.
- [84] T.V. Nguyen, R.E. White, *J. Electrochem. Soc.* 140 (1993) 2178–2186.
- [85] N.E. Vanderborgh, J.R. Huff, J. Hedstrom, *IEEE CH2781-3/89/0000-163* (1989) 1637–1640.
- [86] Y. Sone, P. Ekdunge, D. Simonsson, *J. Electrochem. Soc.* 143 (1996) 1254.

- [87] Y. Wang, C.-Y. Wang, *Electrochim. Acta* 51 (2006) 3924–3933.
- [88] S. Kim, M.M. Mench, *J. Power Sources* 174 (2007) 206–220.
- [89] F. Kagami, F. Ogawa, Y. Hishinuma, T. Ghikahisa, *Fuel Cell Seminar 2002*, Palm Springs, USA, 2002, p. 239.
- [90] G. Li, P.G. Pickup, *Electrochem. Solid-State Lett.* 9 (2006) A249–A251.
- [91] X. Huang, R. Solasi, Y. Zou, M. Feshler, K. Reifsnider, D. Condit, S. Burlatsky, T. Madden, *J. Polym. Sci. Part B Polym. Phys.* 44 (16) (2006), 2346–2357.
- [92] D.A. McKay, W.T. Ott, A.G. Stefanopoulou, Modeling, parameter identification, and validation of reactant water dynamics for a fuel cell stack, in: *Proceedings of the IMECE, ASME Int. Mech. Eng. Congress & Exposition*, 2005.
- [93] W. He, G. Lin, T.V. Nguyen, *AICHE J.* 49 (2003) 3221–3228.
- [94] B.A. Dipierno, M.H. Fronk, US Patent 6,103,409 (2000).
- [95] A.Z. Weber, R.M. Darling, J. Newman, *J. Electrochem. Soc.* 151 (10) (2004) A1715–A1727.
- [96] A. Turhan, K. Heller, J.S. Brenizer, M.M. Mench, *J. Power Sources* 160 (2006) 1195–1203.
- [97] J.J. Kowal, A. Turhan, K. Heller, J.S. Brenizer, M.M. Mench, *J. Electrochem. Soc.* 153 (2006) A1971–A1978.
- [98] S. Ge, C.-Y. Wang, *J. Electrochem. Soc.* 154 (2007) B998–B1005.
- [99] T. Nguyen, J. Hedstrom, N. Vanderborgh, in: R.E. White, A.J. Appleby (Eds.), *The Electrochem. Soc. Softbound Proceedings Series PV 89–14* (1989) 39.
- [100] T.E. Springer, J. Zawodzinski, S. Gottesfeld, in: R.E. White, M.W. Verbrugge, J.F. Stockel (Eds.), *The Electrochem. Soc. Softbound Proceedings Series PV 91–10* (1991) 209.
- [101] P.J. Schutz, in: R.E. White, A.J. Appleby (Eds.), *The Electrochem. Soc. Softbound Proceedings Series PV 89–14* (1989) 87.
- [102] R. Mukundan, Y.S. Kim, T. Rockward, J.R. Davey, B. Pivovar, D.S. Hussey, D.L. Jacobson, M. Arif, R. Borup, *ECS Trans.* 1 (2007) 543–552.

- [103] Y. Hishinuma, T. Chikahisa, F. Kagami, T. Ogawa, *JSME Int. J. B* 47 (2004), 235–241.
- [104] Gou J, Pei P, Wang Y. The dynamic behavior of pressure during purge process in the anode of a PEM fuel cell. *J Power Sources* 2006;162:1104e14.
- [105] Strasser k. The design of alkaline fuel cells. *J Power Sources* 1990;29:149e66.
- [106] J. Zhang, Y. Tang, C. Song, J. Zhang, H. Wang, *J. Power Sources* 163 (2006) 532.
- [107] X. Cheng, J. Zhang, Y. Tang, C. Song, J. Shen, D. Song, J. Zhang, Hydrogen crossover in high-temperature PEM fuel cells, *J. of Power Sources* 167 (2007) 25–31.
- [108] A. Collier, H. Wang, X. ZiYuan, J. Zhang, D.P. Wilkinson, *Int. J. Hydrogen Energy* 31 (2006) 1838.
- [109] J. Yu, T. Matsuura, Y. Yoshikawa, M.N. Islam, M. Hori, *Electrochem. Solid-State Lett.* 8 (2005) A156–A158.
- [110] M. Inaba, T. Kinumoto, M. Kiriake, R. Umebayashi, A. Tasaka, Z. Ogumi, *Electrochim. Acta* 51 (2006) 5746.
- [111] K. Teranishi, K. Kawata, S. Tsushima, S. Hirai, *Electrochem. Solid-State Lett.* 9 (2006) A475–A477.
- [112] Y. Song, J.M. Fenton, H.R. Kunz, L.J. Bonville, M.V. Williams, *J. Electrochem. Soc.* 152 (2005) A539–A544.
- [113] T. Sakai, H. Takenaka, E. Torikai, *J. Electrochem. Soc.* 133 (1986) 88.
- [114] P. Rama, R. Chen, R. Thring, *IMEchE Part A: J. Power Energy* 220 (2006), 535.
- [115] V. Ramani, H.R. Kunz, J.M. Fenton, *J. Membr. Sci.* 266 (2005) 110.
- [116] Y. Si, H. Russell Kunz, J.M. Fenton, *J. Electrochem. Soc.* 151 (2004) A623–A631.
- [117] H.L. Yeager, *ACS Symp. Ser.* 180 (1982) 41.
- [118] T.D. Gierke, W.Y. Hsu, *ACS Symp. Ser.* 180 (1982) 283.
- [119] Z. Ogumi, Z. Takehara, S. Yoshizawa, *J. Electrochem. Soc.* 131 (1984) 769.
- [120] Z. Ogumi, T. Kuroe, Z.-i. Takehara, *J. Electrochem. Soc.* 132 (1985) 2601.
- [121] K. Broka, P. Ekdunge, *J. Appl. Electrochem.* 27 (1997) 117.

- [122] K. Yasuda, A. Taniguchi, T. Akita, T. Ioroi, Z. Siroma, *Phys. Chem. Chem. Phys.* 8 (2006) 746.
- [123] Zhang, B.A. Litteer, W. Gu, H. Liu, H.A. Gasteiger, *J. Electrochem. Soc.* 154 (2007) B1006.
- [124] E.F. Holby, W. Sheng, Y. Shao-Horn, D. Morgan, *Energy Environ. Sci.* 2 (2009) 865.
- [125] T.T. H. Cheng*, E. Rogers, A. P. Young, S. Ye, V. Colbow, S. Wessel, Effects of crossover hydrogen on platinum dissolution and agglomeration, *J. of Power Sources* ,96 ,(2011) ,7985-7988.
- [126] R.S. Yeo, J. McBreen, *J. Electrochem. Soc.*,126 ,(1979),1682.
- [127] A.Z. Weber, J. Newman, *J. Electrochem. Soc.* 151 (2004) A311–A325.

Chapter 5

ANODIC EXHAUST MANAGEMENT: ANALISYS AND OPTIMIZATION

In this chapter an investigation on the performance of the commercial PEMFC, installed in the developed IES, taking into account the anodic exhaust management and its effects on the flooding phenomenon, is described.

To address the problem of flooding, it is necessary to run periodically the purge process of the FC. Indeed, in this study the periodic anodic purge process in dead-end mode has been investigated. This operation is performed by opening a particular control valve, the Outlet Control Valve (OCV), located along the anodic exhaust line.

The purge process has been analyzed at different FC power output levels. For each FC power level the optimized behavior of the FC operation was found, by regulating the time of flooding.

The aim of this analysis is to optimize the purge process to reduce the amount of hydrogen discharged with water, in order to increase the FC efficiency.

Furthermore, an investigation on the benefits in terms of fuel utilization factor and costs, resulting from optimization of the FC purge process, is shown.

It should be noted that this analysis is based on the assumption that the cell is a “black box”, it is not broken down into its individual components, but it is a real system in its own right (the “FC -system”), inserted within the test IES in which acting as energy source. Therefore, it was not possible to investigate the individual components of the cell (such as single cells stack components, membrane, GDL, bipolar plates, etc.), so only "global" indexes and algorithms, able to describe the behavior of the PEMFC, seen as an element of the IES system, were determined.

5.1 THE HYDROGEN PURGING: MOTIVATION, LIMIT AND OPTIMIZATION STRATEGIES

There are two different schemes for supplying hydrogen at the anode side. First, hydrogen may be supplied in the so-called *dead-end mode*. In this mode, hydrogen stoichiometry is equal to 1 or a slightly higher, i.e. hydrogen is supplied at the exact rate as the fuel cell stack needs (Figure 5.1).

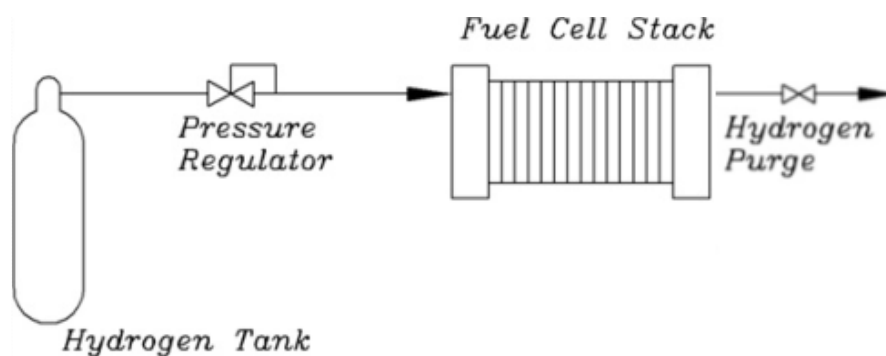


Figure 5.1: Dead end mode: layout.

In the second scheme, which is called *flow-through mode*, hydrogen may be supplied in excess (Figure 5.2). A recirculation mode may also be used in the case of pure hydrogen. In this case the unused gas is not wasted, but returned for consumption back to the stack inlet by means of a pump or an ejector. In this case, the stack may operate at the stoichiometric ratio much higher than 1.

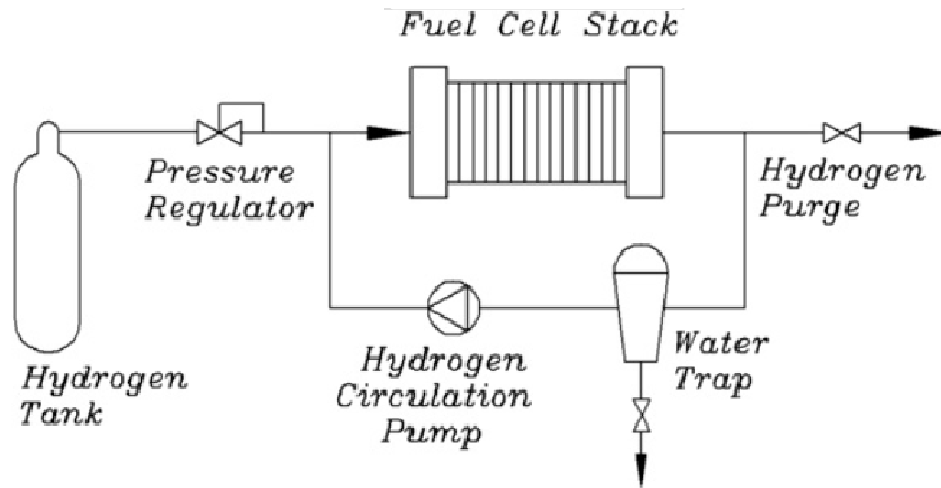


Figure 5.2: Flow-through mode: layout.

To prevent accumulation of inert and impurities, which lead to output voltage loss, the purge process should be periodically run in a FC energy system.

The purge process has a fundamental role on the stability of the power supplied by the FC [1]. Mokmeli et al. [2] showed that the amount and the concentration of impurities in the FC increases with time in absence of purge. Due to this increasing accumulation of impurities, the stack is characterized by loss of voltage increasing over time.

To operate the purging, an outlet control valve (OCV) is usually installed downstream of the FC stack, both for the dead-end and flow-through layout. This valve is kept closed until the purge is required. The purge occurs during the entire OCV opening time window. During this time, in addition to impurities, excess water and inert gas, also a quantity of fuel is discharged and thus it is not used by the FC electrochemical reactions. The amount of not-reacted fuel varies with the amount of time between two consecutive purges, for given opening time of the OCV.

The two main control parameters of the periodic purge process (as shown qualitatively in Figure 5.3) are:

- the time between two consecutive purges, named here T_{fl} , equal to the time interval in which the OCV is closed and, thus, water accumulates in the FC anodic side, causing flooding;
- the purge time, T_{pu} , during which the OCV is open and thus impurities, inert gases and excess water are evacuated from the FC.

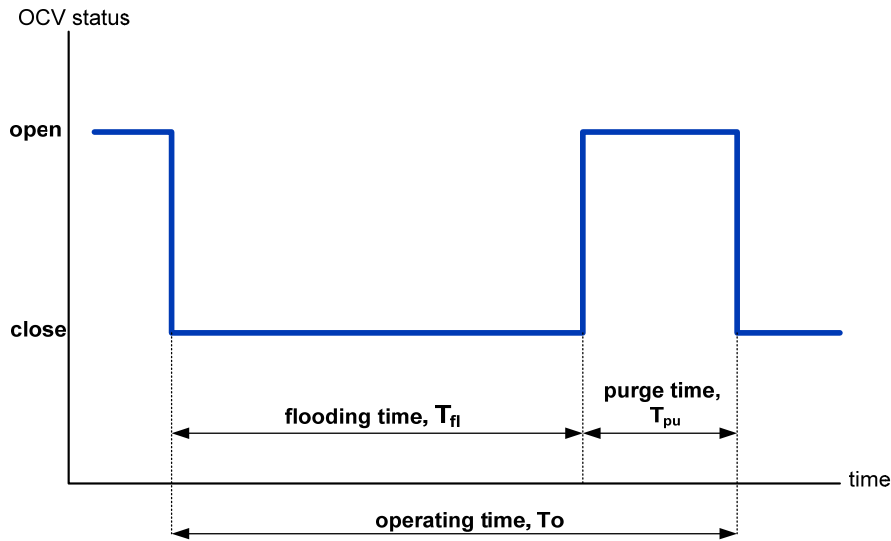


Figure 5.3: Characteristic time settings of purge process.

The purge process setting typically consists in programming these two parameters as function of the FC voltage or as function of time [2]. The optimum flooding time is a compromise between minimum hydrogen waste and minimum voltage loss.

The first approach suggested by Strasser [3] is called "purge controlled by the current". It is based on the observation that the current varies when the FC accumulates both impurities and inert gases and the phenomenon of flooding starts [1].

In fact, in this approach, the reactants are streamed through the stack in opposite directions in a cascading manner, inert gases are collected in the last step of the cascading system, a cell called gas-space cell. The load current in the gas-space cell changes when the inert gas concentration in the cell increase. A current sensor measure the difference between the gas-space cell and another one used as reference, when the difference increase over a defined value, an electronic device activates the OCV opening [3]. This approach is an intelligent method and the hydrogen waste may be minimized but, the complexity and the structural changes due to the connection configuration are the most disadvantages of this method [2].

The second purge programming approach is based, instead, on the setting of the OCV characteristic times, independently on the FC operating conditions.

A simplified way to realize the purging process using this second approach consists in assuming constant values for both T_{pu} and T_{fl} , so the purge could be thought as a periodical process (Figure 5.4) [1]. The values of these two parameters should be chosen as a tradeoff between the minimization of amount of discharged H_2 and of the voltage loss of the FC, resulting in an improvement in terms of fuel utilization.

Finally, the purge can be operated when the stack voltage equals a predetermined threshold value, with the aim to protect and preserve the longevity and performance of the FC. The amount of purge time must be such as to allow the recovery of the voltage loss.

Figure 5.4 shows the degradation of the FC stack voltage during the time when the OCV is closed (flooding time, T_{fl}). The flooding time can be divided into two parts. In the first, the stack voltage is constant for a given value, which represents the absence of liquid water in the gas diffusion layers, and then the tension starts to decay. This effect is caused by the increasing water content in the FC, which compromises the correct occurrence of electrochemical reactions.

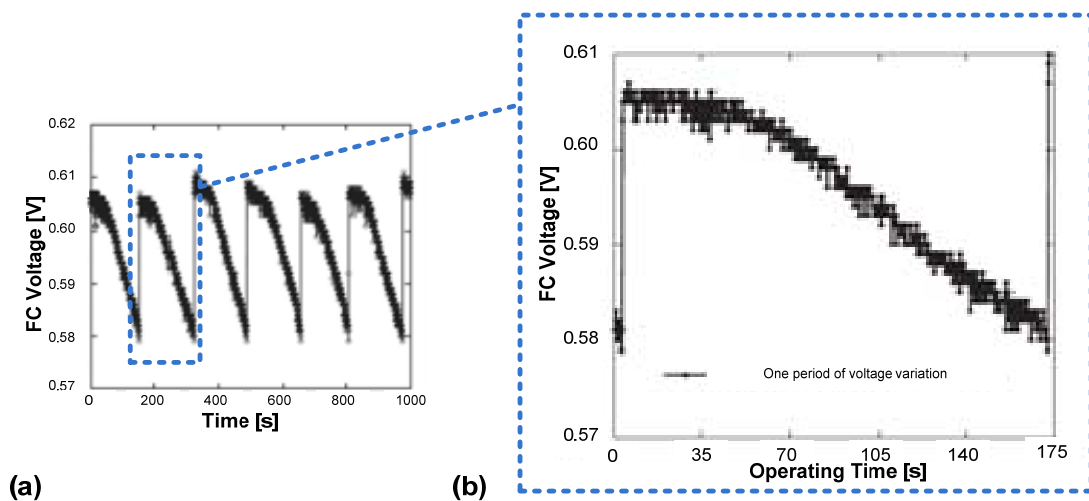


Figure 5.4: (a) FC stack voltage variation versus operating time; (b) one period of FC voltage variation.

In addition to the decay of the FC voltage, a fluctuation of H₂ pressure within the anode channels, linked to the dynamic process of purging, occurs. In fact, the purge is a dynamic process which could change the anode side pressure frequently [4]. Pressure wave transmission generated in the flow channels during the dynamic processes may lead to mechanical vibrations of the membrane electrode assembly (MEA) and accelerate its damaging [1].

Gou et al. [4] have analyzed the dynamic characteristic of pressure during the purge process using one-dimensional non-steady fluid simulation and experiments. They have introduced a new parameter, called *pressure swing*, which represents the top value of pressure variation at certain point in the channel during the purge process and actually it represents the mechanical attack of gas flow to the MEA in this transient process (Figure 5.4), showing that the shorter purge time results in the lower pressure drop along the anode channel far from the purge valve. Also this causes the pressure drop effect to be sensed in the shorter path of the anode. Moreover, they observed that the long flooding time causes the more voltage loss, while the shorter ones results in more hydrogen waste.

5.2 EXPERIMENTAL INVESTIGATION ON THE EFFECTS OF PURGING

An investigation on the flooding phenomenon and its effects on FC performance at different FC power output levels have been carried out. The stack used into the IES follow the dead-end layout, with the Outlet Control Valve (OCV) installed downstream of the FC (Figure 5.5).

The aim of this analysis is to optimize the purging process, to increase FC lifetime (linked with the flooding occurrence) and to reduce the amount of hydrogen (H_2) discharged with water, in order to increase the fuel utilization factor and FC efficiency. The OCV control strategy provided by the FC manufacturer is a simple logic in which the OCV opening time, T_{pu} , and the flooding time, T_{fl} , where kept constant, independently on the FC power output.

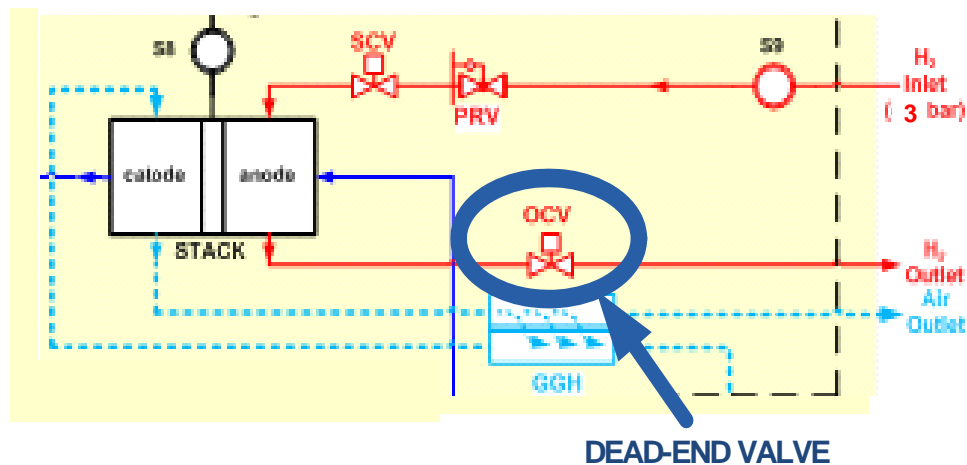


Figure 5.5: The OCV valve position in the IES layout.

Different FC power levels have been investigated, by analyzing the FC performance depending on the purge time, in order to find the corresponding optimum purge process time settings.

Figure 5.6 to Figure 5.10 show the experimental value of the FC voltage (blue line) and the H₂ mass flow rate (red line) versus time, during few consecutive purges (under the original strategy with constant values of $T_{pu}=2.5$ s and $T_{fl}=20$ s), for five different FC power values, equal to 500 W, 1500 W, 2500 W, 3500 W, and 4500 W, respectively.

The periodic OCV opening occurrence clearly induces a sudden increase of H₂ mass flow, measured at the FC anode inlet stream, which is not integrally absorbed by the electrochemical reactions. Indeed, the shown experimental trend of voltage undergoes a sudden drop when the OCV opening occurs. The experimental plots also show the decrease of the voltage due to flooding in the time period, T_{fl} , in which the OCV is closed.

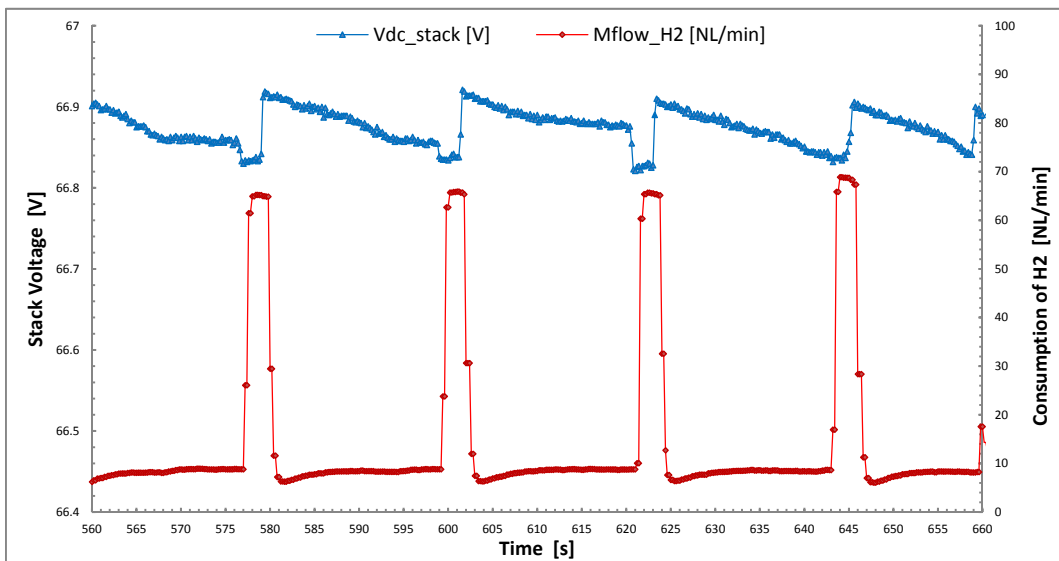


Figure 5.6: $P_{FC} = 500$ W; Voltage and H₂ mass flow VS time ($T_{pu} = 2.5$ s and $T_{fl} = 20$ s).

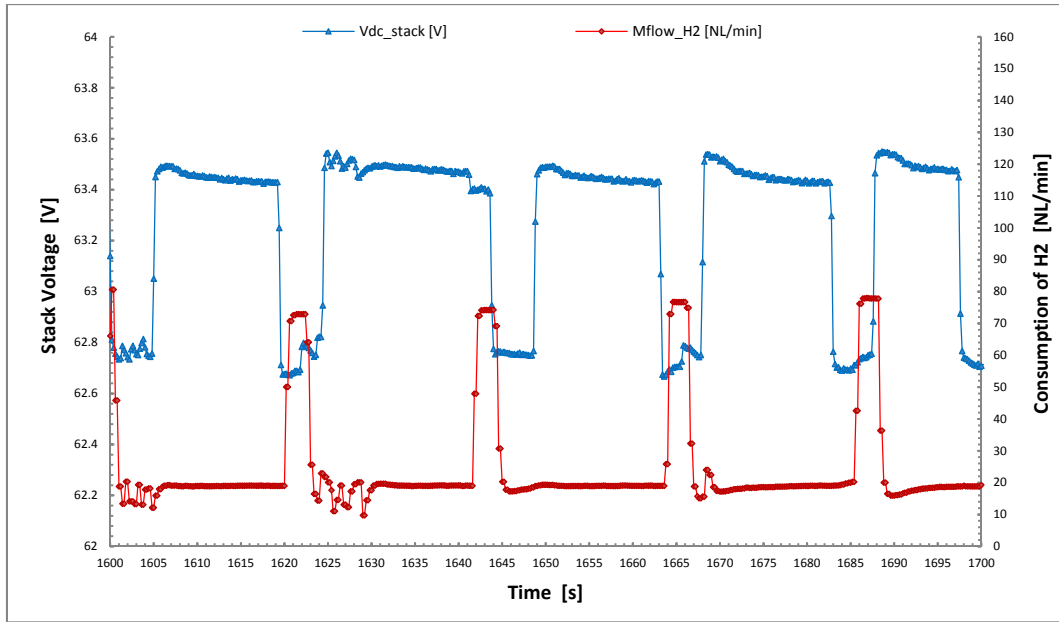


Figure 5.7: $P_{FC} = 1500 \text{ W}$; Voltage and H_2 mass flow VS time ($T_{pu} = 2.5 \text{ s}$ and $T_{fl} = 20 \text{ s}$).

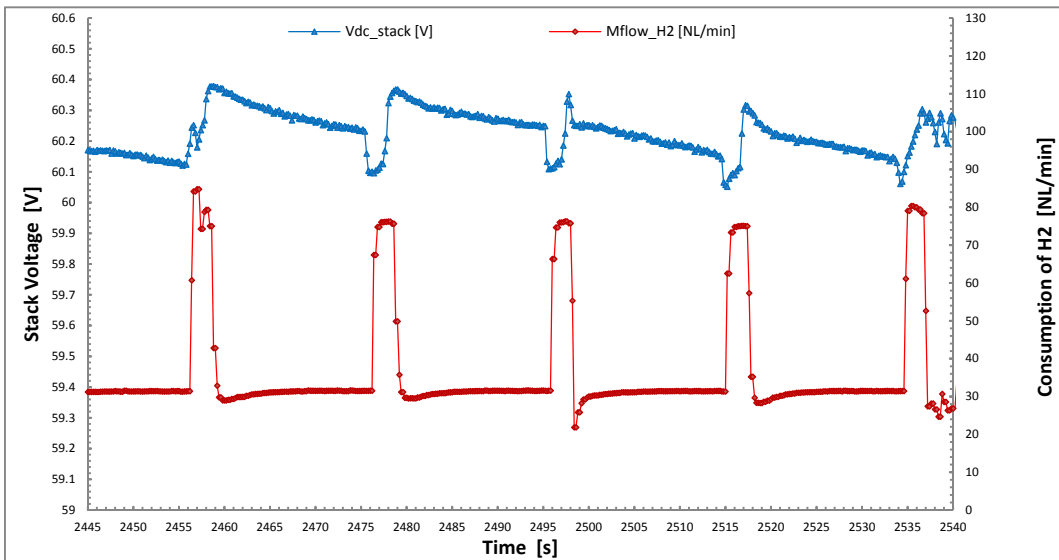


Figure 5.8: $P_{FC} = 2500 \text{ W}$; Voltage and H_2 mass flow VS time ($T_{pu} = 2.5 \text{ s}$ and $T_{fl} = 20 \text{ s}$).

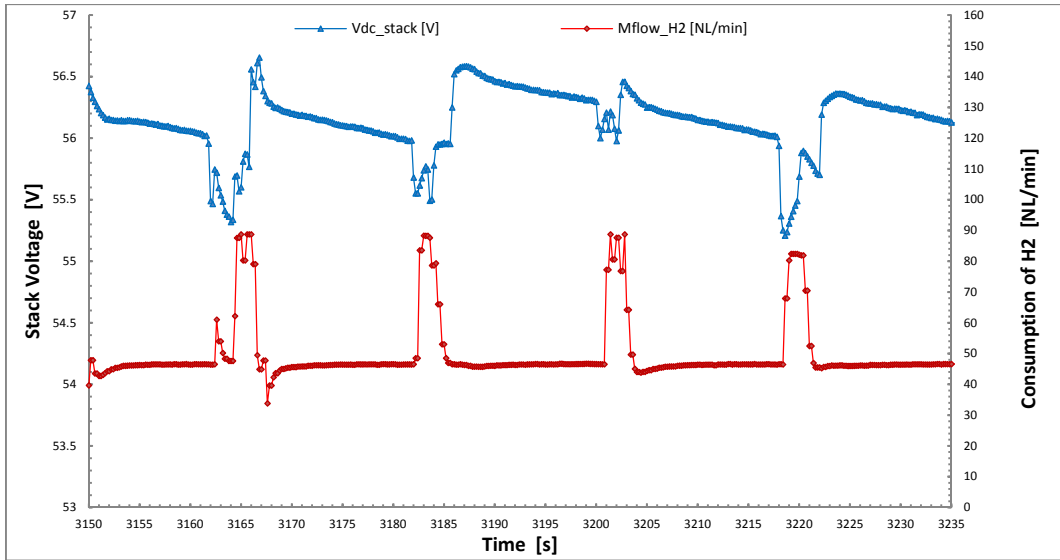


Figure 5.9: $P_{FC} = 3500 \text{ W}$; Voltage and H_2 mass flow VS time ($T_{pu} = 2.5 \text{ s}$ and $T_{fl} = 20 \text{ s}$).

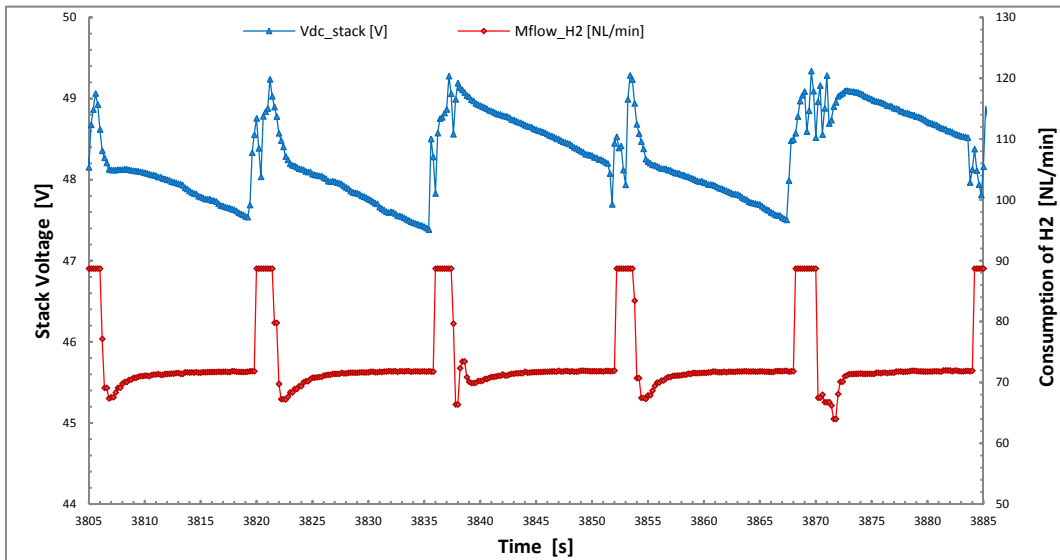


Figure 5.10: $P_{FC} = 4500 \text{ W}$; Voltage and H_2 mass flow VS time ($T_{pu} = 2.5 \text{ s}$ and $T_{fl} = 20 \text{ s}$).

5.2.1 PIECEWISE MODEL OF THE VOLTAGE DROP DUE TO FLOODING

Analyzing the FC voltage behavior during a single operating time, T_o (Figure 5.11), i.e. the time during which a flooding (T_{fl}) and its consecutive purge (T_{pu}) happen, it can identify three different phases:

1. during the flooding phase, when the OCV is closed, the FC voltage decrease due the water accumulation;
2. at the opening of the OCV, i.e. at the beginning of the purge time, the stack voltage undergoes a sharp drop. This behavior is related to the occurrence of a pressure drop of the H_2 stream within the stack (approximately decreasing from the value of 1.3 bar down to 1 bar).
3. finally, the voltage increase again during the recovery phase, due the low water content, and the closing the OCV.

Observing that the voltage versus time dependency in each of these phases can be linearized, a piecewise linear model of the FC voltage trend versus time has been developed (Figure 5.12).

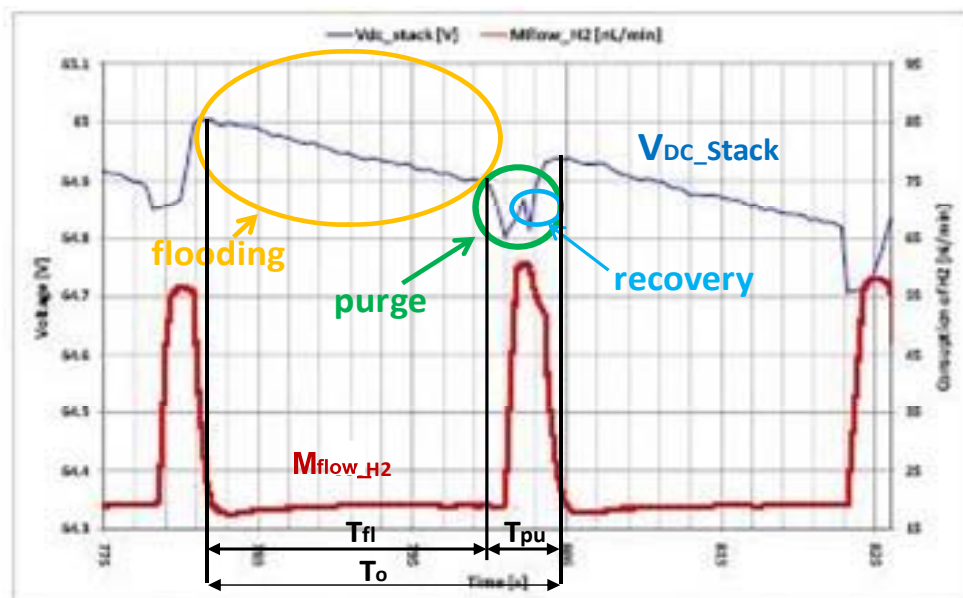


Figure 5.11: The FC voltage behaviour (blue line) and the H_2 flow rate (red line) during a single operating time, $T_o = T_{fl} + T_{pu}$, when P_{FC} is equals to a constant value.

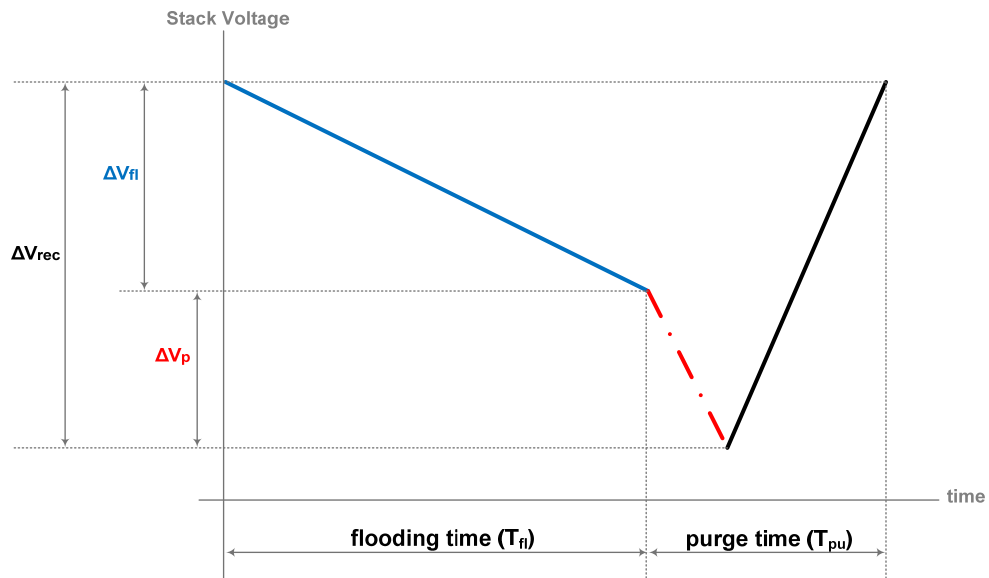


Figure 5.12: Linearized trend of voltage during a purge period; the flooding phase, ΔV_f (blue line), the pressure drop phase, ΔV_p (red line) and the recovery phase, ΔV_{rec} (black line).

5.3 OPTIMIZED PURGING STRATEGY

According to the study reported in [5], the purge process is optimized when the amount of voltage recovered at the time of OCV opening equals the voltage drop occurring between two consecutive purges. Generally, if the purge process is optimized, it can write:

$$\Delta V_{fl} + \Delta V_p = \Delta V_{rec} \quad (5.1)$$

where (Figure 5.12):

ΔV_{fl} is the FC voltage drop during the flooding (blue line);

ΔV_p is the sudden FC voltage drop related to the phenomenon of the OCV opening (red line);

ΔV_{rec} is the voltage recovered after the OCV opening, due to the elimination of the internally accumulated water (black line).

To optimize the purge process a new purge programming logic has been defined. In this new logic the values of purge parameters are not constant and assume different value according to the FC power output.

According the new model, the T_{fl} is defined imposing a maximum permissible FC voltage drop during flooding, ΔV_{max} , and keeping the T_{pu} value constant, equal to 2.5 s, so T_{fl} change with the FC power level.

The calculation of the optimum T_{fl} using the new purge logic is performed using a previously defined piecewise-linear model of the FC voltage drop versus time.

Assuming the quantities ΔV_p and ΔV_{rec} constant and ΔV_{fl} variable, eq. 5.1 can be rewritten as:

$$\alpha T_{fl} + \Delta V_p = \Delta V_{rec} \quad (5.2)$$

where α is the slope of the straight line modeling the FC voltage behavior during the flooding; T_{fl} is the flooding phase time, i.e. the time between two consecutive purges.

Thus, according to eq. 5.2, for each FC power levels, the optimized T_{fl} value has been obtained by solving the simple equation:

$$\alpha T_{fl} + \Delta V_{max} = 0 \quad (5.3)$$

The ΔV_{max} value has been fixed equal to the actual FC voltage drop during the flooding phase at FC maximum power (equal to 0.65 V).

Figure 5.13 shows, for a single operating period, T_o , the comparison between the actual behavior (continuous lines) of the FC stack voltage, estimated by piecewise-linear model and the "optimized" behavior (dotted lines) obtained by applying eq. (5.6). In particular, the blue lines indicate the voltage drop during the flooding; the red ones indicate the voltage drop due to the pressure drop at the OCV opening and the black lines indicate the voltage recovery.

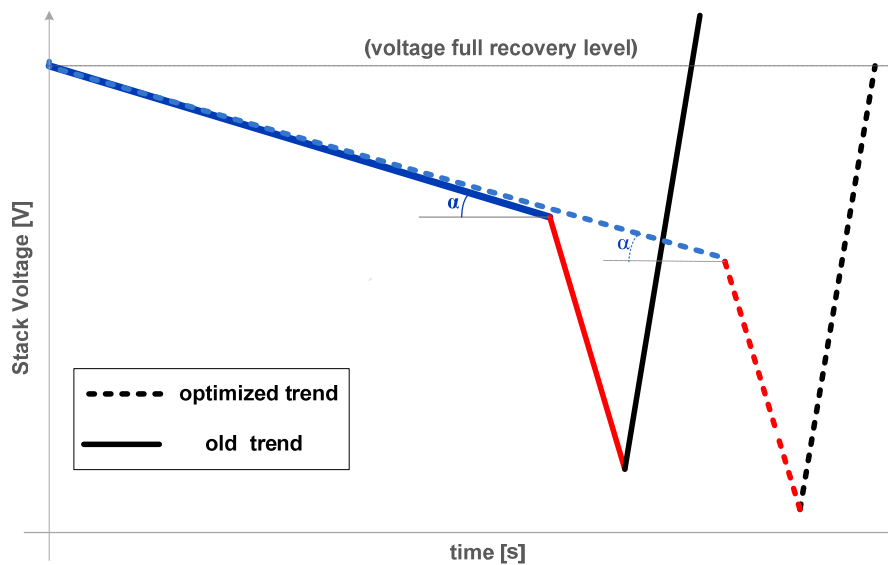


Figure 5.13: Original (continuous lines) and optimized (dotted lines) stack voltage trend during the flooding time (blue line) and the purge time (red and black lines), for a constant FC power output value.

5.3.1 APPLICATION OF THE OPTIMIZED STRATEGY

The optimized strategy algorithm has been used to optimize the purge process of five different FC operating points characterized by power output level equal to: 500 W; 1500 W; 2500 W; 3500 W; 4500 W, respectively.

Figure 5.14 shows the FC voltage drop behavior versus time, comparing the old with the new strategy. Using the old purge logic (continuous lines) with fixed T_{fl} , the final voltage drop at the end of the flooding time is constant and completely different from the new one, because the value of α varies with the FC working set point.

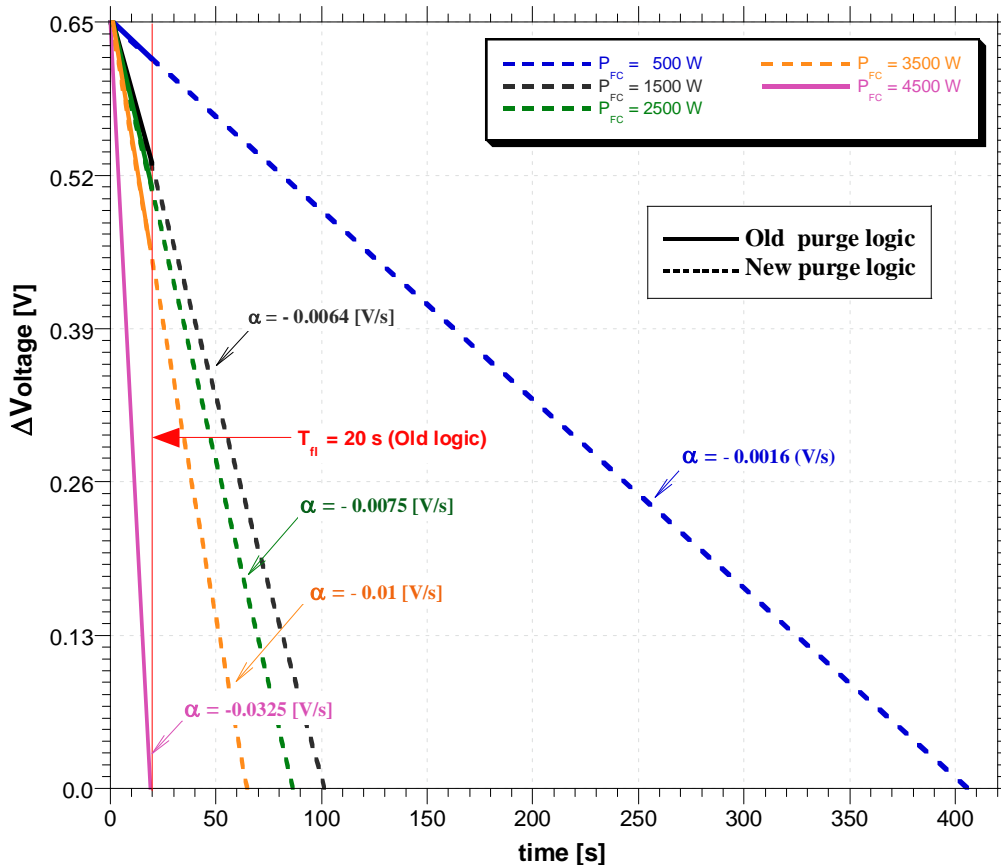


Figure 5.14: FC voltage drop VS time adopting old purge process settings (continuous lines) and new logic (dashed lines), for the five different FC power set points.

By using the new purge programming logic (Figure 5.14, dashed lines) the OCV time setting can be modulated depending on the FC power set point.

For a given FC power output set point, the optimized T_{fl} can be read on the x-axis, where the ΔV value (along the dotted lines, Fig. 5.14) reduces to zero.

The flooding time (T_{fl}) for each of the FC power level are compared in Table 5.1.

FC Power P_{FC} [W]	Old purge T_{fl} [s]	Optimized purge T_{fl+} [s]
500	20	406.2
1500	20	101.5
2500	20	86.6
3500	20	65
4500	20	20

Table 5.1: The flooding time (T_{fl}) versus FC power, old and new optimized purge process settings.

For each investigated FC power level, the corresponding optimum flooding time settings have been defined. The complete OCV management strategy require also the definition of the opening time; in this case the T_{pu} time has been kept constant, equal to 2.5 s.

Figure 5.15 to Figure 5.19 show, over a period T_0 , the comparison between the original FC stack voltages not optimized behavior (named “old time” designed with continuous line) with the optimized one (dotted line), for each of the five FC powers evaluated.

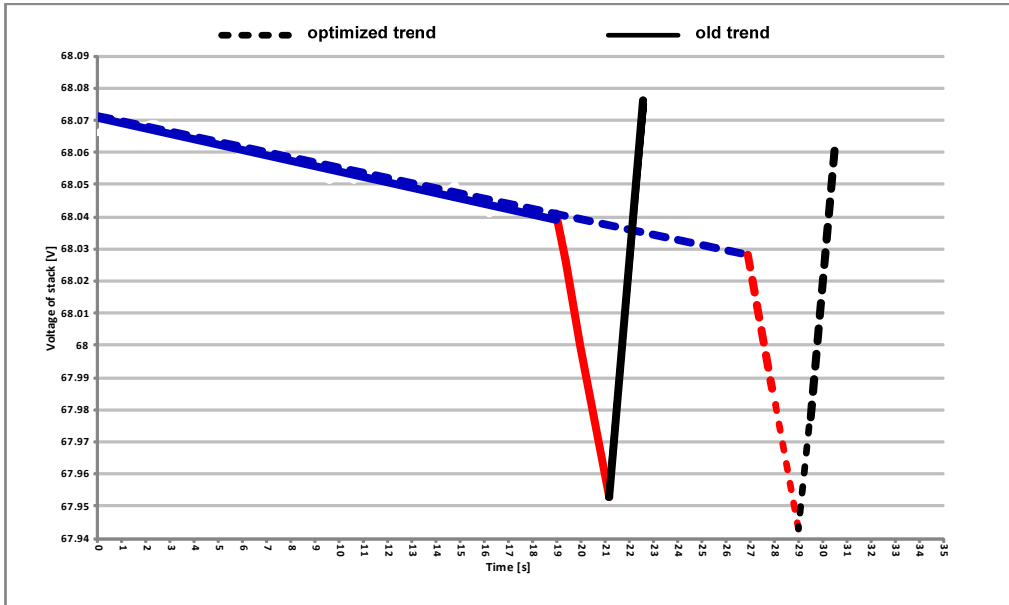


Figure 5.15: $P_{FC}=500$ W, original (continuous lines) and optimized (dotted lines) stack voltage.

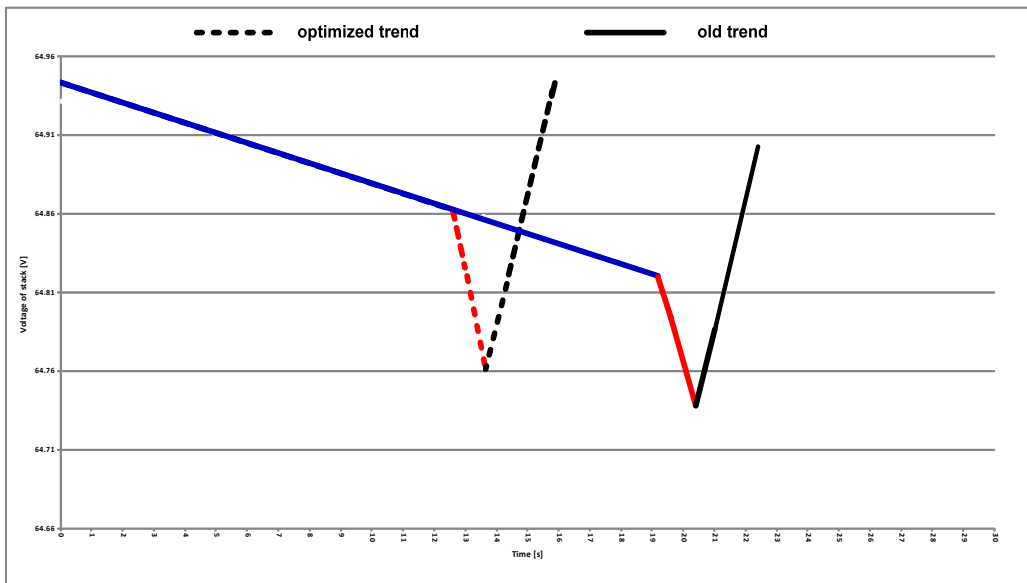


Figure 5.16: $P_{FC}=1500$ W, original (continuous lines) and optimized (dotted lines) stack voltage.

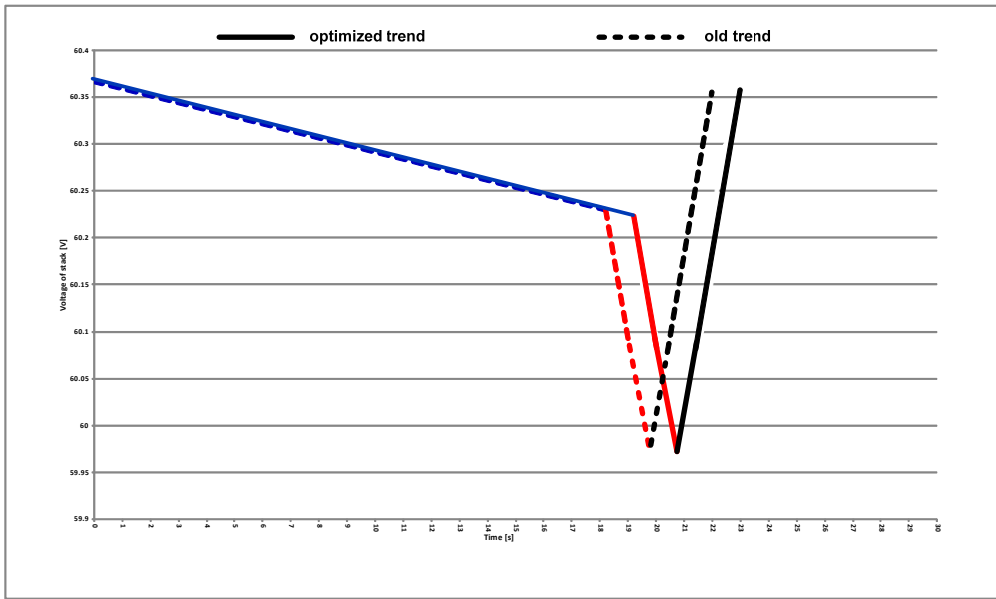


Figure 5.17: $P_{FC}=2500$ W, original (continuous lines) and optimized (dotted lines) stack voltage.

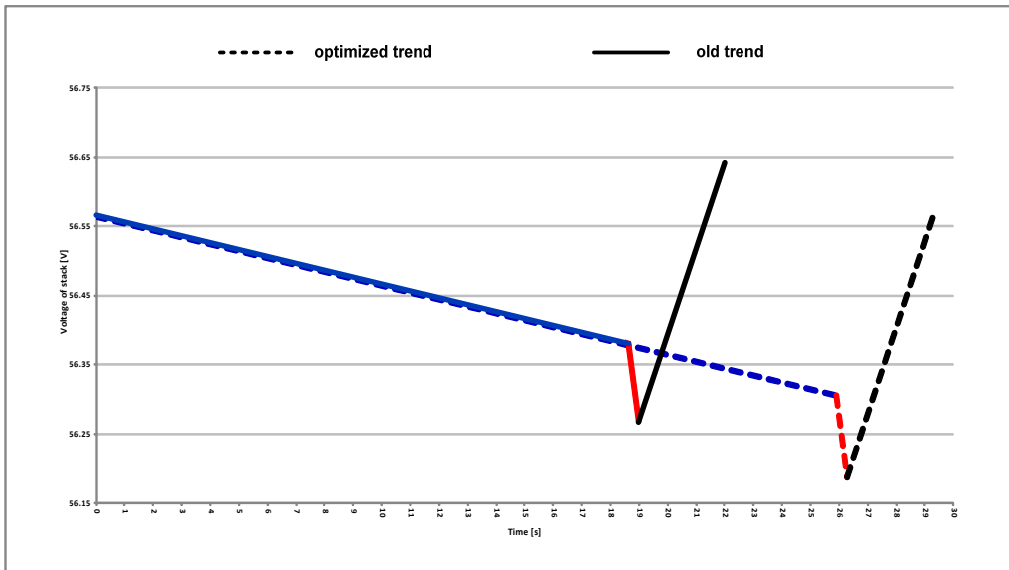


Figure: 5.18 $P_{FC}=3500$ W, original (continuous lines) and optimized (dotted lines) stack voltage.

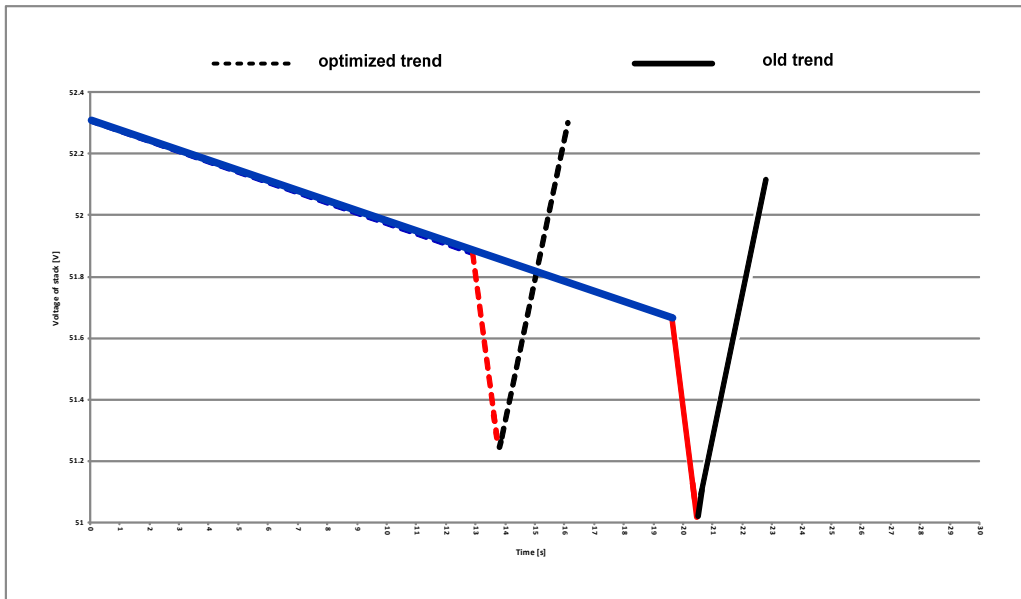


Figure 5.19: $P_{FC}=4500$ W, original (continuous lines) and optimized (dotted lines) stack voltage.

5.4 EFFICIENCY EVALUATION OF THE FC PURGE PROGRAMMING LOGIC

The purge process programming logic, currently implemented in the PEM-FC is a function of the time, as mentioned above. In particular, the original values of T_{n} and T_{pu} were set by the manufacturer and are respectively equal to 20 s and 2.5 s, both kept constant for each FC power output set point. This purge process time setting is optimized for the maximum FC power (4.5 kW), but it is very inefficient for low and medium FC power. This is due to considerable not-reacted H_2 loss during the opening time of the OCV.

To reduce the amount of not-reacted and expelled H_2 during the purge and, at the same time, safeguarding the FC internal components, it is necessary to improve the implemented purge logic, by optimizing the purge process time settings.

The aim of this purge process optimization is to increase the fuel utilization factor, U_f , defined as:

$$U_f = \frac{\dot{m}_i}{\dot{m}_{\text{H}_2}} \quad (5.4)$$

where:

- \dot{m}_i mass flow rate of H_2 that actually reacted, as defined by the Nernst equation;
- \dot{m}_{H_2} mass flow rate of the fuel into the system.

The Nernst equation defines the quantity of hydrogen consumed by the electrochemical reaction, in order to produce a specified current. As seen (Ch.3 – eq. 3.1) it can be written as:

$$\dot{m}_i = i_{\text{DC}} \frac{m_{\text{mol H}_2} \cdot N_{\text{cells}}}{2F} \quad (5.5)$$

where, it remeber:

- i_{DC} is the DC current generated by the FC stack;
- N_{cells} is the number of elementary cells that make up the FC stack (equals to 80 for the stack in study);

- $m_{mol_{H_2}}$ is the H₂ molar mass i.e. the mass (in grams) of one hydrogen mole, equals to 2.02 g/mole;
- $n_e = 2$ represents the number of electrons moles released on the external circuit. This value is related to the moles number of the reagent H₂ and to the reaction which occurs at the anode: $H_2 \rightarrow 2H^+ + 2e^-$;
- F is the Faraday constant, that represent the amount of charge per mole of electrons ($F=96,485$ C/mole of electrons).
- \dot{m}_{H_2} is the H₂ mass flow rate introduced to the anode side of the PEMFC, it can be also defined from the volumetric flow rate according to $\dot{m}_{H_2} = \dot{V}_{H_2} \cdot \rho_{H_2}$ in which ρ_{H_2} is the hydrogen density in normal conditions, equals to 0.0893 kg/m³.

The FC efficiency η_{FC} can be expressed as function of the utilization factor by simple substitution:

$$\eta_{FC} = \frac{P_{FC}}{\dot{m}_{H_2} LHV_{H_2}} = \frac{V_{Stack}}{N_{cells} \cdot V_{LHV}} U_f \quad (5.6)$$

where:

- P_{FC} is the power delivered by the FC;
- LHV_{H_2} is the lower heating value of hydrogen equals to 120,000 kJ/kg;
- V_{Stack} is the FC voltage, fundamental parameter that characterizes the efficiency of the electrochemical process;
- N_{cells} is the number of elementary cells that make up the FC stack;
- V_{LHV} is the equivalent of the fuel Lower Heating Value, in terms of voltage.

The synthetic value for the utilization factor, U_f and for the FC efficiency, η_{FC} , require the definition of reference value for both the H₂ mass flow rate, \dot{m}_{H_2} , and for the FC current, i_{DC} , via the measured input power, P_M , those value have been calculated by time-averaging the instantaneous values over a time window in which the FC set point was kept constant. This time period was chosen sufficiently long to include a high number of purges.

To compare the two purge strategy the savings of fuel input energy to the FC has been introduced; this has been evaluated using the following expression:

$$\Delta E = 1 - \left[\frac{E^+}{E} \right] \quad (5.7)$$

where:

$$E = \int_0^{\tau} m_{H_2} \cdot LHV \cdot dt \quad (5.8)$$

$$E^+ = \int_0^{\tau} m_{H_2}^+ \cdot LHV \cdot dt \quad (5.9)$$

E and E^+ are the mean fuel input energy introduced into the FC during the time, evaluated respectively in the old and new purge logic (with the + superscript).

Table 5.2 shows the values of P_M , \dot{m}_{H_2} and η_{FC} obtained using the old purge programming logic and the new one (values with the superscript +), for each of the five FC power set points, respectively.

FC power setting	Old purge logic			New purge logic			ΔE [-]
	P_M [W]	\dot{m}_{H_2} [kg/s]·10 ⁻⁵	η_{FC} [-]	P_M^+ [W]	$\dot{m}_{H_2}^+$ [kg/s]·10 ⁻⁵	η_{FC}^+ [-]	
500	2273	1.89	0.22	2942	2.45	0.29	30.0
1500	4167	3.47	0.36	4688	3.91	0.40	12.9
2500	6579	5.48	0.38	7576	6.31	0.42	7.6
3500	8975	7.48	0.39	9210	7.67	0.40	2.9
4500	11840	9.87	0.38	11840	9.87	0.38	0.0

Table 5.2: Comparisons between old and new purge logic in term of average fuel input power, H₂ mass flow rate, FC efficiency and energy saving.

The FC efficiency versus the power setting (Figure 5.20), increases using the optimization of the purge process (dotted red line). This increase occurs over the whole range of the power delivered by the fuel cell (500 - 4500 W), in particular at low and medium FC power, where the original purge logic was totally inefficient, as can be noted considering the improvement in fuel energy.

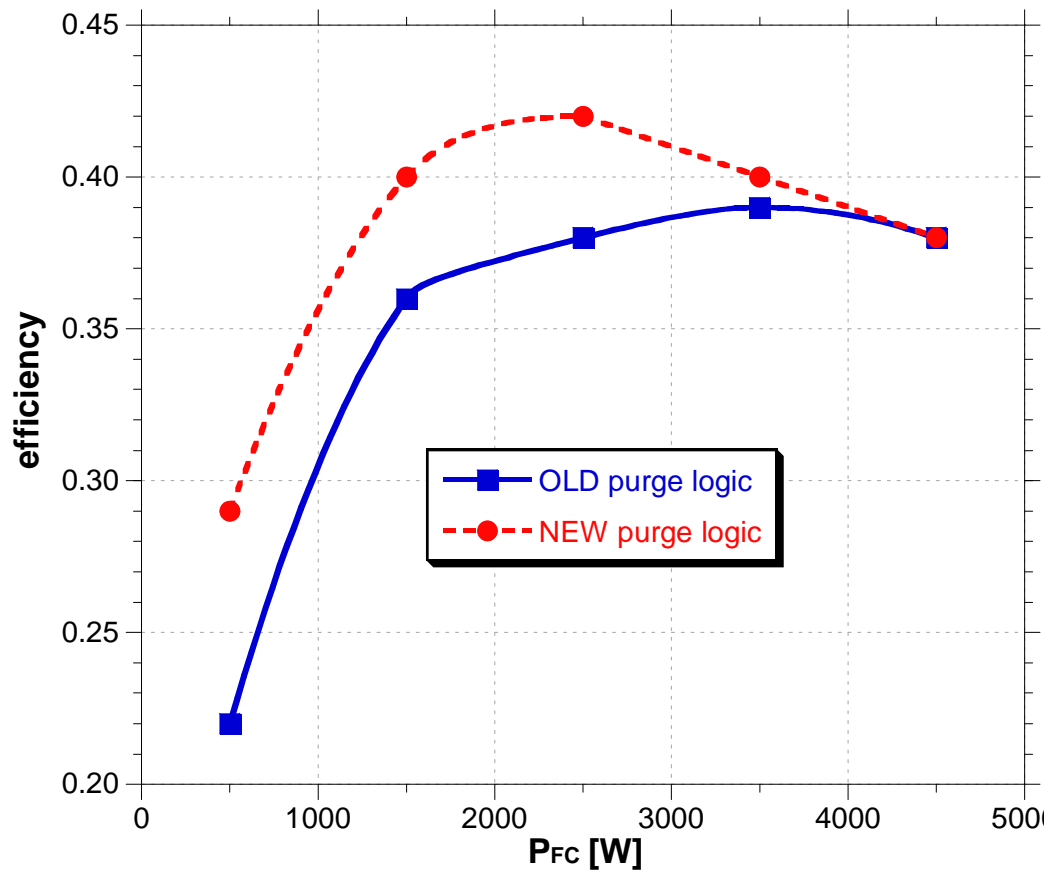


Figure 5.20: FC efficiency versus FC rated power with the original purge programming logic (continuous line) and the optimized one (dotted line).

The values of the coefficients U_f and U_f^+ , for each FC power levels are reported in Table 5.3.

FC Power P_{FC} [W]	Fuel utilization coefficient	
	Old purge U_f [-]	Optimized purge U_f^+ [-]
500	0.53	0.69
1500	0.77	0.86
2500	0.84	0.92
3500	0.90	0.93
4500	0.93	0.93

Table 5.3: Values of the fuel utilization coefficient using the old purge logic, U_f , and the new ones, U_f^+ , for each FC power levels.

The optimized strategy, regarding the U_f , is near optimal only for the medium-high load. In fact, in the range 2000-4000 W the fuel utilization factor is the same of the one at full load (design point for the FC). Instead, at lower load, even if a substantial improvement has been obtained, the value are considerably less (Figure 5.21).

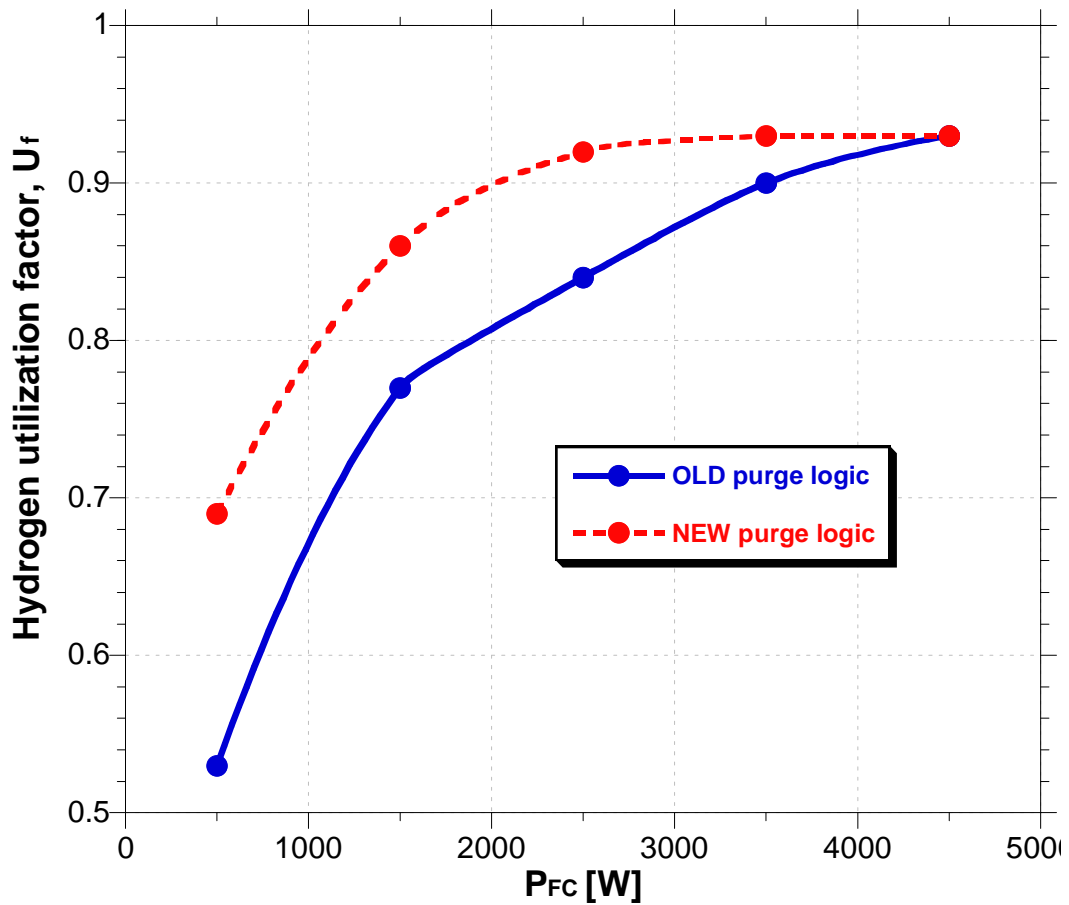


Figure 5.21: Fuel utilization factor versus FC rated power with the original purge programming logic (continuous line) and the optimized one (dotted line).

Further improvements in the fuel utilization factor are difficult to achieve by further modifying the purge logic at part (in the range 1500-3500 W) and lower load conditions. Moreover, the maximum U_f is not near the maximum theoretical value of 100%. This can be due to some undefined causes that will be explored into the following chapter.

5.5 ANALYSIS OF THE UTILIZATION COEFFICIENT

5.5.1 EFFECT OF THE FLOODING DURATION

In order to understand the causes of not-optimization at low loads obtained with the application of the new purge programming logic, an experimental campaign was conducted varying the flooding time, for each of the usual FC power level from 20 s up to the optimal value, as determined with the new purge programming logic (Table 5.4). The power for each point was maintained constant for a sufficient large number of purges.

P_{FC} [W]	ΔT_{fl} [s]					T_{fl_opt} [s]
4500	-	-	-	-	-	20
3500	20	40	60	-	-	65
2500	20	40	60	80	-	86.6
1500	20	40	60	80	100	101.5

Table 5.4: The T_{fl} time steps assumed and the optimal ones, for each FC power level analyzed.

Analyzing the results of the campaign in term of U_f versus the flooding time, T_{fl} , and the FC power (Figure 5.22), it can be observed that, at medium loads U_f increases with T_{fl} and assume the maximum value at the optimal flooding time. Instead, at low loads, the maximum is reached for a T_{fl} minor of the optimal ones.

In order to understand the causes of the U_f behavior at low loads, the quantity of H_2 not-reacted, \dot{m}_{NR} (i.e. the amount of fuel that does not participate in the electrochemical reactions), must be analyzed.

The procedure for the calculation of the fuel utilization coefficient, U_f , described in the previous paragraph, is based on the assumption that the amount of not-reacted fuel entirely coincides with the amount of H_2 ejected during the purge time.

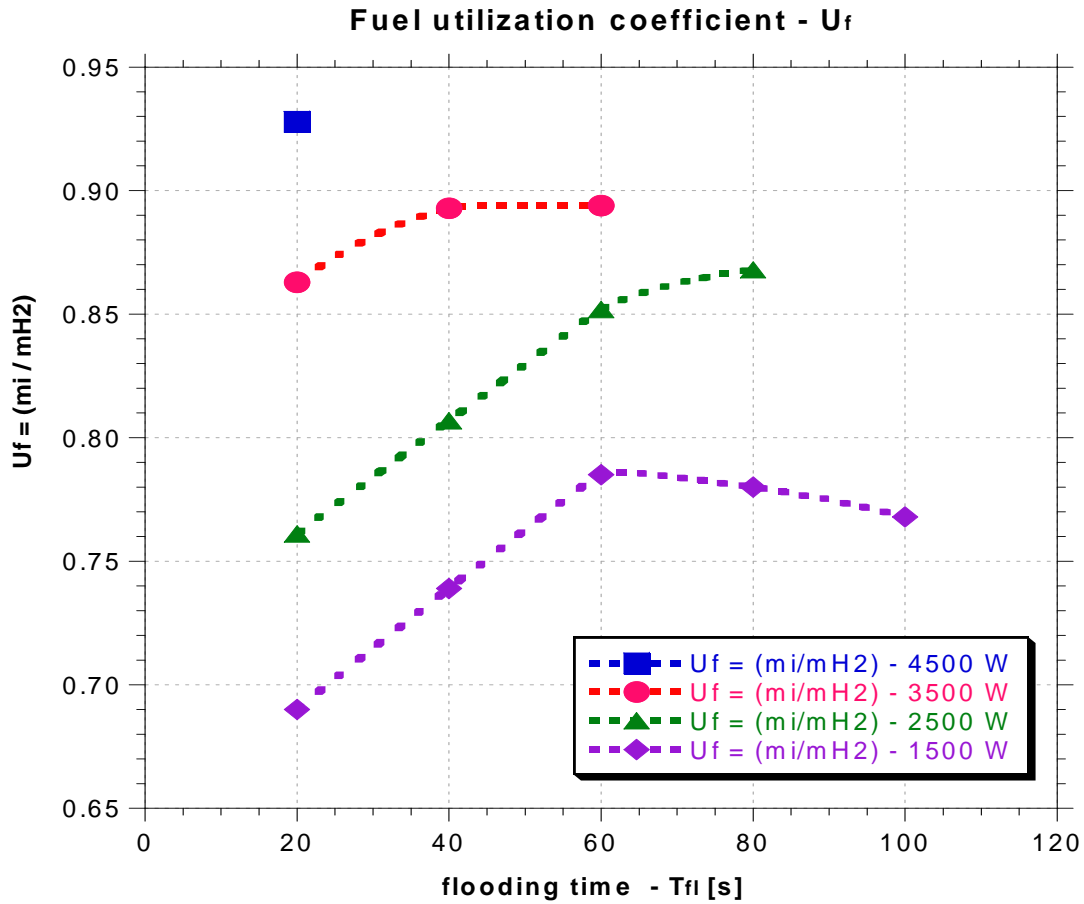


Figure 5.22: The fuel utilization factor, U_f , versus the flooding time and the FC power.

5.5.2 DEFINITION OF THE NOT-REACTED HYDROGEN FRACTION

Indeed there must be different way to disperse the hydrogen, so the amount of H_2 not-reacted (\dot{m}_{NR}), can be decomposed into two terms:

$$\dot{m}_{NR} = \dot{m}_{DE} + \dot{m}_A \quad (5.10)$$

where:

\dot{m}_{DE} quantity of H_2 not- reacted because ejected during the opening of the “dead-end” valve, OCV;

\dot{m}_A quantity of H_2 not-reacted for other causes, such as leakage through the membrane, through the seals, etc. (hereinafter referred to “other”), present in both the flooding time and the purge time.

Therefore, according to the above definitions, can be deduced immediately that the quantity of H₂ not-reacted during the flooding (when the OCV is closed) and the purge time, are, respectively, equal to the following amounts:

$$\dot{m}_{NR} = \begin{cases} \dot{m}_A & , t = T_{fl} \\ \dot{m}_{DE} + \dot{m}_A & , t = T_{OCV} \end{cases} \quad (5.11)$$

With the terms of eq. 5.10 the fuel utilization factor, U_f can be rewritten as:

$$U_f = \frac{\dot{m}_i}{\dot{m}_{H_2}} = \frac{\dot{m}_{H_2} - \dot{m}_{NR}}{\dot{m}_{H_2}} = \frac{\dot{m}_{H_2} - (\dot{m}_{DE} + \dot{m}_A)}{\dot{m}_{H_2}} = 1 - \frac{\dot{m}_{DE}}{\dot{m}_{H_2}} - \frac{\dot{m}_A}{\dot{m}_{H_2}}$$

or:

$$U_f = 1 - x_{DE} - x_A \quad (5.12)$$

Where the x terms are defined as the ratio between the mass flow rate of the not-reacted H₂ for the specified reason and the mass of fuel which is introduced in FC, more precisely:

$$x_{DE} = \frac{\dot{m}_{DE}}{\dot{m}_{H_2}} \quad (5.13)$$

is the H₂ not-reacted because ejected during the opening of the “dead-end” valve, OCV;

$$x_A = \frac{\dot{m}_A}{\dot{m}_{H_2}} \quad (5.14)$$

is the H₂ not-reacted fraction due to other causes.

5.5.3 ALGORITHM FOR THE EVALUATION OF THE NOT-REACTED HYDROGEN FRACTION

In order to determine the two fractions: X_{DE} (eq. 5.13) and X_{DA} (eq. 5.14), from the experimental data an algorithm has been developed.

For each operating condition characterized by the FC power, P_{FC} , constant and the flooding, T_{fl} also constant:

- A. The H_2 flow rate, $M_{flow_H_2}$, introduced to the anode side of the PEMFC (Figure 5.23), and DC current, i_{DC} , generated in the stack are acquired.

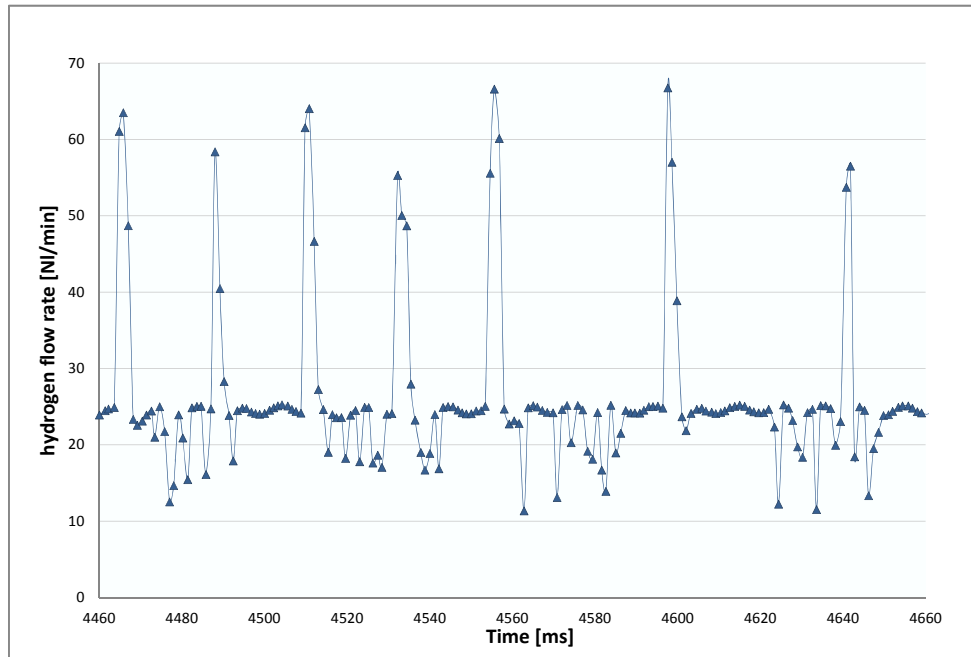


Figure 5.23: Plot of the measured hydrogen flow rate versus time.

- B. Identify the discrete instants of time when the OCV open and close, analyzing the flow rate plot (Figure 5.24). This define the discrete intervals time for both the "purge time", T_{pu} , and the "flooding time", T_{fl} ;

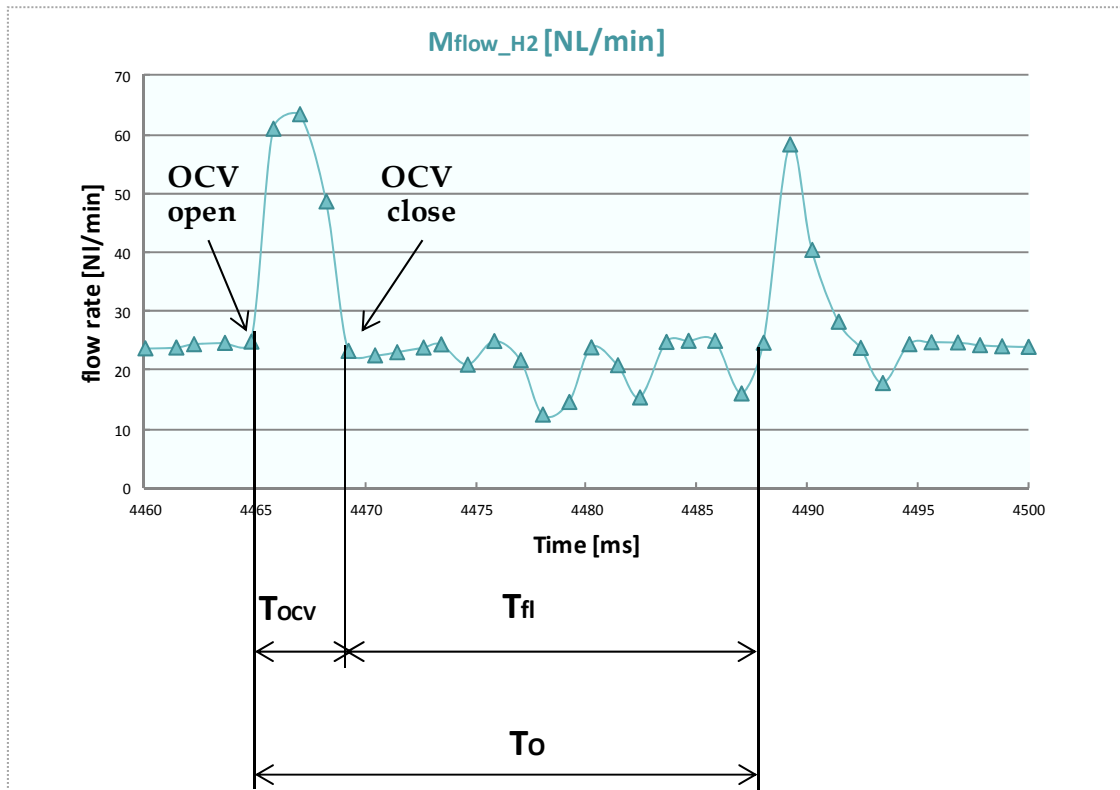


Figure 5.24: Determination of the real flooding time, T_{fl} , and the real purge time, T_{ocv} , during a single operating time, T_o .

- C. Calculate the number of purges carried for the fixed FC power output and T_{fl} .
- D. Evaluates the instantaneous amount of reacted hydrogen through the Nernst equation (eq. 5.5);
- E. Calculate the values of the H_2 mass flow rate reacted, \dot{m}_i (Figure 5.25, green line) and the values of the H_2 mass flow rate introduced, \dot{m}_{H_2} (Figure 5.25, blue line) averaging the instantaneous value over the purge and the flooding time-interval previously determined;

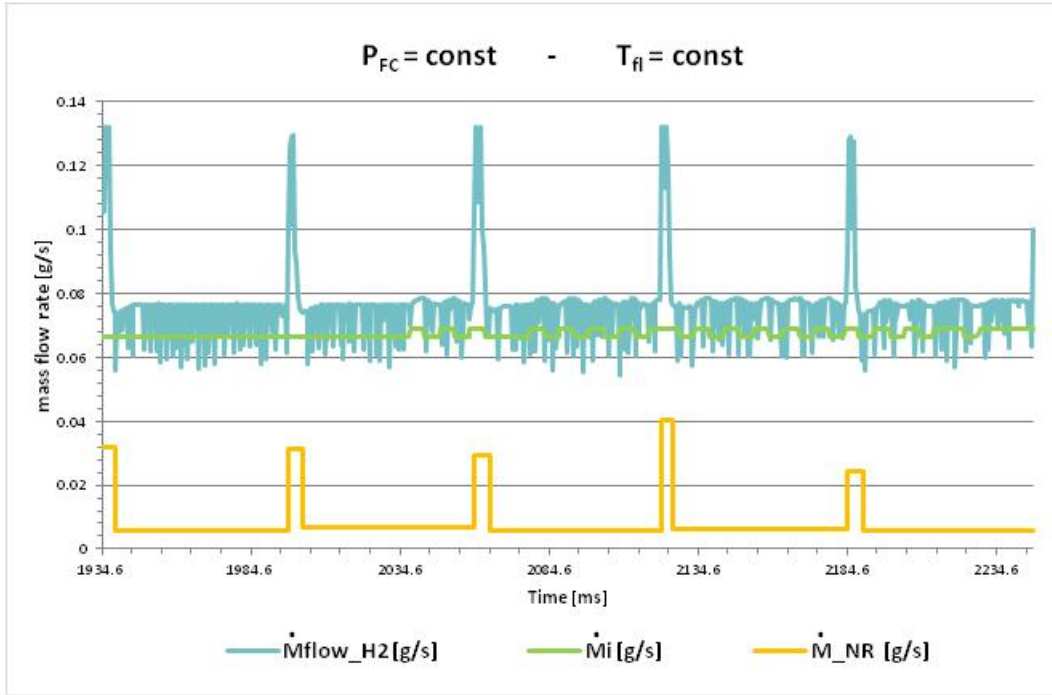


Figure 5.25: Algorithm application: trend of the mass flow rates of the H₂ introduced in the FC (blue line), actually reacted (green line) and not-reacted (orange line), versus time.

- F. Calculate the not-reacted H₂ mass flow rate, \dot{m}_{NR} (Figure 5.25, orange line) as the difference between the mass flow rate of the hydrogen introduced into the FC and the mass flow rate of the hydrogen that actively makes up in the electrochemical reactions:

$$\dot{m}_{NR} = \dot{m}_{H_2} - \dot{m}_i \quad (5.15)$$

- G. Calculate the average mass flow during the flooding time. This quantity obviously coincide with the amount of H₂ not-reacted due to "other" causes, since during the flooding the amount of H₂ purged through the OCV is clearly zero.

$$\dot{m}_{A_fl} = \dot{m}_A(T_{fl}) = \dot{m}_{NR}(T_{fl}) \quad (5.16)$$

- H. Determine the mass flow rate of the not-reacted H₂ due to "other", during the purge time, $\dot{m}_{A_OCV} = \dot{m}_A(T_{OCV})$, as the average of the mass flow of the purge under examination and the one of the previous one (Figure 5.26, purple line).

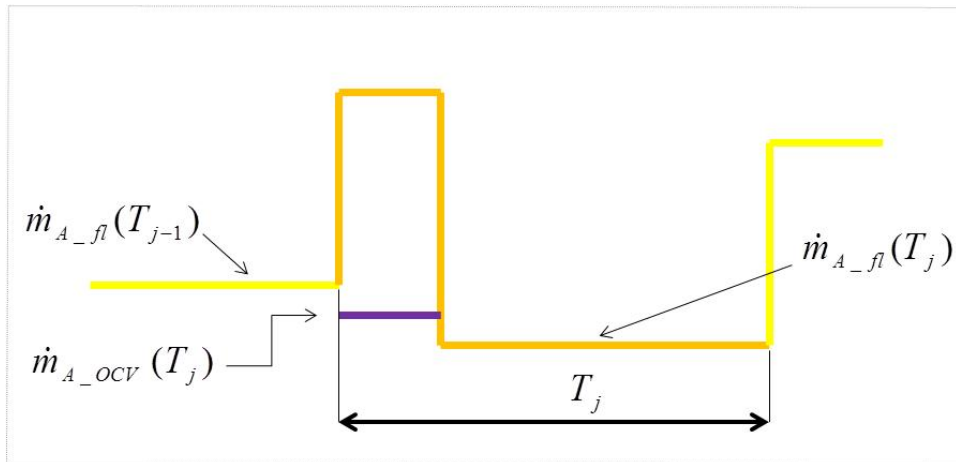


Figure 5.26: The mass flow rate of not-reacted H₂ because lost for other cause, \dot{m}_A , during the time in which the OCV is open (T_{ocv}).

- I. Calculate the mass flow of H₂ expelled through the OCV as the difference between the amount of not-reacted H₂ and the amount of H₂ lost through "other", during the purge time (Figure 5.27, red line):

$$\dot{m}_{DE} = \dot{m}_{NR}(T_{OCV}) - \dot{m}_{A_OCV} \quad (5.17)$$

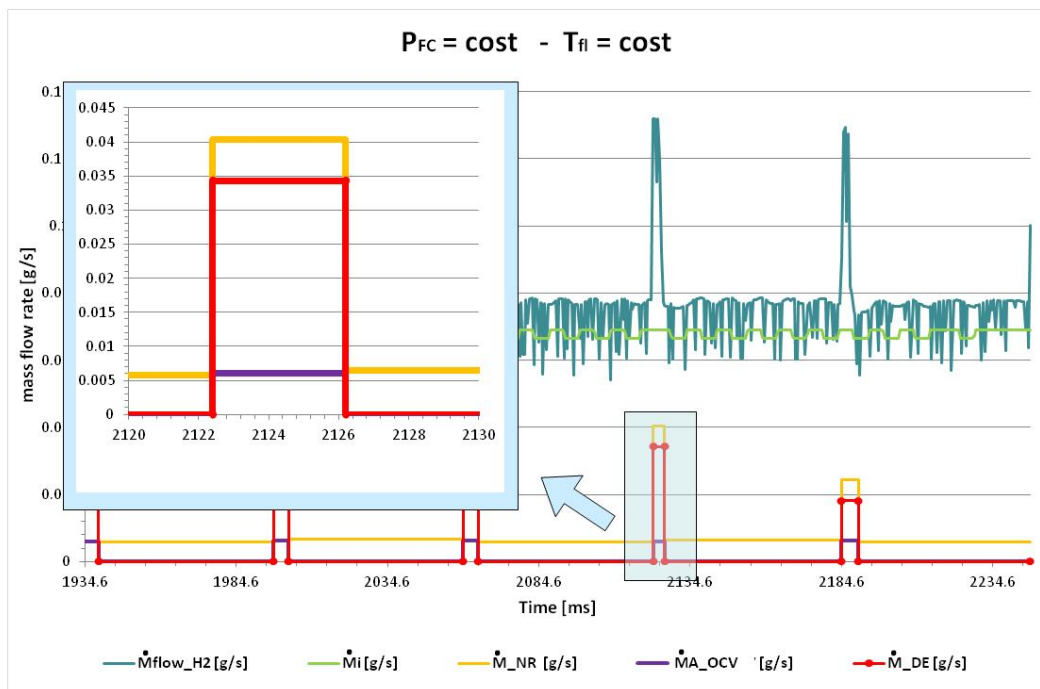


Figure 5.27: Trend of the mass flow rate of the H₂ not-reacted, \dot{m}_{NR} , expelled through the OCV, \dot{m}_{DE} and lost for other causes, \dot{m}_A .

- J. Calculate the related masses simply by multiplying the mass flow rate for its temporal duration (Figure 5.28):

$$m_{H_2} = \bar{\dot{m}}_{H_2} \cdot (T_{fl} + T_{OCV}) \quad (5.18)$$

$$m_i = \bar{\dot{m}}_i \cdot (T_{fl} + T_{OCV}) \quad (5.19)$$

$$m_{DE} = \dot{m}_{DE} \cdot T_{OCV} \quad (5.20)$$

$$m_A = \dot{m}_A \cdot T_{fl} \quad (5.21)$$

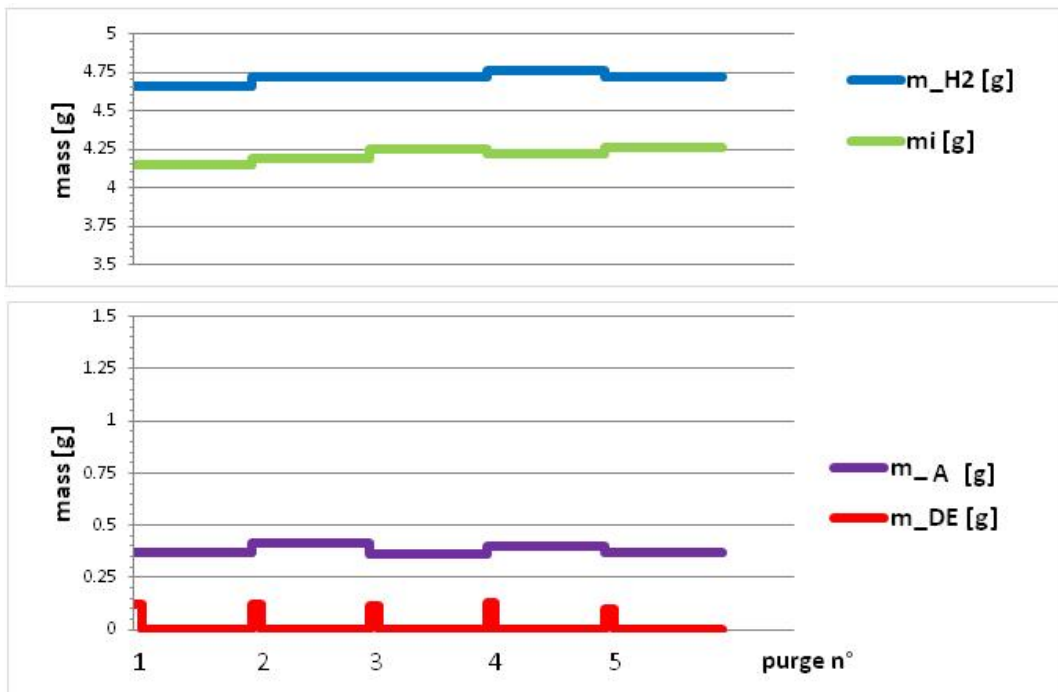


Figure 5.28: The masses trends: mass of the H_2 introduced, m_{H_2} (blue line), mass of H_2 actually reacted, m_i (green line), mass of the H_2 lost for the "other" causes, m_A (purple line) and mass of the H_2 purged, m_{DE} (red line).

- K. Average the masses over the entire test duration to determine an unique value of m_{H_2} , m_A , m_{DE} through which calculate U_f , X_A and X_{DE} with the equations 5.18, 5.19, 5.20.

5.5.4 ANALYSIS OF THE EFFICIENCY USING THE FRACTIONS X_{DE} AND X_A

In order to understand the causes of the non-optimization at low loads in terms of efficiency and fuel utilization coefficient, the fractions X_{DE} (eq. 5.12) and X_A (eq. 5.13) have been analyzed. The two fractions has been determinated using the developed U_f calculation algorithm, previously illustrated.

Figure 5.29 shows the behavior of the amount of the purged H_2 , X_{DE} , versus the flooding time, T_{fl} , by varying the FC power level. The quantity of H_2 expelled through the OCV decreases as the flooding time increase, assuming the minimum value at the optimal flooding time, for each FC power level analyzed. In fact, fixed the FC power, P_{FC} , the fraction X_{DE} has a hyperbolic trend.

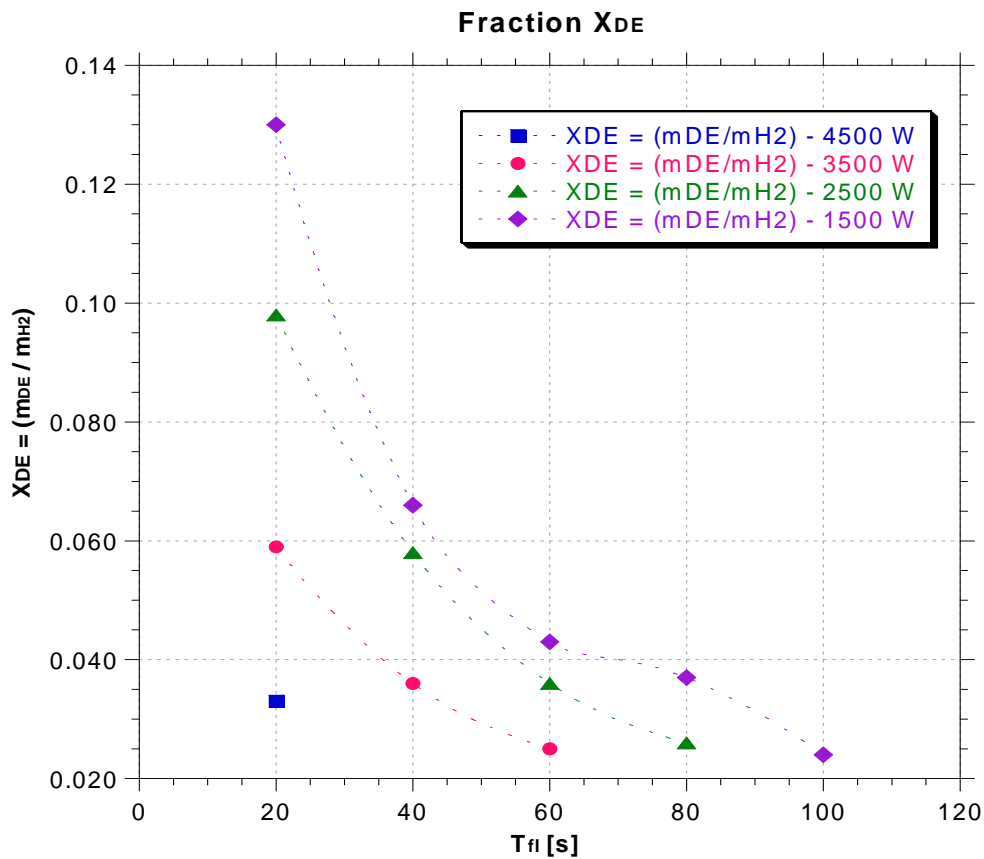


Figure 5.29: The fraction X_{DE} VS flooding time, T_{fl} and FC power level, P_{FC} .

Figure 5.30 shows the behavior of the H_2 that does not react to other causes, fraction X_A , by varying the flooding time, T_{fl} and the FC power level, P_{FC} . The trend

of X_A is completely not continuous and not-monotonic to vary both the T_{fl} and the P_{FC} . This behavior is evident especially at low loads.

From this analysis it can be deduced that the amount of hydrogen that does not react to other causes is particularly significant, especially at low loads.

The literature survey conducted on the degradation mechanisms draw the attention to the H_2 crossover phenomenon as one of the main causes of the membrane-electrode assembly (MEA).

This mechanism consists in the diffusion of H_2 from the anode side to the cathode side, through the membrane. Thus, the fuel crossover involves a loss of hydrogen, which therefore does not participate in the electrochemical reactions, moreover, over the long term, causes the loss of FC performance.

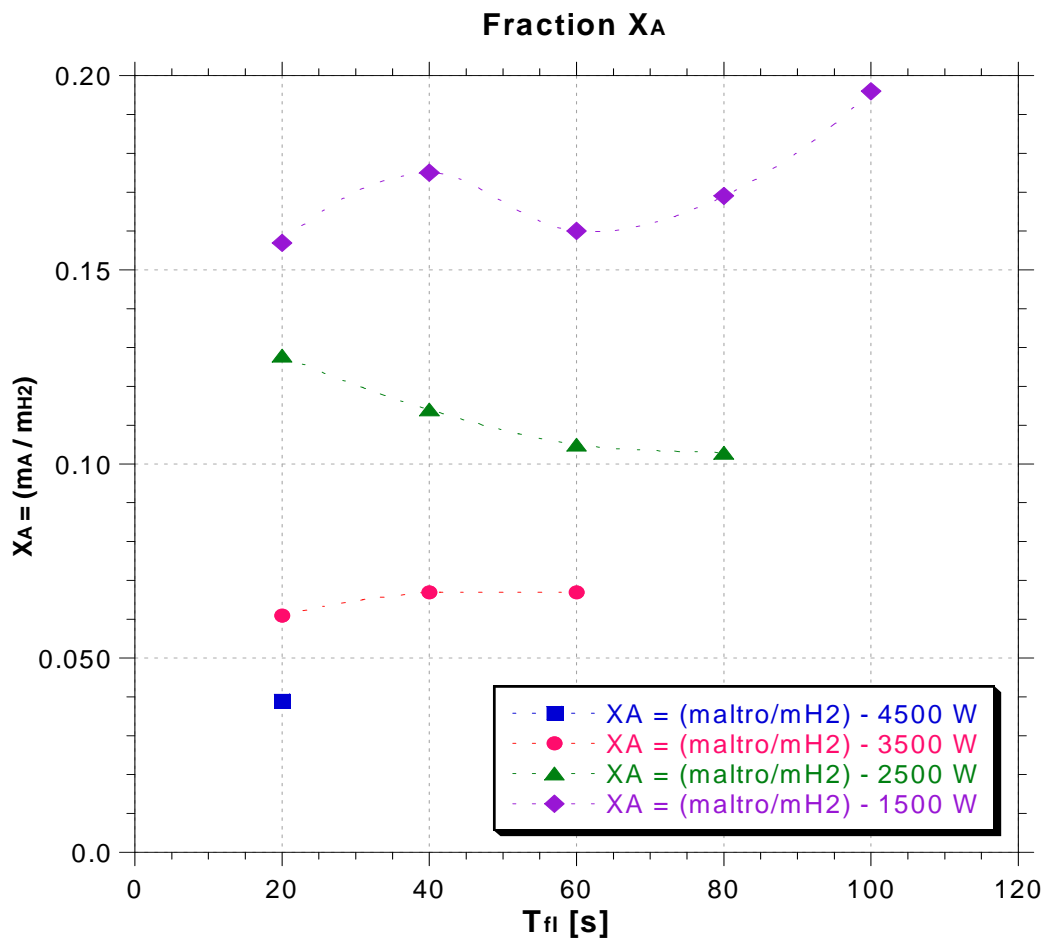


Figure 5.30: The fraction X_A VS flooding time, T_{fl} and FC power level, P_{FC} .

Among the parameters that characterized the H₂ crossover phenomenon, the most significant are: the operating temperature and pressure, the relative humidity and to a lesser extend the thickness of the membrane,

The rate of H₂ crossover is defined as [6]:

$$J_{H_2}^{cross} = \left(\frac{\psi_{H_2}^{PEM}}{l_{PEM}} \right) (P_{H_2}^a) \quad (5.22)$$

where:

- $\psi_{H_2}^{PEM}$ H₂ membrane permeability coefficient;
- l_{PEM} membrane thickness;
- $P_{H_2}^a$ anodic side H₂ partial pressure.

In virtue of what is reported in the literature and on the basis of the experimental analysis carried out, as the crossover phenomenon closely related to the H₂ partial pressure, then it can be possible to associate the fraction X_A to this phenomenon. In fact, considering that the design condition of the PEMFC in study is that at full load (4500 W), is plausible to say that the apparent loss of cell performance at low loads are due to the partial pressure fluctuations at low power levels.

5.6 EXPERIMENTAL RESULT

In this section the results of the fuel utilization factor, U_f , of the fraction of not-reacted H_2 because lost for other causes, X_A and of the purged H_2 , X_{DE} are shown. Those results are obtained using the experimental data acquired during the tests of the 2010 and the 2012.

The tests of the 2010 were performed by fixing the time of flooding, T_{fl} equal to 20s and purging time $T_{pu} = 2.5$ s and varying the FC power level.

Instead, the 2012 experimental tests were conducted keeping the purge time constant, ever equal to 2.5 s and changing the flooding time gradually, from 20 s up to the optimal T_{fl} correlated to that determined FC power (Table), with a steps of 20 s. The power was varied, with a steps of 500 W, from the maximum value, 4500W up to 1500 W. (Precisely, after keeping a certain FC power level for a significant time and, therefore, after acquired an adequate number of data for these FC power level, manually setting the fuel cell at the later power level).

To quantify U_f , X_A and X_{DE} the calculation algorithm developed and described in the previous paragraph has been applied.

The first graph of each page report the various H_2 mass flow rate [g/s] against the time, with the following key:

- introduced, **M**flow_H2 (blue line),
- actually reacted, **M**i (green line),
- not-reacted, **M**_NR (orange line),
- not-reacted and purged, **M**_DE (red line),
- not-reacted for other causes, **M**A_OCV (purple line).

The second of each page report the various H_2 mass [g] obtained from the X-algorithm, with the following key:

- introduced, **m**_H2 (blue line),
- actually reacted, **m**i (green line),
- not-reacted for other causes, **m**A (purple line),
- not-reacted and purged, **m**_DE (red line)

5.6.1 RESULTS OF THE 2010 TESTS (OLD PURGE PROGRAMMING LOGIC)

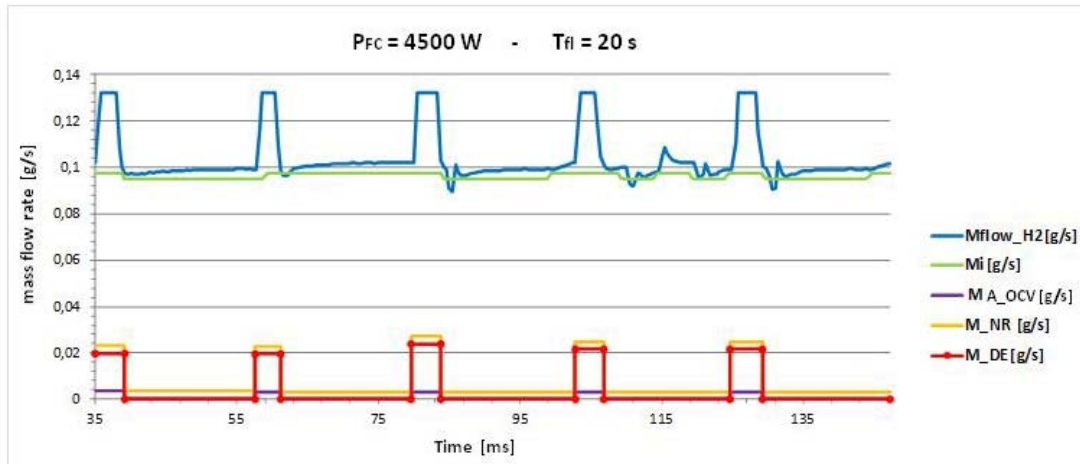


Figure 5.31: Experimental and averaged hydrogen mass flow rate, 2010 data, P_{FC}=4500 W and T_H=20 s.

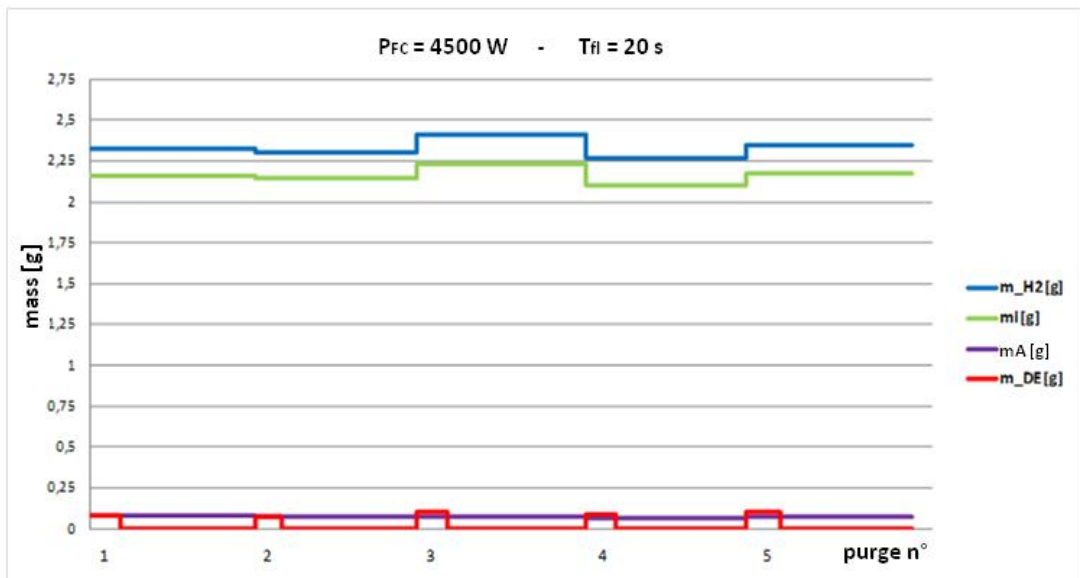


Figure 5.32: Computed hydrogen mass rate, 2010 data, P_{FC}=4500 W and T_H=20 s.

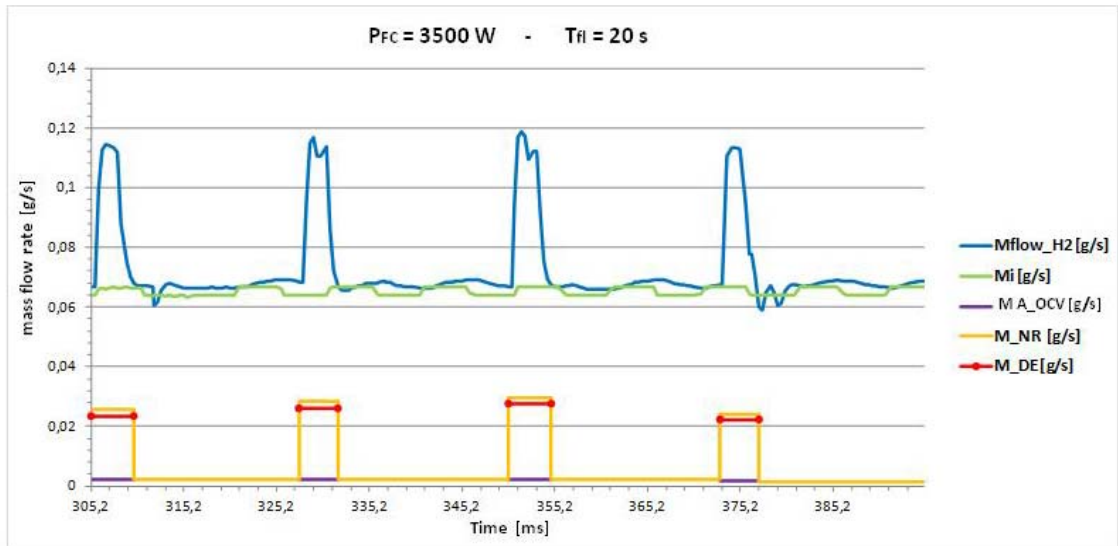


Figure 5.33: Experimental and averaged hydrogen mass flow rate, 2010 data, $P_{FC}=3500\text{ W}$ and $T_H=20\text{ s}$.

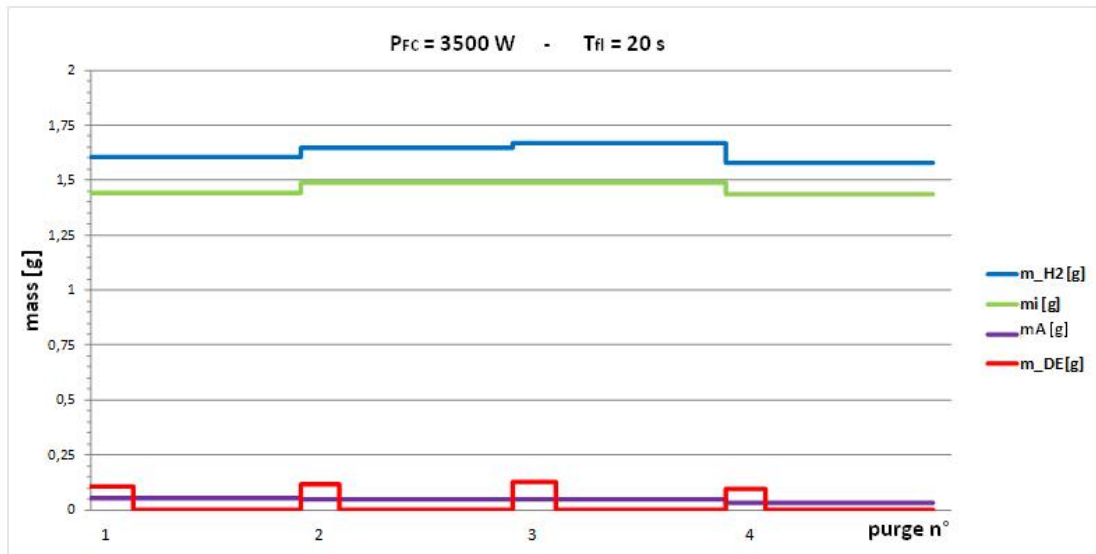


Figure 5.34: Computed hydrogen mass rate, 2010 data, $P_{FC}=3500\text{ W}$ and $T_H=20\text{ s}$.

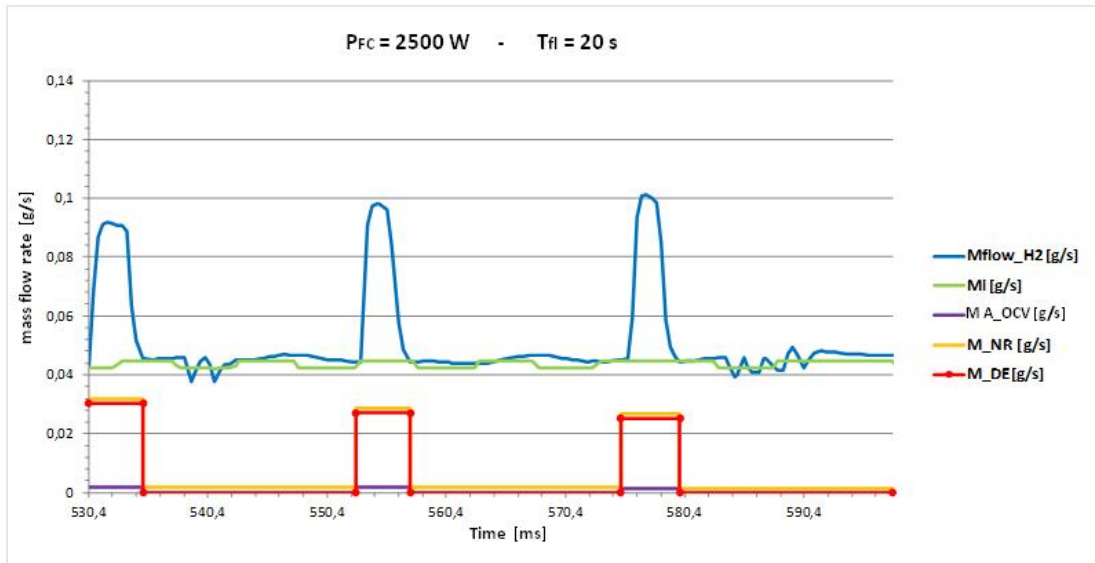


Figure 5.35: Experimental and averaged hydrogen mass flow rate, 2010 data, $P_{FC}=2500\text{ W}$ and $T_H=20\text{ s}$.



Figure 5.36: Computed hydrogen mass rate, 2010 data, $P_{FC}=2500\text{ W}$ and $T_H=20\text{ s}$.

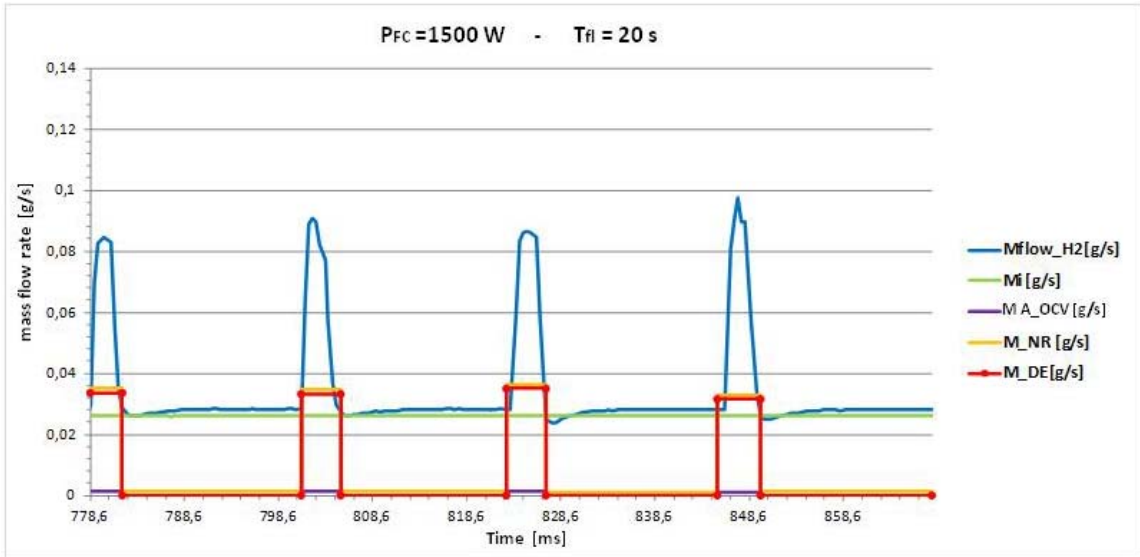


Figure 5.37: Experimental and averaged hydrogen mass flow rate, 2010 data, $P_{FC}=1500\text{ W}$ and $T_H=20\text{ s}$.

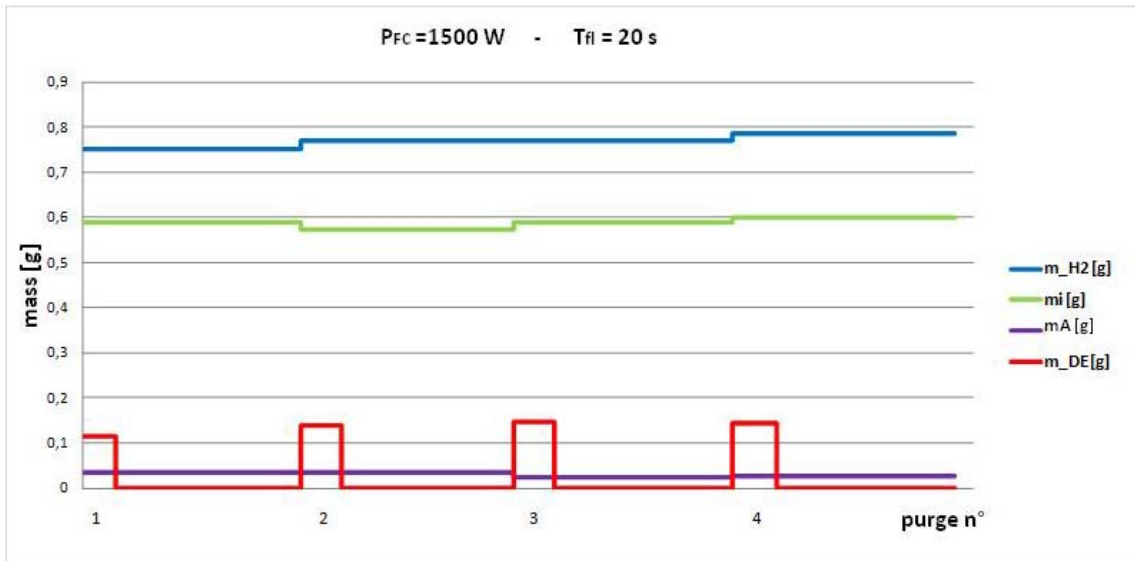


Figure 5.38: Computed hydrogen mass rate, 2010 data, $P_{FC}=1500\text{ W}$ and $T_H=20\text{ s}$.

5.6.2 RESULTS OF THE 2012 TESTS (NEW PURGE PROGRAMMING LOGIC)

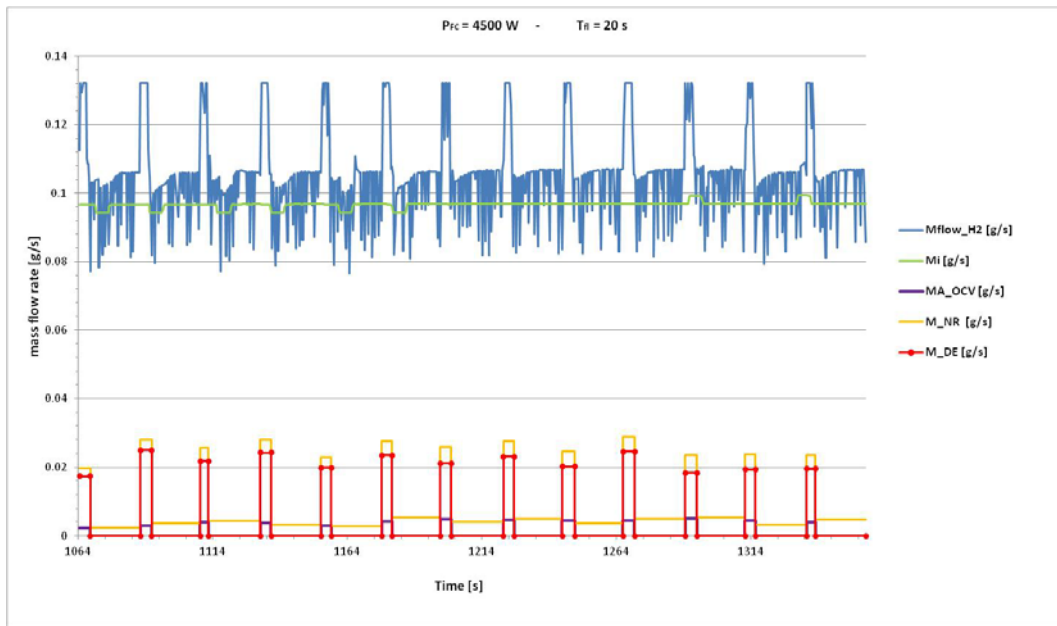


Figure 5.39: Experimental and averaged hydrogen mass flow rate, 2012 data, $P_{FC}=4500$ W and $T_H=20$ s.

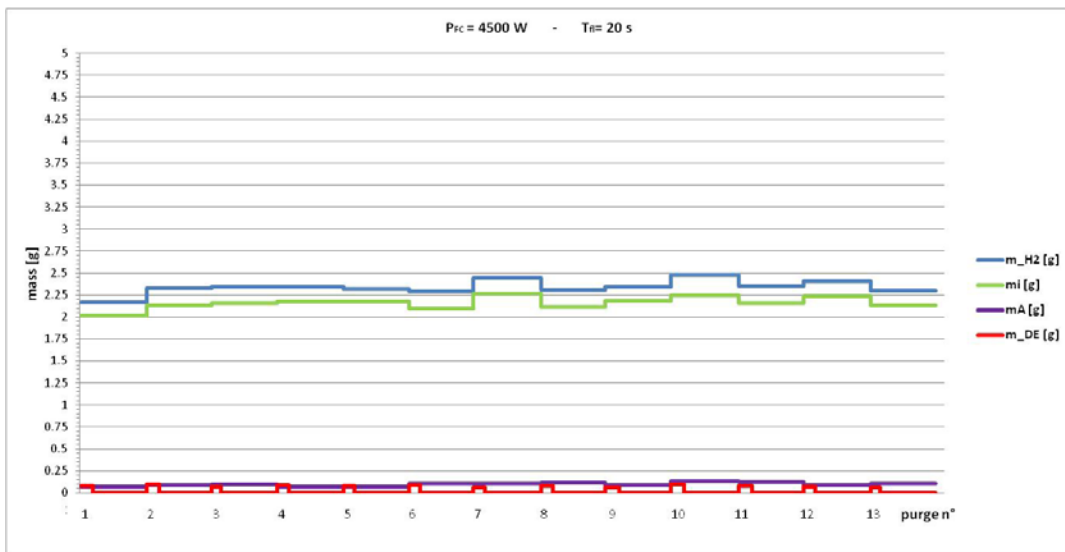


Figure 5.40: Computed hydrogen mass rate, 2012 data, $P_{FC}=4500$ W and $T_H=20$ s.



Figure 5.41: Experimental and averaged hydrogen mass flow rate, 2012 data, P_{FC}=3500 W and T_H=20 s.



Figure 5.42: Computed hydrogen mass rate, 2012 data, P_{FC}=3500 W and T_H=20 s.

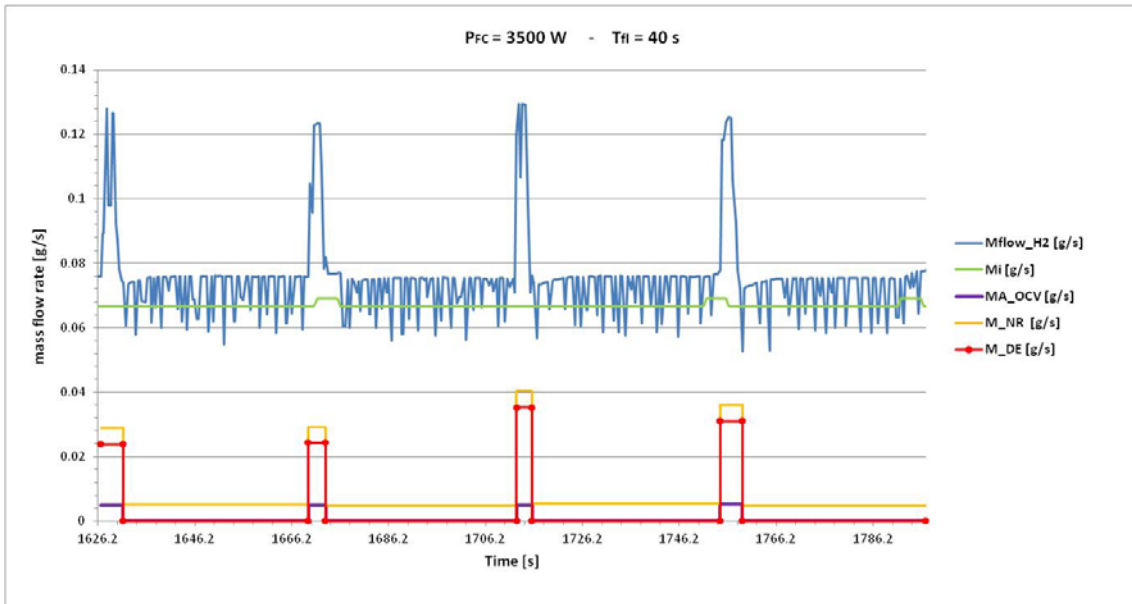


Figure 5.43: Experimental and averaged hydrogen mass flow rate, 2012 data, $P_{FC}=3500\text{ W}$ and $T_{fl}=40\text{ s}$.

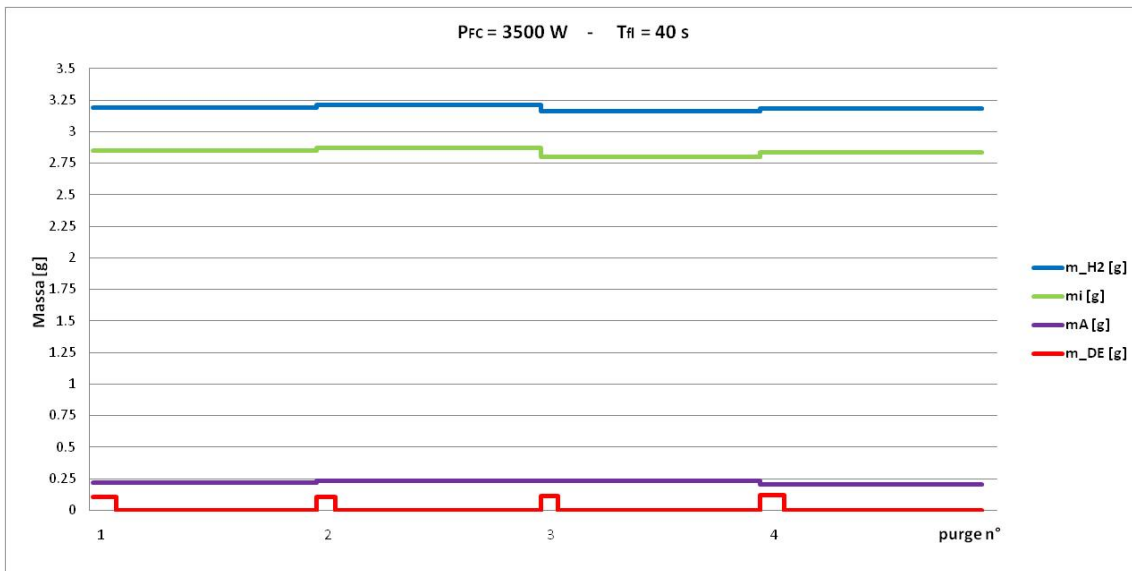


Figure 5.44: Computed hydrogen mass rate, 2012 data, $P_{FC}=3500\text{ W}$ and $T_{fl}=40\text{ s}$.



Figure 5.45: Experimental and averaged hydrogen mass flow rate, 2012 data, P_{FC}=3500 W and T_H=60 s.

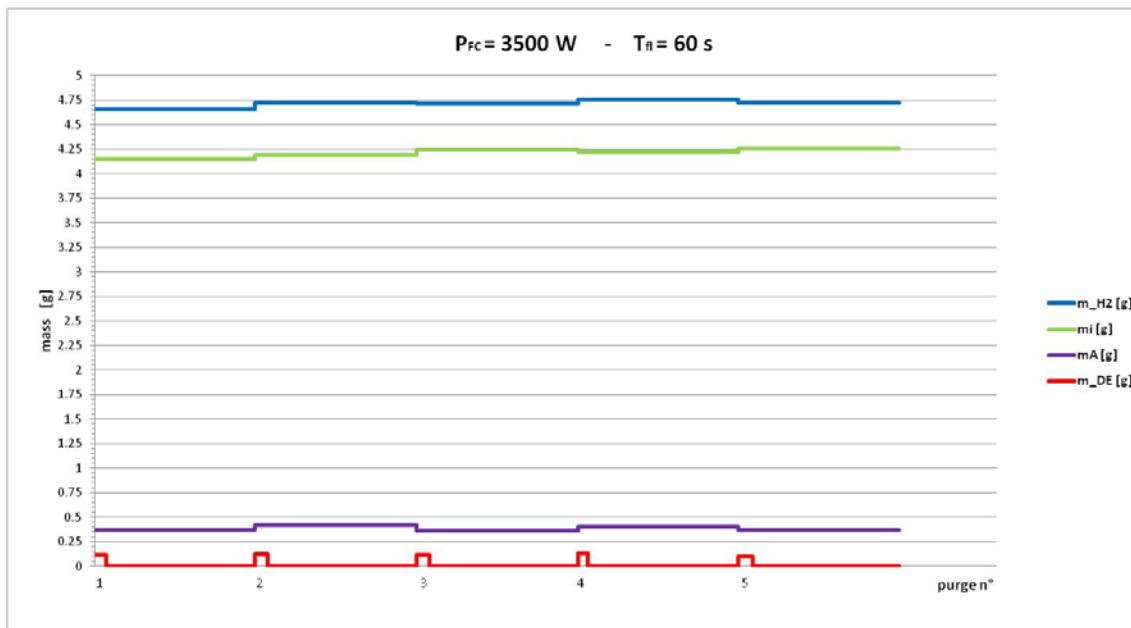


Figure 5.46: Computed hydrogen mass rate, 2012 data, P_{FC}=3500 W and T_H=60 s.

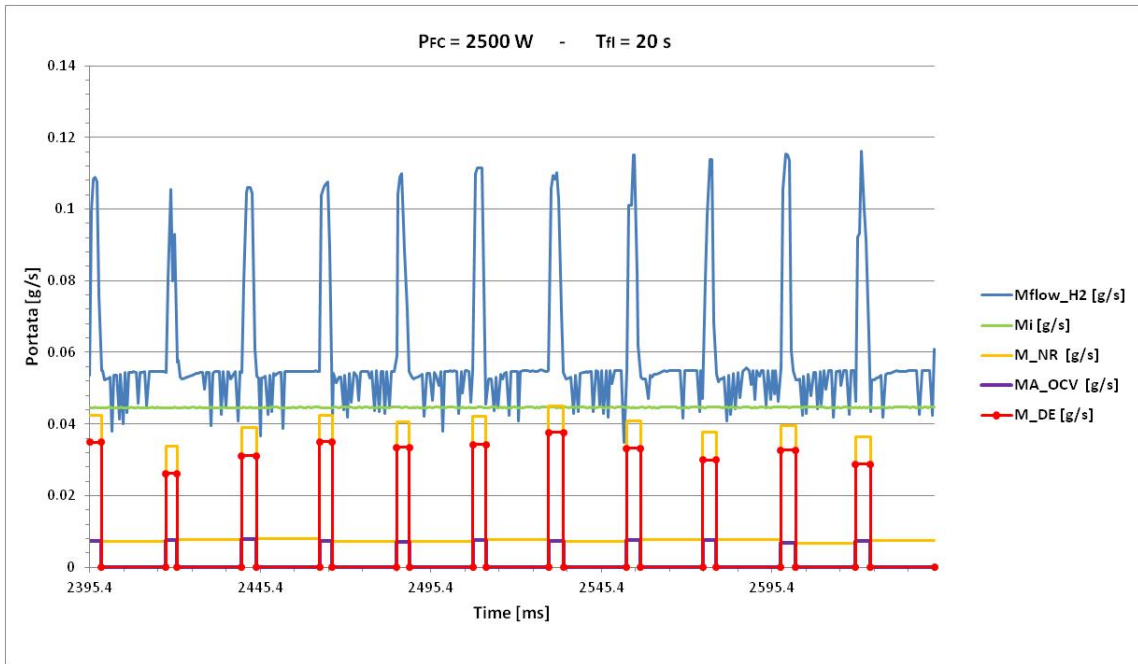


Figure 5.47: Experimental and averaged hydrogen mass flow rate, 2012 data, $P_{FC}=2500\text{ W}$ and $T_{fil}=20\text{ s}$.

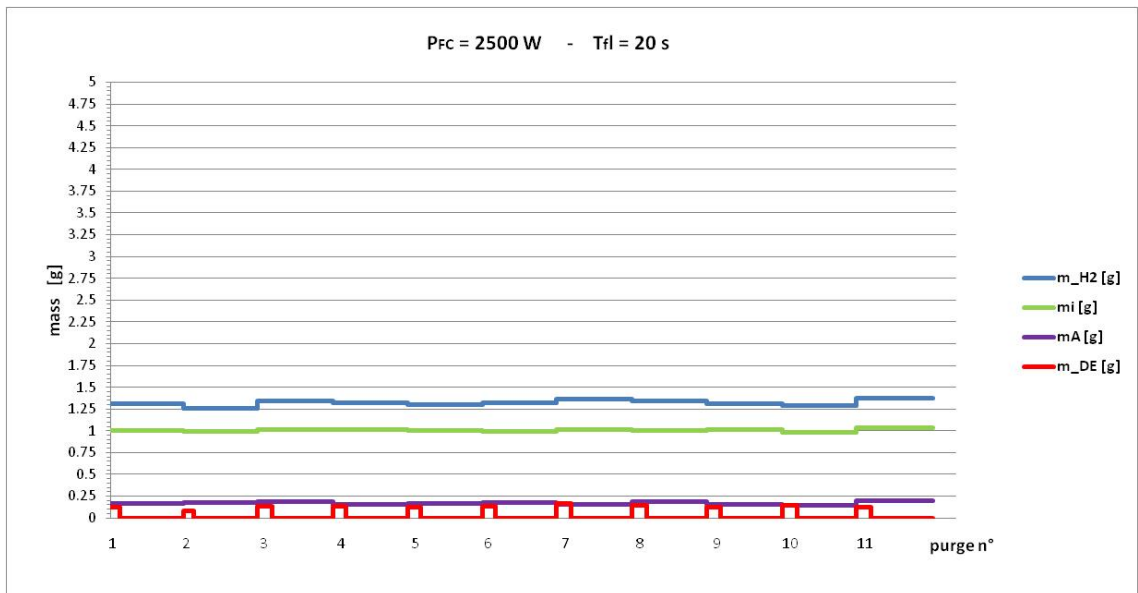


Figure 5.48: Computed hydrogen mass rate, 2012 data, $P_{FC}=2500\text{ W}$ and $T_{fil}=20\text{ s}$.

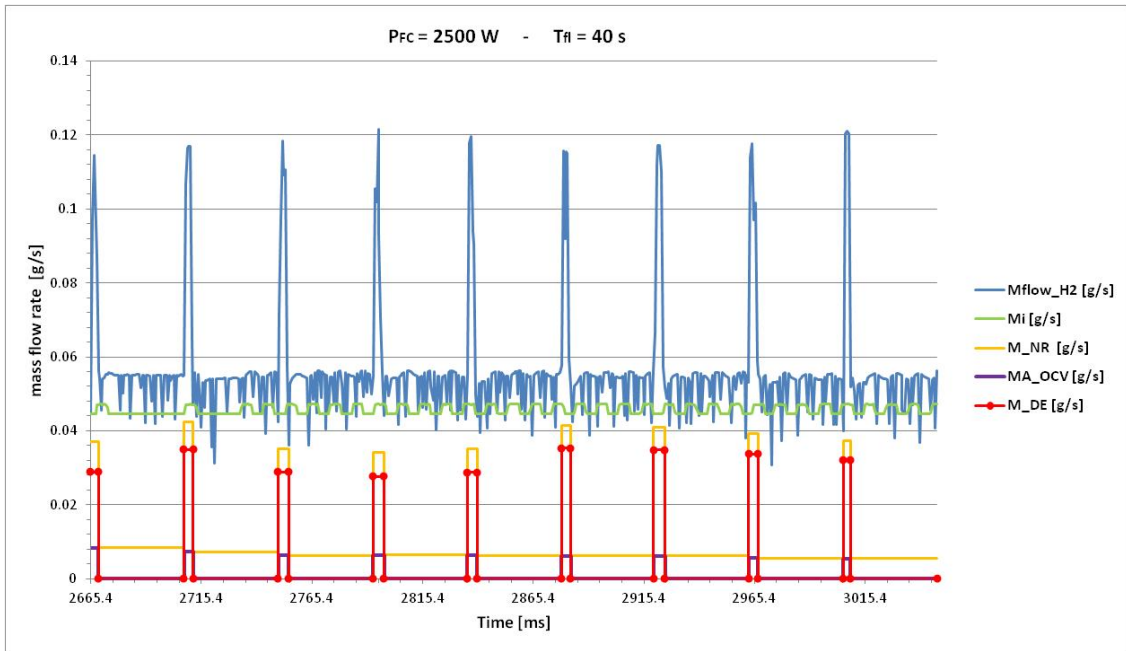


Figure 5.49: Experimental and averaged hydrogen mass flow rate, 2012 data, $P_{FC}=2500\text{ W}$ and $T_{fil}=40\text{ s}$.

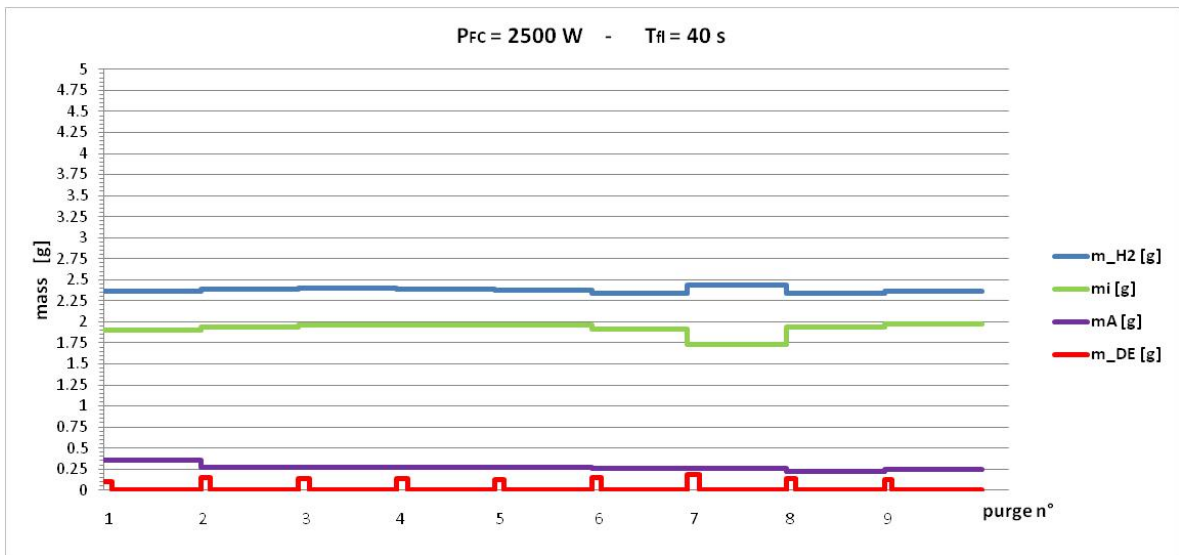


Fig.: 5.50 Computed hydrogen mass rate, 2012 data, $P_{FC}=2500\text{ W}$ and $T_{fil}=40\text{ s}$.

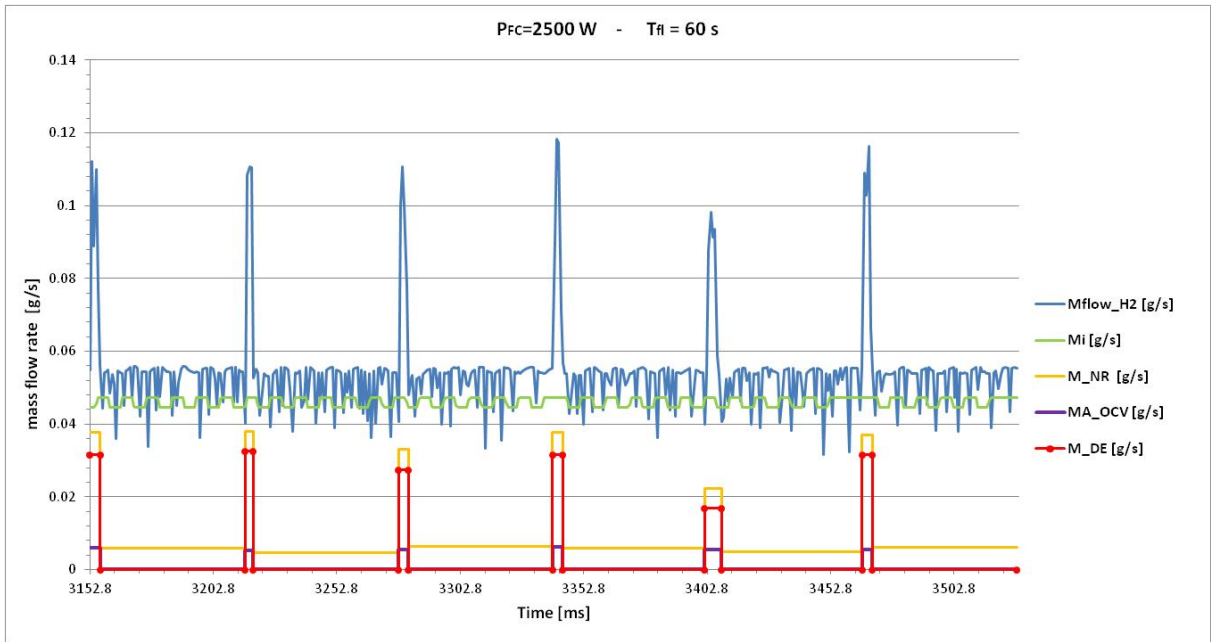


Figure 5.51: Experimental and averaged hydrogen mass flow rate, 2012 data, P_{FC}=2500 W and T_{fl}=60 s.

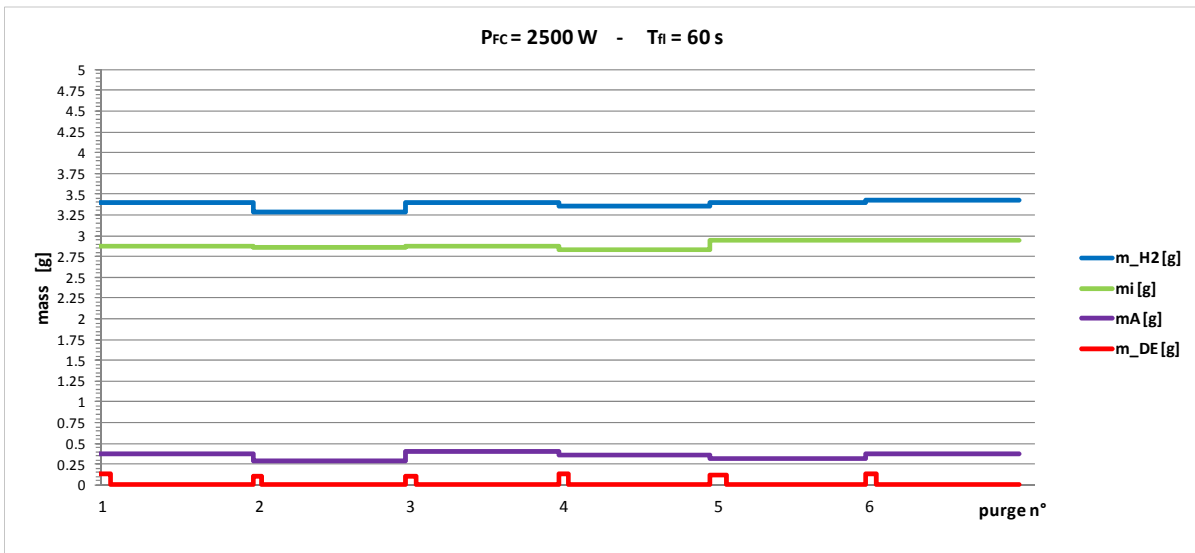


Figure: 5.52: Computed hydrogen mass rate, 2012 data, P_{FC}=2500 W and T_{fl}=60 s.

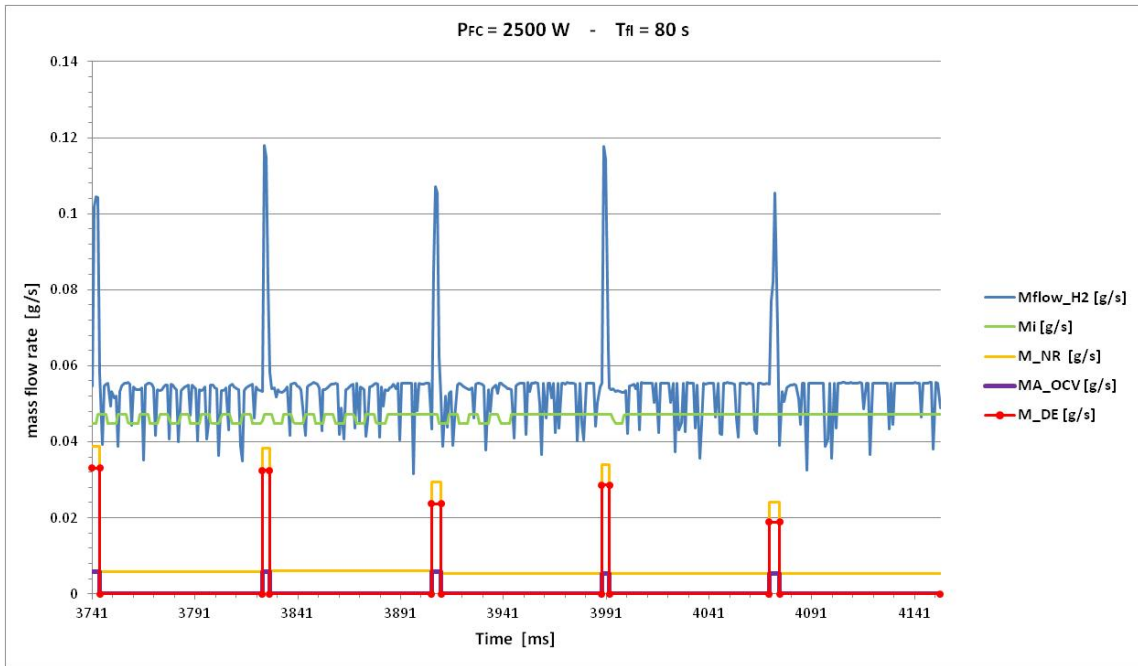


Figure 5.53: Experimental and averaged hydrogen mass flow rate, 2012 data, P_{FC}=2500 W and T_{fl}=80 s.

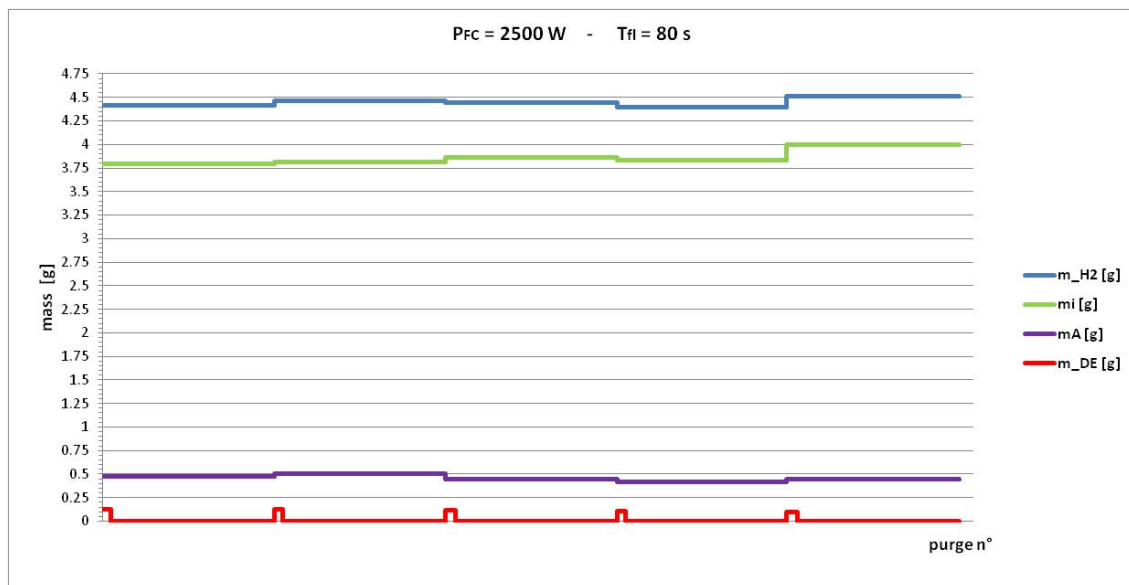


Figure 5.54: Computed hydrogen mass rate, 2012 data, P_{FC}=2500 W and T_{fl}=80 s.

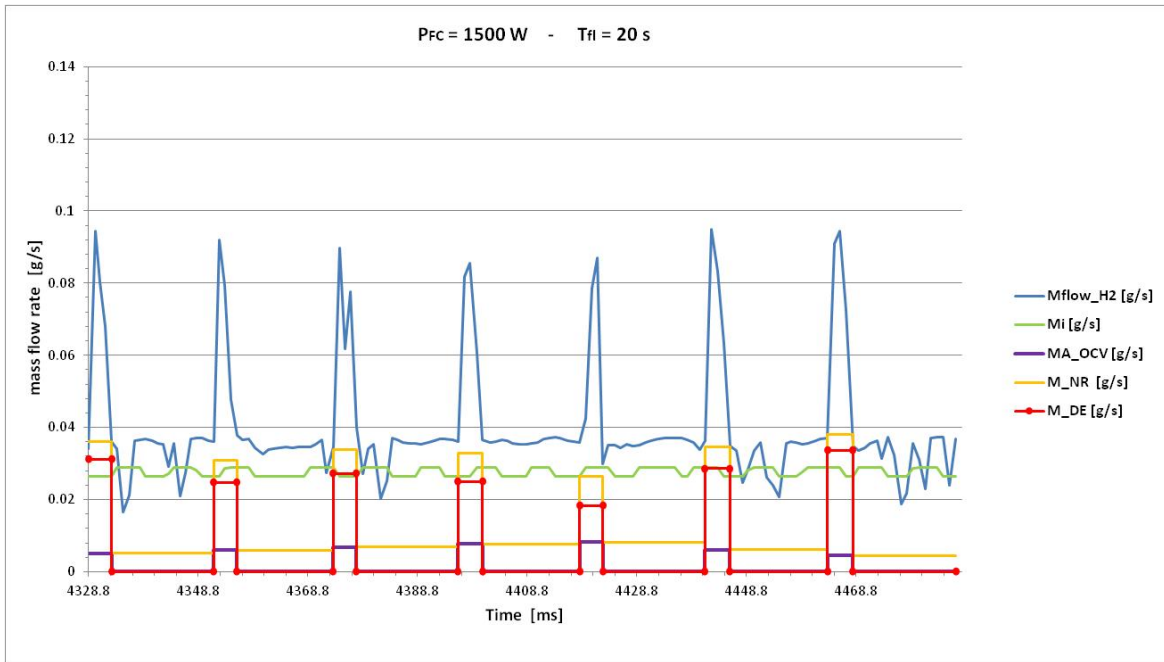


Figure 5.55: Experimental and averaged hydrogen mass flow rate, 2012 data, $P_{FC}=1500\text{ W}$ and $T_{fl}=20\text{ s}$.

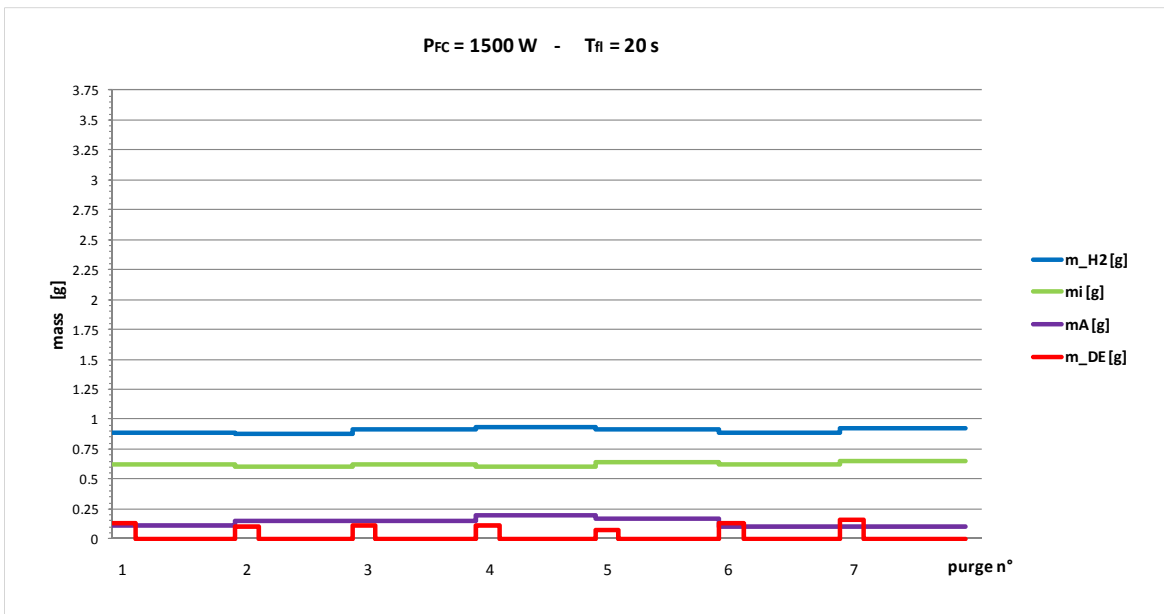


Figure 5.56: Computed hydrogen mass rate, 2012 data, $P_{FC}=1500\text{ W}$ and $T_{fl}=20\text{ s}$.

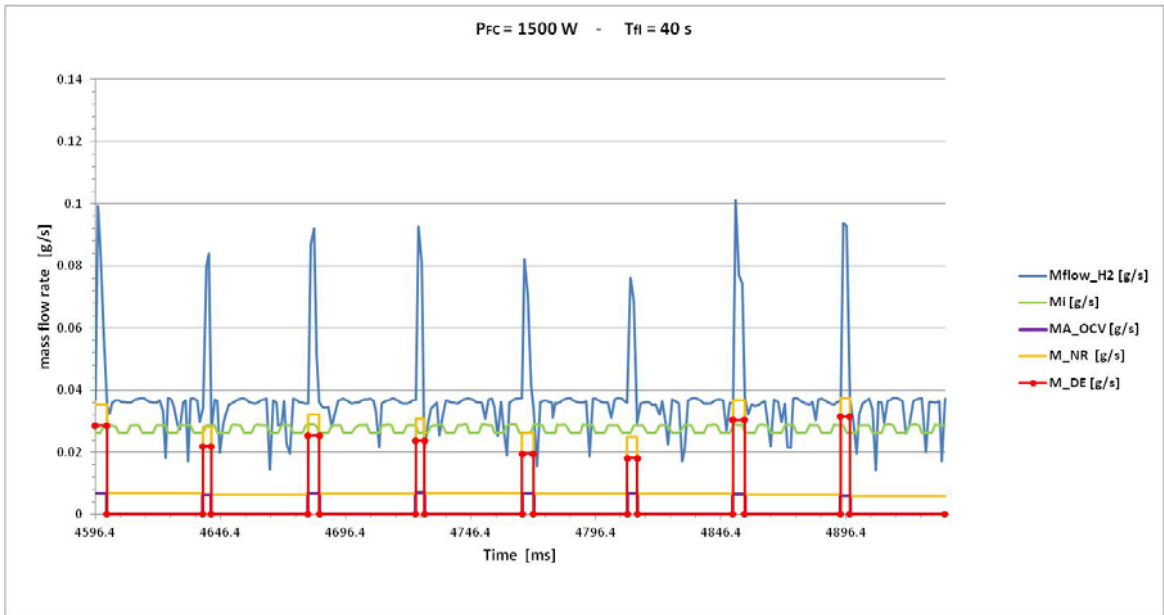


Figure 5.57: Experimental and averaged hydrogen mass flow rate, 2012 data, $P_{FC}=1500\text{ W}$ and $T_{fil}=40\text{ s}$.

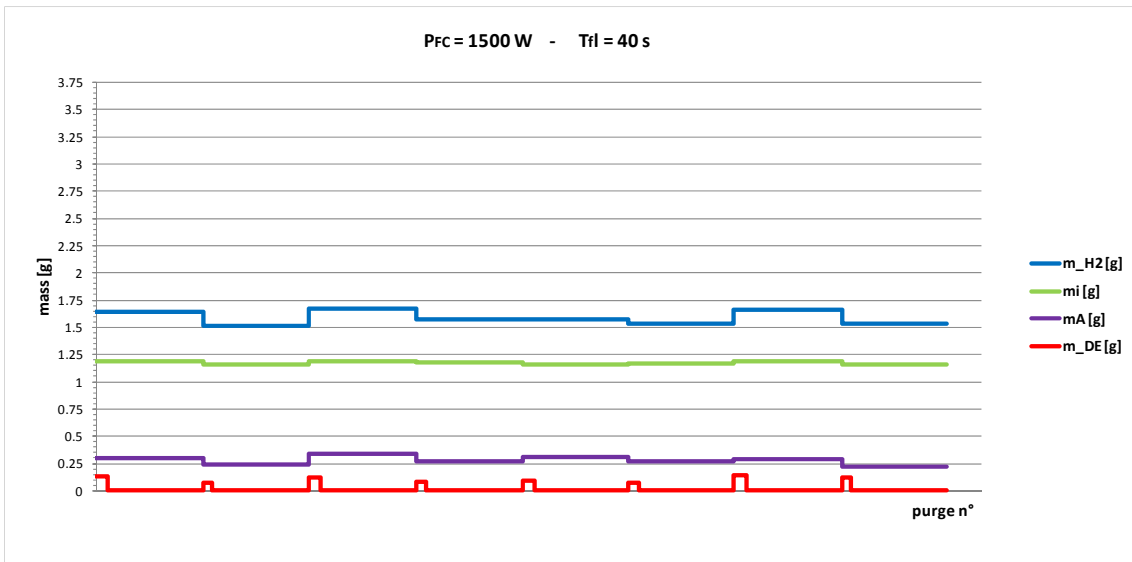


Figure 5.58: Computed hydrogen mass rate, 2012 data, $P_{FC}=1500\text{ W}$ and $T_{fil}=40\text{ s}$.



Figure 5.59: Experimental and averaged hydrogen mass flow rate, 2012 data, $P_{FC}=1500\text{ W}$ and $T_{fi}=60\text{ s}$.

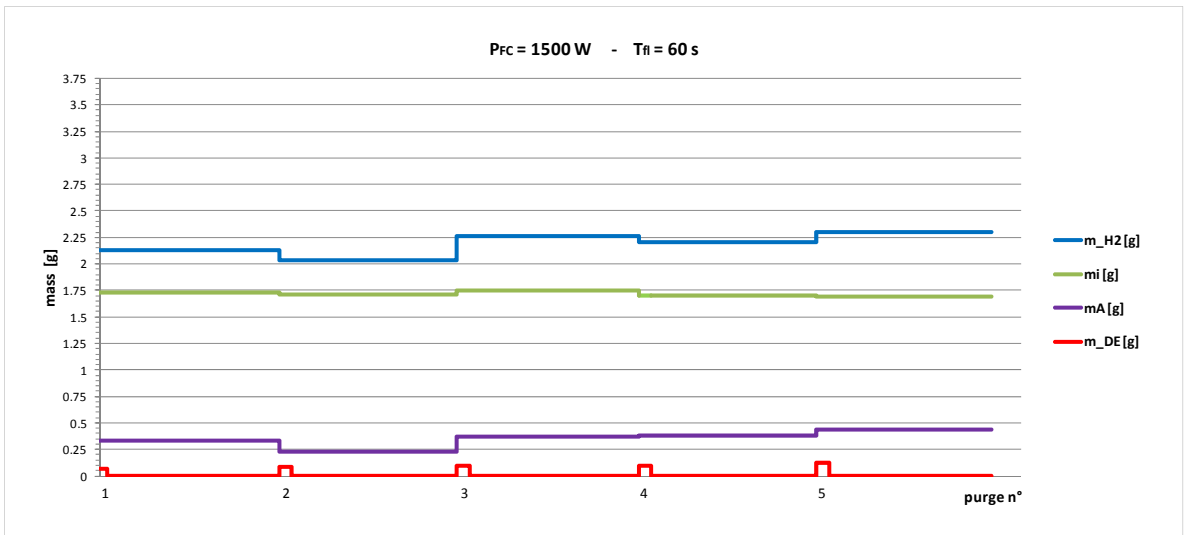


Figure 5.60: Computed hydrogen mass rate, 2012 data, $P_{FC}=1500\text{ W}$ and $T_{fi}=60\text{ s}$.



Figure 5.61: Experimental and averaged hydrogen mass flow rate, 2012 data, $P_{FC}=1500\text{ W}$ and $T_H=80\text{ s}$.

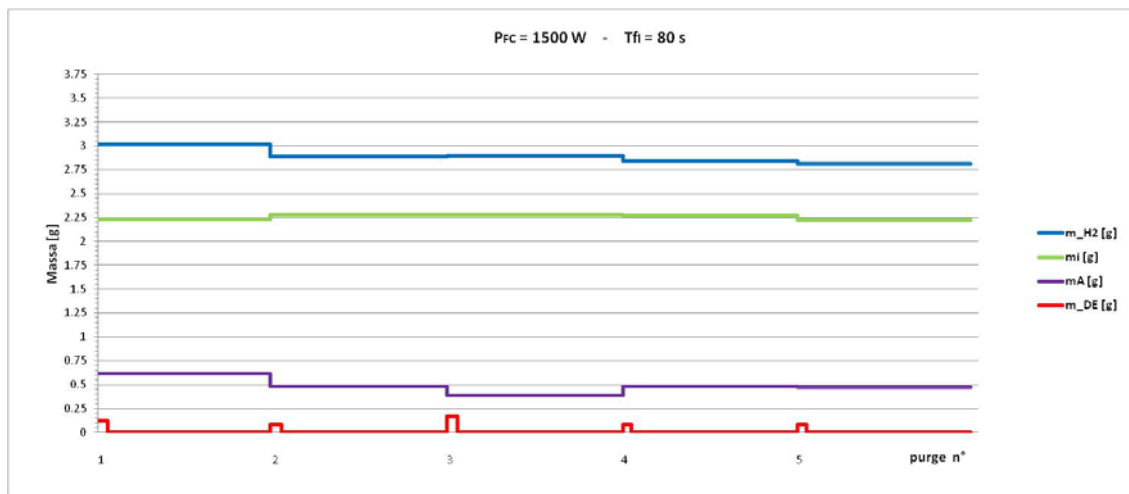


Figure 5.62: Computed hydrogen mass rate, 2012 data, $P_{FC}=1500\text{ W}$ and $T_H=80\text{ s}$.

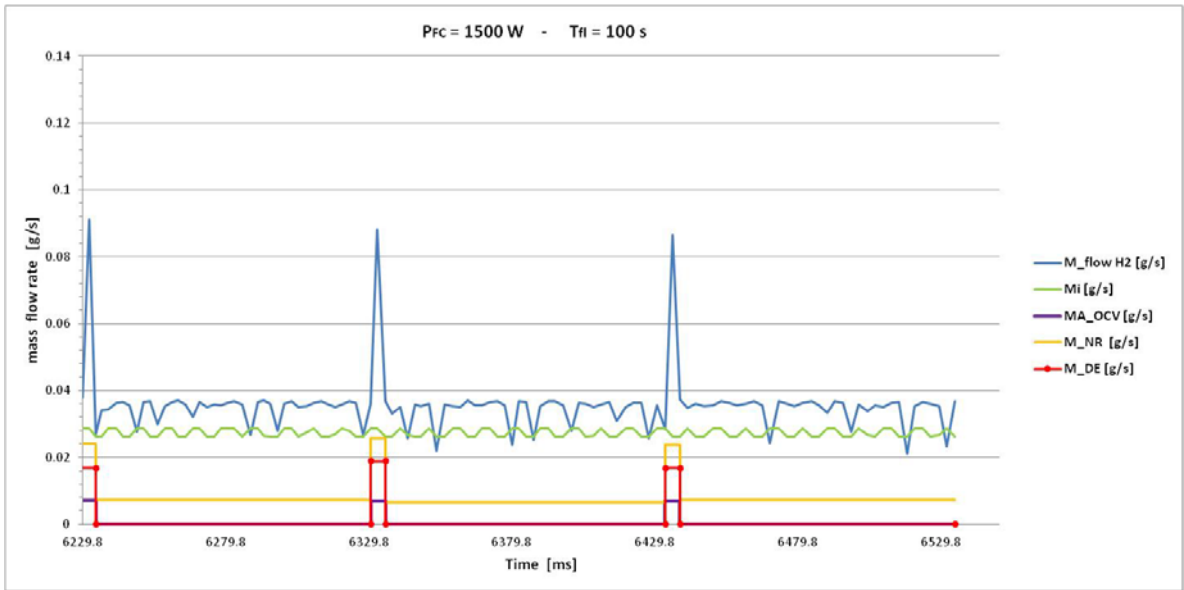


Figure 5.63: Experimental and averaged hydrogen mass flow rate, 2012 data, $P_{FC}=1500\text{ W}$ and $T_{fl}=100\text{ s}$.

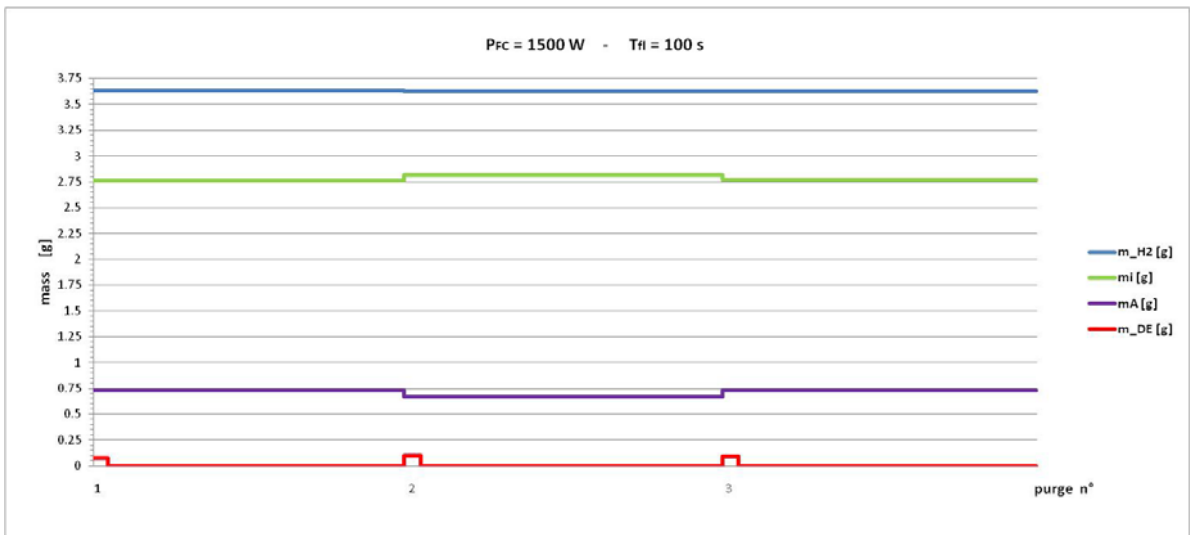


Figure 5.64: Computed hydrogen mass rate, 2012 data, $P_{FC}=1500\text{ W}$ and $T_{fl}=100\text{ s}$.

References to the chapter 5

- [1] B. Belvedere, M. Bianchi, A. Borghetti, A. De Pascale, M. Paolone, **R. Vecci**, Experimental analysis of a PEM fuel cell performance at variable load with anodic exhaust management optimization, (Original Research Article) International Journal of Hydrogen Energy, Volume 38, Issue 1, 11 January 2013, 385-393.
- [2] Mokmeli A, Asghari S. An investigation into the effect of anode purging on the fuel cell performance, International Journal of Hydrogen Energy 35, (2010), 9276-9282.
- [3] Strasser k. The design of alkaline fuel cells. J Power Sources 1990; 29 : 149 e 66.
- [4] Gou J, Pei P, Wang Y. The dynamic behavior of pressure during purge process in the anode of a PEM fuel cell. J Power Sources 2006; 162 :1 104 e 14.
- [5] B. Belvedere, M. Bianchi , A. De Pascale, Experimental analysis of a cogenerative performance of a PEM fuel cell based energy system, Proceedings of ICAE 2011, 16-18 May 2011 - Perugia, Italy.
- [6] X. Cheng, J. Zhang, Y. Tang, C. Song, J. Shen, D. Song, J. Zhang, Hydrogen crossover in high-temperature PEM fuel cells, J. of Power Sources 167 (2007) 25–31.

Chapter 6

AGEING OF THE PEMFC

The investigation of PEMFC ageing mechanisms is fundamental in order to promote the development of fuel cell technology offering high performance and durability to consumers [1, 2].

As aforementioned, the durability of proton exchange membrane (PEM) fuel cells is one of the biggest challenges and barriers for commercializing this promising technology [2, 3]. The 2015 US Department of Energy (DOE) [3] lifetime requirements for transportation applications range from 5000 h for cars to 20,000 h for buses, and for stationary applications the requirement is 40,000 h of continuous operation. Currently, the lifetimes of fuel cell vehicles and stationary cogeneration systems are around 1700 h and 10,000 h, respectively [1-3].

As a result, numerous research activities have investigated the failure modes of degradation in order to reduce the wide gap that exists between the ideal and the state-of-the-art lifetimes of PEM fuel cells [1-23].

Only a relatively small number of studies have investigated degradation across real PEM fuel cell lifetimes due to high costs and prolonged testing periods required. However, various in situ [4] and ex situ [5] accelerated tests have been proposed and implemented to explore degradation mechanisms of individual components in PEM fuel cells [1, 2].

The most well-known ageing conditions are: fuel gas starvation [1, 6], inappropriate hydration of the membrane [7], temperatures at too high levels or in cycling conditions, operation at low current densities [8] and even at open circuit voltage [9, 10], presence of pollutants [11], current cycling [12, 13] as done for transport applications. Fuel cell degradation induced by one of the above ageing conditions can occur as corrosion phenomena at bipolar plates [14, 15], ageing of the inner FC components e.g. gas diffusion layers [16, 17], electrodes [8, 18-20] or membranes [21-23] , as well described previously (chapter 4).

In this chapter the ageing analysis carried out on the PEM fuel cell in study is described. The methodology and the coefficient previously defined (chapter 5) for the optimization of the FC, in particular the fuel utilization factor and its fraction (X_{DE} and X_A) behavior, is here applied to assess the PEMFC degradation and the effect of the aging.

6.1 THE FC AGEING ANALYSIS

The analysis on the FC ageing is carried out by considering about 50 hours of not-continuous operation of the system. Precisely, the FC performance has been analyzed comparing the 2010 and 2012 year tests, as shown in the following.

Figure 6.1 shows the polarization curves referring to 2010 tests (blue line) and 2012 test (red line), respectively. An overall aging, for each power level delivered by the fuel cell has been observed. Furthermore, although full load aging is almost absent, at medium and low loads is well evident.

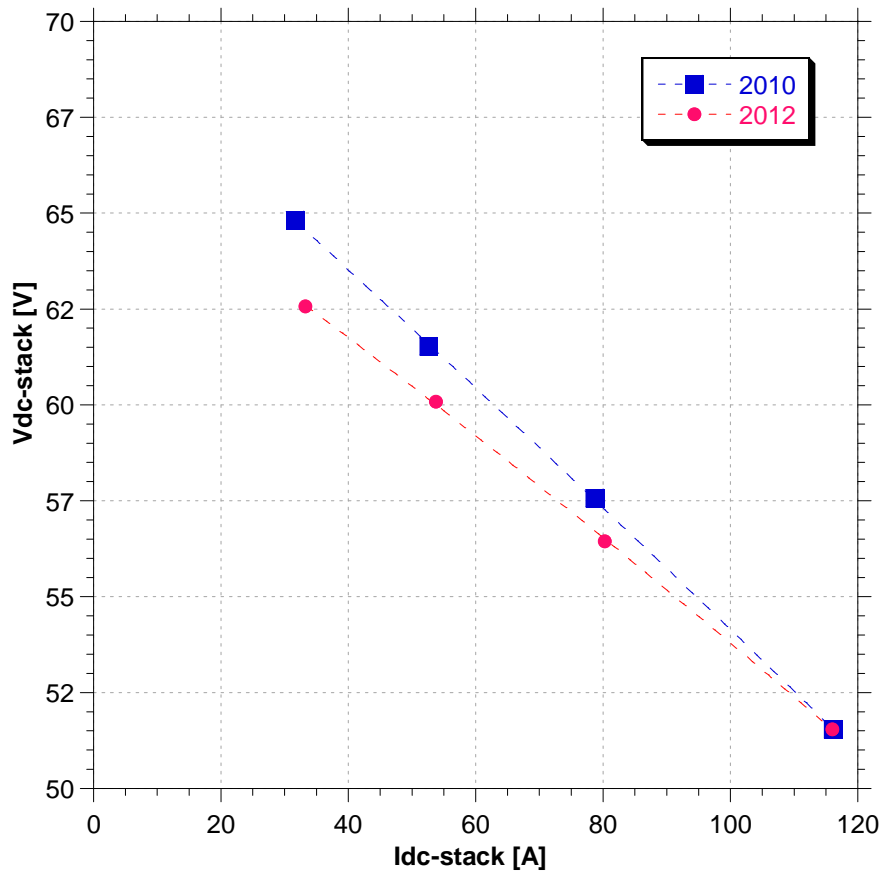


Figure 6.1: Ageing analysis: The polarization curves referring to 2010 tests (blue line) and 2012 test (red line).

In order to verify what the components most affected the performance loss, the powers and the efficiencies of the electrical and the mechanical components have been analyzed. Also the FC stack power and efficiency have been investigated.

The value of the utilization factor (U_f) is proportional to all efficiencies values trough the following equation:

$$\eta_{FC} = \frac{P_{FC}}{\dot{m}_{H_2} LHV_{H_2}} = U_f \eta_s \eta_{inv} \eta_{aux} \quad (5.1)$$

The value of fuel utilization factor, U_f , is mainly due to the stack efficiency, η_s , and to the FC efficiency, η_{FC} . Instead, the inverter (η_{inv}) and auxiliary (η_{aux}) are less influential having high efficiency values, as can be noted from the full load FC performance (Figure 6.1-Figure 6.4).

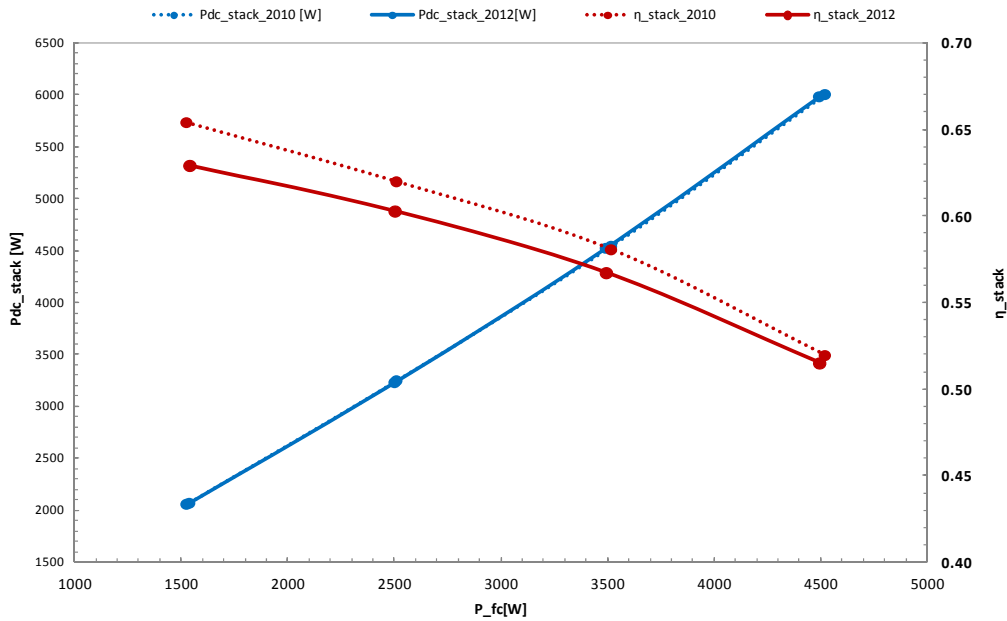


Figure 6.2: Ageing of the FC stack: efficiency (red line) and power (blue line) VS FC power level, considering 50 h of operation. (2010 tests (dotted line) VS 2012 tests (continuous line)).

A significant drop of the stack efficiency, can be shown comparing the 2012 performance (Figure 6.2, red continue line) with the 2010 ones (Figure 6.2, red dotted line).

Remembering that the stack efficiency is defined as:

$$\eta_s = \frac{V_{DC} \cdot i_{DC}}{\dot{m}_i LHV_{H_2}} \quad (5.2)$$

where V_{DC} and i_{DC} are voltage [V] and current [A] of the stack, respectively, while \dot{m}_i is the mass flow rate of the actually reacted H₂ and LHV_{H_2} is the H₂ lower heating value (120,000 kJ/kg).

Thus, it is necessary to introduce to date (2012 – continuous line) a greater amount of H₂, in order to ensure the power target (Figure 6.2 blue lines)

Consequently, in order to evaluate the influence on the FC performance loss of the electrical and the mechanical components, their power and efficiency versus FC power level has been investigated, as Figure 6.3 and Figure 6.4 shown.

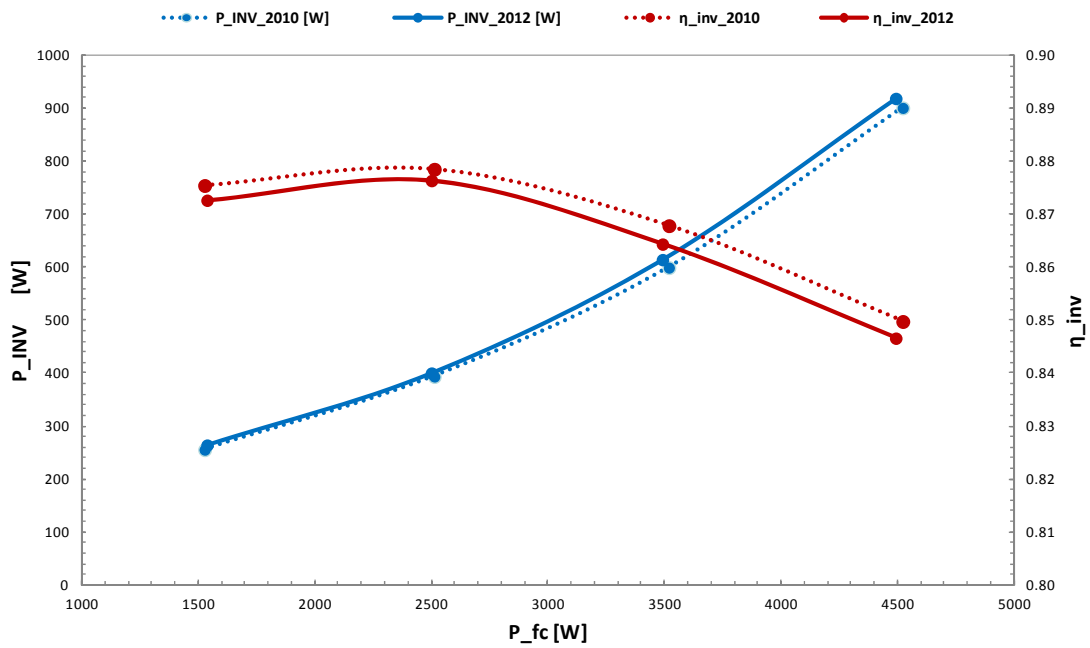


Figure 6.3: Ageing of the inverters: efficiency (red line) and power (blue line) versus FC power level, considering 50 h of operation. (2010 tests (dotted line) VS 2012 tests (continuous line)).

Both inverters (Figure 6.3) and auxiliaries (Figure 6.4) performance have been degraded. In fact, comparing the 2010 data with the 2012 ones, efficiency and also power drop are present. However, these losses do not result in a significant contribution to the system energy balance.

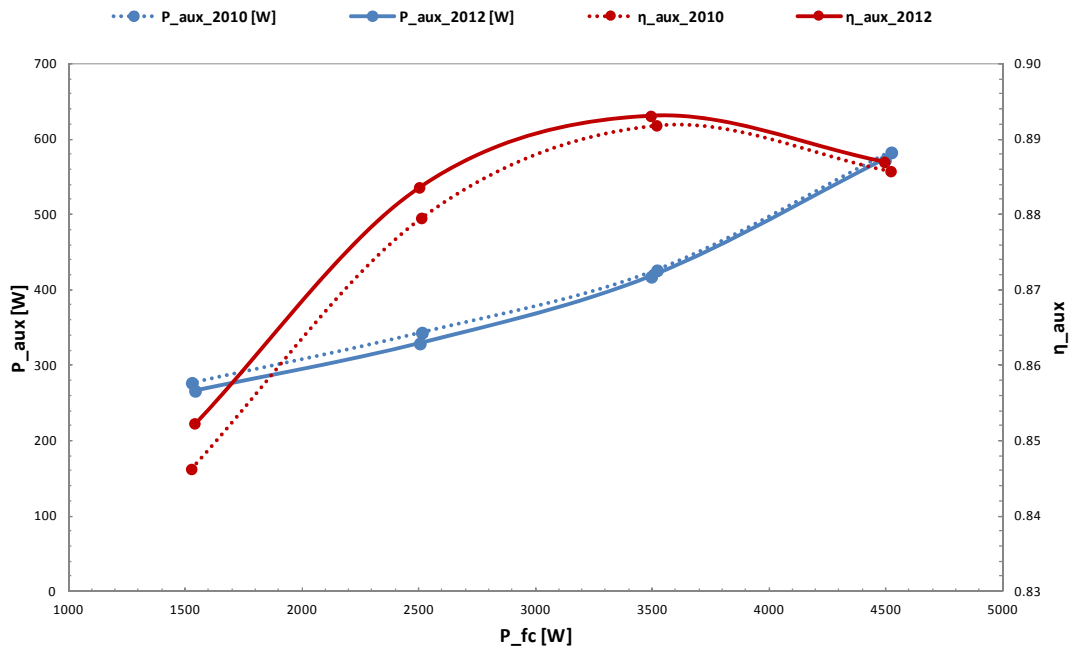


Figure 6.4: Ageing of the auxiliaries: efficiency (red line) and power (blue line) VS FC power level.

Using the developed U_f calculation algorithm (chapter 5), the mass flow rates of the H_2 introduced at the anode side, reacted in the electrochemical reactions and not-reacted, with the corresponding mass has been calculated (Figure 6.8 to Figure 6.15) for different power level 1500 W to 4500 W, with a step of 1000 W. For the comparison between the 2010 data and 2012 ones, a flooding time of 20 s and a purge time of 2.5 s as the purge programming logic have been assumed.

The significant contribution to aging is given by the fuel utilization coefficient, U_f . As shown in Figure 6.5, U_f have a very high drop at both low and medium loads.

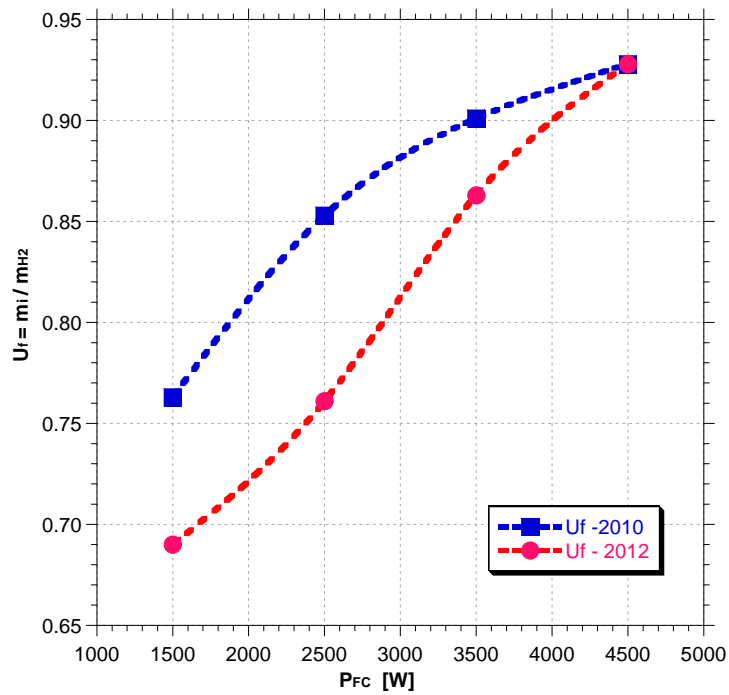


Figure 6.5: Ageing of the PEMFC: the fuel utilization factor, U_f versus FC power level, considering 50 h of operation. (2010 tests (blue line) VS 2012 tests (red line)).

Furthermore, the two fractions of the not-reacted H_2 due the purging, X_{DE} , (Figure 6.6), and to the crossover phenomenon, X_A , (Figure 6.7), have been analyzed.

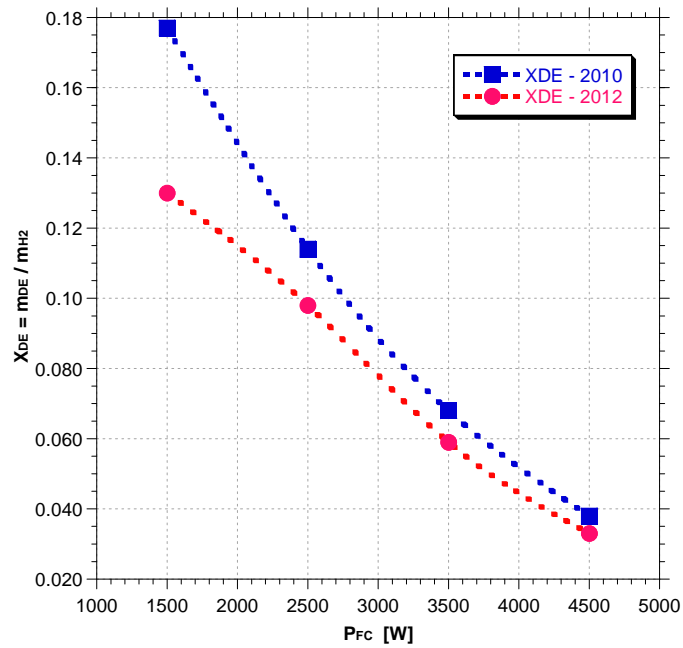


Figure 6.6: Ageing of the PEMFC: the amount of H₂ expelled through the OCV, X_{DE} versus FC power level, considering 50 h of operation (2010 tests (blue line) VS 2012 tests (red line)).

After 50 h of operation the effect of the ageing on X_{DE} (Figure 6.6) is present but limited, more sensible at low loads than at middle-high.

Instead the fraction X_A, due to the crossover, (Figure 6.7) shows, even after only 50 h of discontinuous operation an evident degradation particularly at low loads.

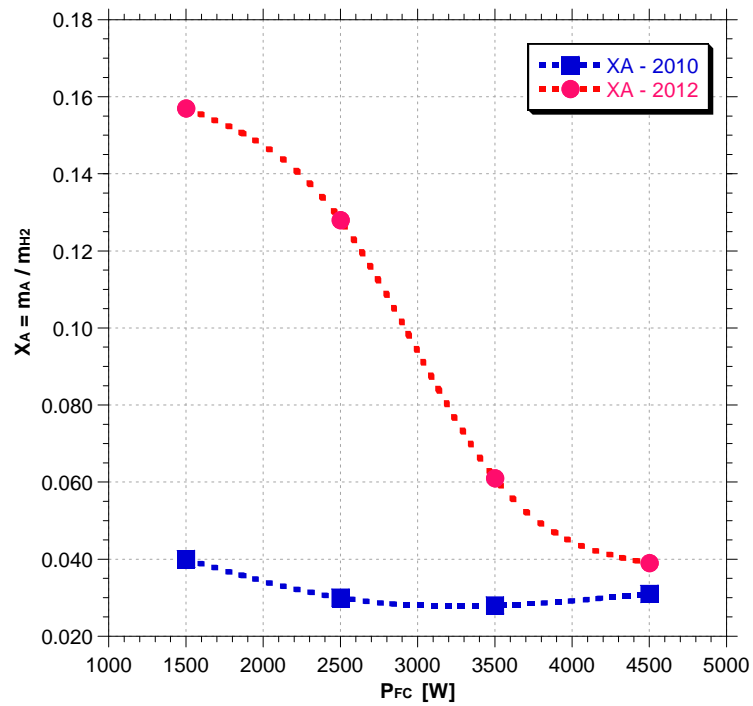


Figure 6.7: Ageing of the PEMFC: the amount of H₂ not-reacted due to crossover phenomenon, X_A versus FC power level, considering 50 h of operation (2010 tests (blue line) VS 2012 tests (red line)).

Hence, the main cause of the PEMFC aging is to be attributed to the H₂ crossover phenomenon (Figure 6.7).

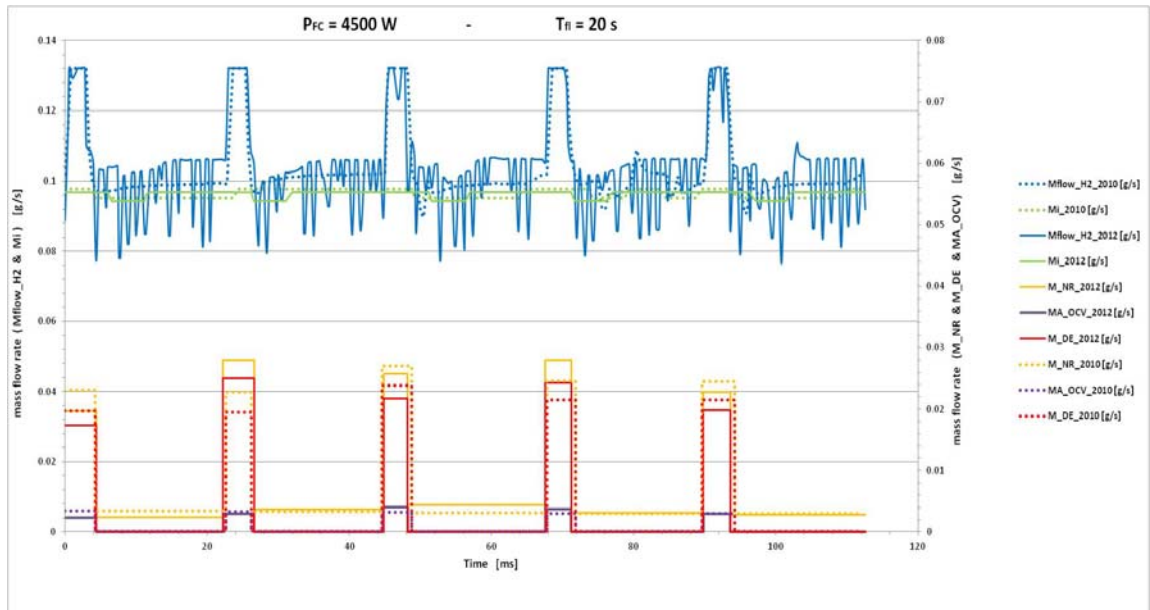


Figure 6.8: Ageing analysis, considering 50 h of operation: 2010 tests (dotted line) VS 2012 tests (continuous line): the mass flow rate of the H₂: introduced, (M_{flow_H2}, blue line), actually reacted (M_i, green line), not-reacted (M_{NR}, orange line), purged (M_{DE}, red line) and lost due to crossover phenomenon (M_{A_OCV}, purple line) VS time, with $P_{FC} = 4500 \text{ W}$; $T_{fl} = 20 \text{ s}$.

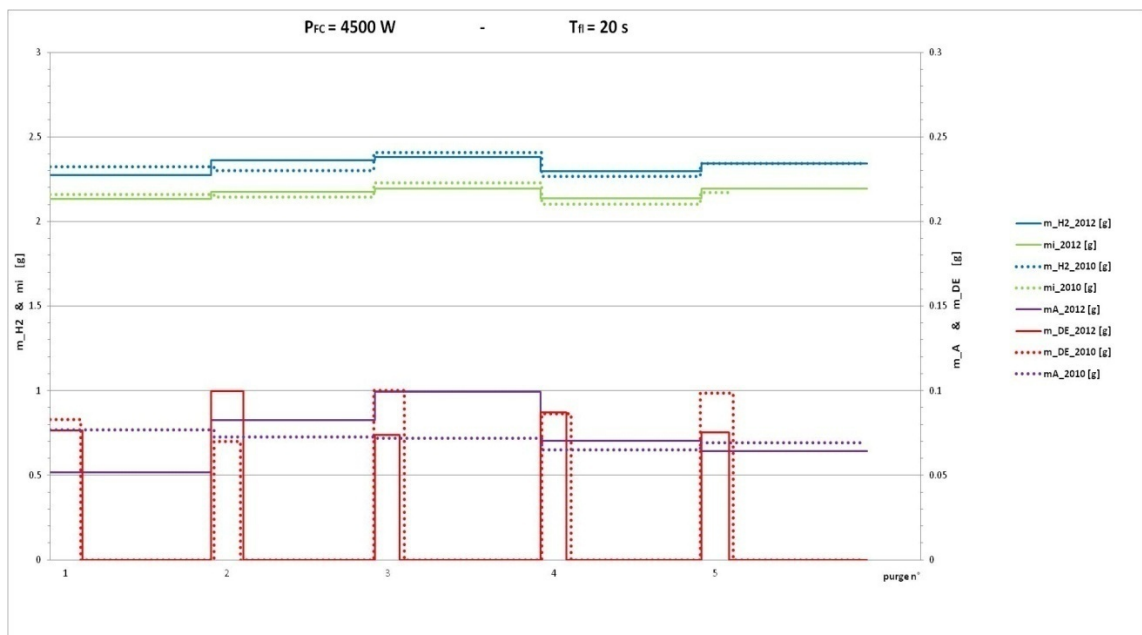


Figure 6.9: Ageing analysis, considering 50 h of operation: 2010 tests (dotted line) VS 2012 tests (continuous line): the mass of the H₂: introduced, (m_{H2}, blue line), actually reacted (m_i, green line), purged (m_{DE}, red line) and lost due to crossover phenomenon (m_A, purple line) VS time, with $P_{FC} = 4500 \text{ W}$; $T_{fl} = 20 \text{ s}$.

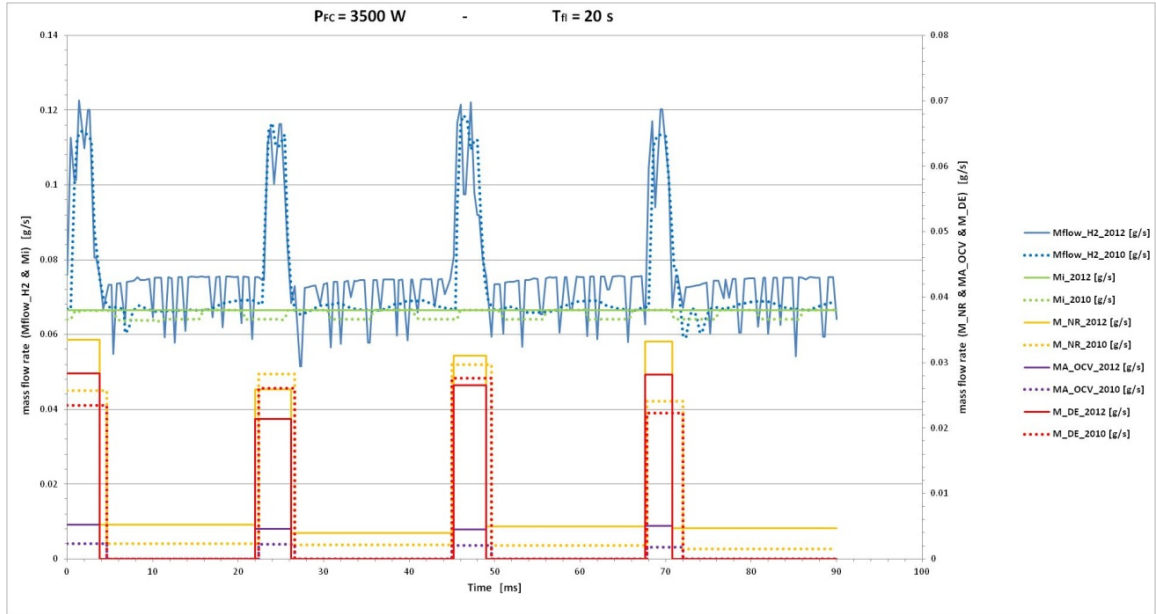


Figure 6.10: Ageing analysis, considering 50 h of operation: 2010 tests (dotted line) VS 2012 tests (continuous line): the mass flow rate of the H₂: introduced, (Mflow_H₂, blue line), actually reacted (Mi, green line), not-reacted (M_NR, orange line), purged (M_DE, red line) and lost due to crossover phenomenon (MA_OCV, purple line) VS time, with $P_{FC} = 3500 \text{ W}$; $T_{fl} = 20 \text{ s}$.

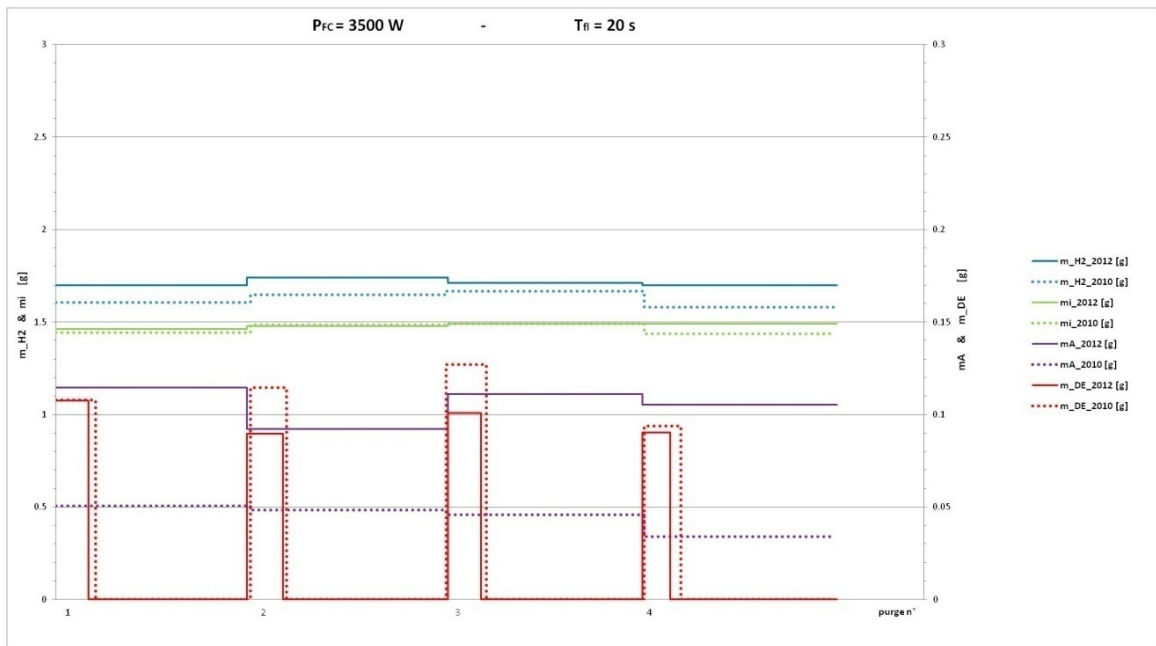


Figure 6.11: Ageing analysis, considering 50 h of operation: 2010 tests (dotted line) VS 2012 tests (continuous line): the mass of the H₂: introduced, (m_H₂, blue line), actually reacted (mi, green line), purged (m_DE, red line) and lost due to crossover phenomenon (mA, purple line) VS time, with $P_{FC} = 3500 \text{ W}$; $T_{fl} = 20 \text{ s}$.

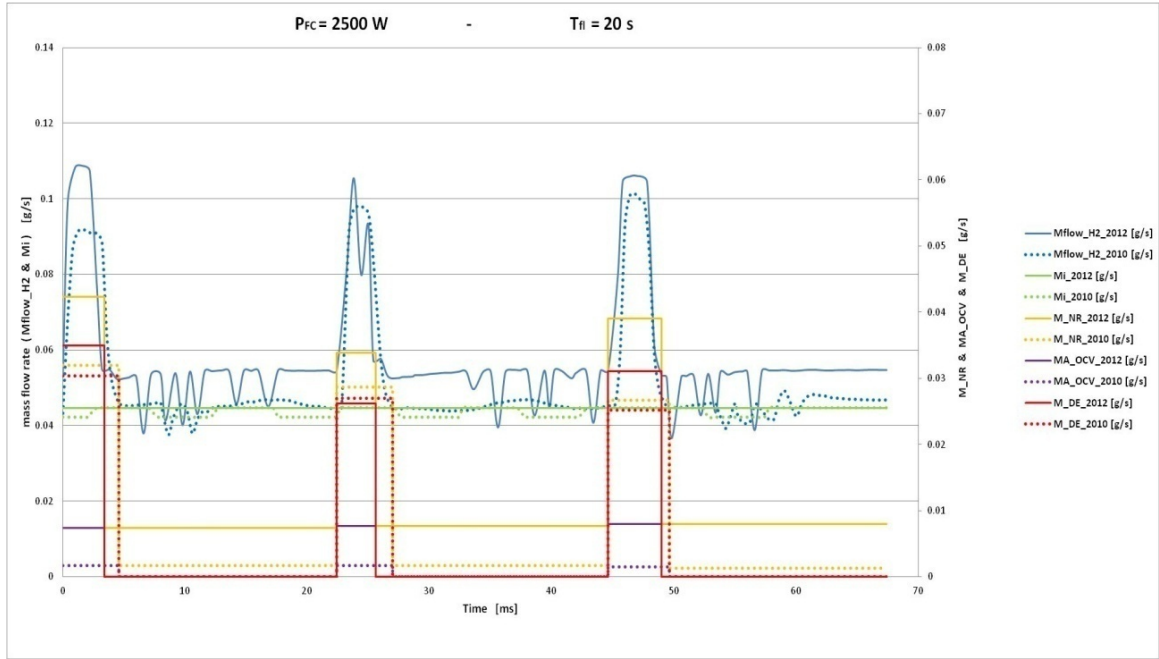


Figure 6.12: Ageing analysis, considering 50 h of operation: 2010 tests (dotted line) VS 2012 tests (continuous line): the mass flow rate of the H2: introduced, (Mflow_H2, blue line), actually reacted (Mi, green line), not-reacted (M_NR, orange line), purged (M_DE, red line) and lost due to crossover phenomenon (MA_OCV, purple line) VS time, with $P_{FC} = 2500 \text{ W}$; $T_{fl} = 20 \text{ s}$.

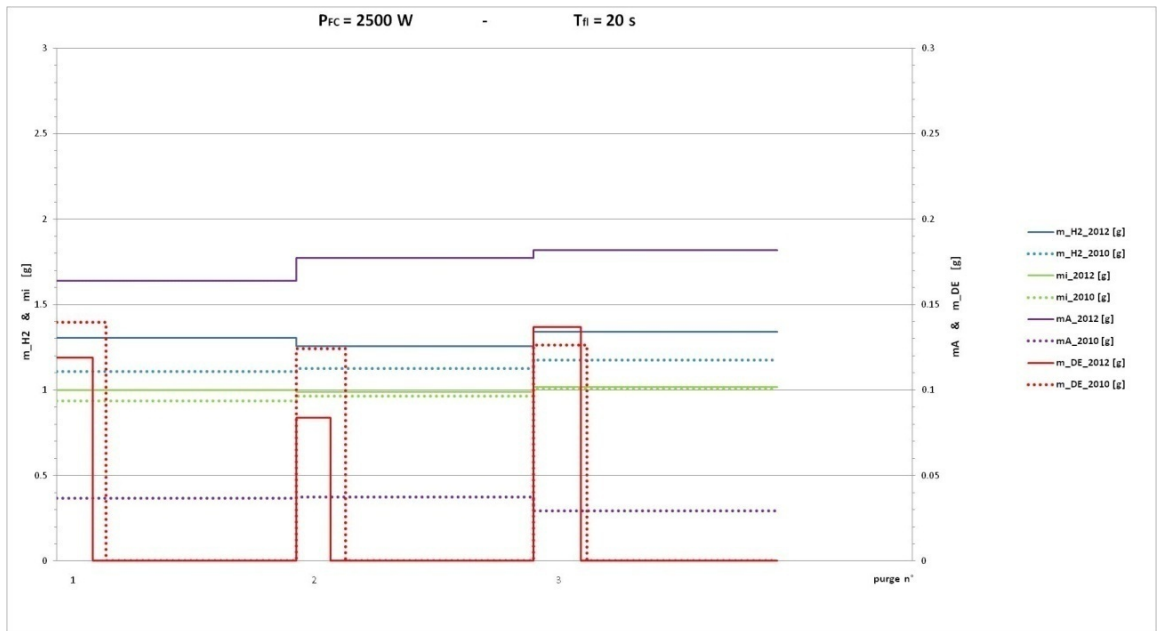


Figure 6.13: Ageing analysis, considering 50 h of operation: 2010 tests (dotted line) VS 2012 tests (continuous line): the mass of the H2: introduced, (m_H2, blue line), actually reacted (mi, green line), purged (m_DE, red line) and lost due to crossover phenomenon (mA, purple line) VS time, with $P_{FC} = 2500 \text{ W}$; $T_{fl} = 20 \text{ s}$.

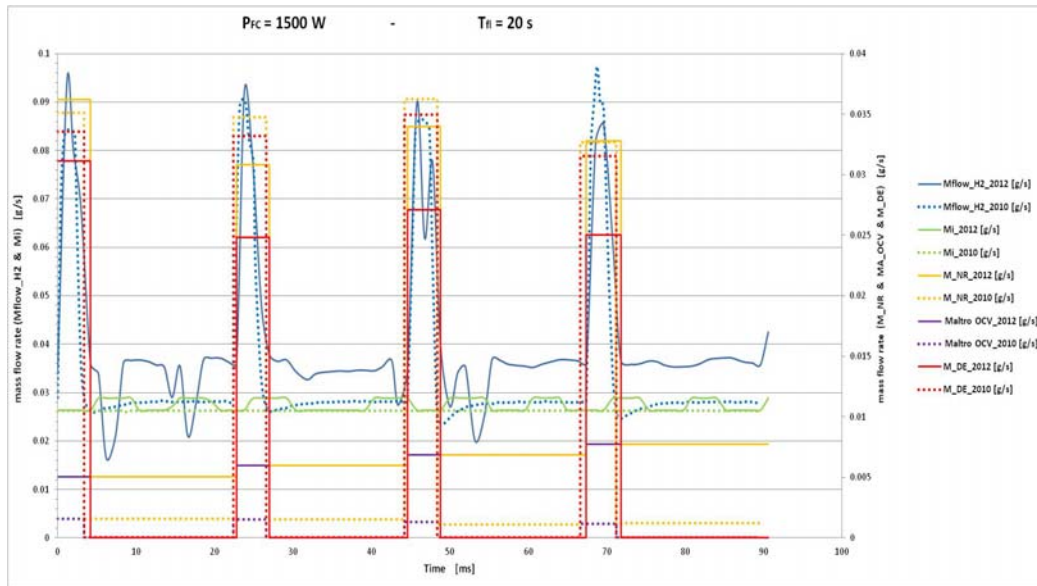


Figure 6.14: Ageing analysis, considering 50 h of operation: 2010 tests (dotted line) VS 2012 tests (continuous line): the mass flow rate of the H_2 : introduced, (M_{flow_H2} , blue line), actually reacted (M_i , green line), not-reacted (M_{NR} , orange line), purged (M_{DE} , red line) and lost due to crossover phenomenon (MA_{OCV} , purple line) VS time, with $P_{FC} = 1500 \text{ W}$; $T_{fl} = 20 \text{ s}$.

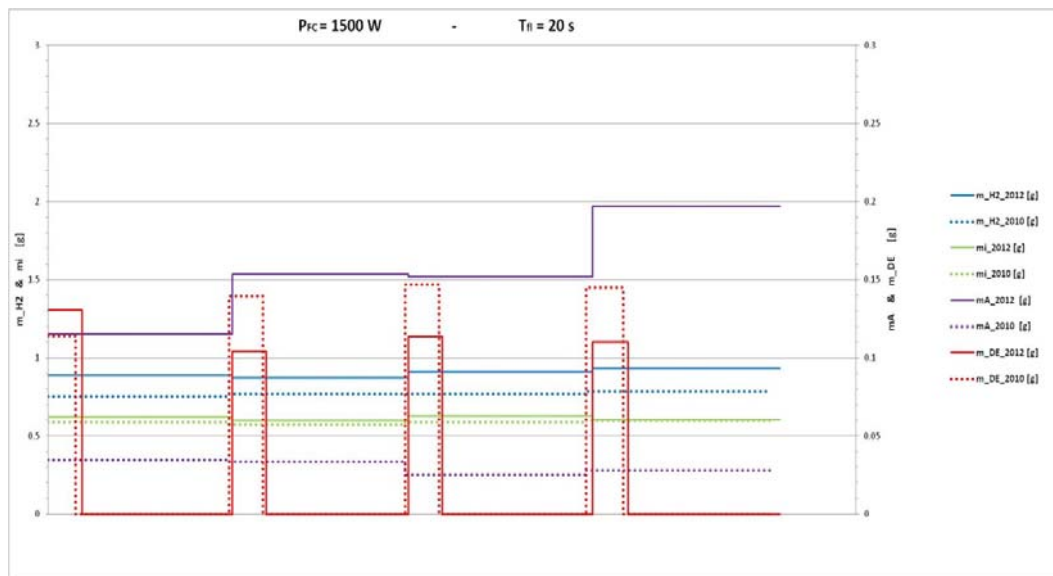


Figure 6.15: Ageing analysis, considering 50 h of operation: 2010 tests (dotted line) VS 2012 tests (continuous line): the mass of the H_2 : introduced, (m_{H2} , blue line), actually reacted (m_i , green line), purged (m_{DE} , red line) and lost due to crossover phenomenon (m_A , purple line) VS time, with $P_{FC} = 1500 \text{ W}$; $T_{fl} = 20 \text{ s}$.

References for chapter 6

- [1] Knights SD, Colbow KM, St Pierre J, Wilkinson DP. Aging mechanisms and lifetime of PEFC and DMFC. *J Power Sources* 2004;127:127.
- [2] T. Payne, *Fuel Cells Durability & Performance*, US Brookline: The Knowledge Press Inc., 2009.
- [3] US DOE -
<http://www1.eere.energy.gov/hydrogenandfuelcells/fuelcells.html>
- [4] X. Yuan, S. Zhang, H. Wang,*, J. Wu, J. C. Sun, R. Hiesgen, K. A.Friedrich, M. Schulze, A.Haug, Degradation of a polymer exchange membrane fuel cell stack with Nafion®membranes of different thicknesses: Part I. In situ diagnosis, *J. of Power Sources*, 195,(2010), 7594–7599.
- [5] X. Yuan, S. Zhang, S. Ban, C. Huang, H.Wang, V. Singara, M. Fowler, M. Schulze, A. Haug, K. A. Friedrich, R. Hiesgen, Degradation of a PEM fuel cell stack with Nafion® membranes of different thicknesses. Part II: Ex situ diagnosis, *J.of Power Sources*, 205, (2012), 324– 334.
- [6] Taniguchi A, Akita T, Yasuda K, Miyazaki Y. Analysis of electrocatalyst degradation in PEMFC caused by cell reversal during fuel starvation. *J Power Sources* 2004;130:42.
- [7] Endoh E, Terazono S, Widjaja H, Takimoto Y. Degradation study of MEA for PEMFC's under low humidity conditions. *Electrochem Solid-State Lett* 2004;7:A209.
- [8] Pe'ron J., Ne'dellec Y., Jones D.J., Roziere J.. The effect of dissolution, migration and precipitation of platinum in Nafion_-based membrane electrode assemblies during fuel cell operation at high potential. *J Power Sources* 2008;185:1209.
- [9] Ferreira PJ, Ia O'GJ, Shao-Horn Y, Morgan D, Makharia R, Kocha S, et al. Instability of Pt/C electrocatalysts in proton exchange membrane fuel cells. *J Electrochem Soc* 2005;152:A2256.

- [10] Ohma A, Suga S, Yamamoto S, Shinohara K. Membrane degradation behavior during open-circuit voltage hold test. *J Electrochem Soc* 2007;154:B757.
- [11] Mohtadi R, Lee W-K, Van Zee JW. Assessing durability of cathodes exposed to common air impurities. *J Power Sources* 2004;138:216.
- [12] Schulze M, Wagner N, Kaz T, Friedrich KA. Combined electrochemical and surface analysis investigation of degradation processes in polymer electrolyte membrane fuel cells. *Electrochim Acta* 2007;52:2328.
- [13] Rong F, Huang C, Liu ZS, Song D, Wang Q. Microstructure changes in the catalyst layers of PEM fuel cells induced by load cycling. Part 1. Mechanical model. *J Power Sources* 2008;175:699.
- [14] De Bruijn F. The current status of fuel cell technology for mobile and stationary applications. *Green Chem* 2005;3:132.
- [15] Rossberg K, Trapp V. In: Vielstich W, Gasteiger HA, Lamm A, editors. *Handbook of fuel cells: Fundamentals technology and applications*, vol. 3. J. Wiley & Sons Ltd; 2003. p. 308.
- [16] Williams MV, Kunz HR, Fenton JM. Analysis of polarization curves to evaluate polarization sources in hydrogen/Air PEM fuel cells. *J Electrochem Soc* 2005;152:A635.
- [17] Weber AZ, Newman J. Effects of microporous layers in polymer electrolyte fuel cells. *J Electrochem Soc* 2005;152:A677.
- [18] Guilminot E, Corcella A, Charlot F, Maillard F, Chatenet M. Detection of Pt²⁺ ions and Pt nanoparticles inside the membrane of an used PEMFC. *J Electrochem Soc* 2007;154:B96.
- [19] Maass S, Finsterwalder F, Frank G, Hartmann R, Merten C. Carbon support oxidation in PEM fuel cell cathodes. *J Power Sources* 2008;176:444.
- [20] Chung CG, Kim L, Sung YW, Lee J, Chung JS. Degradation mechanism of electrocatalyst during long-term operation of PEMFC. *Int J Hydrogen Energ* 2009;34:8974.

- [21] Collier A, Wang H, Yuan X, Zhang J, Wilkinson DP. Degradation of polymer electrolyte membranes. *Int J. Hydrogen Energ* 2006;31:1838.
- [22] Ohma A, Yamamoto S, Shinohara K. Membrane degradation mechanism during open-circuit voltage hold test. *J Power Sources* 2008;182:39.
- [23] Shah AA, Ralph TR, Walsh FC. Modeling and simulation of the degradation of perfluorinated ion-exchange membranes in PEM fuel cells. *J. Electrochem Soc* 2009;156:B465

CONCLUSIONS

The development, from the idea to the actual construction, of the IES has permitted to build an infrastructure capable to connect different energy source for a future exploration of micro-CHP solution.

Focusing on the fuel cell installed into the IES an assessment of its electrical and CHP performance have been done, with particular interest for low and middle power level.

The analysis of the effect of the water management of the anodic exhaust at variable FC loads has been carried out, and the purge process programming logic has been optimized, showing that a fixed flooding time strategy is not optimal if the FC must deliver variable.

Furthermore, the degradation mechanisms of the PEMFC system, in particular due to the flooding of the anodic side, have been assessed using an algorithm that considers the FC like a black box, and it is able to determine the amount of not-reacted H₂ and, therefore, the causes which produce that.

The results obtained clearly show that the primary loss cause, after the purging process, is the H₂ crossover phenomenon.

The algorithm and the index defined will be and useful tool to monitor the FC during its normal life.

Using experimental data that cover a two-year time span, the ageing suffered by the FC system has been tested and analyzed using the same black box method. The cell has seen a degradation of its non full-load characteristic, even if its real number of working hours was very low. Again this loss can be imputed to a degradation of the membrane, as supported by the literature, and consequently by a crossover phenomenon.